Dissertation zur Erlangung des Doktorgrades
der Fakultät für Chemie und Pharmazie
der Ludwig-Maximilians-Universität München

The role of Roquin proteins in B cell physiology and pathology

David Karl Rieß

aus

Mannheim, Deutschland

2017

Erklärung

Diese Dissertation wurde im Sinne von §7 der Promotionsordnung vom 28. November 2011 von Frau Prof. Dr. Elena Conti betreut.

Eidesstaatliche Versicherung

Diese Dissertation wurde eigenständig und ohne unerlaubte Hilfe erarbeitet.

München, 17.7.2017

David Karl Rieß

Dissertation eingereicht am: 30.05.2017
1. Gutachterin: Prof. Dr. Elena Conti
2. Gutachter: Prof. Dr. Hans-Martin Jäck
Mündliche Prüfung am: 06.07.2017

Summary

In jawed vertebrates, B lymphocytes are part of the adaptive branch of the exceptionally complex immune system, which protects the organism from pathogenic infections. B cells are central for antibody-mediated immunity, which relies on the ability of B cells to assemble a BCR receptor that they can secrete as a soluble form, i.e. antibody, upon differentiation to plasma cells. B cells can generate a near infinite number of B cell receptor (BCR) specificities despite the constraint of a size-limited genome. The basis for this BCR diversity is somatic recombination of a vast repertoire of different receptor gene segments encoding the heavy and the light chain of the BCR in the bone marrow. This repertoire is further refined upon antigen encounter and recruitment of naive B cells into germinal centers, specific structures in secondary lymphoid organs, in which somatic hypermutation and class switch recombination improve antigen recognition and effector functions. An elaborate network of transcription factors coordinates the sequential stages of B cell development in the bone marrow by integrating external signals and regulating the somatic rearrangement of the BCR genes. An essential checkpoint that ensures integrity of the heavy chain before enabling subsequent recombination of the light chain and differentiation into small pre B cells is the pre-BCR checkpoint at the large pre B cell stage. Key features of this checkpoint are signaling events downstream of the interleukin-7 receptor (IL-7R), which trigger proliferation of B cells expressing a functional heavy chain. Recent evidence has emphasized that proper B cell development additionally requires post-transcriptional gene regulatory mechanisms.

The novel RNA-binding ROQ domain is present in the recently described Roquin protein family, which comprises Roquin1 and Roquin2. Roquin paralogs post-transcriptionally regulate expression of factors of development and immunity. Following the description of mutated Roquin1 in the *sanroque* mouse strain, which develops a disease resembling human systemic lupus erythematosus, most of the work on the Roquin paralogs has centered on their functions in T lymphocytes. Roquin family proteins are important regulators of the cell fates of follicular helper T cells, T_H17 and NKT17 cells. Recently, a series of publications has presented conserved cis-regulatory motifs, stem-loop structures in target mRNAs, bound by Roquin proteins resulting in recruitment of the CCR4-NOT complex and subsequent mRNA degradation.

In my PhD thesis, I present the first extensive *in vivo* analyses of the role of Roquin1 and 2 during B cell development, maturation and activation by conditional loss-of-function studies in the mouse. B cell-specific ablation of Roquin proteins during early B cell development

(Mb1cre) demonstrates a pivotal role at the pre-BCR checkpoint with loss of all four alleles of Roquin1 and 2 resulting in a complete block at the pro to pre B cell transition, whereas inactivation of two Roquin1 alleles or two Roquin1 alleles and one Roquin2 allele results in intermediate phenotypes. This block appears independent of heavy chain expression or formation of the pre-BCR and is characterized by a defect of Roquin1/2-deficient large pre B cells to maintain high levels of the IL-7R and correlating proliferative defects. Additionally, Roquin1/2-deficient large pre B cells fail to upregulate the chemokine receptor CXCR4, which relies on pre-BCR signaling and governs migratory processes involved in the transition of large to small pre B cells. Pre-BCR-dependent signaling in Roquin1/2 double-deficient pre B cells fails to properly upregulate the transcription factors IRF4 and Aiolos. Consequently, peripheral B2, but also B1 cells are completely absent in these mice. Insertion of a pre-rearranged light chain shows that this developmental defect is independent of light chain expression deficits in Roquin1/2-deficient pre B cells. Insertion of a pre-rearranged BCR heavy chain in Roquin1/2-deficient B cells on the other hand rescues the pre B cell compartment, but these B cells do not develop past the immature stage.

B cell-specific ablation of Roquin paralogs in B cells at a later developmental stage (CD19cre), leads to generation of significant numbers of splenic and mature B cells, highlighting the control of specific developmental checkpoints by Roquin1 and 2. Yet, Roquin1/2-deficient peripheral B cells are impaired in their maturation and are counterselected. These double-deficient peripheral B cells seem hyperactivated in the absence of stimulation and exhibit signs of altered BCR signaling. Likewise a hyperactivated state is observed in B cells with Mb1cre-mediated inactivation of two alleles of Roquin1 with or without additional loss of one allele of Roquin2. The B cell activation status correlates in all three mouse models with significant B cell extrinsic effects, such as an increase of the $CD4^+$ and $CD8^+$ effector memory T cell compartments.

Additionally, I present my efforts at investigating the structure of the RNA-binding ROQ domain and unraveling novel RNA targets to further enhance our understanding of the importance of post-transcriptional gene regulation in B cell immunology. My findings on Roquin-mediated mRNA binding were confirmed and extended by publications that were released during the course of my PhD work and ended my own efforts.

In conclusion, my investigation of the function of Roquin1 and 2 contributes significantly to the appreciation of the role of post-transcriptional gene regulation in the development of B cells and in the generation of B cell-mediated immunity. Furthermore, my results open new exciting research questions on the function of post-transcriptional gene regulation in B cells.

Table of contents

I. Introduction

1. B lymphocytes as critical players in the immune system

All the protective means that have evolved to guard an organism against invading pathogens can be collectively encompassed in an organism's immune system. Mammalian immunity has been separated into two types of reactions, innate and adaptive responses that are intertwined in manifold and complex ways to provide systemic protection. Generally, innate immune reactions are rapidly initiated following detection of conserved structures on pathogenic microbes via germline-encoded pattern recognition receptors [1].

The adaptive arm of the immune system defends the host from intruders by continuously generating an enormous amount of distinct B and T lymphocytes, which can potentially detect any pathogen via their unique antigen receptors. Differentiation into antibody-producing plasma cells and memory B cells with the capacity to rapidly respond to reinfection are key features of the B lineage that confer protection from pathogens. The receptors of B and T cells are generated by somatic gene rearrangements of a vast repertoire of different receptor genes. This capacity allows lymphocytes of equal i.e. clonal origin to specifically recognize a certain antigenic epitope. Upon activation, B cells that receive help form cognate follicular T helper (T_{FH}) cells are recruited into structures called germinal centers (GCs). Here, random mutations are introduced into the antigen-recognizing part of their antigen receptor gene in a process termed somatic hypermutation. B cells are then selected based on their ability to recognize antigen presented by follicular dendritic cells with high affinity and present the antigen to T_{FH} cells. B cells also switch their antigen receptor isotype through class-switch recombination and subsequently differentiate into plasma or memory B cells.

The quasi-randomness of somatic rearrangements and hypermutations often leads to autoreactive antigen receptors, with potentially deleterious consequences. Hence, during the development of a B cell, several mechanisms at distinct checkpoints are in place to control the specificity and prevent autoreactivity of a B cell antigen receptor (BCR) [2, 3]. This underlines the importance of preventing alterations in B cell activation. Malfunctioning of these regulatory mechanisms in suppressing an immune reaction to a self-structure can lead to different autoimmune diseases such as rheumatoid arthritis, systemic lupus erythematosus (SLE) and psoriasis.

The following section will emphasize the stages in the primary and secondary lymphoid organs (SLOs), which a B cell passes during its development. Upon encounter of cognate antigens mature B cells terminally differentiate into plasma cells and memory B cells, mostly via the GC reaction. I will emphasize how somatic rearrangement in the bone marrow generates a diverse BCR repertoire, which is then further refined in the GC reaction in terms of antigen recognition and effector functions. This ultimately provides the foundation of BCR-mediated antigen recognition and durable immune protection.

1.1 Early hematopoiesis and lineage commitment

The bone marrow is a hematopoietic organ located inside bones. It comprises the parenchyma, the site of adult hematopoiesis, and the stroma, a vascular component [4]. The bone marrow is composed of numerous different microniches that each support distinct hematopoietic processes and comprises different cell types [5]. Pluripotent, self-renewing hematopoietic stem cells (HSCs), which are the origin of every hematopoietic lineage, can be found in the fetal liver. From there they colonize the fetal bone marrow during fetal development [6, 7]. HSCs lose their self-renewal potential as they differentiate. Lineage commitment is mainly achieved by ordered activation of key transcription factors eventually resulting in precursors restricted to single lineages. HSCs differentiate into multipotent progenitors (MPPs) [8]. In the prevailing model, MPPs undergo the initial step of lineage commitment separating myelopoiesis and lymphopoiesis by development into the oligopotent common myeloid progenitors (CMPs) or the common lymphoid progenitors (CLPs), respectively [8]. In the so far generally accepted model, CMPs can differentiate into granulocyte/monocyte progenitors (GMPs) or into megakaryocyte/erythroid progenitors (MkEP). GMPs are the origin of granulocytes (basophils, eosinophils and neutrophils) and monocytes and macrophages whereas MkEPs can develop further into megakaryocytes and erythrocytes. Recently, the concept of a uniform CMP population has been challenged. CMPs were suggested to rather consist of a pool of unipotent progenitors, which can directly give rise to the above-mentioned lineages [9]. The CLPs can give rise to dendritic cells, NK cells, T cells and B cells [8].

1.2 Commitment to the B cell lineage

Commitment to B cell lymphopoiesis is the result of serial action of many pivotal transcription factors. IRF8 regulates expression of PU.1, which synergizes with Ikaros, to

induce MPP development, at which stage E2A proteins further determine commitment [10-12]. E2A proteins activate early B cell factor (EBF1), an essential step for differentiation of prepro B cells. EBF1 acts synergistically with forkhead box O1 (FOXO1) to confer the B cell fate onto prepro B cells [13, 14], which critically involves activation of paired box protein 5 (PAX5) by these factors [15-17]. EBF1 and PAX5 act together to repress other hematopoietic potentials [15, 18].

1.3 Orchestration of B cell development in the bone marrow

V(D)J recombination and classical non-homologous end joining repair (cNHEJ). A characteristic feature of B and T lymphocytes is the generation of a near infinite number of different receptors despite the constraints of a size-limiting genome [19]. In B cells, this is achieved by the process of somatic gene recombination of variable (V), diversity (D) and joining (J) gene segments in the loci encoding for the Ig heavy chain (IgH: V, D and J) and light chain (IgL, respectively Igκ and Igλ: V and J). Consecutive stages of early B cell development in the bone marrow have been designated based on the ordered patterns of V(D)J recombination in the IgH and IgL chain loci together with surface marker expression (Fig. 1) [20]. The V(D)J recombination products, a V_HDJ_H gene exon (IgH) and a $V_\kappa J_\kappa$ or $V_\lambda J_\lambda$ (IgL) gene exon respectively, encode for the variable component of the antigen receptor. This variable part comprises the three complementary determining regions (CDRs) where antigen contact is made. The recombination activating gene (RAG) protein complex, consisting of RAG1 and RAG2, initiates V(D)J recombination upon binding to recombination signal sequences (RSSs). The RSSs flank recombining V, D and J segments, followed by site-specific cleavage. The resulting DNA hairpin ends are processed by RAG and factors of the classical non-homologous end joining (cNHEJ) repair pathway to join gene segments [21]. RSSs are composed of two highly conserved DNA motifs, a palindromic heptamer sequence and an AT-rich nonamer sequence. These sequences are separated by a spacer region of 12 or 23 bases forming either a 12RSS or a 23RSS respectively [22]. Recombination in the IgH and the IgL loci follows the 12/23-rule, a restriction confining joining of gene segments by V(D)J recombination to complementary 12 and 23RSSs [23].

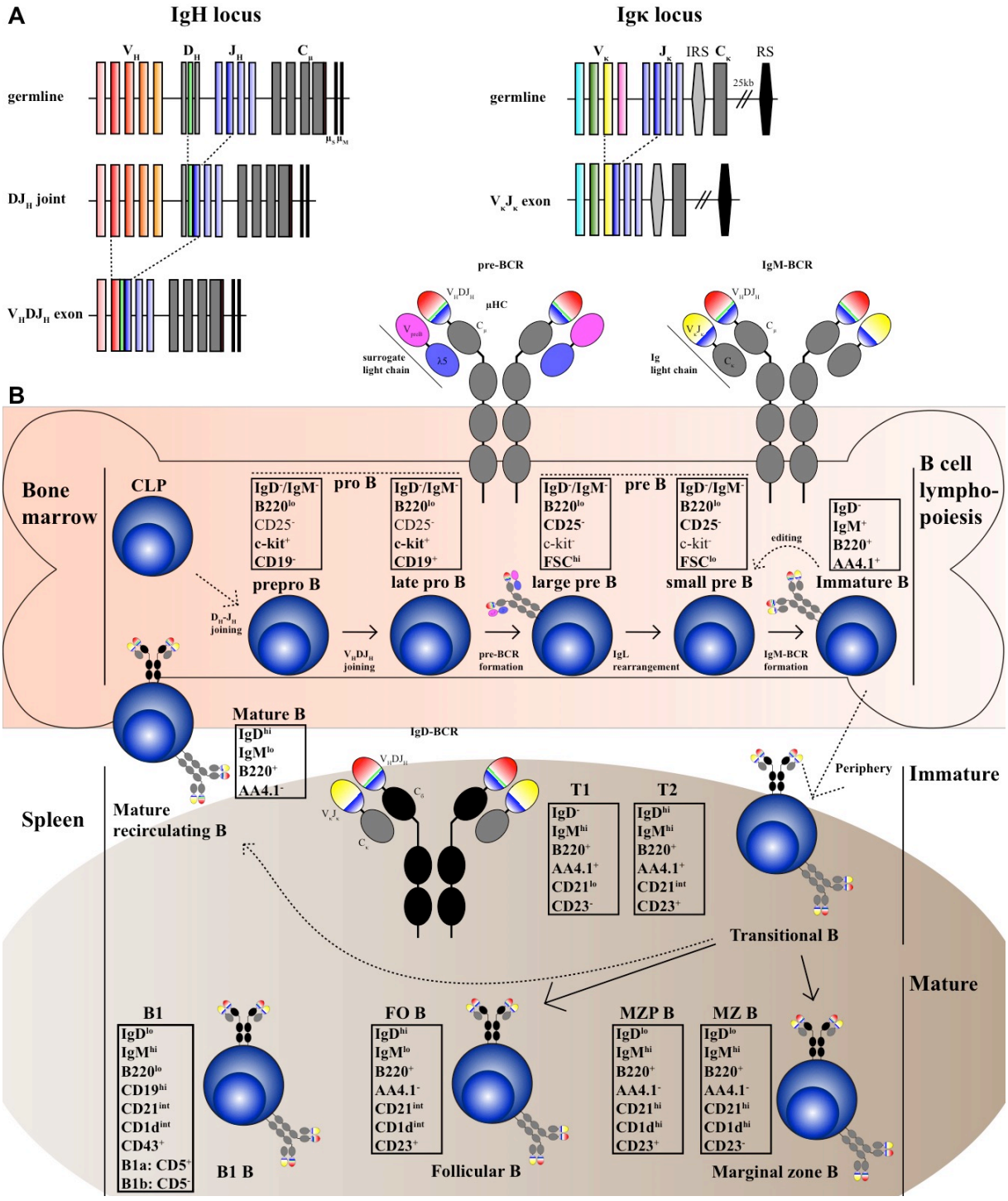

Figure 1: Simplified illustration of early B cell lymphopoiesis and B cell maturation in the periphery.
(A) Simplified scheme of the Ig heavy chain (IgH) and the Igκ light chain loci in germline and rearranged configurations. The V_HDJ_H exon encodes the variable part of the μHC and Cμ its constant region, which joins the V_HDJ_H exon through splicing. Alternative splicing governs expression of a secreted BCR as antibody (μ_S) or a membrane-bound BCR (μ_M). The arrangement of Vκs and Jκs allows for multiple successive rearrangement attempts at the Igκ locus, while joining of a Vκ segment or intronic recombination signal sequence (IRS) to the non-coding recombining sequence (RS) closes the locus for further rearrangements. (B) Simplified overview of B cell development in the bone marrow (BM) and periphery with expressed surface markers used for flow cytometry at defined stages. B cell development is initiated with V(D)J recombination at the IgH locus during the pro B cell stage, which results in expression of μHC together with a surrogate light chain as the pre-BCR on large pre B cells. Pre-BCR signaling induces IgL chain rearrangement, first at the Igκ locus, enabling expression of the IgM-BCR, the first BCR expressed on the surface of immature B cells. *(Continued on next page)*

Immature B cells can egress from the bone marrow and enter the periphery as transitional (T1, T2) B cells, which migrate to the spleen, where they mature into follicular (FO B) or via marginal zone precursor B cells (MZP B) into marginal zone (MZ B) B cells. T2 B cells acquire the ability to recirculate to the BM. Mature B1 cells are also present in spleen.

In the IgH locus, V_Hs are flanked by 23RSSs, D_Hs on both ends by 12RSSs and J_Hs by 23RSSs, whereas in the IgL loci V_κs and J_λs are flanked by 12RSSs and J_κs and V_λs by 23RSSs [24]. The 12/23-rule guides V(D)J recombination by preventing direct V_H to J_H rearrangements and enables additional regulatory processes, such as secondary rearrangements in the IgL loci [19, 25].

The structure of the κ locus is unique, with an upstream set of V_κ gene segments, followed by four J_κs genes, an intronic recombination signal sequence (IRS), the κ constant (C_κ) region and the non-coding recombining sequence (RS), 25 kb downstream of the C_κ region (Fig. 1) [26, 27]. In case of a non-functional or self-reactive $V_\kappa J_\kappa$ joint, this can be replaced by further rearrangement of a more 5' V_κ gene and a more 3' J_κ gene, thereby deleting the intervening previous $V_\kappa J_\kappa$ joint. Most of the λ light chain expressing B cells have terminally rearranged the κ locus. This closure of the κ locus can occur by secondary rearrangement of either a V_κ gene or the IRS to the RS sequence thereby deleting the C_κ region and precluding further productive rearrangements in this locus [27-29].

RAG nucleases tightly connect introduction of DSBs with specific repair by cNHEJ, a function primarily attributed to RAG2. This function greatly minimizes the risk of chromosomal translocations [30-32]. At the beginning of V(D)J rearrangement, RAG proteins form a synaptic complex by simultaneous binding to a 12RSS and a 23RSS [25]. The RAG complex introduces DSBs between the gene segments and the RSSs and holds all four ends in a post-synaptic complex. Gene segments end in hairpin structures, while RSSs have blunt ends [22], which are both subsequently bound by the Ku70/80 heterodimer [21]. Ku70/80 initiate cNHEJ by serving as a scaffold and recruiting DNA-dependent protein kinase catalytic subunit (DNA-PKcs), the nuclease Artemis, X-ray cross complementing protein 4 (XRCC4), DNA Ligase IV (Lig4), terminal deoxynucleotidyl transferase (TdT) and components of the DNA-damage response [22]. The blunt ends of the RSSs are immediately ligated by action of an XRCC4/Lig4 complex forming an RSS joint. In contrast, the hairpin ends are opened by Artemis, which enables processing of the open DNA ends. This step is followed by subsequent XRCC4/Lig4-mediated ligation generating a coding joint [22]. Junctional diversification of gene segment ends in the coding joint is achieved by nucleotide loss as consequence of cNHEJ repair and addition of non-templated nucleotides in opened hairpins by TdT.

TdT expression in B cells is confined to pro and pre B cell stages [19, 21, 32]. RAG-mediated V(D)J recombination is essential for the development of mature T and B lymphocytes [33, 34], yet harbors the potential to promote lymphocytic malignancies [35, 36]. Tight regulatory mechanisms control V(D)J rearrangement in an allele-, stage- and lineage-specific manner [37]. These include restriction of RAG expression, regulating RSS accessibility, subnuclear localization of gene segments and topology of Ig gene receptor loci [25, 38, 39].

The relation and regulation of V(D)J rearrangement and B cell stages. D_H to J_H segment recombination occurs on both IgH alleles producing DJ_H joints in prepro B cells (Fig. 1). V_H to DJ_H joining is initiated subsequently in pro B cells [40, 41]. Upon productive in-frame assembly of a V_HDJ_H exon, which results in expression of an Igμ heavy chain protein (μHC or Igμ), the late pro B cells transits to the large pre B cell stage [42]. Transcription of μHC-encoding mRNA is initiated at the promoter of a V gene, runs through the rearranged V_HDJ_H exon and adjacent 3' exons, which encode the constant (C_H) region Cμ and in some cells also a second constant region, Cδ [43, 44]. Alternative splicing of these IgH transcripts regulates usage of the constant region (Igμ vs. Igδ decision) as well as expression of a membrane-bound BCR (μ_M) or its secreted form, the antibody (μ_S) (Fig. 1) [45]. The immature bone marrow B cell subsets, the first B cell subset that continuously expresses a surface B cell receptor (BCR), solely expresses membrane-bound Igμ [46]. This Igμ protein is expressed transiently on the cell surface of large pre B cells in a membrane complex with the surrogate light chain proteins V_{preB} and λ5 which are joined by the transmembrane proteins Igα and Igβ to form the pre-B cell receptor (pre-BCR) [47, 48]. Pre-BCR surface expression and signaling constitutes a quality feedback control mechanism essential for allelic exclusion in B lymphopoiesis. Pre-BCR expression at this developmental stage confirms successful rearrangement of one IgH allele and shuts down rearrangement on the other [49, 50]. Large pre B cells express the pre-BCR on the surface, which promotes a proliferative burst that ensures that enough cells carrying a productive IgH joint can undergo V(D)J recombination of the IgL chain loci. Somatic rearrangement of the Igκ locus normally precedes Igλ rearrangement at the ensuing small pre B cell stage [51]. Successful $V_\kappa J_\kappa$ or $V_\lambda J_\lambda$ gene segment recombination forms a light chain variable region that is transcribed in association with a downstream constant (C_κ or C_λ) region for subsequent expression of an IgL chain protein that can assemble with the existing μHC protein to form an IgM molecule [43]. Consecutively, a membrane-bound IgM molecule is expressed on the surface of immature B cells, the BCR common to all (antigen-)naive B cells. BCR expression represents a further major quality control checkpoint in B cell development and the first in which the newly

formed BCR is tested for self-reactivity, to avoid BM egress of autoreactive B cells [3, 52]. This is a crucial feedback mechanism as at least 50% of the initial BCR output in human and mice was reported to be self-specific [53, 54]. Autoreactive B cells can undergo receptor editing changing the specificity of their BCR to avoid clonal deletion. Clonal deletion is the apoptotic cell death of B cells with persisting self-reactivity, a mechanism of central B cell tolerance [3]. Reacquisition of self-tolerance relies largely on secondary IgL rearrangements that allow autoreactive B cells to change the expressed light chain [3]. In contrast, the extent of contribution of V_H replacement, a process in which the V_H part of an expressed V_HDJ_H exon is replaced by an upstream V_H element, as a means of central tolerance remains under investigation [55-57]. Furthermore, self-reactive BCRs of low avidity can escape clonal deletion, differentiate and convert to an anergic stage [52].

Molecular signaling events downstream of IL-7R and pre-BCR. Developing B cells maintain genomic integrity by clear segregation of their two major signaling cascades. These are the opposing IL-7 receptor (IL-7R, composed of IL-7Rα and the common γ chain) and pre-BCR signaling pathways [58]. The intertwined signaling pathways originating from these two receptors provide the intricate foundation of the pre-BCR checkpoint. This checkpoint connects proliferation mainly mediated by the IL-7R with signaling from the pre-BCR to induce V(D)J recombination in the IgL gene loci [59]. This separation is already reflected by the confinement of V(D)J recombination to the G_0 and G_1 phases of the cell cycle. This is partly achieved by the phosphorylation of RAG2 at Thr490 by CDK2, the most prominent CDK in late G_1 phase, signaling the degradation of RAG2 [19, 25]. The underlying regulatory molecular network ensures dominance of the respective pathway to properly decide early B cell fate [60]. Pro B cell survival and proliferation is largely driven by IL-7R signaling through signal transducer and activator of transcription 5 (STAT5) and the phosphoinositide 3-kinase (PI3K)-AKT pathway [61]. Downstream of STAT5, expression of the B cell lymphoma 2 (BCL2) family members myeloid cell leukemia 1 (MCL1) and BCL2 is activated and mediates pro B cell survival [60]. Key targets of the PI3K pathway are transcription factors of the FOXO family, which are phosphorylated by AKT promoting their nuclear export and subsequent proteosomal degradation [42]. Nuclear FOXO1 and FOXO3a are among the factors that induce expression of the RAG complex leading to pre-BCR expression and transition to the pre B cell stage [62, 63]. Recent studies have highlighted a role of the transcription factor BTB and CNC homologue 2 (BACH2) in the negative selection of pro B cells that fail to productively rearrange the IgH locus [64, 65]. Initial low levels of the negative regulator of the PI3K-AKT pathway, SH2-domain-containing

leukocytes protein of 65kDa (SLP65) are thought to allow the newly formed large pre B cells to undergo four to five rounds of proliferation concomitant with high expression levels of IL-7R [59, 60, 66]. Signals downstream of the pre-BCR result in upregulation of SLP65 levels terminating proliferation and activating RAG expression as well the expression of several factors including interferon regulator factors 4, 8 (IRF4, IRF8) and BCL6 [67]. Tyrosine kinases such as spleen tyrosine kinase (SYK) or ζ-chain-associated protein kinase of 70 kDa (ZAP70) are among the first factors recruited to the pre-BCR upon receptor engagement to further relay and amplify the signaling. They activate SLP65 by multiple phosphorylations [42]. BCL6 positively selects pre B cells, which express a productive, signaling competent μHC by counteracting the apoptosis inducing function of BACH2 through repression of DNA damage response and checkpoint genes [65, 68]. Transcription of BCL6 is activated by FOXO1, which is retained in the nucleus as a consequence of SLP65 signaling, and aids in maintaining a quiescent state, which further stabilizes RAG2 [67]. IRF4 is essential for inducing expression of Ikaros and Aiolos, all of which are pivotal to render the IgL gene loci accessible for V(D)J recombination, to downregulate SLC components and to terminate proliferation [42, 69, 70]. Moreover, expression of Aiolos is activated by extracellular signal-regulated kinase (ERK) downstream of pre-BCR signaling independent of IRF4 [71]. However, pre-BCR signaling is insufficient to initiate V(D)J recombination in small pre B cells. IgL recombination occurs only if IL-7R signaling is attenuated, which depends on the action of SLP65 [71, 72].

Instructive roles of distinct bone marrow niches. The diverse microniches of the bone marrow provide spatial and temporal cues for HSCs and developing B cells in the context of cytokines, chemokines, growth factors and cell-cell contacts [73]. The chemokine CXCL12 and its receptor CXCR4 are the main regulators of HSC migration during adult life and are already central to B cell development in the fetal liver and immigration of HSCs into the emerging fetal bone marrow [7, 73]. Both contribute essentially to the localization and the maintenance of developing B cells in the adult bone marrow [74, 75]. CXCL12 is found within the entire bone marrow as part of the extracellular matrix, immobilized to stromal cells or soluble [76]. Prepro B cells localize with $CXCL12^{hi}$ expressing cells, whereas pro B cells are associated with stromal cells producing high levels of IL-7 in a $CXCL12^{lo}$ environment [77]. Retention of pro B cells in their microniche has been shown to rely on CXCR4-based activation of focal adhesion kinase (FAK). FAK increases affinity of very late antigen 4 (VLA4/α4β1integrin) for its ligand vascular cell adhesion molecule 1 (VCAM1) [76]. CXCR4 levels steadily decline from the pro to immature B cell stage [78], yet following pre-

BCR signaling, IRF4 induces transient high expression levels of CXCR4 [79]. This induced CXCR4 expression was suggested to result in migration of pre B cells away from bone marrow niches rich in IL-7 towards CXCL12-expressing stromal cells, providing an essential step in the dampening of IL-7R signaling in small pre B cells [60]. Termination of IL-7R signaling besides pre-BCR signaling enables V(D)J recombination in the IgL loci in small pre B cells [71, 72]. After the successful expression of an innocuous BCR, immature B cells that are located close to the bone marrow sinusoids can egress. Immature B cells leave the parenchyma with the bone marrow perfusing blood stream and enter the sinusoids from the bone marrow by down regulating CXCR4 [78, 80]. Many immature B cells in lupus models express high levels of CXCR4 [81] and BCR engagement of immature B cells results in failure to downmodulate CXCR4 expression [80]. Therefore, CXCR4-mediated BM retention of self-reactive immature B cells likely enables receptor editing and contributes thereby to central tolerance.

1.4 Maturation of naive B cells in the periphery

Immature or transitional B cells. Immature B cells carrying a non self-specific BCR can egress from the bone marrow into the periphery as immature or transitional B cells. Immature B cells have short half-lives and express markers of immaturity, such as AA4.1 (CD93) (Fig. 1). Splenic transitional B cells have been resolved into three different populations with their successful development culminating in the binary commitment choice between a marginal zone and a follicular B cell fate. Survival of transitional T1 cells is governed by tonic BCR signaling, these cells lack the ability to recirculate and locate to the bone marrow and spleen. In mature B cells, tonic BCR signaling has been shown to rely on downstream PI3K activity involving FOXO1 [82]. Upon entering splenic follicles, these cells mature into T2 B cells, which acquire the ability to recirculate through spleen and bone marrow. T2 cells are characterized by surface expression of CD23, IgD through alternative splicing to the Cδ constant region supported by the protein ZFP318, and the receptor for B cell activating factor belonging to TNF family (BAFFR) [46, 83]. Splenic follicles are rich in BAFF, which provides survival signals in addition to the tonic BCR signal for T2 B cells and ensuing developmental stages [84, 85]. The originally described IgM^{lo} T3 B cells have meanwhile been shown to be enriched for self-reactive and anergic B cell clones and it remains to be resolved whether they are developmental intermediates or rather a group of anergic cells [86, 87]. Transitional B cells are either deleted by negative selection, driven into anergy or receive

positive selection signals allowing their development into either follicular (FO) or marginal zone precursor (MZP) B cells, which give rise to marginal zone (MZ) B cells [85, 88].

Follicular versus marginal zone B cell commitment in mice. Newly generated FO B cells, which have a lifespan of some weeks, but constitute the majority of mature B cells, repeatedly circulate through the blood and lymph to the bone marrow and migrate into follicles of secondary lymphoid organs (SLOs), such as spleen, lymph nodes (LNs) and Peyer's Patches (PP) [84]. These follicles are located in the vicinity of T cell rich areas, an anatomical arrangement, which enables FO B cells to present protein antigens to T cells and drive T cell dependent (TD) immune responses [85]. The exact combination of temporal and spatial cues that drive the follicular versus marginal zone commitment remains to be fully elucidated [84], however BCR signaling, also in response to autoantigens, appears central in refining the mature peripheral B cell compartment [87, 89]. Strong BCR signaling is regarded as a predisposing factor for the development of FO B cells and weaker signaling for MZ B cells [85, 90]. Complex interactions of BAFFR signaling and activation of NF-κB transcription factors also contribute to this fate choice [84, 91]. Notch2 signaling induced by Delta-like-1 binding (DL-1), which is expressed intraluminally in venules inside marginal zones and the red pulp of the spleen, is pivotal for the development of MZ B cells and their precursors (MZPs) [85, 92]. A recent study has revealed the key role of DL-1 expression on fibroblast-like cells in SLOs in this process [93]. In contrast to FO B cells, long-lived, self-renewing MZ B cells are rather sessile and reside adjacent to the marginal sinus in the marginal zone, the outer area of the white pulp. This localization in proximity to the sinus enables MZ B cells to act as key initiators of rapid T cell independent (TI) immune responses against blood-borne pathogens (Fig. 1) [85]. MZ B cells may also contribute to TD immune responses against lipid and protein antigens as a result of high expression of CD1d, MHC class II, CD80 and CD86 [85]. Some of these and additional feats of MZ B cells, such as the rapid production of natural antibodies by differentiation into short-lived plasmablasts in the absence of BCR ligation have led to the grouping of MZ B and the below discussed B1 cells as "innate-like" cells [94].

B1 cells. Besides the FO and MZ B cells, which are grouped as B2 B cells, a distinct mature B cell population exists, termed B1 cells. B1 cells, which develop earlier in ontogeny than B2 cells, are present in the periphery of mice. B1 cell development dominates during fetal and neonatal stages and is almost absent in mature mice [95]. The mature B1 population is sustained by self-renewal and B1 cells in adult mice nearly lack *de novo* generation, unlike the B2 subset, which is constantly replenished from developing bone marrow precursors [96].

B1 cells constitute the major B cell population in the coelomic cavities, the peritoneal and pleural cavities, and are a scarce B cell subset in other lymphoid tissues, such as bone marrow, spleen or lymph nodes [96]. B1 cells are distinguished as "innate-like" cells by production of "natural" antibodies of the IgM subtype, which employ a restricted set of mostly un-mutated IgH V-genes and are also present in "antigen-free" mice [97]. These antibodies have an overall low affinity, but provide polyspecific, TI immune response against a broad range of pathogens by binding recurrent structural motifs on pathogens [98]. Contrary to B2 cells, which are negatively selected for self-reactivity of their BCR, B1 cell formation critically requires strong BCR signaling [99, 100], which was suggested to positively select for self-reactivity of B1 cells [101], and activation of classical NF-κB signaling [102]. Together, peripheral B1 and B2 B cells comprise a pool of mature, yet (antigen-)naive B cells.

1.5 Antigen-induced B cell activation and terminal differentiation

Mature (antigen-)naive B cells are activated upon antigen encounter [94, 103]. While FO B cells require BCR ligation, innate-like B cells can also be activated by pattern recognition receptors (PRRs), such as Toll-like receptors (TLRs), independent of BCR engagement [84, 104]. Binding of a cognate antigen to the BCR induces the assembly of BCR-proximal signaling molecules resulting in the activation of genes associated with B cell activation [103]. The BCR-antigen complex is subsequently internalized and the contained antigen processed and presented on major histocompatibility complex class II (MHC-II), as a consequence of these signaling cascades. Presentation in an MHC-II-context enables $CD4^+$ helper T cells to recognize their cognate antigen [105]. A long-lived interaction between T and B cells is established in the interfollicular region of lymph nodes (LNs) or at the border of the T cell and B cell zones in the spleen, the so called "immunological synapse". This "synapse" involves cell-cell contacts through inducible costimulator (ICOS) and its ligand ICOSL, CD40 and CD40L and co-stimulatory cytokines [105, 106]. B cells activated in this TD manner can transform into short-lived extrafollicular plasmablasts that migrate to the medullary cords of LNs or the space between the red pulp and the T cell zone in the spleen, whereas the T cells start to acquire a follicular helper (T_{FH}) cell phenotype [107]. Alternatively, activated B cells seed transient structures called germinal center (GC), the anatomical site of the GC reaction [108]. B cell activation in TI immune responses occurs in the absence of T cell help and involves strong co-stimulation through PRRs by conserved microbial structures or extensive BCR crosslinking [107].

The germinal center reaction

Initiation of mature GC formation. GCs are formed in SLOs following B cell activation in TD immune responses [109]. They are the anatomical sites where B cells differentiate terminally into antibody-producing plasma cells or memory B cells. A mature GC is a polar structure composed of a light and a dark zone (LZ and DZ, respectively), which is contained within an area of naive FO B cells termed mantle zone [110]. These names were given according to the histological appearances of the respective zones. The DZ is composed of CXCL12 expressing reticular cells and densely packed B cell blasts, while proportionate fewer B cells populate the CXCL13 rich LZ, together with T_{FH} cells, follicular dendritic cells (fDCs) and macrophages [110]. The dynamics of the ordered events that take place in the GC reaction subsequent to B cell activation have been thoroughly analyzed in mice. The maturation of a GC takes approximately eight days and it can persist for many weeks, depending on its experimental induction [109-111]. GC reactions are continuously triggered by commensal bacteria in the gut-associated lymphoid tissue (GALT), independent of further external stimulation [112]. Subsequent to its activation and interaction with a cognate T cell, a GC-founding B cell migrates into the center of a follicle. In this center, marked by the presence of fDCs, the B cell proliferates massively and pushes non-activated FO B cells to the sides, thereby establishing the mantle zone [113]. At this time, the expanding GC B cells have upregulated expression of BCL6, the key transcription factor of GC B and T_{FH} cell fates, leading to the establishment of the mature GC [110]. Murine GC B cells bind to peanut agglutinin (PNA), downregulate CD38, lose IgD expression and express high levels of Fas (CD95) [114]. The LZ/DZ spatial separation of GC B cells is established and maintained by expression of chemokine receptors, CXCL12 attracts $CXCR4^{hi}$ DZ GC cells ($CXCR5^{lo}$, $CD83^{lo}$, $CD86^{lo}$), while migration and localization of $CXCR5^{hi}$ LZ GC B cells ($CXCR4^{hi}$, $CD83^{hi}$, $CD86^{hi}$) is mediated by CXCL13 [113].

Regulatory molecular pathways of GC initiation and maintenance. Upregulation of BCL6 and continuous signaling throughout the first four days post induction are essentially required for formation of a mature GC. BCL6 signaling regulates the expression of many target molecules, such as CXCR4, which orchestrate the migration of the GC B cell into the center of a follicle and its initial migration into the DZ [115, 116]. c-Myc-dependent proliferation is pivotal in the first four days following induction of GC formation [110]. Similar to BCL6, IRF4 has T and B cell-intrinsic functions that are essential for the formation of T_{FH} and GC B cells [117-119], but its initiating function in B cells has been suggested to be temporally restricted to the first two days of GC formation [110].

Recently, the PI3K pathway and its target FOXO1 were demonstrated to have an important role in the functional and polar LZ/DZ separation of the mature GC, with active FOXO1 enabling proliferation and appropriate CXCR4 expression in the DZ and PI3K signaling antagonizing FOXO1 function in LZ GC B cells [120-122]. c-Myc expression by positively selected LZ GC B cells is pivotal for reentry into the DZ as well as enabling these cells to terminally differentiate [121, 123]. Moreover, it was suggested that a subset of c-Myc$^+$ LZ GC B cells initiate a DZ specific transcriptional program by upregulating FOXO1 and CXCR4 to reenter the DZ for additional rounds of proliferation and somatic hypermutation [122].

Affinity maturation and somatic hypermutation (SHM). Once a mature GC has been established, the affinity of the BCR repertoire present in a GC is steadily increased in a phenomenon known as affinity maturation. Iterative cycles of SHM in the DZ, a process in which random point mutations are introduced into the variable gene exons (V_HDJ_H for the IgH locus, $V_\kappa J_\kappa$ or $V_\lambda J_\lambda$ for the IgL loci) of the BCR, and their subsequent selection mainly in the LZ culminate in affinity maturation [114]. Affinity maturation is crucial for the ultimate generation of high-affinity antibodies by plasma cells [124]. SHM and proliferation are tightly linked in the DZ, with the frequency of newly introduced point mutations resulting from SHM being estimated at 10^{-3} per division [125, 126]. Point mutation introduced by SHM are particularly enriched in the CDRs and result in transition and transversion mutations [43, 127, 128]. The enzyme activation-induced cytidine deaminase (AID), whose action is restricted to G1 cell cycle phase [129, 130], triggers the first steps of SHM and class switch recombination (CSR) alike by deaminating cytosines to uridines in single-stranded DNA [128, 131]. B cells containing mutations introduced by SHM resulting in decreased binding affinities or self-reactivity of their respective BCRs are cleared by apoptotic cell death in the LZ [114]. Whether this clearance occurs by negative selection or through death by neglect as a consequence of absent positive selection remains debated [132-134]. GC B cells are sensitive to extrinsic activation of apoptosis by expression of high levels of the Fas receptor (Fas/CD95) as well as low levels of the pro survival protein BCL2 [114, 135].

Theories of survival-mediated selection of BCR clones in the GC are founded on the assumption of B cells competing for limited amounts of selection triggering signals. Moreover, GC B cells were shown to strongly rely on survival signals produced by the GC microniche [114]. In the prevailing model of selection of BCR affinities in the GC, BCR-ligand affinity is measured as a function of antigen binding, uptake and presentation in an MHC-II-context. In this model T_{FH} cells provide the means of selection.

This model is supported by intravital imaging studies visualizing migration of GC B cells and T_{FH} cells, their transient interactions, specific expansion of GC B cells in MHC-II-TCR contact with T_{FH} cells and release of IL-4 and IL-21, factors that induce GC B cell proliferation and differentiation [136, 137]. The essential function of T cells in selection of GC B cells is further corroborated by studies, which suggest that BCR signaling must be dampened in G1 phase GC B cells to sustain the GC reaction. These results argue against a direct involvement of BCR signaling in the selection process but support the notion that antigen capture and internalization by the BCR is the critical determinant for positive selection [138-140]. The later finding is not mutually exclusive with earlier models of GC B cell selection via their binding to antigen presented by fDCs in the LZ [141]. As BCR signaling is still active in G_2/M phase GC B cells, this data could therefore be integrated in a model involving selection cues from T_{FH} cells as well as BCR based signaling [110, 114]. Roles for T_{FH} cells and the recently described follicular regulatory T_{FR} cells, which exert regulatory functions on T_{FH} and GC B cells, in positive and negative selection in the GC reaction and prevention of autoimmunity have been suggested [142-144]. Questions remain unsolved regarding the specific role of Fas-induced apoptotic clearance of GC B cells, the Fas ligand (FasL)-signal delivering cell type or the role of the antiapoptotic BCL2 family member MCL1 in DZ/LZ processes [144, 145]. However, negative selection of GC B cells via this pathway provides a means of establishing peripheral B cell tolerance [143, 146, 147]. Besides the crucial signals from T_{FH} cell, several other factors were shown to contribute to efficient affinity maturation. Limiting the access of GC B cells to antigen loaded on fDCs by secreted antibodies, which mask the epitopes, has been demonstrated to enforce evolution of BCR affinities to replace these antibodies in an intra and inter GC-specific manner [148]. The migration of T_{FH} cells between GCs and the emigration of newly activated B cells into existing GCs further support the generation and selection of BCRs with highest affinity possible [110]. Some of the selected LZ GC B cells undergo class switching and terminally differentiate into memory B cells or plasma cells, while some of the switched GC B cells recircle to the DZ to undergo further rounds of affinity maturation.

Class switch recombination (CSR). The process by which GC B cells stably alter the expressed BCR isotype is known as CSR. CSR occurs through replacement of the C_H region of their BCR, Cμ, with a different class, such as Cγ, Cε or Cα, resulting in expression of IgG, IgE or IgA respectively, while maintaining its antigen-binding part [22]. CSR permanently alters the effector function of secreted antibodies, contributing essentially to a more effective clearance of pathogens and changes BCR signaling capacities [67, 140].

Switch (S) regions, are long (1-10 kb), repetitive motives, enriched for the same SHM-attracting "DGYW"-nucleotide motif present in the CDRs, located upstream of all constant regions except Cδ [22, 43]. CSR is not allelically excluded and is induced by AID-dependent DSBs in the donor region Sμ and an acceptor S region on both IgH alleles. This results in the fusion of the two S regions, thereby deleting the intrachromosomal sequences, by cNHEJ repair juxtaposing the C_H region downstream of the acceptor S region to the V_HDJ_H exon [22, 127]. AID-introduced U/G mismatch-pairs are processed by components of the base excision repair (BER) and mismatch repair (MMR) pathways to yield point mutations in V(D)J exons during SHM and DSBs in S regions during CSR. Common to SHM and CSR is the intermediate introduction of both, mutations and DSBs, by AID at either location [43, 128]. AID expression is not restricted to lymphoid cells, unlike RAG expression [22]. While DSBs introduced by RAG enzymes in V(D)J recombination are cooperatively guided by signal and RSS joint, a mechanism to dictate directionality of fusing DSBs in CSR remains elusive. However, similar to V(D)J recombination, germline transcription targets AID in SHM/CSR to different V(D)J exon or S regions, respectively [22]. Other factors beyond the DGYW-motif that contribute to AID targeting and outcome are still debated and include DNA-sequence context of V(D)J exons and S regions [43], differential use of co-factors [149, 150] or employed repair mechanisms [151].

Exit of GC B cells as plasma cells or memory B cells

The ability to develop immunological memory is a hallmark of vertebrate immune systems [152]. This is provided by long-lived plasma cells secreting protective high-affinity antibodies, sustained antibody titers in the serum as well as antigen-induced reactivation of long-lived memory B cells, which can recirculate to SLOs [152, 153]. While memory B cells and short-lived plasmablasts can develop outside the GC, GC provide the main source of both memory B and plasma cells [153, 154]. It remains unclear whether terminal differentiation occurs in a cell autonomous manner, which might be temporally pre-imposed [108, 152], or is induced in B cells extrinsically by GC microenvironments, which remain incompletely understood [121]. IRF4 has been implicated to play a central role in triggering the switch from GC B cells recycling in the GC to induction of terminal differentiation into plasma cells [110]. BCR signaling strength increases with ongoing affinity maturation, increasing IRF4 expression, which may either directly repress BCL6, as IRF4 can exert BCL6-activating and repressive functions [118, 155], and/or induce B lymphocyte-induced maturation protein 1 (BLIMP1, encoded by *Prdm1*), a repressor of BCL6 and PAX5 and master regulator of plasma cell differentiation [156].

Plasma cells. Differentiation into antibody secreting cells (ASCs) requires silencing of the B cell specific transcriptional program in an IRF4, BLIMP1 and X-box-binding protein 1 (XBP1)-dependent manner [142]. In the B cell lineage, BLIMP1 is exclusively expressed in ASCs. It is expressed at intermediated levels in plasmablasts, a type of ASCs generated rapidly in the extrafollicular response, which retain migratory and proliferative capacities. Plasmablasts may further differentiate into the post-mitotic plasma cells, which express high levels of BLIMP1 and are the type of ASC that emerges from GCs [108]. The second determinant of plasma cell differentiation is XBP1, which acts downstream of BLIMP1 to induce molecular alterations required for the production of large quantities of antibodies, such as remodeling of the endoplasmatic reticulum, induction of the unfolded protein response and autophagy pathways that among other functions ensure membrane-homeostasis [157, 158]. Zinc finger and BTB domain-containing protein 20 (ZBTB20) has recently been shown to contribute significantly to enforcing ASC phenotypes by enhancing the expression of IRF4, XBP1 and BLIMP1 [108]. Antibodies produced by plasmablasts can be class switched, but exhibit low levels of SHM [156]. Under physiological conditions, long-lived plasma cells reside mainly in distinct bone marrow niches. Their precursors are thought to phenotypically resemble plasmablasts. These precursors home to the bone marrow in a CXCR4-dependent manner, where they upregulate BLIMP1 expression and attach to CXCL12-producing stromal cells via VLA4 binding to VCAM1 [108, 156]. In these niches they receive survival cues produced by hematopoietic cells via the IL-6 receptor and B cell maturation antigen (BCMA). The stimulation of BCMA by a proliferation inducing ligand (APRIL) induces MCL1 expression, which is essential for plasma cell survival in this niche [159, 160].

Memory B cells. After encountering and responding to a primary antigen challenge some B cells subsequently return to a quiescent state. These B cells, which are present in increased clonal numbers compared to naive B cells and are capable of rapidly responding upon rechallenge, are functionally defined as memory B cells [152]. Memory B cells are very heterogeneous with regards to their phenotype, function and origin. For instance they may vary in their expression of IgM-BCRs or class switched-BCRs, GC-dependent or GC-independent origin in TD immune responses or emergence from B1 or FO B cells [153, 154]. In contrast to plasma cells, memory B cells maintain BCR expression, which activates expression of antiapoptotic BCL2 family members BCL2 and BCL2a supporting longevity as well as a B cell-specific transcriptional profile achieved by persisting expression of PAX5 [108, 153]. PAX5 expression also reinforces expression of BACH2, which is essential for the ability of memory B cells to respond to antigen rechallenge, and IRF8, both contributing to

the repression of *Prdm1* [65, 108]. However, due to the immense heterogeneity of memory B cells this pool of terminally differentiated B cells remains incompletely understood.

2. The RNA-binding proteins Roquin1 and Roquin2

Roquin1 and 2 constitute a novel family of RNA-binding proteins that regulate important mediators of development and immunity. Mutated Roquin1 was initially described in a mouse strain exhibiting features of human SLE and led to the characterization of many functions of both Roquin paralogs in T cells. These include repression of T_{FH}, T_H17 and NKT17 cell fates, as well as the molecular mechanism of Roquin binding to cis-regulatory motifs in target mRNAs, which results in mRNA degradation.

2.1 Initial description of Roquin in the *sanroque* strain

In an attempt to identify mechanisms that repress autoimmune responses, Vinuesa and colleagues performed an ethylnitrosourea (ENU) mutagenesis screen in mice and discovered the *sanroque* (san) strain [161]. This strain shows characteristics, which resemble systemic lupus erythematosus, including splenomegaly, lymphadenopathy, plasmacytosis, polyclonal hypergammaglobulinemia and high titers of anti-nuclear antibodies [161]. In addition, this strain exhibits necrotizing hepatitis, anemia and renal pathology showing focal proliferative glomerulonephritis with IgG-containing immune complexes [161, 162]. The causative mutation alters amino acid 199 from a methionine to an arginine (M199R) in Roquin1, a ubiquitously expressed cytoplasmic protein with a RING-type E3 ubiquitin ligase domain. This mutation is located in a novel protein domain termed ROQ, which so far has been identified only in Roquin1 and its paralog, membrane-associated nucleic acid binding protein Mnab or Roquin2 [163]. The name "*sanroque*" derives from the patron saint invoked in bubonic plague, since the enlarged spleen and lymph nodes in this mouse strain are reminiscent of those seen in plague victims [164]. The homozygous Roquin1$^{san/san}$ mutation was believed to act mainly in $CD4^+$ T cells resulting in spontaneous follicular T helper cell (T_{FH}) differentiation, ectopic expression of the inducible costimulator (ICOS) with ensuing inappropriate B cell activation, GC formation and production of self-reactive antinuclear antibodies (ANAs) despite the presence of elevated numbers of functional regulatory T (T_{reg}) cells [162]. Subsequent work showed that Roquin1 can directly bind to and repress *Icos* mRNA via processing body components and mRNA decay pathways [165]. Ectopic ICOS expression on $CD4^+$ T cells in Roquin1$^{san/san}$ mice was demonstrated to employ downstream signaling components of CD28, thereby relieving naive $CD4^+$ T cells of the requirement for simultaneous TCR and CD28 stimulation by antigen presenting cells for induction of

differentiation into T effector cells [166]. A subsequent study demonstrated that homozygous ICOS-deficiency neither rescued the increased splenic cellularity nor the autoimmunity in *sanroque* mice corroborating the requirement for a novel mechanism driving the autoimmune disease in these mice [167].

A central driver of the development of T_{FH} and $CD8^+$ short-lived effector-like ($CD44^+$ $CD62L^{lo}$ $KLRG1^{hi}$ SLEC-like) cells present in $Roquin1^{san/san}$ mice, is overproduction of the cytokine IFNγ produced by several T cell subsets in this mouse strain, in which an increased half-life of *Ifng* mRNA was determined [167, 168]. IFNγ signaling induces high expression levels of BCL6 in T_{FH} cells and their precursors in $Roquin1^{san/san}$ mice [167]. Moreover, experimentally generated absence of T_{FH} cells or IFNγ signaling in T cells confirmed aberrant T_{FH} cell development caused by excessive IFNγ signaling as a central pathomechanism of the lupus like autoimmune syndrome [167].

2.2 Messenger RNA (mRNA) quality control and degradation pathways

mRNA quality control and degradation needs to be monitored at every step from early transcription to translation in order for aberrant mRNAs to be removed as well as to maintaining cellular mRNA homeostasis. While there are several mechanisms in place for surveillance of every kind of RNA species, such as ribosomal RNAs (rRNAs), transfer RNAs (tRNAs) or small nuclear RNAs (snRNAs), in the following part I will focus on the mechanisms that regulate protein-coding mRNAs. These pathways rely on the action of two types of RNA-degrading enzymes, endoribonucleases, such as Regnase1 or SMG6, or exoribonucleases. Endoribonucleases act via nonsense-mediated decay (NMD) and cleavage occurs within the mRNA thereby initiating its degradation, whilst exoribonucleases digest the mRNA molecule from either end [169]. Surveillance of mRNA molecules in the nucleus is intimately linked to initiation of RNA polymerase II activity [170]. Pre-mRNAs lacking a 5' 7-methyl-guanosine cap (m^7G-cap) as well as mRNAs exhibiting defects in transcriptional elongation, splicing or export in the cytoplasm are degraded from the 3'-end towards the 5'-end by the nuclear exosome or in 5' to 3' direction by nuclear exoribonucleases [170]. Following export in the cytoplasm, several degradation pathways can be triggered, including no-go decay (NGD), no-stop decay (NSD) and the most thoroughly studied NMD pathway. Free ribosomes that got stalled on secondary structures of mRNAs can cause NGD, mRNAs that lack stop codons mediate NSD mRNAs that contain a premature termination codon (PTC) are degraded via NMD. In NMD mRNA degradation is stimulated by the RNA

helicase up-frameshift protein1 (UPF1) [171], which in mammals locates in the vicinity of the PTC and upstream of the exon junction complex (EJC). In a subsequent step, UPF1 translocates to the 3' end of the EJC and SMG5, SMG6 and SMG7 bind the complex, initiating the degradation of the mRNA by SMG6-mediated internal cleavage of the transcript and recruitment of the CCR4-CAF1-NOT deadenylase complex in a SMG5- and SMG7-dependent manner [172, 173]. Many of these proteins involved in mRNA decay are enriched in so called processing bodies (P bodies), distinct cytoplasmic foci in unstressed cells [174]. Intact mRNA molecules are protected from exoribonuclease-specific degradation by virtue of their 5' m^7G-cap and the 3' poly(A) tail [175, 176]. Translationally silent messenger ribonucleoprotein (mRNP) complexes can localize to different cytoplasmic granules, P bodies or in stressed cells, so called stress granules in which translation can be reinitiated [174]. Both major deadenylase complexes, Pan2-Pan3 and CCR4-CAF1-NOT, are present in P bodies and mediate shortening of the poly(A) tail, which results in generation of a linear mRNA molecular amenable to further degradative processing from the 3' as well as 5' end (Fig. 2).

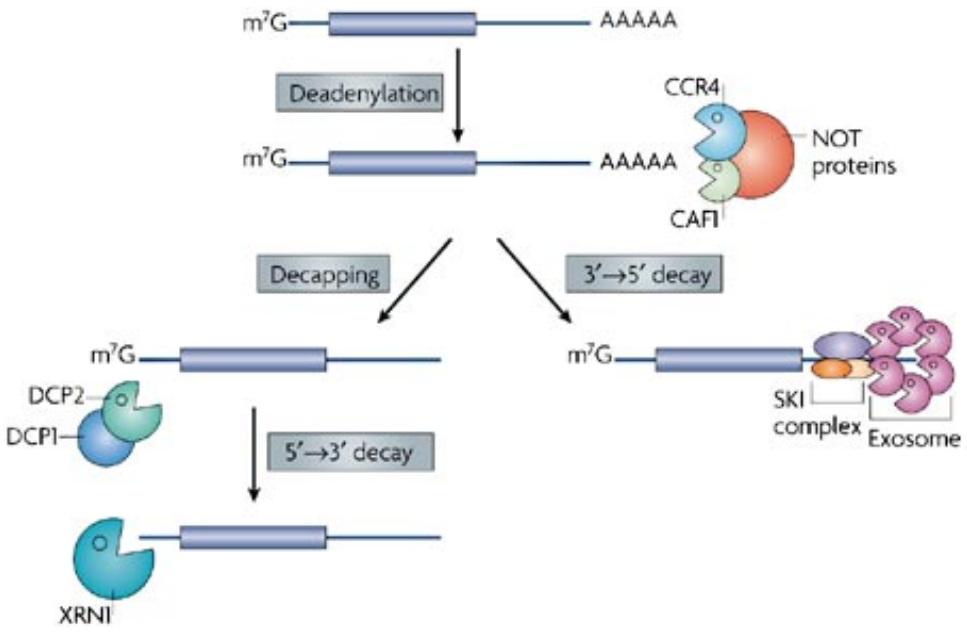

Figure 2: Simplified overview of bulk mRNA degradation pathways.
The most common initial step in mRNA decay is the opening of the closed loop form of the mRNA by action of the 3'-5' deadenylase complexes Pan2-Pan3 and CCR4-CAF1-NOT. The latter complex consists of the components NOT, which provide an essential scaffold function, and the deadenylases CCR4 and CAF1, all of which localize to P bodies. The resulting linear mRNA can either be degraded in 3'-5' direction by action of the exosome/ski-complex and its nuclease component Dis3/Dis3l or in 5'-3' direction by Xrn1 following removal of the m^7G-cap. Decapping in mammals is performed by Dcp2 as part of a ribonucleoprotein complex with regulatory partners such as Dcp1, Edc4 and Rck/p54 (Edc4 and Rck/p54 not shown) [169]. Most components of these pathways are enriched in P bodies. Alternative mRNA decay pathways independent of initial deadenylation include those involving uridylation of the mRNA 3'-end [169] (Figure taken from [177]).

The exosome/ski-complex possesses 3' to 5' exoribonuclease activity, which can result in complete degradation of the target mRNA [178]. Alternatively, the 5' m^7G-cap is hydrolyzed by the Dcp1/Dcp2 complex exposing the unprotected mRNA 5' end to complete digestion by Xrn1 in a 5'-3' manner [179]. In mammals many factors aid in the establishment of the Dcp1/Dcp2 complex, among which is the Lsm1-7/Pat1 complex that binds to the poly(A)-tail and together with enhancers of decapping, such as Edc4 or Rck/p54 facilitates binding and activity of the complex (Fig. 2) [179]. In contrast, endoribonucleases, such as Regnase1 can act on capped mRNA and hydrolyze internal ester-bonds yielding two RNA fragments that are subjected to degradation by the presented pathways [180]. Specificity of mRNA decay is maintained by cis-acting mRNA sequence motifs as well as a plethora of regulatory trans-acting protein and non-coding RNA factors, many of which play fundamental roles in the immune system [169]. In AU-rich and GU-rich element (ARE/GRE)-mediated decay, the short half-lives of mediators of cytokine signaling and cell growth are regulated by ARE/GRE-binding proteins [181, 182]. Furthermore, miRNA-dependent mRNA decay in many organisms has been found to rely on the protein GW182, which recruits the CCR4-NOT complex [183]. An additional group of RNA-binding proteins that can recognize cis-regulatory elements in coding sequences or the 3'UTR and subsequently induce CCR4-NOT mediated deadenylation include Smaug [184], Nanos2 [185], the Puf protein family as well as the Roquin paralogs [186].

2.3 The genomic loci encoding Roquin1 and 2

Roquin proteins have a unique combination of E3 ligase (RING) and zinc finger CCCH (C_3H) domains, based on which they were assigned the gene symbols *Rc3h1/2* (mouse) or *RC3H1/2* (human) [161]. *Rc3h1* situated on chromosome 1 in mice and humans encodes for a protein of 1130 amino acids (aa) in length (1133aa in humans) and a molecular weight (MW) of 125 kDa [187], while the murine *Rc3h2* gene locates to chromosome 2 and encodes the 1187 aa long Roquin2 with a MW of 131kDa (human *RC3H2*: chromosome 16, 1191 aa and about 132kDa) [188]. Moreover, different splice variants occur in humans and mice giving rise to shorter protein isoforms. The murine *Rc3h1* gene comprises 20 exons, which can be transcribed into three transcripts, two of which are protein-coding, whereas the murine *Rc3h2* contains 22 exons, which can be transcribed into ten transcripts of which three are protein coding [189]. *Rc3h1* is nearly ubiquitously expressed [161] and the two transcripts encode nearly identical proteins that differ only nine amino acids in length at the C-terminus. Instead

two of the three protein-coding *Rc3h2* mRNAs are translated into isoforms of 1187 aa and the third into a 1125 aa long isoform, which are identical in their N-termini and differ only in their C-termini [190]. The expression of Roquin paralogs was examined in many mouse tissues, with exception of the bone marrow, and the highest expression levels were seen in tissue extracts from thymus and lymph nodes and lower expression in spleen, brain and lung [191]. Usually Roquin1 and 2 are expressed in the same tissues with lower expression levels of Roquin2 compared to Roquin1. For example, quantification in $CD4^+$ and $CD8^+$ T cells revealed approximately five-fold higher expression levels of Roquin1 in both T cell subsets [190].

2.4 Regulation of Roquin gene expression and protein abundance

A gene duplication event in the ancestral vertebrates led to the presence of both Roquin paralogs, since the genomes of *Drosophila melanogaster* and *Caenorhabditis elegans* encode only a single homolog, DmRoquin and RLE-1, respectively [190, 192]. Extensive 5' juxtaposed sequences were also involved in this gene duplication event, thus it is possible that both genes share 5' regulatory elements [190]. Yet, investigations on the regulation of gene expression of Roquin1 and 2 have only been started recently. Colonic intraepithelial lymphocytes of IL-10 deficient mice have decreased *Rc3h1* gene expression levels, which are restored upon *in vitro* treatment with IL-10 [193]. In addition, IL-10 treatment moderately increased *Rc3h1* gene expression in the mouse EL4 T cell line [194] suggesting a regulatory role for IL-10 in *Rc3h1* expression. IL-10 signaling employs the JAK-STAT pathway [195]. IL-10 stimulation of EL4 T cells was shown to induce the transcription of the transcription factors STAT1, STAT3, c-Rel, IKZF2 and GATA2, all of which were shown to bind within a 2.2 kb region upstream of the 5'UTR of Roquin1. STAT1, STAT3, c-Rel and GATA2 were suggested to trigger *Rc3h1* gene expression, while IKZF2 was suggested to have inhibitory effects on its transcription following IL-10 stimulation [194]. Additionally, expression of Roquin paralogs has been suggested to be subject of post-transcriptional gene regulation [193, 196]. miR-223 was found to be significantly upregulated in Roquin1$^{san/san}$ T cells compared to wild-type T cells [197]. Inhibition of miR-223 in colonic intraepithelial lymphocytes resulted in increased *Rc3h1* mRNA levels and the 3'UTR of Rc3h1 was subsequently shown to be amenable to miR-223-mediated repression in a luciferase reporter assay [193]. These findings suggest that Roquin1 mRNA levels may be fine-tuned by miRNAs, including some that are regulated by Roquin1.

In addition, it was suggested that Roquin paralogs limit the expression of their own transcripts as they were shown to contain the constitutive decay element (CDE), a cis-regulatory motif found in some mRNA targets of Roquin1 and 2 (see below) [196]. Furthermore, abundance of active protein of Roquin paralogs as well as Regnase1 in T cells is regulated by the paracaspase function of mucosa-associated lymphoid tissue lymphoma translocation protein 1 (MALT1) [198, 199]. MALT1 is part of the CARMA1-BCL10-MALT1 (CBM) complex that is strongly linked with induction of canonical NF-κB signaling downstream of TCR and BCR ligation [102] as well as regulation of lymphocyte activation by the proteolytic function of MALT1 [200]. MALT1 cleaves mouse Roquin1 preferentially after Arg510 or alternatively after Arg579, while murine Roquin2 is cleaved between Arg510 and Gly511 [199] separating the N- and the C-terminal part of the proteins and thereby inactivating their mRNA-regulating activities (Fig. 3A).

2.5 The Roquin proteins – domain organization and function

Roquin proteins are cytosolic proteins, which are enriched in P bodies and stress granules [191, 192, 201]. Amino acid sequences of murine Roquin paralogs are highly similar with their homologs in different species. Human and mouse Roquin1 are more than 90% identical, the sequence identity in the N-terminal part, the first 450 amino acids that comprise distinguishable domains (Fig. 3A), even exceeds 99% [187]. The C-terminal part comprising approximately 650 amino acids is predicted to be intrinsically disordered [187] and accordingly shows less homology in between species. Accordingly, the RING and zinc finger (ZF) domains of Roquin1 and 2 have over 80% and the name-giving ROQ domain even 99% sequence similarity in mice [202]. Moreover, the first 450 amino acids of murine Roquin2 are 75% similar to that of DmRoquin and RLE-1 [192]. The N-termini of both Roquin paralogs comprise a RING-type E3 ubiquitin ligase motif followed by a higher eukaryotes and prokaryotes nucleotide binding (HEPN) domain bordering the ROQ domain C- and N-terminally followed by a CCCH-type zinc finger (Fig. 3A). The novel ROQ domain is the most highly conserved part among the paralogs [203]. When this PhD project was initiated, the ROQ domain had solely been described based on sequence conservation [161] as well as the ability of the mRNA-binding capacity of the sequence between amino acid 130 and 360 [165, 192]. The RING domain of murine and human Roquin paralogs adopts a canonical cross-braced double zinc finger fold [197, 203] with a typical Cys_4 and an atypical Cys-Cys-His-Asp coordination site [197, 203, 204].

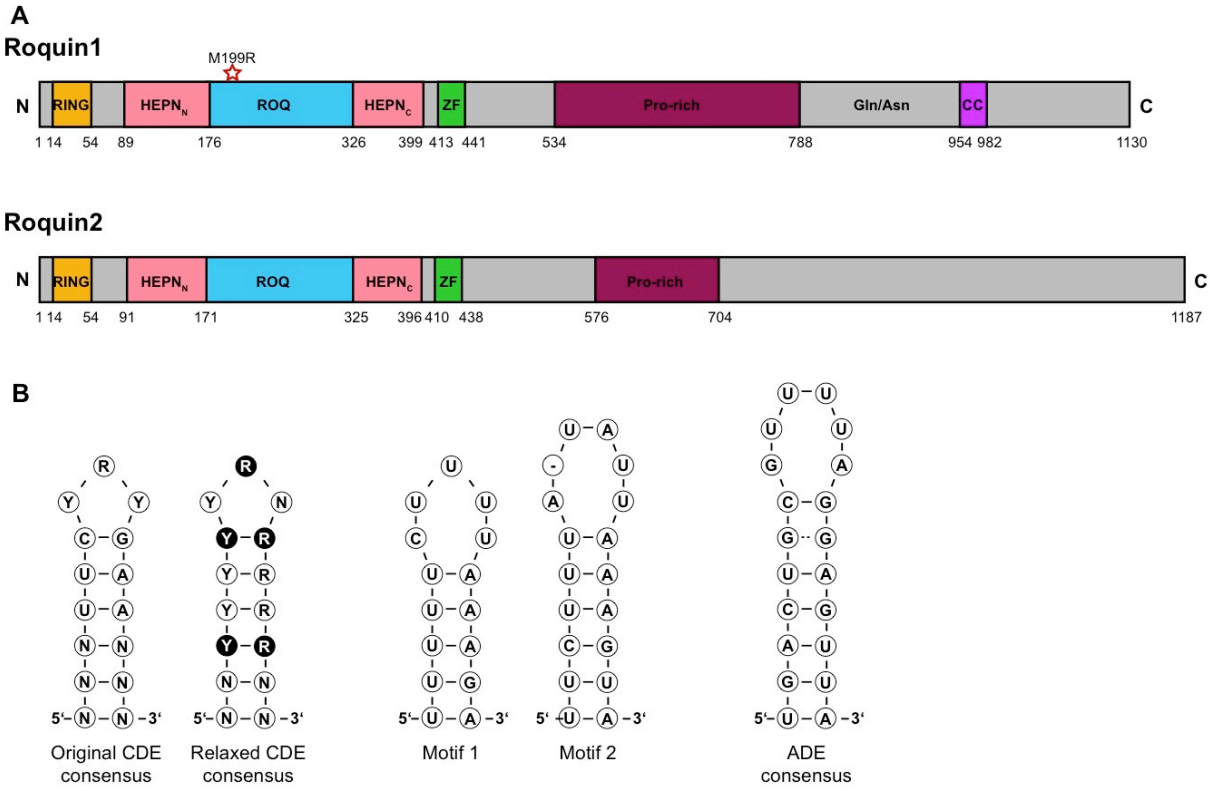

Figure 3: Domain organization of Roquin paralogs and described cis-regulatory motif in target mRNAs. (A) Numbers below the schematic mark position of amino acids and N- and C-terminal ends are indicated. The star highlights the position of the *sanroque*-Met to Arg mutation at amino acid position 199. RING really interesting new gene; HEPN (N- or C- terminal part of) higher eukaryotes and prokaryotes nucleotide-binding; ROQ novel RNA-binding domain; ZF Cys_3-His/CCCH-type zinc finger; Pro-rich proline-rich region; Gly/Asn region containing stretches enriched in Gly and Asn; CC coiled-coil stretch. Figure based on [188, 197, 203, 205-207] with the additional helix N-terminal to $HEPN_N$ [197] incorporated into $HEPN_N$ as suggested by Schlundt and colleagues [187] (B) Stem-loop structures of cis-regulatory motifs identified in target mRNAs of Roquin1 and 2 with indicated 5' and 3' ends. The conserved decay element CDE [208], predicted stem-loop motifs 1 and 2 for which an enrichment was observed [209] and alternative decay element ADE [210] as described in the respective publications. N any nucleotide; R purine; Y pyrimidine. Purines/pyrimidines in a black circle can be individually substituted by pyrimidines with moderate affinity loss provided base pairs are maintained. A dashed line indicates putative non-Watson-Crick base pairing as suggested by the authors [210].

Whether the RING domain retains E3 ubiquitin ligase function remained elusive for a long time. An initial report demonstrated that the *C. elegans* ortholog of Roquin, RLE-1, interacts with DAF-16, the nematode-ortholog of FOXO3a [211]. Knockout of *rle-1* resulted in a prolonged lifespan and increased resistance to environmental stress [211]. DAF-16, the molecular target of RLE-1, displayed increased protein but not mRNA levels in RLE-1 deficient worms. Subsequently RLE-1 and DAF-16 were demonstrated to co-localize to the cytoplasm and interact with DAF-16 resulting in its polyubiquitination [211]. The role of the RING domains was studied in the *ringless* Roquin1 and 2 mouse strains [202]. While Roquin1 *ringless* mice die perinatally, similar to Roquin1$^{-/-}$ mice [202, 212], Roquin2 *ringless* mice do not show any phenotype [202].

Specific deletion of the RING domain in T cells ("*Tringless"* mice), which exhibit only a very mild immune phenotype in promoting GC B cell reactions following immunization, impaired the localization of Roquin proteins to stress granules but not P bodies [202]. Repression of adenosine monophosphate-activated protein kinase (AMPK) activity is essential for correct mTOR signaling in $CD4^+$ T cells, a signaling pathway that contributes to $CD4^+$ effector T cell expansion and T cell-specific support of the GC B cell reaction [204]. The RING domain was subsequently demonstrated to be important for interaction of Roquin with the catalytic α1 subunit of AMPK and sequestration of the complex into stress granules as well as antagonizing AMPK activity [204]. Although, repression of AMPK activity was independent of its ubiquitination, Roquin1 was demonstrated to be capable of autoubiquitination, a process that was speculated to be important for co-localization of Roquin and AMPK into stress-granules [204]. Recently, apoptosis signal-regulating kinase1 (ASK1), a signaling protein involved in mediating resistance to reactive oxygen species-induced cell death, was found be polyubiquitinated on Lys48 by Roquin2, but not Roquin1, in human cell lines triggering its proteosomal degradation [213]. Maryuma and colleagues additionally presented evidence that RLE-1 regulates abundance of NSY-1, the worm ortholog of ASK1 [213]. These findings support the hypothesis that differences in the RING domain enable diverging functions of Roquin1 and Roquin2. Indeed, a recent *in vitro* study confirmed that the RING domain of both paralogs can function as an E3 ubiquitin ligase, but did not confirm autoubiquitination of Roquin1 [203]. However, in this study Roquin paralogs were shown to have both overlapping E2 enzyme partners such as Ubc13, an E2 ligase that assembles Lys63 linked ubiquitin chains and that is also involved in B cell signaling processes [203, 214]. Additionally, specific, non-shared E2 partners, such as UBE2L3 that only interacts with Roquin1 but not Roquin2, were demonstrated [203]. This highlights that the RING domains of Roquin1 and 2 support formation of not only Lys48 linked polyubiquitin chains and that they differ in their preferences for E2 partners potentially enabling them to trigger dissimilar molecular effects. Similar to the RING domain, also the function of the ZF domain remains largely elusive. The Roquin ZF domain is predicted to resemble the structure of other Cys_3-His ZFs, such as those found in the ARE-binding proteins TIS11d and tristetraprolin. Although inactivating mutations in the ZF or the complete ZF domain ablation [165, 192], affected *in vitro* RNA binding of Roquin1 only mildly, there is evidence that it might contribute to functional *in vivo* RNA binding by establishing additional contact sites such as AREs present in the vicinity of ROQ-bound cis-regulatory motifs [165, 209].

Common to many RNA binding proteins, Roquin paralogs express more than one RNA-binding domain, the ZF and the ROQ domain [187]. Until the publication of many high resolution structures of the ROQ domain-containing N-terminal region of Roquin1 in 2014, secondary structure predictions for the region of amino acids 60-410, predicted a predominantly helical fold [D. Rieß, unpublished data]. Limited proteolysis of the N-terminal regions of mouse and human Roquin identified the ROQ domain boundaries yielding a core ROQ domain of approximately 20 kDa ranging from aa176 and aa326 in murine Roquin1 [205, 206]. The regions flanking the ROQ core are susceptible to proteolytic cleavage and were subsequently shown to comprise flexible linker regions connecting the ROQ and the HEPN domains, similarly present in Roquin2 [188, 197, 203, 207]. The novel ROQ domain fold exhibits an extended winged helix-turn-helix motif comprising three α helices and three β strands (WH, residues 191-274) as well as additional helices packed against the WH motif [205, 206]. This WH motif is the essential RNA binding element [187]. Three groups have meanwhile reported the molecular structure of larger Roquin1 and 2 fragments [197, 203, 207]. The subdomain I identified by Tan and colleagues was later shown to comprise the ROQ-flanking HEPN domains, each part consisting of 3 helices [197, 203, 207]. Subdomain III contains the WH motif, termed A site, and together with subdomain II forms the ROQ core [207]. All reported structures of the ROQ core are essentially identical with regard to fold and domain arrangement. The ROQ core is therefore a novel RNA-binding domain which organization was not predicted from the primary amino acid sequence. The ROQ domain structures reported in the absence of mRNA substrate [197, 205, 206] all showed dimeric arrangement in the asymmetric unit, yet all studies concluded that the ROQ domain is likely to be a monomer in solution and dimerization resulted from unphysiological ROQ concentrations. Therefore, it remains still elusive whether Roquin paralogs form homo- or heterodimers *in vivo*. Interestingly, while the HEPN domain was demonstrated to contribute to RNA binding in a so-called B site [207], a nucleotide-binding motif remains to be determined [203]. The consensus sequence of the first cis-regulatory motif, termed constitutive decay element (CDE), bound by Roquin proteins is characterized by a pyrimidine-purine-pyrimidine (Py-Pu-Py) tri-loop, a closing C-G base pair, followed by two U-A base pairs on top of a stem comprising another two to five unspecific base pairs (Fig. 3A) [196]. Concomitant with the description of the CDE, a mechanistic explanation for Roquin-based mRNA degradation was demonstrated as Roquin was shown to interact with the CCR4-CAF1-NOT deadenylase complex causing mRNA degradation [196].

The CDE sequence was identified in a set of approximately 50 evolutionary conserved target mRNAs in vertebrate genomes [196]. The structural basis for the recognition of this CDE structure in the A site by the WH motif was demonstrated by several groups for Roquin1 and 2 [188, 203, 205-207]. While the CDE stem-loop structure is recognized by the WH motif, the B site was demonstrated to bind complementary dsRNA, which had formed from the CDE of *TNFα* mRNA instead of a stem-loop ssRNA structure, in a sequence-independent manner [207]. While it cannot be excluded that this binding of dsRNA by Roquin at a second site might have been an artifact of the high *TNFα* mRNA concentration employed for co-crystallization, it is suggestive of a second RNA binding site in Roquin paralogs. However, mutational analysis subsequently showed that the A site is absolutely essential for decay of CDE-containing mRNAs and residues of the B site may contribute therein [207]. The obtained structures of the ROQ-CDE complex revealed a primarily sequence-independent interaction and indicated that requirements for CDE recognition might not be as restrictive as originally described (Fig. 3B) [205, 208]. Indeed, it was demonstrated that the ROQ domain still binds altered CDE sequences *in vitro* as long as the overall stem-loop with the Py-Pu-Py tri-loop is maintained [205]. Subsequently, a structure-based binding of Roquin to non-CDE like motifs was confirmed [209]. Roquin was shown to bind stem-loop structures with U-rich penta- or hexa-nucleotide loops [209]. One such motif was identified in the 3'UTR of A20, a negative regulator of signaling leading to NF-κB transcription factor activation. Post-transcriptional regulation of A20 and downstream mediators of NF-κB signaling involving the ROQ and ZF domains of Roquin was demonstrated in cell lines (Fig. 3B) [209]. This finding helped explain why many of the mRNA targets bound by Roquin paralogs did not fulfill the strict CDE requirements [196], which was concomitantly modified by the authors presenting a more relaxed CDE sequence, including a less restricted tri-loop composition [208]. Recently, an additional cis-regulatory element termed alternative decay element (ADE) (Fig. 3B) [209], comprising an U-rich hexa-loop structure was presented and its role in post-transcriptional regulation of OX40 demonstrated [210]. ADE and CDE share some features, including an important role of sequence-independent contacts of amino acids in the ROQ A site to the RNA stem and the recognition of the hexa- and tri-loops primarily mediated by their shapes (Fig. 3B) [210]. Whereas the cis-regulatory motifs, such as the ADE and CDE sequences, and their roles in posttranslational repression are being unraveled the functional role and contribution of potential binding of dsRNA in the B site remains elusive.

The Stoecklin group first demonstrated that the C-terminal part of Roquin1 contributes significantly to Roquin-mediated mRNA decay by recruiting the CCR4-CAF1-NOT deadenlyase complex [196], while work from the Heismeyer group in T cells indicated Roquin paralogs interact with members of the decapping pathway, such as Dcp2, Edc4 and Rck [165, 191], for degradation of target mRNA. A recent study confirmed the mRNA-independent interaction of Roquin1 with members of the CCR4-CAF1-NOT complex [209]. Additionally, the C-terminus of Roquin1 and 2 harbors an extended proline-rich sequence stretch, a motif commonly found in signaling adaptor proteins, such as spliceosomal proteins [187]. The functional relevance of Gly/Asn-rich stretches or of a bioinformatically predicted coiled-coil region in the C-terminus of Roquin1 has not been investigated, but they could represent sites essential for formation of RNP complexes or protein-protein interactions [187]. Zhang and colleagues postulated that in solution and in absence of bound mRNAs, the N- and C-terminal part of HEPN align and move together with the RING domain, independent of the ROQ domain which moves together with the ZF domain [197, 203]. This could facilitate a cooperative scanning of mRNA targets.

2.5 Roquin in T cells

Since T cells were demonstrated to be the cause of the autoimmune syndrome in the Roquin1$^{san/san}$ mouse strain, most mouse models were designed to unravel the function of Roquin proteins in the T cell compartment to identify signs of a lupus-like phenotype. Strikingly, the systemic ablation of Roquin1 in mice resulted in perinatal death, which could be partially rescued by crossing the complete knockout onto an outbred genetic CD1 background [212]. Surprisingly, the ablation of Roquin1 did not cause overt autoimmunity, although it resulted in elevated ICOS expression through T cell-intrinsic and -extrinsic mechanisms. Furthermore, absence of Roquin1 in T cells in CD4$^{cre/+}$ (cre: inserted, wild type: +) Roquin1$^{F/F}$ mice did not lead to an increase in T_{reg} or T_{FH} cell differentiation or formation of spontaneous GCs, although an increase of CD8^{+} SLEC-like cells in peripheral lymphoid organs was noted [212]. The discrepancy between the Roquin1$^{san/san}$ mice and Roquin1-knockout mice pointed to a compensatory role for Roquin2 in case of Roquin1 deficiency. Further analyses to clarify the causative alterations leading to aberrant T_{FH} differentiation in the *sanroque* strain resulted in identification of the function of IFNγ in the pathology [167]. Systemic Roquin2 deficiency causes postnatal death with delayed kinetics compared to systemic Roquin1 ablation, which could be rescued in the same manner as the Roquin1

complete knockout. Mice with systemic Roquin2 deficiency as well as T cell-specific ablation of Roquin2 develop a normal immune system with unchanged ICOS levels on T cells [191]. The near-identical subcellular localization [165, 192], shared interaction with components of the RNA decay system, including enhancer of decapping Edc4 [191], and the striking sequence homology between the paralogs, especially in the protein regions attributed to functional domains, strongly argued for a compensatory role of Roquin2 in the case of Roquin1-deficiency, but not in the Roquin1$^{san/san}$ mutation. Indeed, mice with T cell-specific ablation of Roquin1 and 2 (CD4$^{cre/+}$ Roquin1-2$^{F/F}$) present many features of the Roquin1$^{san/san}$ mouse, such as splenomegaly, lymphadenopathy, increased frequencies of thymic and peripheral T_{reg} cells and striking activation of CD4$^+$ and CD8$^+$ T cells, exceeding activation of these subsets observed in *sanroque* mice [191]. Likewise, ICOS levels on all T cells are increased even more than in the Roquin1$^{san/san}$ or CD4$^{cre/+}$ Roquin1$^{F/F}$ mice, suggesting hypomorphic activity of the Roquin1^{san} allele [191]. Despite elevated numbers of T_{FH} and GC B cells comparable to the *sanroque* strain, CD4$^{cre/+}$ Roquin1-2$^{F/F}$ do not produce similar levels of anti-nuclear antibodies (ANAs), potentially due to the demonstrated collapsed splenic microarchitecture in this mouse strain [191]. Absence or deficits of follicular structures, the underlying reason for the defective splenic structure, were observed already in young CD4$^{cre/+}$ Roquin1-2$^{F/F}$ mice three weeks after birth [191]. In addition, Vogel and colleagues presented activation-induced tumor necrosis receptor superfamily 4 (Tnfrs4 or Ox40) as a third T cell-specific target regulated by Roquin proteins. They showed binding of Roquin1 and 2 to the 3'UTR of *Ox40* mRNA and 3'UTR-dependent posttranscranscriptional repression of *Ox40* mRNA [191]. On the other hand, it remains elusive how Roquin proteins act in T cells to reduce the half-life of *IFNg* mRNA [167]. The concerted post-transcriptional gene regulation by Roquin1 and 2 together with Regnase1 was subsequently described to critically antagonize the differentiation of naive CD4$^+$ T cells into IL-17 producing T_H17 cells by repressing the T_H17-promoting factors ICOS, IRF4, IL-6, c-Rel, IκBNS and IκBζ [199]. Furthermore, it was shown that Roquin1/2-deficient naive T cells, when stimulated under T_H0 or T_H1 conditions, differentiated at significantly increased frequencies into IFNγ-producing T_H1 cells compared to wild type controls [199]. Remarkably, the thymic NKT cell compartment, a small subset of glycolypid-recognizing T cells that in mice mainly express a semi-invariant TCR [215], has recently been demonstrated to comprise a massively expanded NKT17 cell subset caused by increased NKT17 polarization of developing NKTs in CD4$^{cre/+}$ Roquin1-2$^{F/F}$. On the other hand, other NKT cell subsets are essentially absent in these mice [216].

In contrast to Roquin1/2-deficient conventional T cells, Roquin1/2-deficient NKT cells exhibit an impaired ability to secrete cytokines [216]. Due to the ability of Roquin paralogs to inhibit many terminal T cell differentiation fates by repressing key signaling mediators and the concomitant regulation of Roquin protein by MALT1 downstream of TCR signaling, it has been suggested that Roquin paralogs molecularly translate TCR and costimulatory signaling strength into graded expression of activation- or differentiation-inducing transcription factors [199]. In this model, TCR-based activation of MALT1 induces cleavage of Roquin paralogs to relieve repression of these factors [198, 199]. Besides these loss-of-function studies on Roquin paralogs in T cells, also gain-of-function studies employing T cell-restricted overexpression of Roquin1 *in vivo* and in cell lines were performed [217-219]. Surprisingly, mice with T cell-specific Roquin1 overexpression mount stronger immune reactions in models of arthritis and hepatitis, with expanded T_H17 populations and elevated serum levels of IFNγ, IL-6 and TNFα [217, 218]. However, drawing definitive conclusions from this model has been obstructed by the reduced number of T_{reg} cells in this model [217] and the pending requirement to analyze their suppressive function among other unresolved questions. Taken together, the tight regulation of mRNAs encoding mediators of T cell activation and differentiation by Roquin1 and 2 is essential for preventing the onset of the lupus-like phenotype observed in the *sanroque* mice. The Roquin paralogs are causaly linked to regulation of cell fate choices of naive T cells into T_{FH} and T_H17 cells and inhibition of NKT17 differentiation in thymic NKT cells.

2.6 Roquin in B cells

In contrast to the well-described role of Roquin paralogs in T cells, analyses of their function in B cells remain significantly less comprehensive. Bone marrow B cell numbers and early B cell development in the *sanroque* strain was reported to be unaltered, however the frequency of $B220^+$ $AA4.1^+$ immature B cells among $CD19^+$ bone marrow B cells appears to be increased [161]. The increased ratio of GC B cells in mixed bone marrow chimeras, reconstituted with 50:50 san/wt compared to 50:50 wt/wt bone marrow, provided a first hint at a potential B cell-intrinsic function of Roquin1 in the GC reaction [161]. Furthermore, neither ablation of T_{FH} cell development by systemic ablation of signaling lymphocytic activation molecule (SLAM)-associated protein (SAP) nor other means of ameliorating T cell-driven aspects of the lupus-like phenotype in the *sanroque* strain were able to cure splenomegaly, lymphadenopathy or hypergammaglobulinemia [162, 167].

Strikingly, systemic IFNγ-receptor deficiency in Roquin1$^{san/san}$ mice rescues the autoimmune-phenotype, splenomegaly and lymphadenopathy, yet effects on excessive CSR in these mice were not conclusively shown. Additionally, in bone marrow reconstitution experiments designed to specifically address the pathomechanistic role of IFNγ signaling in T cells, a significant contribution of IFNγ signaling in non-T cell populations of the spleen to the increased GC B cell numbers in the *sanroque* phenotype was demonstrated [167]. Indications for a potential additional role of Roquin in sustaining self-tolerance in TI immune responses in FO and B1 B cells were obtained when the Roquin1$^{san/san}$ mice were crossed with Obf1 complete knockout mice. In Obf1$^{-/-}$ mice, MZ B cells are absent and FO B cells lack the ability to undergo a GC reaction [220]. Remarkably, the hypergammaglobulinemia observed in Roquin1$^{san/san}$ Obf1$^{-/-}$ mice stems from specific generation of GC-independent IgM autoantibodies and selection of self-reactive B cells seems to occur independently of T cells [221]. A B cell-specific role of Roquin1 was more specifically interrogated in CD19$^{cre/+}$ Rc3h1$^{F/F}$ mice [212]. These mice have enlarged spleens as a consequence of expanded populations of B cells, T_{reg} cells, effector-like (CD44$^+$ CD62L^{lo}) CD4$^+$ and CD8$^+$ and eosinophils [212]. Moreover, the cell numbers of monocytic/macrophage and memory-like CD44$^+$ CD62L$^+$ CD4$^+$ and CD8$^+$ populations tended to be increased in this mouse line [212]. In contrast, ablation of Roquin1 in the whole hematopoietic system in Vav$^{cre/+}$ Rc3h1$^{F/F}$ mice, did not cause an expansion of the splenic B cell compartment but a significant reduction of immature and mature recirculating B cell numbers in the bone marrow [212]. This early block in B cell generation in Vav$^{cre/+}$ Rc3h1$^{F/F}$ mice could neutralize the B cell expansion observed by later ablation of Roquin1 in B lineage cells by CD19Cre. As Vavcre initiates recombination of loxP-flanked alleles in HSCs [222], every hematopoietic population is affected from its earliest stages onwards. Development of B cells in the bone marrow is largely an autonomous process driven by rearrangement of the IgH and IgL chain loci in defined stromal niches of HSC-independent origin [223]. Therefore, the partial block in B cell development observed in Vav$^{cre/+}$ Rc3h1$^{F/F}$ mice suggested a regulatory role of Roquin paralogs in early B cell development.

II. Aim of the thesis

Extensive work on the RNA-binding binding proteins Roquin1 and 2 characterized their function in sustaining peripheral tolerance in the germinal center reaction by antagonizing aberrant T_{FH} development through post-transcriptional repression of key signaling mediators, including IFNγ, ICOS and OX40 [167, 191]. Furthermore, Roquin paralogs critically regulate T cell differentiation in T_H17 cells and potentially T_H1 cell fates as well as inhibiting NKT differentiation into NKT17 cells. Initial experiments indicated B cell-specific roles of Roquin1 *in vivo*. Additionally, at the time when this project was initiated, no cis-regulatory elements in Roquin1 and 2 target mRNAs were described and the molecular organization of the novel ROQ domain, its boundaries, as well as the mechanisms underlying binding of Roquin paralogs to an obscure mRNA target motif remained enigmatic.

The objective of this thesis was to investigate the precise function of Roquin1 and 2 in early B cell development and peripheral B cell maturation *in vivo*. This research aim was complemented by efforts to molecularly characterize the binding of the ROQ domain to target mRNAs. Together, my objectives should unravel the roles of Roquin1 and 2 in B lymphocytes in physiology and pathology, the central aim of this thesis.

In achieving these aims, the following conclusions were made in my research and are further presented in the results part of this thesis:

1. Roquin family proteins are central regulators of B cell lymphopoiesis in the bone marrow and early B cell physiology.
2. Roquin proteins regulate the maturation, activation and differentiation of peripheral B cells.
3. Roquin proteins bind target mRNAs directly through defined structural principles.

III. Material and Methods

1. Basic materials, reagents and methods

Main standard methods of extraction, purification, quantification, analysis and manipulation of DNA, RNA and proteins were essentially performed as stated in Sambrook et al. (1989) and Sambrook and Russel (2001), unless indicated otherwise in the following sections.
Plasmid DNA isolation and gel extraction was performed employing kits from Qiagen and Macherey-Nagel.
Reagents and materials for molecular biological methods were obtained from the following manufacturers: Invitrogen, New England Biolabs, Promega, Metabion, Eurofins, GenScript, and Thermo Fischer Scientific.
Chemicals were purchased from: Applichem, Calbiochem, Fluka, Merck, Roth and Sigma-Aldrich.
Consumables were purchased from suppliers including BD Biosciences, Braun, Corning, Costar, Eppendorf, Greiner bio-one, Sarstedt and TPP.
General lab equipment from the following suppliers was employed: Bio-Rad, Bosch, Eppendorf, Gilson, Heraeus, Integra, Liebherr, Thermo Fisher Scientific and Zeiss.

2. Analyses of genetically modified mouse strains

2.1 Genetically modified mouse strains

All mouse lines described in this PhD thesis were maintained on a C57BL/6 genetic background. Mice were housed in specific pathogen-free animal facilities of the Max-Planck-institute of biochemistry and the Klinikum rechts der Isar of the Technische University München. All animal procedures were approved by the Regierung of Oberbayern.
Recombination of loxP flanked alleles in early B cell lymphopoiesis was realized by crossing these alleles to the Mb1cre mouse line [224]. Continiuous deletion of these alleles during B cell maturation was achieved employing crosses to the CD19cre mouse strain [225]. The IgH^{MOG} and $IgL^{D23\kappa}$ knockin alleles encoding a prearragend IgH and Igκ light chain have been described previously [28, 226].

Most mice were sacrificed for experimental use at 8 weeks to a maximum of 24 weeks of age (termed "young"), depending on the genetic model, as specificied in the results part. Mb1cre/+ Rc3h1$^{F/F}$-2$^{F/F}$ mice were analyzed at varying ages from 8 weeks to 1 year of age, to ensure stability of the phenotype (data not shown).

2.2 Genotyping of mouse strains

Genomic DNA was prepared from mouse earclip biopsies. The genotyping PCR for the IgH^{MOG} allele was established during the course of this work, to circumvent flow cytometry based genotyping. The primers used for genotyping are listed in Table 1.

Table 1: Genotyping oligonucleotide primers.
Sequences are shown in 5' to 3' orientation; for forward, rev reverse.

Designation	Direction	Sequence
Mb1cre	for	ACC TCT GAT GAA GTC AGG AAG AAC
	for	CTG CGG GTA GAA GGG GGT C
	rev	GGA GAT GTC CTT CAC TCT GAT TCT
	rev	CCT TGC GAG GTC AGG GAG CC
CD19cre	for	CCC AGA AAT GCC AGA TTA
	rev	AAC CAG TCA ACA CCC TTC C
	rev	CCA GAC TAG ATA CAG ACC AG
Rc3h1	for	AAA GCC CTC AAG ATT CTT TGG GCA
	for	GTA AAT GAG ATT CAG TGT GTC CAG
	rev	TAC AAG GTA GAG ACG TTT GGG AAG
Rc3h2	for	TGC AGC CAC CTC ATA TTA AC
	for	GCC CAC AGT CTT ATT GGA TG
	rev	CCA TGT TTT ATT AGC AGG CAC
IgH^{MOG}	for	AGA ATG GCC TCT CCA GGT CT
	for	CCT GCA AGG CTA CTG GCT AC
	rev	TCT CCA ACT ACA GCC CCA AC
IgL$^{D23\kappa}$	for	CTT GGC TTG GTA CCA GC
	rev	TTC AGC TCC AGC TTG GTC
R26^{CARStopFL}	for	AAA GTC GCT CTG AGT TGT TAT
	for	GGA GCG GGA GAA ATG GAT ATG
	rev	GGG CTA TGA ACT AAT GAC CCC G

2.3 Mouse organs employed for analyses

For analyses of bone marrow, two femurs and two tibias were used and total bone marrow cell numbers are based on the number of cells obtained from these bones.

Numbers of Peyer's Patches or mesenteric lymph nodes are based on total number of lymphoid structures removed. Samples resulting from lavage of peritioneal cavity were excluded if erythrocytes were visible by the naked eye.

2.4 Flow cytometry

Single cell suspension were prepared from mouse lymphoid organs, red blood cell lysis was performed using Gey's solution. Fc receptors were blocked by incubation with anti-mouse CD16/CD32 (clone 93, eBioscience) to reduce unspecific antibody binding before extra- and intracellular staining of single cell suspensions with antibodies listed in Table 2 or peanut gglutinin (PNA, Vector Laboratories). Streptavidin fluorophore conjugates (BD Biosciences, BioLegend, eBioscience) were used to visualize biotinylated primary antibodies. The FoxP3-transcription factor staining buffer kit (eBioscience) was employed according to the manufacturer's protocol for intracellular stainings. Analyses of viable cells was ensured by applying 7-AAD staining solution (7-amino-actinomycin D, eBioscience) or live/dead fixable near-IR (infrared) dead cell staining kit (Invitrogen). Primary intracellular Bim staining (clone C34C5, Cell signaling, host: rabbit) was visualized by secondary staining using rabbit specific fluorophore conjugates, as described before [227]. Single cell analyses were based on consecutive gating for FSC-H/-A and SSC-W/-A properties. Visualization of DNA content for *in vitro* cell cycle analyses was achieved using DRAQ5 (Abcam) and was based on BrdU in *in vivo* analyses as correlate of proliferation. For BrdU analyses, 2mg of diluted BrdU (BD Biosciences) were injected intra-peritoneally into mice. Mice were sacrificed, single cell suspensions prepared and intracellular BrdU (BD Biosciences) staining preformed according to the manufacturer's protocol. Analyses of apoptotic cells were performed using 7-AAD in combination with either the CaspGlow active staining kit (flourescein, BioVision) or the AnnexinV apoptosis detection kit (APC, eBioscience) according to the manufacturer's instructions.
A FACS Canto II (BD Biosciences) flow cytometer was used for sample acquisition and cells were sorted on a FACS Aria II or a FACS Aria III (BD Biosciences).

2.5 Magnetic activated cell sorting (MACS)

Single cell suspensions were labelled with anti-CD43 magnetic microbeads (Miltenyi Biotec) according to the manufacturer's protocol. Labelled samples were separated on an AutoMACS

Pro Separator (Miltenyi Biotec) machine employing the recommended program for negative depletion.

Table 2: Flow cytometry antibodies.
Antibodies employed in flow cytometry together. Information on recognized antigens in cluster of differentiation (CD) and alternative nomenclature, clone number manufacturer are listed.

Specificity	Clone	Manufacturer	Specificity	Clone	Manufacturer
AA4.1/CD93	AA4.1	eBioscience	CD86	GL1	eBioscience
Aiolos	8B2	eBioscience	CD95/Fas	Jo2	BD Biosciences
B220	RA3-6B2	eBioscience, BioLegend	CD117/c-kit	2B8	eBioscience
BCL6	K112-91	BD Biosciences	CD127/IL-7Rα	SB/199	eBioscience
CAR	Rmcb	Millipore	CD184/CXCR4	2B11	eBioscience
CD1d	1B1	eBioscience	FcεRIα	MAR-1	eBioscience
CD3	500A2	eBioscience	F4/80	CI:A3-1	AbD serotec
CD4	RM4-5	eBioscience	Gr1	RB6-8CS	eBioscience
CD5	53-7.3	eBioscience	IRF4	3E4	eBioscience
CD8a	53-6.7	eBioscience	IRF8	V3GYWCH	eBioscience
CD11b/Mac1	M1/70	eBioscience	IgM	polyclonal II/41	Dianova eBioscience
CD11c	N418	eBioscience	IgM[a]	DS-1	BD Biosciences
FcγRIIB CD16/CD32	93	eBioscience	IgD	11-26c	eBioscience
CD19	1D3 6D5	eBioscience, BioLegend	IgE	23G3	eBioscience
CD21/CD35	8D9	eBioscience	Igκ	187.1	BD Biosciences
CD23	B3B4	eBioscience	Igλ (1, 2, 3)	R26-46	BD Biosciences
CD24	M1/69	eBioscience	Ki-67	SolA15	eBioscience
CD25	3C7, PC61.5	eBioscience	λ5	LM34	BD Biosciences
CD38	90	eBioscience	MHC-II	M5/114.15.2	eBioscience
CD43	R2/60	eBioscience	Siglec-F	E50-2440	BD Biosciences
CD44	IM7	eBioscience	ST2/IL-33R	RMST2-2	eBioscience
CD62L	MEL-14	eBioscience	TCRβ	H57-597	eBioscience
CD69	H1-2F3	eBioscience	Ter119	Ter119	eBioscience
CD80	16-10A1	eBioscience	ZAP70	1E7.2 RUO	eBioscience

2.6 Primary mouse and mast cell culture

B cells obtained from CD43-based MACS depletion or splenocytes were cultured in RPMI1640 GlutaMAX medium supplemented with 5% FCS, HEPES, NEAA, sodium-pyruvate and penicillin/streptomycin (all Gibco). Stimulants were added for the following final concentrations: anti-CD40 4µg/ml (Sigman-Aldrich), anti-IgM 10 µg/ml (Jackson ImmunoResearch Laboratories), CpG 0.1 µM (InvivoGen) and LPS 20 µg/ml (Sigma-Aldrich). Kitcre$^{ERT2/+}$ Rc3h1-2$^{F/F}$ CAR$^{StopFL/StopFL}$ mast cells were generated and treated as described elsewhere [228].

2.7 Cloning the NFκbid reporter and Roquin1 expression constructs

Golden Gate [229] and Gateway cloning (Invitrogen) methods were employed to generate the NFκbid reporter plasmids flanked by Sleeping Beauty transposon recognition sites [230]. Required modules for Golden Gate cloning were either present in the Schmidt-Supprian laboratory or cloned from existing plasmids in the course of this thesis. The Golden Gate module carrying the NFκbid sequence was amplified from genomic DNA of splenocytes and subsequently mutated using site-specific olignucleotide primer pairs.
Expression constructs for crystallization purposes were cloned into pCoofy expression vectors employing the seamless ligation independent cloning (SLIC) method established by the core facilty of the MPI of biochemistry [231].

2.8 Mouse embryonic fibroblast (MEF) cell culture

Wild type, Roquin1-2$^{F/F}$ and Roquin1-2$^{\Delta/\Delta}$ MEFs [191] were maintained in Dulbecco's Modified Eagle's Medium (DMEM) cell culture medium (Gibco) supplemented with 10% FCS, L-glutamine, NEAA, sodium pyruvate, HEPES and penicillin/streptomycin (Gibco) at 37° C and 5% CO_2. For the generation of MEFs stably expressing the NFκbid reporter, plasmids comprising the wild type or mutated reporter plasmids were cotransfected. MEFs were incubated for 14h with 2µM sterile recombinant His-TAT-NLS-Cre (HTNC) fusion protein [232] dissolved in serum free-media for deletion of loxP-flanked alleles and treated as described elsewhere [233].

2.9 Lentiviral transduction of MEF cells

Roquin constructs were cloned into the pF 5x upstream activating sequence (UAS) vector. Transcription from this promoter is initiated upon binding of GEV16-ERT2. GEV16-ERT was transduced employing a separate lentiviral vector [234, 235]. 4-hydroxy tamoxifen treatment (100nM) induced nuclear localisation of GEV16-ERT2 resulting in the initiation of Roquin transcription.

To generate lentiviral particles, HEK cells were transfected with packaging constructs psPAX and pMD2.G and the relevant lentiviral plasmid in a ratio of 2.5/1/1.5. Supernatant containing the virus of interest was harvested and filtered after 48h. MEFs were spin-infected using this supernatant and 10 mg/ml polybrene. The medium was changed after 24h and antibiotic-mediated selection of transduced cells was initiated. 2-5 µg/ml puromycin were added for selection of the pF 5xUAS construct and 100 µg/ml hygromycin were employed for selection of the GEV16-ERT2 construct.

2.10 Quantitative realtime-PCR (qRT-PCR)

Total RNA was isolated from flow-cytometry sorted B cell populations using the RNeasy Plus Micro kit (Qiagen) according to the supplier's instructions. The First Strand cDNA Synthesis Kit (Fermentas) was employed in accordance with the supplier's protocol for preparation of cDNA. Gene expression analyses were based on the Roche Universal ProbeLibrary (UPL) system and performed according to the Roche protocol. Primers and probes employed are listed in Table 3. Samples for qRT-PCR analysis were run on the LightCycler (Roche).

Table 3: Primer and probe setup for qRT-PCR experiments.
Amplified targets of qRT-PCR reaction and employed UPL probe number and primer sequences are listed. Primer sequences are shown in 5' to 3' orientation; UPL Universal ProbeLibrary, for forward, rev reverse.

Target	Direction	UPL probe number	Primer sequence
Rc3h1	for	17	AAC CAG CAT TGG GCA TGT
	rev		CTT CAT CAC GTT TGG TGA CCT
Rc3h2	for	31	TTG GCA CTC TAC TTA AAA CCA CTA AG
	rev		TCG CAT AGC TCT GAC ACG AC
PBGD	for	22	CAG TGA TGA AAG ATG GGC AAC
	for		AAC AGG GAC CTG GAT GGT G

2.11 Western blot

Protein extracts from whole cell lysates of defined cell numbers were prepared by incubation of cells for 30 min on ice in a RIPA lysis buffer (50mM Tris pH 7.5, 0.25% sodium deoxycholate, 150mM NaCl, 1% NP-40) comprising 1 mM DTT (dithiothreitol), 1mM PMSF (phenylmethylsulfonylfluorid), 5mM NaF (sodium fluorid), 1mM Na_3VO_4 (sodium orthovanadate), 8mM β-glycerophosphate, 10µg/µl leupeptin and 10µg/µl aprotinin. Protein samples were run and proteins separated by sodium dodecyl sulfate polyacrylamide gel electrophoresis (SDS-PAGE, Bio-Rad) and blotted (Bio-Rad system) onto 0.45µM polyvinylidene fluoride (PVDF, Immobilon-P, Millipore) membranes, which were subsequently incubated with primary antibody against α-actinin (#3134, Cell Signaling) or serum containing polyclonal primary antibodies directed against Roquin1 and 2 [191] followed by incubation with HRP-conjugated secondary antibodies (Dianova). Blots were developed using a chemiluminescent HRP substrate (Immobilon Western, Millipore) on a digital imager (FLA 4000, GE Healthcare Life Sciences).

2.12 Enzyme-linked immunosorbent assay (ELISA)

ELISA was performed to determine serum concentrations of IL-6 and TNFα using kits (BD Biosciences) according to the supplier's protocols. Absolute concentrations were calculated based on serial dilutions. Tetramethylbenzidine (TMB) was used as an HRP-substrate (BD OptEIA, BD Biosciences).

2.13 Data and statistical analyses and visualization

Data from flow cytometry was analyzed with FlowJo (Treestar). The Watson pragmatic model of the FlowJo platform was applied for cell cycle analyses. The UPL assay design center software (Roche) was used to create gene-specific combinations of primers and UPL probes. Quantification of Western blot images was performed using ImageJ [236]. Excel (Microsoft) was employed for calculations. Statistical analyses and graphical representations were performed in R [237] and GraphPad Prism (GraphPad Software). Generally, visual representation of statistically not significant results is omitted, whereas statistical significance and p values are provided in the figure legends. Figures were prepared using Adobe illustrator (Adobe Systems) and this entire thesis was compiled in Word (Microsoft).

IV. Results

1. Roquin family proteins are central regulators of B cell lymphopoiesis in the bone marrow and early B cell physiology

1.1 Early loss of Roquin1 and 2 alleles perturbs bone marrow B cell lymphopoiesis at different time points

To ablate the loxP-flanked Rc3h1 [212] and Rc3h2 [191] alleles in early B cell lymphopoiesis, I used the Mb1cre mouse strain (cre: inserted/+: wild type) in which Cre transcription is controlled by the B cell-specific Igα promoter (CD79a/*mb1*) [224]. In the Mb1cre mouse, loxP-flanked alleles are recombined with a high efficacy starting from the earliest pro B cell stage [224, 238]. Mice with an early B cell-specific inactivation of both Roquin1 and both Roquin2 alleles ($Mb1^{cre/+}$ $Rc3h1^{F/F}$-$2^{F/F}$), of both Roquin1 and one Roquin2 allele ($Mb1^{cre/+}$ $Rc3h1^{F/F}$-$2^{F/wt}$) or ablation of Roquin1 or Roquin2 alone ($Mb1^{cre/+}$ $Rc3h1^{F/F}$, $Mb1^{cre/+}$ $Rc3h2^{F/F}$, respectively) were generated by crossing the relevant conditional, loxP-flanked allele carrying mice with the Mb1cre mouse strain. For all studies employing Mb1cre-based ablation of Rc3h1 and/or Rc3h2, age-matched $Mb1^{cre/+}$ and loxP-flanked/wild type mice (collectively referred to as "controls" or "wild type controls") were used as pooled controls, since the $Mb1^{cre/+}$mouse line does not show B cell-specific alterations [239, 240]. The effect of Rc3h1 ablation with or without additional inactivation of Rc3h2 alleles was studied in mice aged 8-20 weeks, while the consequences of Mb1cre-based Rc3h2 ablation alone was studied in 8-24 weeks old mice.

Initial flow cytometric analyses of B cell lymphopoiesis in the bone marrow of young $Mb1^{cre/+}$ $Rc3h1^{F/F}$ mice revealed a reduction of the percentage of immature and mature B cells (Fig. 4). Both bone marrow B cell populations were defined according to two different gating schemes yielding equivalent results. This prompted the investigation of redundant functions of Roquin2, which could potentially compensate the loss of Roquin1 during B cell lymphopoiesis. $Mb1^{cre/+}$ $Rc3h1^{F/F}$-$2^{F/F}$ mice developed normally and no alterations in mouse weight or total number of cells in the bone marrow at time of analysis were detected (Fig. S1).

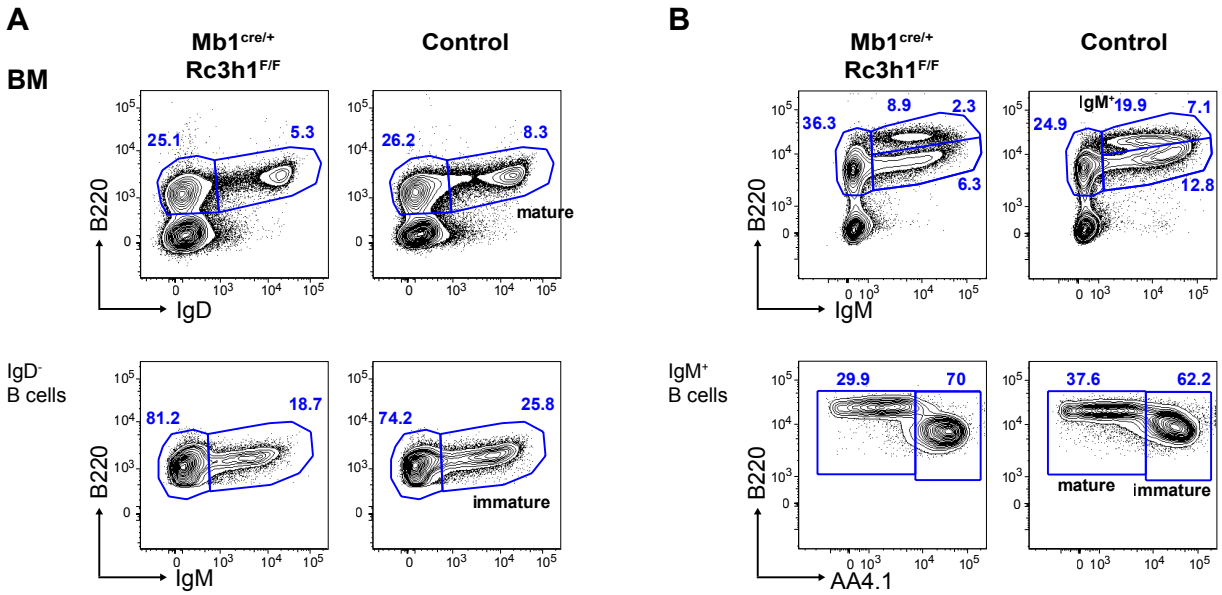

Figure 4: Reduction of immature and mature B cells in the bone marrow of Mb1$^{cre/+}$ Rc3h1$^{F/F}$ mice.
Representative flow cytometry plots of immature and mature B cells illustrating two possible gating strategies based on (A) IgD (mature B220$^+$ IgD$^+$; immature B220$^+$ IgD$^-$ IgM$^+$) or (B) AA4.1 (mature B220$^+$ AA4.1$^-$; immature B220$^+$ AA4.1$^+$) expression. Gates depict proportions of viable lymphocytes if not indicated otherwise and percentages of these gates refer to an individual, representative experiment; Mb1$^{cre/+}$ and wild type mice (collectively referred to as controls) were used as controls for comparison of Mb1^{cre} based experiments if not mentioned otherwise.

Mb1cre-mediated Rc3h1/2-deficiency causes a nearly complete loss of mature and immature B cell numbers in the bone marrow (Fig. 5A). Furthermore, whereas total pro B cell numbers are unchanged, a dramatic loss of pre B cells can be detected (Fig. 5B, 6). Within the pre B cell compartment, the number of large pre B cells in Mb1$^{cre/+}$ Rc3h1$^{F/F}$-2$^{F/F}$ mice is massively reduced and equals approximately one fourth of that in controls. However, the diminution of small pre B cells is even more pronounced, as small pre B cell numbers in Mb1$^{cre/+}$ Rc3h1$^{F/F}$-2$^{F/F}$ mice are almost reduced tenfold compared to controls (Fig. 5B, 6). As we observed dramatic defects in early B cells development, we included Mb1$^{cre/cre}$ mice in our experiments. Mb1$^{cre/cre}$ mice represent functional Igα knockouts and B cell lymphopoiesis is therefore arrested at the late pro B stage with V_HDJ_H rearrangement producing functional IgH chains [241]. The B cell numbers determined in these mice were compared to the numbers in Mb1$^{cre/+}$ Rc3h1$^{F/F}$-2$^{F/F}$ and control mice and thus serve as an additional control to further characterize the apparent block of bone marrow B cell development in Mb1$^{cre/+}$ Rc3h1$^{F/F}$-2$^{F/F}$ mice. There are significantly fewer late pro B cells in Mb1$^{cre/+}$ Rc3h1$^{F/F}$-2$^{F/F}$ than in Mb1$^{cre/cre}$ mice (Fig. 5B, 6), where this population is expanded due to the developmental block. Late pro B cells are defined in this thesis as CD19$^+$ B220^{lo} ckit$^+$ B cells to distinguish them from their developmental precursors, CD19$^-$ B220^{lo} ckit$^+$ prepro B cells.

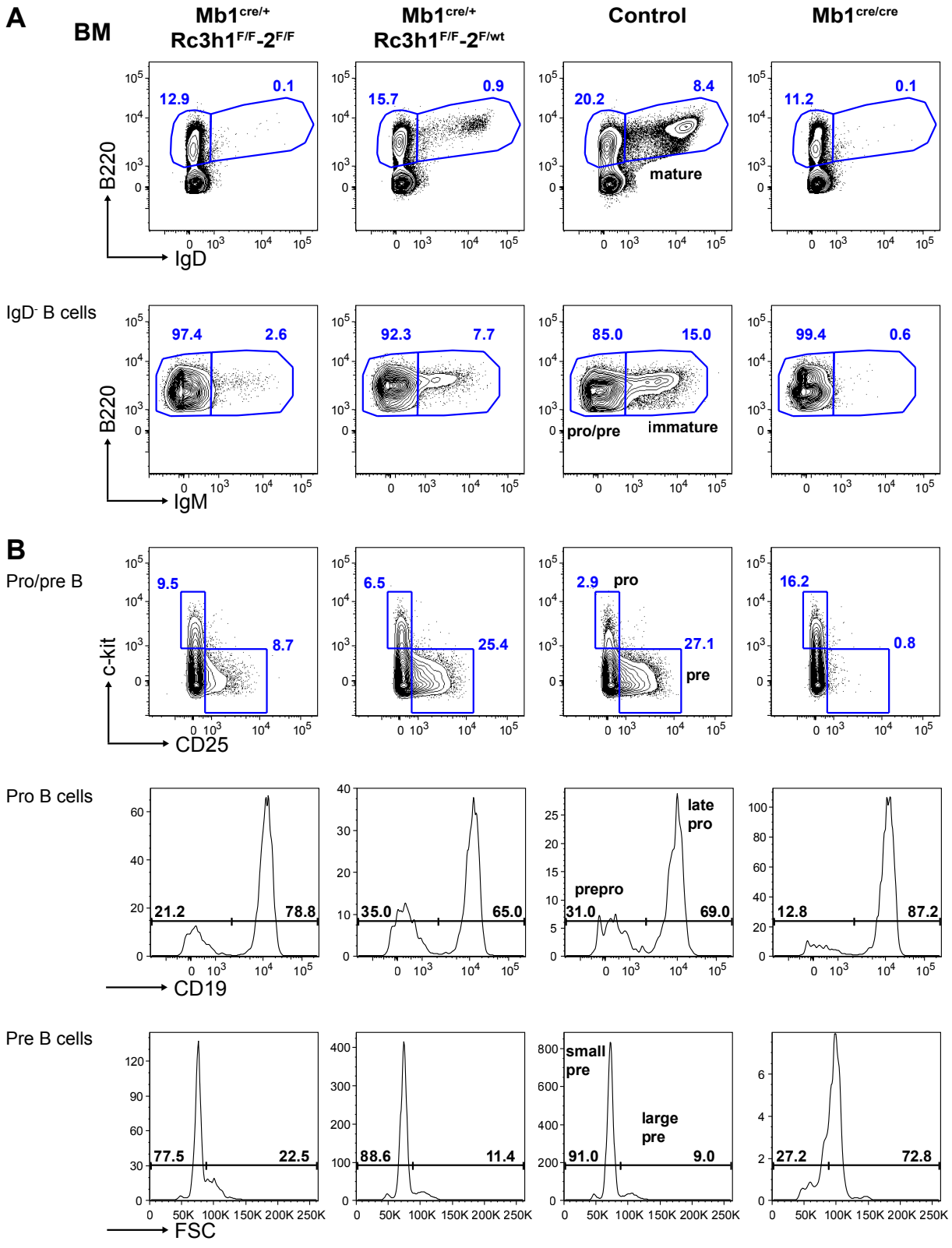

Figure 5: Bone marrow B cells of Mb1$^{cre/+}$ Rc3h1$^{F/F}$-2$^{F/F}$ and Mb1$^{cre/+}$ Rc3h1$^{F/F}$-2$^{F/wt}$ mice.
Representative flow cytometry plots depicting the gating strategy for bone marrow B cells (A) of mature and immature B cells and (B) pro and pre B cell subsets within the pro/pre B cell compartment. Gated B cell subsets: prepro B B220^{lo} CD19^{-} c-kit^{+} CD25^{-} IgD^{-} IgM^{-}; late pro B B220^{lo} CD19^{+} c-kit^{+} CD25^{-} IgD^{-} IgM^{-}; pro B B220^{lo} c-kit^{+} CD25^{-} IgD^{-} IgM^{-}; pre B B220^{lo} CD19^{-} c-kit^{-} CD25^{+} IgD^{-} IgM^{-}; large pre B B220^{lo} CD19^{-} c-kit^{-} CD25^{+} IgD^{-} IgM^{-} FSC^{hi}; small pre B B220^{lo} CD19^{-} c-kit^{-} CD25^{+} IgD^{-} IgM^{-} FSC^{lo}; pro/pre B B220^{lo} IgD^{-} IgM^{+}.

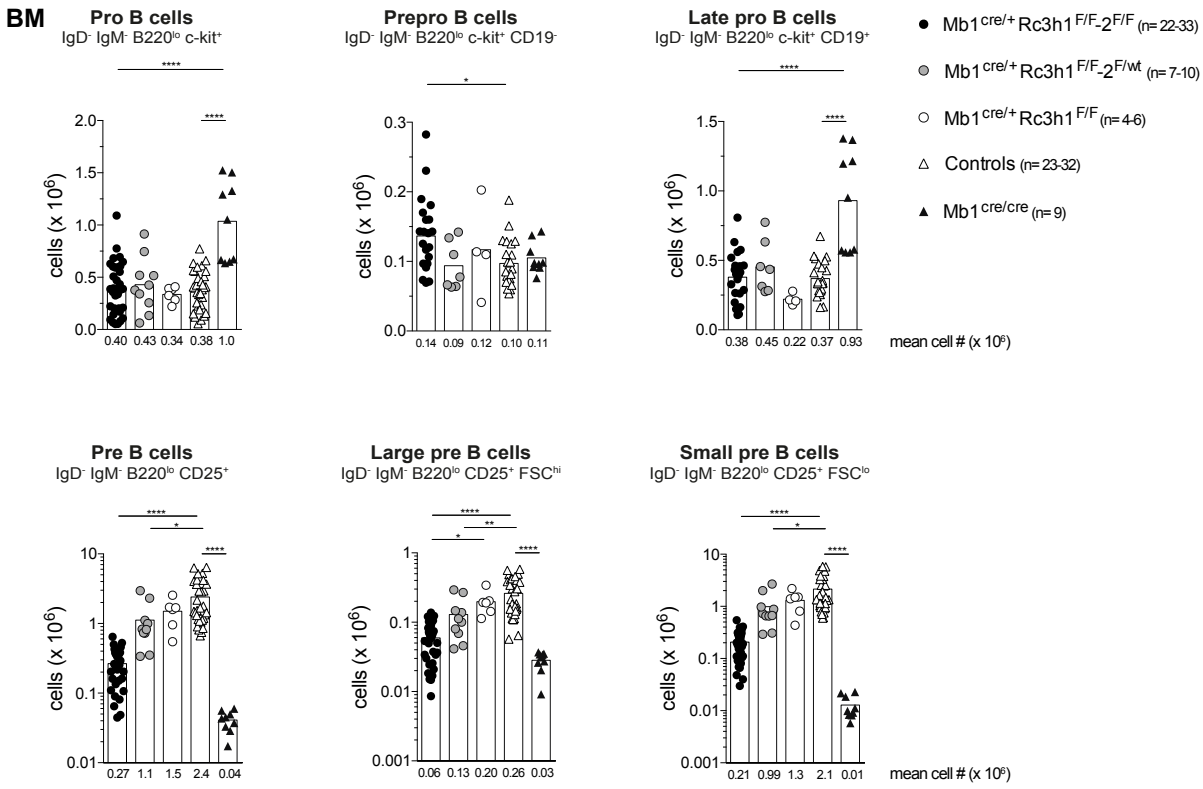

Figure 6: Pre B cell numbers are severely diminished in Mb1$^{cre/+}$ Rc3h1$^{F/F}$-2$^{F/F}$ mice, reduced in Mb1$^{cre/+}$ Rc3h1$^{F/F}$-2$^{F/wt}$ mice and not significantly decreased in Mb1$^{cre/+}$ Rc3h1$^{F/F}$ mice.

Total cell numbers of indicated bone marrow B cell populations as determined by flow cytometry. Gating strategy is shown in Fig. 5. BM: bone marrow; #: number. Numbers below bars show mean values (x 10^6). ****p ≤ 0.0001, **p ≤ 0.01, *p ≤ 0.05, ANOVA. Significances for Mb1$^{cre/cre}$ versus Mb1$^{cre/+}$ Rc3h1$^{F/F}$-2$^{F/wt}$ and versus Mb1$^{cre/+}$ Rc3h1$^{F/F}$ are not shown. Since the pro B cell compartment essentially comprises prepro and late pro B cells and pre B cells contain large and small pre B cells, I have omitted information on pro and pre B cells if data on prepro or late pro and large and small pre B cells was available.

Pre B cells are strongly reduced in Mb1$^{cre/+}$ Rc3h1$^{F/F}$-2$^{F/F}$ mice, while the B cells detected in Mb1$^{cre/cre}$ mice beyond the pro B cell stage essentially represent background staining (Fig. 5B, 6). Reduced pre B cell numbers were also observed in Mb1$^{cre/+}$ Rc3h1$^{F/F}$-2$^{F/wt}$ mice, albeit to a lesser extent, while there is no significant change at the pre B cell stage in Mb1$^{cre/+}$ Rc3h1$^{F/F}$ mice. Immature B cells are almost completely absent and mature recirculating B cells are lacking completely in Mb1$^{cre/+}$ Rc3h1$^{F/F}$-2$^{F/F}$ mice (Fig. 7A, 7B). Correspondinly, cell counts of immature and mature B cells are strongly reduced in Mb1$^{cre/+}$ Rc3h1$^{F/F}$-2$^{F/wt}$ and are also significantly reduced in Mb1$^{cre/+}$ Rc3h1$^{F/F}$ mice (Fig. 7A, 7B). Mb1cre-based ablation of Rc3h2 alone does not alter the total number of bone marrow cells nor the cell numbers of pro, pre and immature B cells, yet the number of mature recirculating B cells are significantly reduced (Fig. S2).

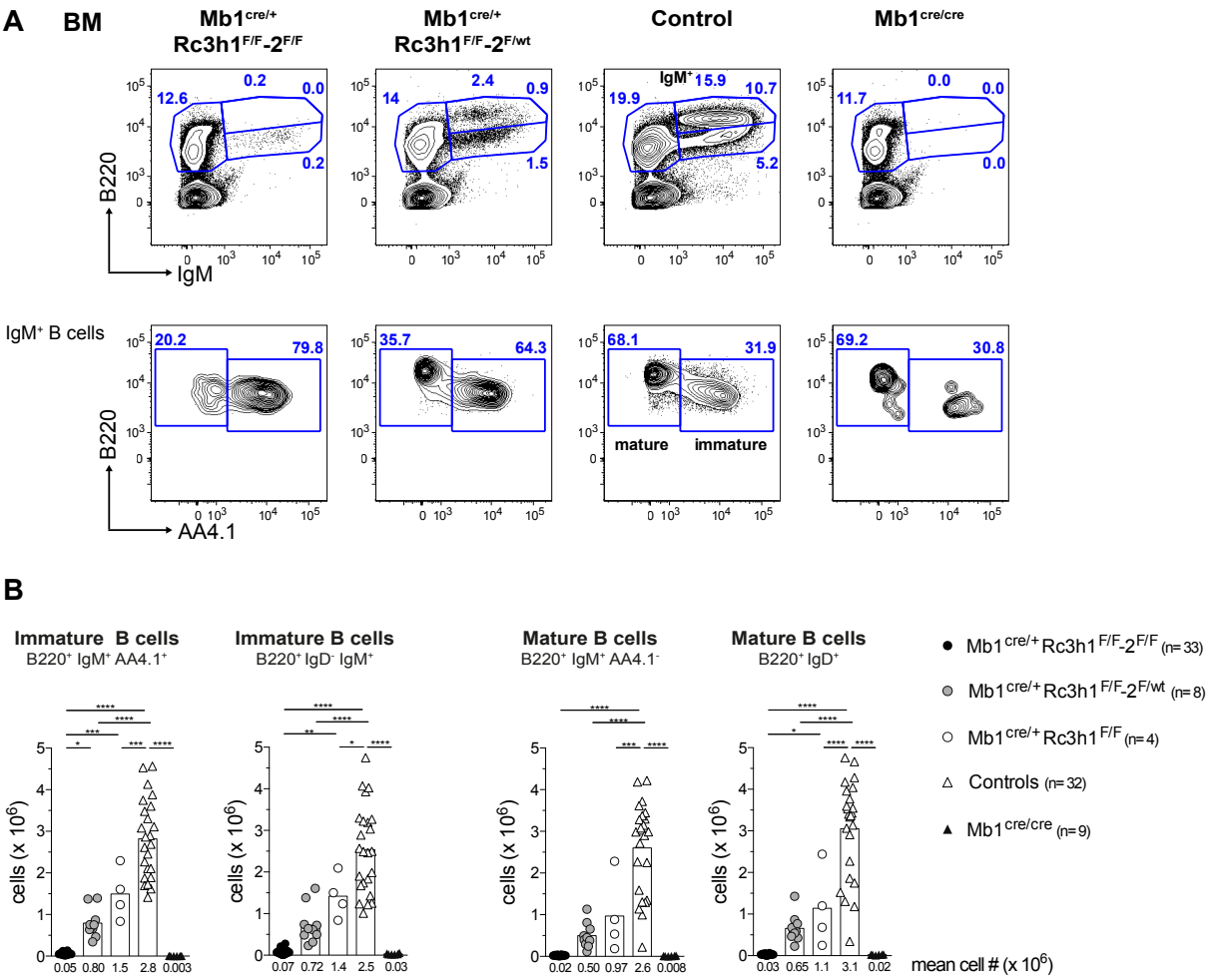

Figure 7: Bone marrow B cell development block in Mb1$^{cre/+}$ Rc3h1$^{F/F}$-2$^{F/F}$ and impediment in Mb1$^{cre/+}$ Rc3h1$^{F/F}$-2$^{F/wt}$ and Mb1$^{cre/+}$ Rc3h1$^{F/F}$ mice.

(A) Representative flow cytometry plots of immature and mature bone marrow B cells. (B) Percentages of immature and mature B cells of total BM cells and total immature and mature B cell numbers. BM: bone marrow. Numbers below graphs and bars represent mean percentages and cell numbers (#). ****p ≤ 0.0001, ***p ≤ 0.001, **p ≤ 0.01, *p ≤ 0.05, ANOVA. Significances for Mb1$^{cre/cre}$ versus Mb1$^{cre/+}$ Rc3h1$^{F/F}$-2$^{F/wt}$ and versus Mb1$^{cre/+}$ Rc3h1$^{F/F}$ are not shown.

In conclusion, Roquin1 and 2 are crucial regulators of B lymphocyte development in the bone marrow and inactivation of all alleles culminates in a massive block of pro to pre B transition, while inactivation of two Roquin1 alleles or two Roquin1 alleles and one Roquin2 allele produces intermediate phenotypes. Roquin1 appears to fulfill a main regulatory function at the pro to pre and pre to immature B cell transition, whereas Roquin2 exerts redundant functions that can partially compensate loss of Roquin1.

1.2 Absence of peripheral B cells upon B cell specific Roquin1 and 2 ablation and gene dosage effect on splenic B cell maturation

As bone marrow B cell lymphopoiesis is severely blocked in $Mb1^{cre/+}$ $Rc3h1^{F/F}$-$2^{F/F}$ mice and strikingly impeded in $Mb1^{cre/+}$ $Rc3h1^{F/F}$-$2^{F/wt}$ and $Mb1^{cre/+}$ $Rc3h1^{F/F}$ mice, I further investigated peripheral B cell stages [84]. Surprisingly, the weight of the spleens of $Mb1^{cre/+}$ $Rc3h1^{F/F}$-$2^{F/wt}$ and $Mb1^{cre/+}$ $Rc3h1^{F/F}$ mice are increased while the increase in splenocyte numbers is less pronounced (Fig. 8A). The percentage of B cells among total splenocytes are reduced in these two mouse strains, yet total B cell numbers are unchanged as a consequence of slightly increased splenocyte numbers. This decline in percentage was noted in immature/transitional, mature and B1 cell populations in $Mb1^{cre/+}$ $Rc3h1^{F/F}$-$2^{F/wt}$ mice, while only the cell numbers of B1 cells are significantly reduced in this strain. In $Mb1^{cre/+}$ $Rc3h1^{F/F}$ mice, there is an increment of percentage and total cell numbers of immature B cells, the ratios of mature and B1 cells among splenocytes are reduced with cell numbers remaining unchanged (Fig. 8B, 8C). In contrast, the weight of the spleens of $Mb1^{cre/+}$ $Rc3h1^{F/F}$-$2^{F/F}$ mice as well as the number of splenocytes in this line, are heavily diminished (Fig. 8A). Immature, mature and B1 B cell populations in the spleen are almost absent. Ratios and cell numbers determined for $Mb1^{cre/cre}$ mice were employed as a means to assess background staining and to identify B cell populations present or absent in $Mb1^{cre/+}$ $Rc3h1^{F/F}$-$2^{F/F}$ mice (Fig. 8B, 8C). This comparison demonstrates that the immature B cell population is the only population in which percentage of splenocytes and cell numbers are higher in $Mb1^{cre/+}$ $Rc3h1^{F/F}$-$2^{F/F}$ than $Mb1^{cre/cre}$ mice, establishing a complete absence of the mature splenic B cell populations and minimal counts for immature/transitional B cells in $Mb1^{cre/+}$ $Rc3h1^{F/F}$-$2^{F/F}$ mice. Spleen weight and splenocyte numbers are not altered in $Mb1^{cre/+}$ $Rc3h2^{F/F}$ mice (data not shown), while the percentage of splenic B cells is reduced. A trend towards decreased total numbers of immature and mature B cells in the spleen of these mice is observed, but the differences did not reach statistical significance (Fig. S3). Further discrimination of immature/transitional splenic B cells based on surface expression of CD23 and IgM, yielded significantly reduced percentages and total numbers of $CD23^{-}$ IgM^{-} and transitional T1 B cells in $Mb1^{cre/+}$ $Rc3h1^{F/F}$-$2^{F/F}$ mice. Analysis of this $CD23^{-}$ IgM^{-} subset was prompted by initial experiments indicating an increase of these cells (Fig. 9). In constrast, in $Mb1^{cre/+}$ $Rc3h1^{F/F}$ mice there is a significant increase in percentage and total cell numbers of these splenic B cell subsets (Fig. 9, 10).

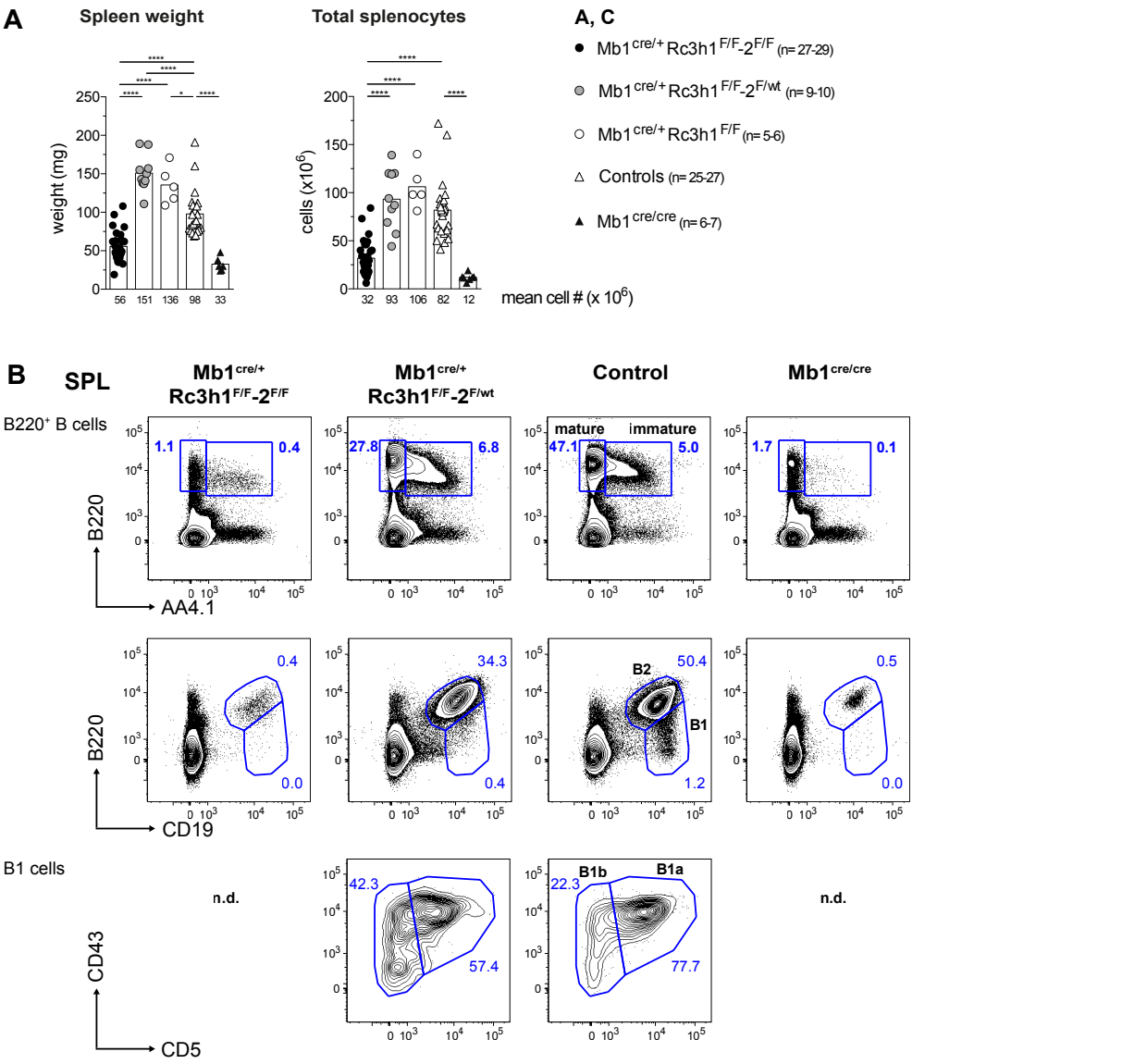

Legend on the next page

Figure 8 *(*previous page): Spleens and splenic B cells of $Mb1^{cre/+}$ $Rc3h1^{F/F}$-$2^{F/F}$, $Mb1^{cre/+}$ $Rc3h1^{F/F}$-$2^{F/wt}$ and $Mb1^{cre/+}$ $Rc3h1^{F/F}$ mice.

(A) Representative flow cytometry plots depicting gating scheme for immature, mature, B1, B1a and B1b B cells. (B) Spleen weight and total splenocyte number. (C) Percentages of splenocytes and total cell numbers of indicated B cell subsets. SPL: spleen; n.d.: not depicted. Numbers below graphs and bars show mean percentages and cell numbers (#). ****$p \leq 0.0001$, ***$p \leq 0.001$, **$p \leq 0.01$, *$p \leq 0.05$, ANOVA. Significances for $Mb1^{cre/cre}$ versus $Mb1^{cre/+}$ $Rc3h1^{F/F}$-$2^{F/wt}$ and versus $Mb1^{cre/+}$ $Rc3h1^{F/F}$ are not shown. Plots of gates on populations that were equal to or lower than 0.0% were omitted.

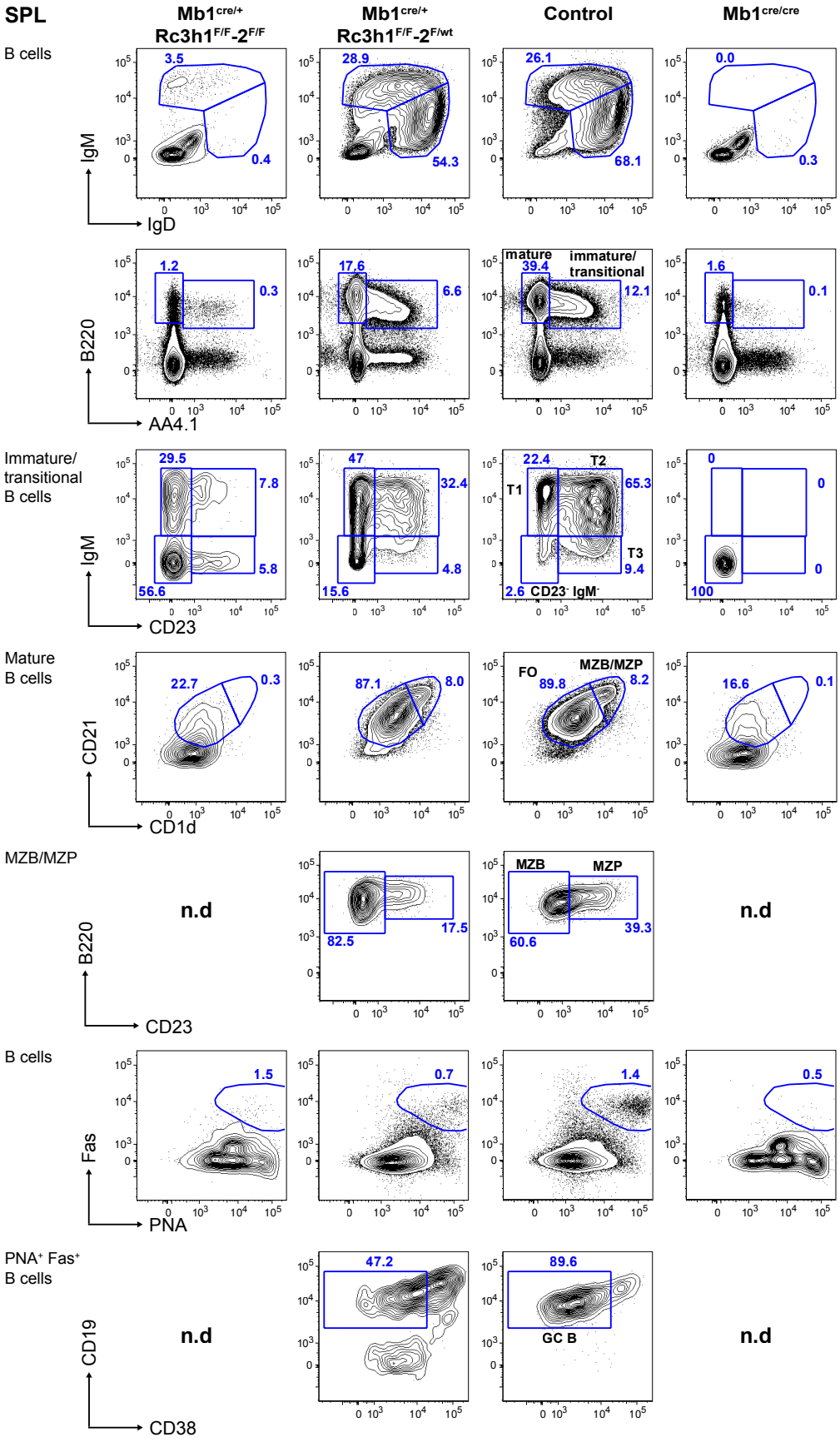

Legend on the next page

Figure 9 (previous page): Splenic B cells of Mb1$^{cre/+}$ Rc3h1$^{F/F}$-2$^{F/F}$, Mb1$^{cre/+}$ Rc3h1$^{F/F}$-2$^{F/wt}$ and Mb1$^{cre/+}$ Rc3h1$^{F/F}$ mice.
Representative flow cytometry plots illustrating gating scheme for splenic (SPL) immature/transitional, mature and GC B cells. Gated B cell subsets: immature/transitional B B220$^+$ AA4.1$^+$; mature B B220$^+$ AA4.1$^-$; CD23$^-$ IgM$^-$ immature B B220$^+$ AA4.1$^+$ CD23$^-$ IgM$^-$; transitional 1 (T1) B B220$^+$ AA4.1$^+$ CD23$^-$ IgM$^+$; transitional 2 (T2) B B220$^+$ AA4.1$^+$ CD23$^+$ IgM$^+$; transitional 3 (T3) B B220$^+$ AA4.1$^+$ CD23$^+$ IgM$^-$; follicular (FO) B B220$^+$ AA4.1$^-$ CD21^{int} CD1d^{int}; marginal zone (MZB/MZP) B B220$^+$ AA4.1$^-$ CD21^{hi} CD1d^{hi}; mature marginal zone (MZB) B220$^+$ AA4.1$^-$ CD21^{hi} CD1d^{hi} CD23$^-$; marginal zone precursor (MZB) B B220$^+$ AA4.1$^-$ CD21^{hi} CD1d^{hi} CD23$^+$; germinal center (GC) B B220$^+$ Fas$^+$ PNA$^+$ CD19$^+$ CD38^{lo}. Plots of gates on populations that showed less than 100 events were omitted (n.d. not depicted).

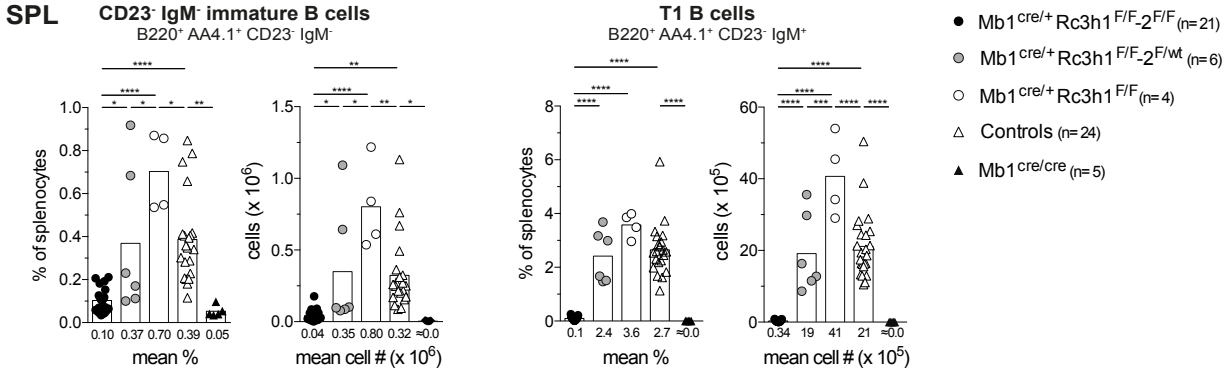

Figure 10: Essentially no B cell stages past transitional T1 found in spleens of Mb1$^{cre/+}$ Rc3h1$^{F/F}$-2$^{F/F}$ mice.
Percentages of viable splenocytes and total cell numbers of indicated B cell subsets show graphs and bars are mean values. ****p ≤ 0.0001, ***p ≤ 0.001, **p ≤ 0.01, *p ≤ 0.05, ANOVA. Significances for Mb1$^{cre/cre}$ versus Mb1$^{cre/+}$ Rc3h1$^{F/F}$-2$^{F/wt}$ and versus Mb1$^{cre/+}$ Rc3h1$^{F/F}$ are not shown.

Since total transitional T2 B cell numbers in Mb1$^{cre/+}$ Rc3h1$^{F/F}$-2$^{F/F}$ mice are just marginally above the T2 B cell number calculated for Mb1$^{cre/cre}$ mice, and also mature B cell populations in the spleen are just minimally higher compared to Mb1$^{cre/cre}$ mice, I focused my analyses of naive and germinal center B cell populations on the Mb1$^{cre/+}$ Rc3h1$^{F/F}$-2$^{F/wt}$ and Mb1$^{cre/+}$ Rc3h1$^{F/F}$ mouse lines. Naive B cells of transitional T2 and T3 and mature follicular (FO) and marginal zone precursor (MZP) type are reduced in percentage and cell numbers in Mb1$^{cre/+}$ Rc3h1$^{F/F}$-2$^{F/wt}$ mice but not in Mb1$^{cre/+}$ Rc3h1$^{F/F}$ mice (Fig. 11). Interestingly, spontaneous germinal center (GC) B cells are expanded in percentage and total cell number specifically in Mb1$^{cre/+}$ Rc3h1$^{F/F}$ mice (Fig. 11), as observed previously in CD19$^{cre/+}$ Rc3h1$^{F/F}$ mice [212]. In Mb1$^{cre/+}$ Rc3h2$^{F/F}$ mice there is a slight trend of reduction of naive B cell populations or GC B cell populations in the spleen but no significant alterations (data not shown). Next, I analyzed additional lymphoid organs for naive and germinal center B cell populations. B cells, and especially B1 cells are near absent in the peritoneal cavity of Mb1$^{cre/+}$ Rc3h1$^{F/F}$-2$^{F/F}$ mice and are significantly reduced in Mb1$^{cre/+}$ Rc3h1$^{F/F}$-2$^{F/wt}$ and Mb1$^{cre/+}$ Rc3h1$^{F/F}$ mice (Fig. 12A, 12B). In the latter two genotypes, reduction of B1a B cells is even more pronounced than reduction of B1b.

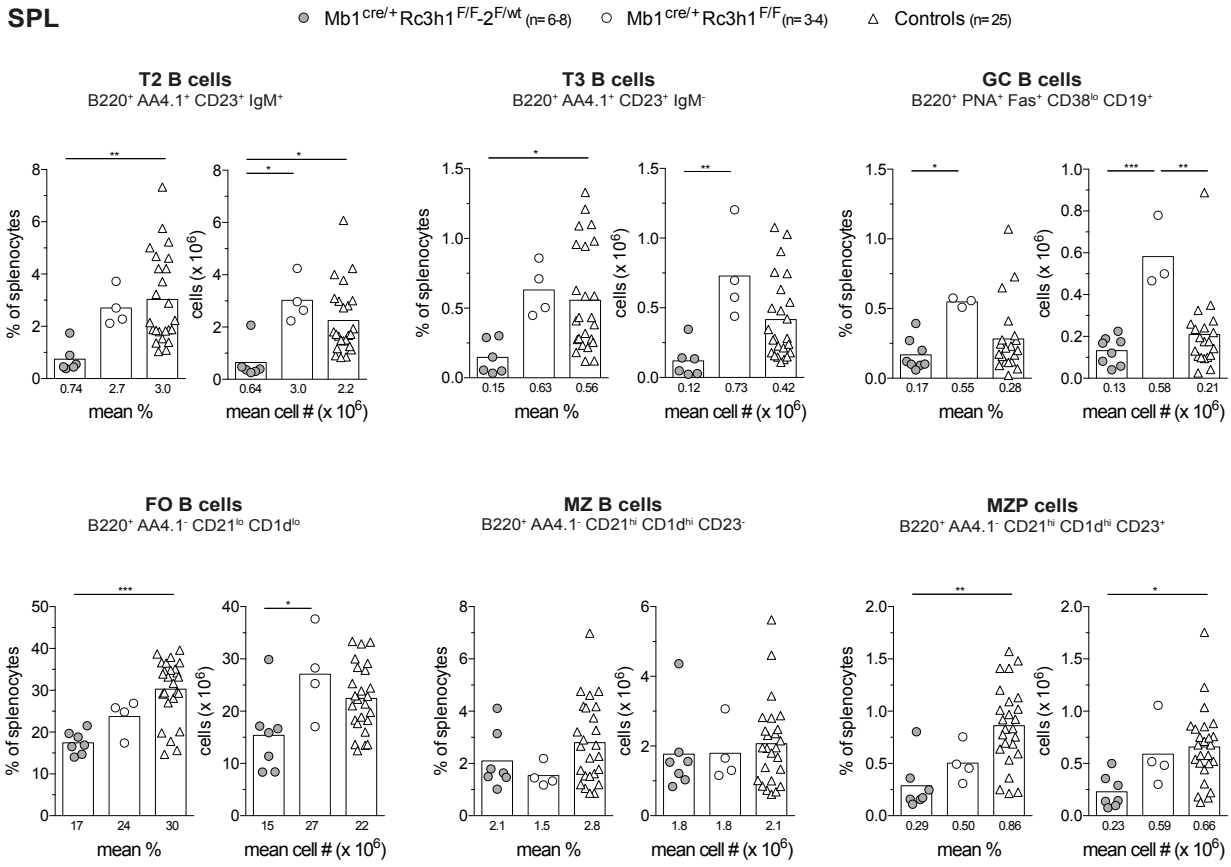

Figure 11: Reduction of splenic B cell populations in Mb1$^{cre/+}$ Rc3h1$^{F/F}$-2$^{F/wt}$ mice and expansion of the GC B cell subset in Mb1$^{cre/+}$ Rc3h1$^{F/F}$ mice.

Percentages of viable splenic cells and total cell numbers of indicated B cell subsets. T2: transitional 2; T3: transitional 3; FO: follicular; MZ: mature marginal zone; MZP: marginal zone precursor cells; GC: germinal center; SPL: spleen. Numbers below graphs and bars represent mean percentages and cell numbers (#). ***p ≤ 0.001, **p ≤ 0.01, *p ≤ 0.05, ANOVA.

Remarkably, Peyer's patches (PPs) are generally absent in Mb1$^{cre/+}$ Rc3h1$^{F/F}$-2$^{F/F}$ mice and therefore no B cells or GC B cells could be detected in PP of this strain. Furthermore, B cells and spontaneous GC B cells in mesenteric lymph nodes (mLN) are almost completely missing in in these mice (Fig. 13A, 13B). Similarly in Mb1$^{cre/+}$ Rc3h1$^{F/F}$-2$^{F/wt}$ mice the total number of cells in PPs tends to be reduced (Fig. 13B). B cells and spontaneous GC B cells are reduced in percentage and cell number in mLN of these mice. While B cell percentages and numbers in PP are also decreased, the ratio of spontaneous GC B cells in PPs of the Mb1$^{cre/+}$ Rc3h1$^{F/F}$-2$^{F/wt}$ mouse strain is not altered compared to controls (Fig. 13B). In mLN of Mb1$^{cre/+}$ Rc3h1$^{F/F}$ mice, percentage and cell number of B cells are decreased, while GC B cells are unchanged. The percentages and total B cell numbers in the PPs of Mb1$^{cre/+}$ Rc3h1$^{F/F}$ mice are unchanged. Remarkably, the percentage of GC B cells but not the total cell number is significantly increased, despite unchanged total cell counts in PP (Fig. 13), possibly due to the low sample number (n=3).

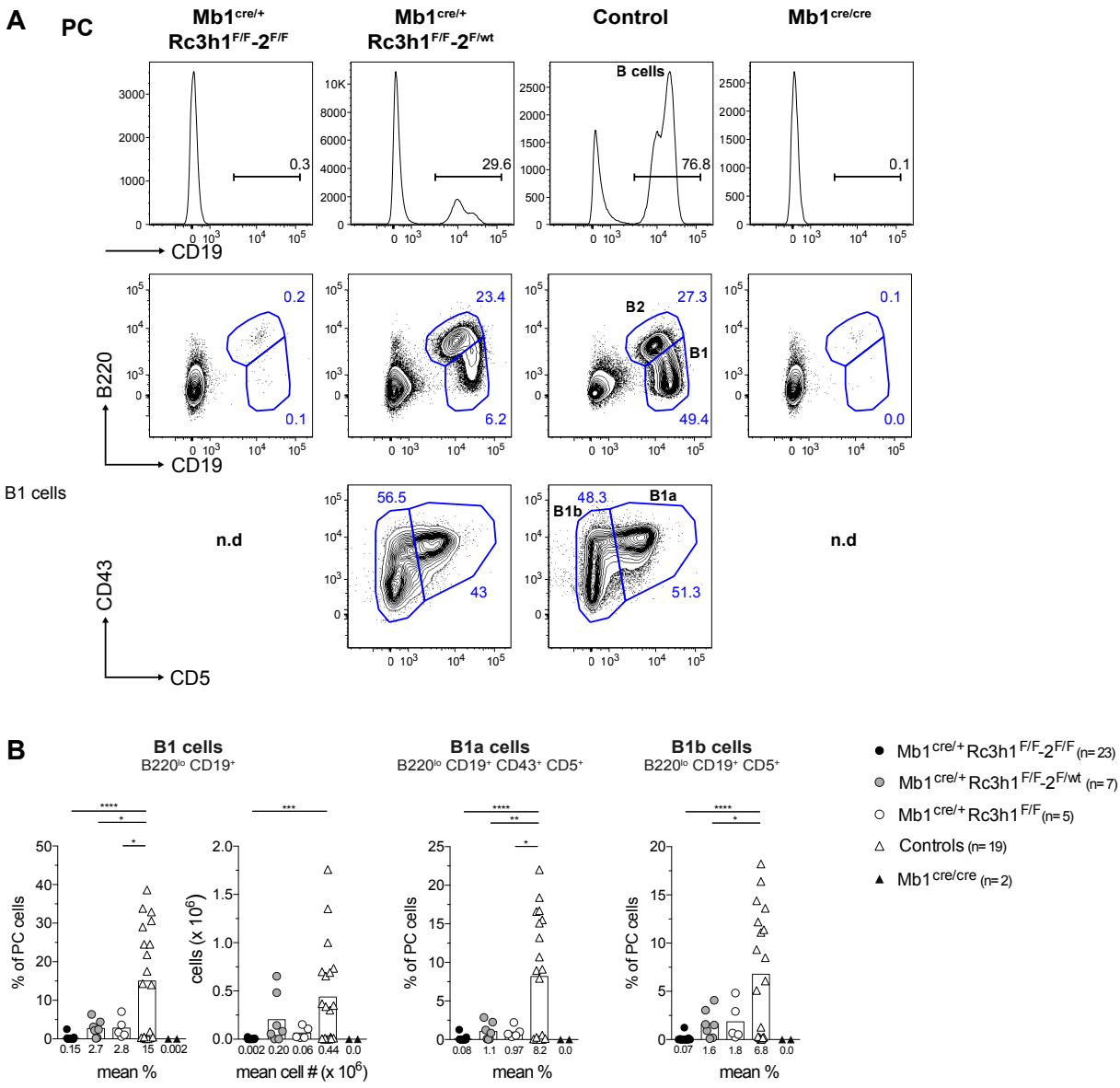

Figure 12: Peritoneal cavitiy B cells of Mb1$^{cre/+}$ Rc3h1$^{F/F}$-2$^{F/F}$, Mb1$^{cre/+}$ Rc3h1$^{F/F}$-2$^{F/wt}$ and Mb1$^{cre/+}$ Rc3h1$^{F/F}$ mice.

(A) Representative flow cytometric analysis of peritoneal cavity (PC) B cells. (B) Percentages of indicated B cell subsets among viable peritoneal cavitiy cells and total cell numbers. Numbers below graphs and bars show mean percentages and cell numbers (#). ****p ≤ 0.0001, ***p ≤ 0.001, **p ≤ 0.01, *p ≤ 0.05, ANOVA. Significances versus Mb1$^{cre/cre}$ were not determined since only two data points were obtained. Plots of gates on populations that showed less than 100 events were omitted (n.d. not depicted).

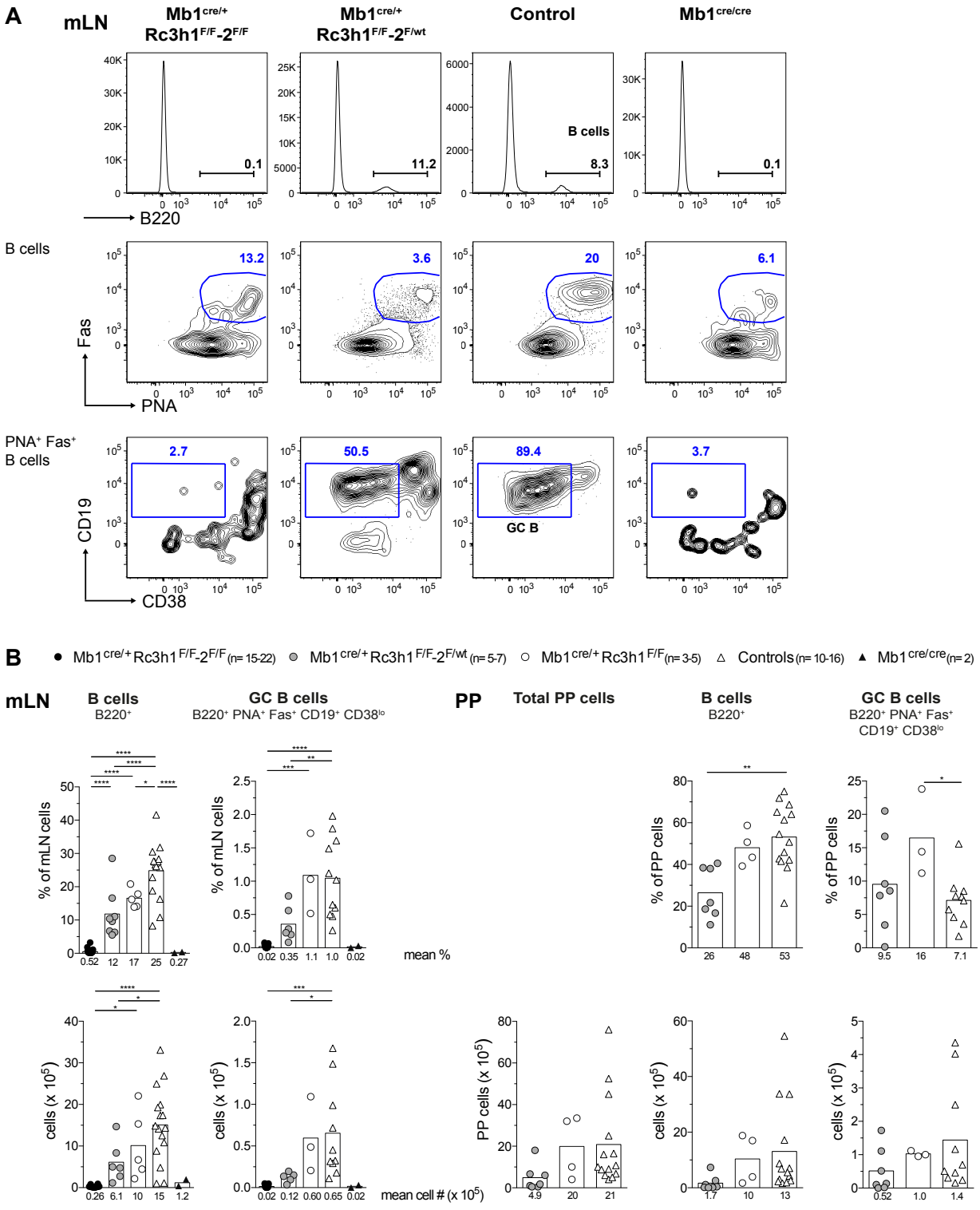

Figure 13: B and GC B cells of Mb1$^{cre/+}$ Rc3h1$^{F/F}$-2$^{F/F}$, Mb1$^{cre/+}$ Rc3h1$^{F/F}$-2$^{F/wt}$ and Mb1$^{cre/+}$ Rc3h1$^{F/F}$ mice in the GALT.

(A) Representative flow cytometric analysis of B and GC B cells in the GALT (mLN shown here, PP not shown). (B) Percentages of B cell subsets among viable cells of mLN or PP and total cell numbers as indicated. GALT: gut-associated lymphoid tissue; mLN: mesenteric lymph nodes; PP: Peyer's patches; GC: germinal center. Numbers below graphs and bars represent mean percentages and cell numbers (#). ****p ≤ 0.0001, ***p ≤ 0.001, **p ≤ 0.01, *p ≤ 0.05, ANOVA. Significances versus Mb1$^{cre/cre}$ were not determined since only two data points were obtained. Calculated cell numbers of < 100 were rounded to 0 and denoted as ≈0.0.

The B cell populations observed in peritoneal cavity or gut-associated lymphoid tissue B cell populations in Mb1$^{cre/+}$ Rc3h2$^{F/F}$ mice did not differ from control mice (data not shown). These findings indicate a gene-dosage effect of ablation of Roquin1 and 2 on peripheral B cell development and post-activation behavior. Complete loss of both Roquin1 alleles seems to only sligthly impact peripheral B cell development but causes a B cell-activating effect, as judged by the increase in germinal center B cell numbers. Ablation of Roquin1 together with loss of one or both alleles of Roquin2 impedes peripheral B cell development severely, culminating in virtual absence of peripheral B cells in the double knockout. B1 cell development appears to be more sensitive to loss of Roquin proteins, as it is already significantly inhibited by B cell-specific loss of Roquin1 alone. Interestingly, B1b development appears less affected by loss of Roquin proteins.

1.3 Highly efficient ablation of Rc3h1 and 2 from pro B to immature B cells in the bone marrow of Mb1$^{cre/+}$ Rc3h1$^{F/F}$-2$^{F/F}$ mice

In order to monitor efficiency of Mb1cre-mediated inactivation of Roquin1/2 alleles, qRT-PCR analysis was performed to detect *Rc3h1* and *2* mRNA in flow cytometry-sorted pro B, pre B and immature B cells of Mb1$^{cre/+}$ Rc3h1$^{F/F}$-2$^{F/F}$ mice (Fig. 14A). Primers were designed such that they only amplify cDNA derived from the loxP-flanked, but not the recombined mRNA (Fig. 14B). This analysis demonstrates the presence of intact *Rc3h1* mRNA in 6% of pro B and pre B cells and 4% in immature B cells as well as remaining expression of intact *Rc3h2* mRNA in 3% of pro B and pre B cells and 1% in immature B cells (Fig. 14A). 6% of RNA expression can come from two intact Roquin alleles in 6% of the cells or from one intact Roquin allele in 12% of the cells. Therefore, assuming that no cell retains more than one intact loxP-flanked Roquin1 or Roquin2 allele, a maximum of 18% (12% *Rc3h1* + *6% Rc3h2*) pro B, 18% of pre B and 10% of immature B cells may still express one intact *Rc3h1* or *2* allele. This analysis thus suggests that subsequent analyses were performed in cell populations where at least 82% of cells completely lacked Roquin. Analysis of Roquin1 and 2 protein levels in pro and pre B cells by Western blotting was precluded by the small number of cells that one can isolate from Mb1$^{cre/+}$ Rc3h1$^{F/F}$-2$^{F/F}$ mice. To date, no antibodies are available to detect Roquin proteins in intracellular flow cytometry experiments.

To identify cells in which Cre-mediated recombination had occurred at the single cell level through an indirect approach, I therefore employed the R26/CAG-CARΔ1^{StopF} (R26^{CARStopFL}) allele (Fig. 14C, 14D) [242]. These cells start expressing a truncated version of the human

coxsackie adenovirus receptor (CARΔ1, for simplicity also referred to as CAR) upon excision of a loxP-flanked stop cassette by Cre. CAR expression can be monitored by flow cytometry with antibodies directed against CAR. Hence, Cre-induced intracellular or surface expression of CAR functions as an indirect assessment of recombination status of other loxP-flanked alleles within the same cell subset. Experiments assessing CAR expression were performed in 8 to 28 weeks old mice. The proportion of CAR expressing B cells in Mb1Cre $R26^{CARStopFL}$ mice is lowest among pro B cells and then increases to over 90% from the small pre B cell stage onwards. The proportion of CAR-expressing pro B cells is lower than expected from Mb1cre-mediated expression of YFP [240] and might indicate a temporal delay of CAR surface expression. CAR expression is significantly reduced on all bone marrow B cell populations, except small pre B cells, of $Mb1^{cre/+}$ $Rc3h1^{F/F}$-$2^{F/F}$ $R26^{CARStopFL}$ mice compared to corresponding subsets of $Mb1^{cre/+}$ $R26^{CARStopFL}$ control mice (Fig. 14D). This decrease in CAR expression on bone marrow B cells from $Mb1^{cre/+}$ $Rc3h1^{F/F}$-$2^{F/F}$ $R26^{CARStopFL}$ mice, which is most apparent at the large pre B cell stage, is indicative of a selective advantage of cells with delayed or incomplete Cre-mediated recombination. The drop in CAR expression in B cell populations from $Mb1^{cre/+}$ $Rc3h1^{F/F}$-$2^{F/F}$ $R26^{CARStopFL}$ compared to $Mb1^{cre/+}$ $R26^{CARStopFL}$ mice corresponds quite well to the estimation of cells still expression one intact Roquin1 or 2 alleles based on RNA expression. Pro B: 19% less CAR^+ cells, 18% of cells retain maximally one Roquin allele; large pre B: 29% less CAR^+ cells, small pre B: 5% less CAR^+ cells, total pre B: 18% of cells retain maximally one Roquin allele; immature B: 23% less CAR^+ cells, 10% of cells retain maximally one Roquin allele. The high percentages of CAR^+ pro, pre and immature B cells in $Mb1^{cre/+}$ $Rc3h1^{F/F}$-$2^{F/F}$ $R26^{CARStopFL}$ mice thus underscore the notion that these cell populations are only slightly counterselected. Specifically, the percentage of CAR^+ double-deficient small pre B cells is not reduced, indicating that those double-deficient B cells that pass the pre-BCR checkpoint stage at the large pre B cell stage can differentiate normally into small pre B cells. In contrast, mature Roquin1/2-deficient bone marrow B cells are strongly counterselected in $Mb1^{cre/+}$ $Rc3h1^{F/F}$-$2^{F/F}$ $R26^{CARStopFL}$ mice, evidenced by a reduction of 70% of CAR^+ cells in AA4.1- B cells and 59% of CAR^+ cells in IgD+ cells compared to $Mb1^{cre/+}$ $R26^{CARStopFL}$ mice (Fig. 14D). Correspondingly, CAR levels steadily decline from transitional T1 over T2/T3 to any mature B cell subset in $Mb1^{cre/+}$ $Rc3h1^{F/F}$-$2^{F/F}$ $R26^{CARStopFL}$ mice, mirroring B cell numbers determined for these subsets (Fig. S4). Likewise, CAR expression is near absent in double-deficient B cells analyzed from peritoneal cavity or mesenteric lymph nodes.

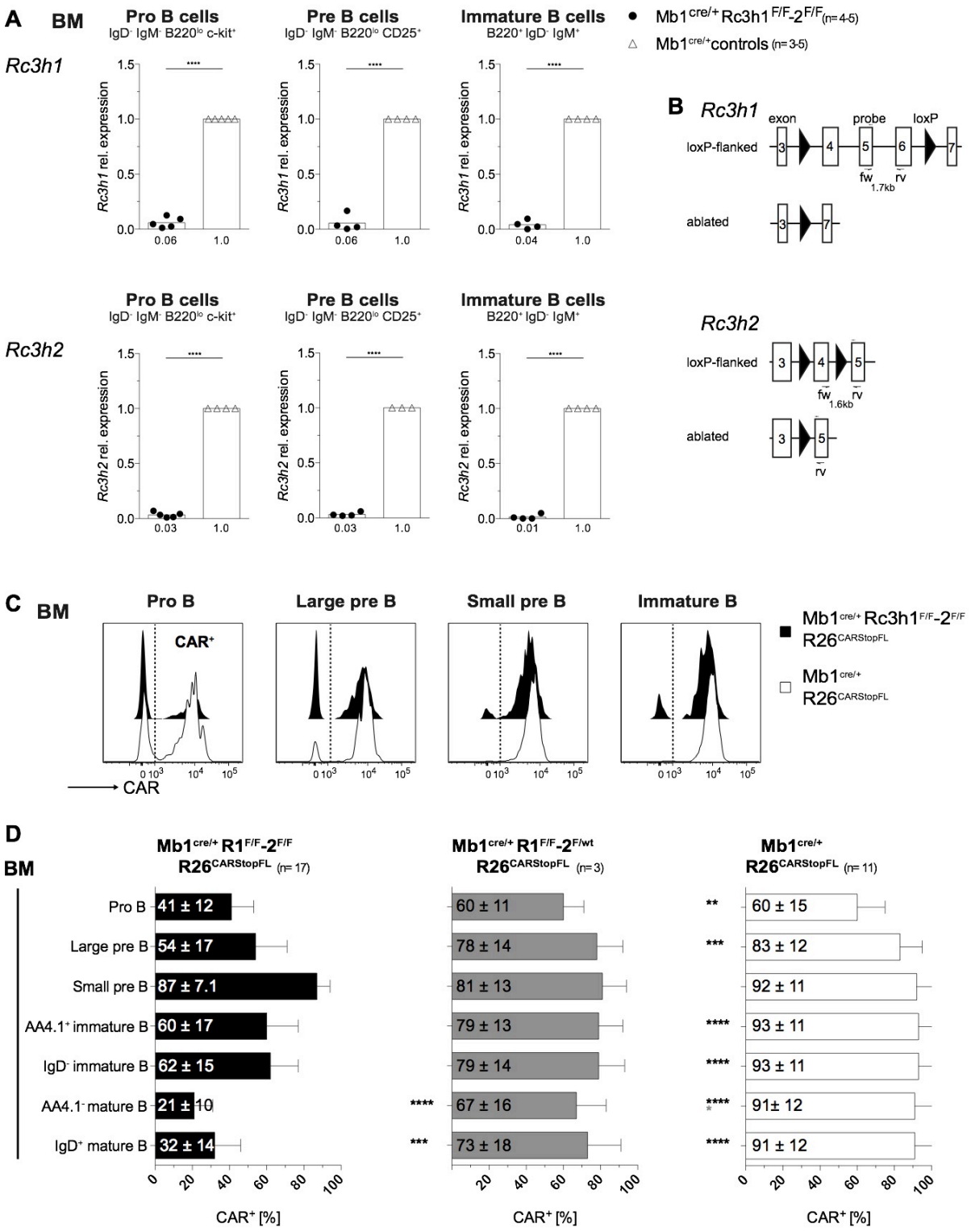

Figure 14: Analyses of Rc3h1-2 deletion in BM B cells of of Mb1$^{cre/+}$ Rc3h1$^{F/F}$-2$^{F/F}$ mice by qRT-PCR and employment of R26^{CARStopFL} reporter allele.

(A) Indicated bone marrow B cell subsets were sorted. Measured *Rc3h1-2* mRNA levels were normalized to PBGD and relative expression compared to Mb1$^{cre/+}$ controls is depicted. (B) Schematic on the design of the qRT-PCR assays for *Rc3h1* and *2*, indicating position of primers (arrows), probes and loxP sites in intact (loxP-flanked) and rearranged (ablated) loci as well as the distance between the involved exons. (C) Representative flow cytometric analysis of cell surface expression on indicated B cell subsets of the CAR reporter after Mb1cre-mediated deletion. The dotted line indicates CAR expressing (CAR$^+$) cells. *(Continued on next page)*

(D) Percentages of CAR^+ B cells among the respective subsets. Black * represent significant differences of $Mb1^{cre/+}$ $Rc3h1^{F/F}$-$2^{F/F}$ $R26^{CARStopFL}$ versus $Mb1^{cre/+}$ $Rc3h1^{F/F}$-$2^{F/wt}$ $R26^{CARStopFL}$ or $Mb1^{cre/+}$ $R26^{CARStopFL}$ B cells as indicated by position of the *, gray * describe significant differences of $Mb1^{cre/+}$ $Rc3h1^{F/F}$-$2^{F/wt}$ $R26^{CARStopFL}$ versus $Mb1^{cre/+}$ $R26^{CARStopFL}$ B cells. CAR signal on respective B cell populations in wt and $Mb1^{cre/+}$ mice was always < 1% (data not shown). Mature recirculating B BM B cells were included despite near absence in $Mb1^{cre/+}$ $Rc3h1^{F/F}$-$2^{F/F}$ $R26^{CARStopFL}$ mice to highlight counterselection. Gated B cell subsets: pro B $B220^{lo}$ c-kit^+ $CD25^-$ IgD^- IgM^-; large pre B $B220^{lo}$ c-kit^- $CD25^+$ IgD^- IgM^- FSC^{hi}; small pre B $B220^{lo}$ c-kit^- $CD25^+$ IgD^- IgM^- FSC^{lo}; $AA4.1^+$ immature B $B220^+$ IgM^+ $AA4.1^+$; IgD^- immature B $B220^+$ IgD^- IgM^+, $AA4.1^-$ mature B $B220^+$ IgM^+ $AA4.1^-$; IgD^- immature B $B220^+$ IgD^+, BM: bone marrow; fw: forward; rv: reverse; R: Rc3h. Bars represent means and error bars standard deviation. ****$p \leq 0.0001$, ***$p \leq 0.001$, **$p \leq 0.01$, *$p \leq 0.05$, ANOVA.

There are no recombined splenic T cells, as judged by CAR expression, confirming B cell specificity of Rc3h1 and 2 ablation. The lack of significance of observed reductions of CAR expression percentages on B cells of $Mb1^{cre/+}$ $Rc3h1^{F/F}$-$2^{F/wt}$ $R26^{CARStopFL}$ mice, might be due to the low number of mice analyzed (n=3) (Fig. 14C, 14D, S4). The reduction of pre, immature and mature recirculating B cells of $Mb1^{cre/+}$ $Rc3h1^{F/F}$-$2^{F/wt}$ $R26^{CARStopFL}$ expressing CAR compared to $Mb1^{cre/+}$ $R26^{CARStopFL}$ control mice, coincides with the observed partial impairment of pre to immature B cell transition in these mice (Fig. 14C, 14D). Similarly, CAR expression is significantly reduced on splenic T3 and mature B cell populations, most significantly on follicular B cells as well as germinal center B cells and B cells from mesenteric lymph nodes and Peyer's patches of $Mb1^{cre/+}$ $Rc3h1^{F/F}$-$2^{F/wt}$ $R26^{CARStopFL}$ mice compared to $Mb1^{cre/+}$ $R26^{CARStopFL}$ mice (Fig. S4). Surprisingly, more innate like B cell populations, such as marginal zone B or B1 cell subsets in these mice, do not show reduced recombination efficiencies, as assessed by CAR, compared to respective $Mb1^{cre/+}$ $R26^{CARStopFL}$ controls (Fig. S4). In summary, ablation of Roquin1 and 2 by Mb1cre occurs very early and very efficiently in B cell development. Roquin1-deficient B cells additionally missing one allele of Roquin2 are under slight counterselection during B cell development and maturation in the bone marrow and periphery. Roquin1/2-deficient B cells are under strong counterselection at the large pre B cell stage and from the immature B cell stage onwards. However, unchanged CAR levels at the small pre B cell stage indicate that a double-deficient B cell, which has passed the pre-BCR checkpoint at the large pre B cell stage can mature normally into a small pre B cell.

1.4 Rc3h1 and 2 are pivotal for normal expression of IgH and IgL chains in bone marrow B cells

Successful somatic rearrangement of V_H, D_H and J_H segments at the pro B cell stage results in a variable region V_HDJ_H exon, which allows for subsequent expression of μ heavy chain protein (μHC) [19]. Most commonly, differentiation proceeds to the pre B cell stage by pairing of μ to surrogate light chain to generate the pre-BCR, an Igα/β-dependent signaling unit [19, 243, 244]. To investigate if pre-BCR assembly or signaling might be affected by loss of Roquin1 and 2, I performed intracellular staining for the pre-BCR components λ5 and μHC (Igμ) in bone marrow B cells (Fig. 15, 16). The percentage of pro/pre B cells ($B220^{lo}$ surface IgM^-), which express an intracellular μHC, is massively decreased in $Mb1^{cre/+}$ $Rc3h1^{F/F}$-$2^{F/F}$ mice (Fig. 15B, 16B). Percentages of $μHC^+$ pre and immature B cells in these mice are immensely reduced (Fig. 15B), whereas intracellular μHC expression levels are unchanged or even increased (small pre B and immature B cells) in $μHC^+$ double-deficient bone marrow B cell populations compared to controls (Fig. 15B, 15C). Similarly, percentages of intracellular $μHC^+$ pro/pre B cells and total $μHC^+$ pro/pre B cell numbers are reduced in $Mb1^{cre/+}$ $Rc3h1^{F/F}$-$2^{F/wt}$ mice (Fig. 15B, 16B) and expression levels in $μHC^+$ cells are unchanged (Fig. 15C).

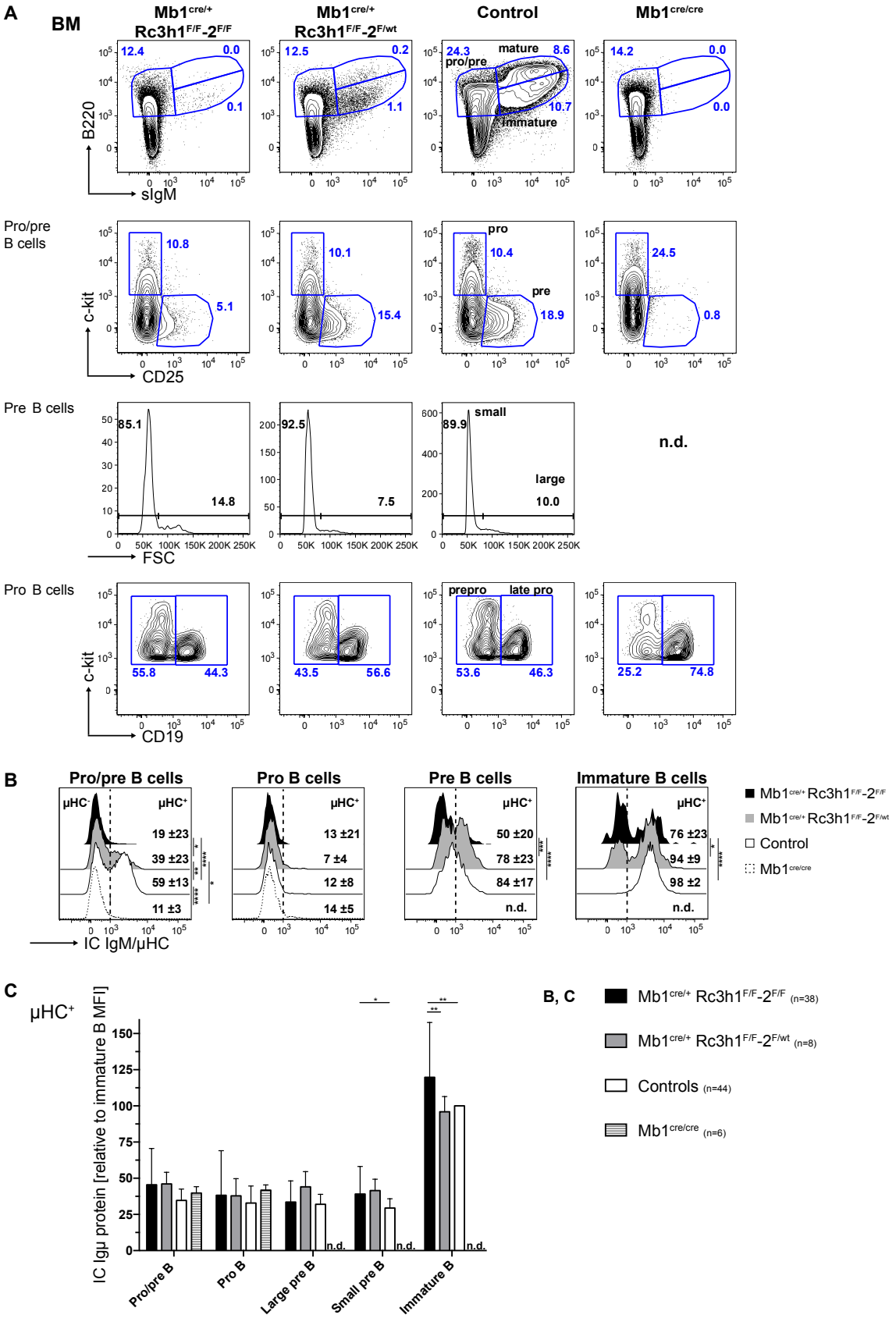

Figure 15: Reduced percentage of intracellular µHC (Igµ) expression at the pro to pre B transition in Roquin1/2-deficient B cells.

(A) Representative flow cytometric analysis of intracellular (IC) protein expression of IgM (Igµ). *(Continued on next page)*

The antibody employed for IgM detection binds to Ig heavy chain (HC), thus detects exclusively intracellular µHC expression in pro and pre B cells and µHC bound to Ig light chain as IgM in immature B cells. In this thesis, this intracellular detection is collectively referred to as Igµ or µHC. (B) Representative histogram overlays of IC µHC expression in indicated B cell populations, numbers are median percentages with standard deviation and significances. µHC expressing cells are denoted as μHC^+. (C) Flow cytometric determination of IC protein expression of Igµ relative to immature control B cells in denoted IC μHC^+ bone marrow (BM) B cell populations. In (B) and (C) B cells from $Mb1^{cre/cre}$ mice were excluded from pre and immature analyses. BM: bone marrow; sIgM: surface IgM; n.d.: not determined. Bars represent means and error bars standard deviation. ****p ≤ 0.0001, ***p ≤ 0.001, **p ≤ 0.01, *p ≤ 0.05, (B) ANOVA, (C) 2way ANOVA with Tukey test applied.

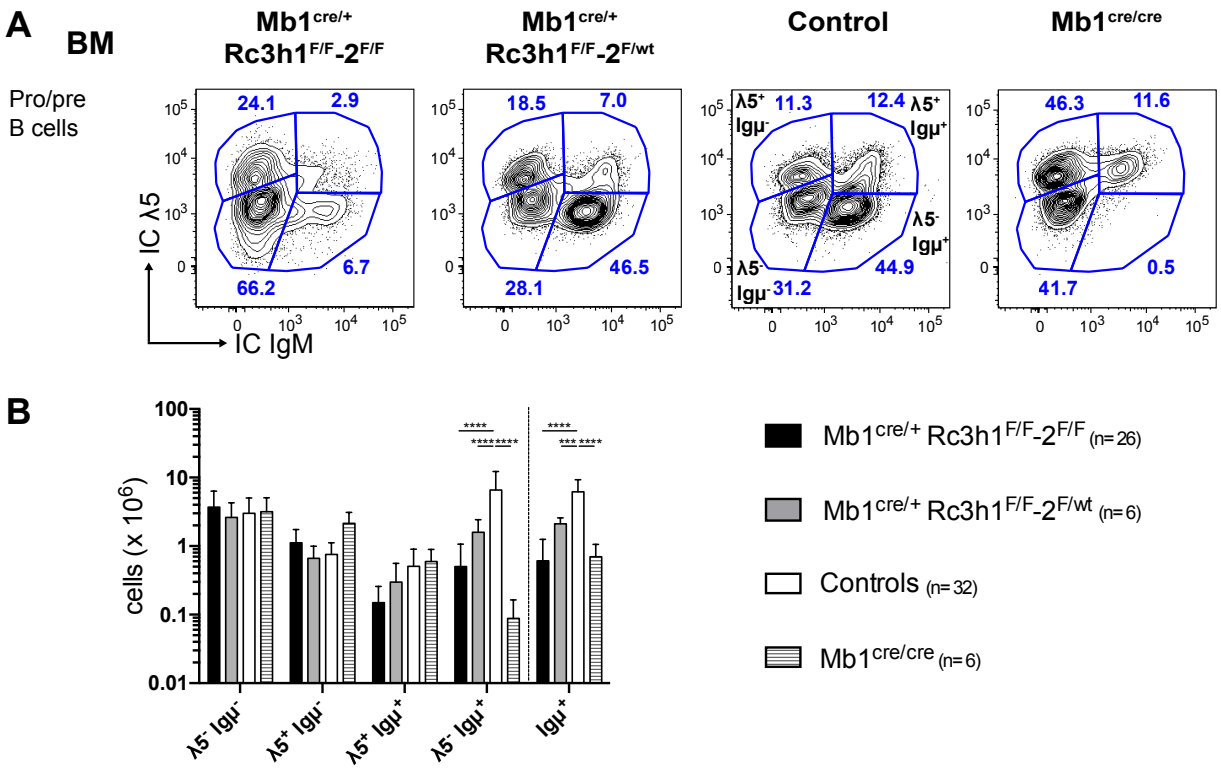

Figure 16: Analysis of intracellular expression of λ5 and µHC (Igµ) in $B220^{lo}$ IgM^- pro/pre B cells.
(A) Representative flow cytometric analysis of intracellular (IC) expression of λ5 and Igµ in the pro/pre ($B220^{lo}$ IgM^-) B cell compartment. (B) Total cell number of pro/pre B cells in the designated IC λ5 and Igµ expression stages; $Igµ^+$ denotes total IgM intracellular (IC) positive pro/pre B cells independent of IC λ5 expression as indicated by dotted line and shown in Fig. 15B. (B) Bars represent means and error bars standard deviation. B cells from $Mb1^{cre/cre}$ mice were excluded from pre and immature overlays. ****p ≤ 0.0001, ***p ≤ 0.001, 2way ANOVA with Tukey test applied.

Intracellular expression of λ5 is not affected by absence of Roquin proteins (Fig. 16A). Hence, expression of V_{preB} protein is presumably also not affected, since these surrogate light chain (SLC) proteins stabilize each other and no decrease of λ5 protein levels was noted (Fig. 16) [245, 246]. Pro/pre B cells of $Mb1^{cre/cre}$ mice are arrested at an intracellular λ5 and Igμ double positive stage and cannot mature to a $\lambda5^-$ $Ig\mu^+$ stage. This reflects the fact that the pre-BCR cannot signal due to absence of Igα. In pro/pre B cells of $Mb1^{cre/+}$ $Rc3h1^{F/F}$-$2^{F/F}$ mice there is a tendency of decreased numbers of $\lambda5^+$ $Ig\mu^+$ pro/pre B cells and significantly decreased numbers of $\lambda5^-$ $Ig\mu^+$ pro/pre B cells (Fig. 16). At the stage of $\lambda5^+$ $Ig\mu^+$ pro/pre B cells, the pre-BCR forms to signal downregulation of SLC components and the cell differentiates into a $\lambda5^-$ $Ig\mu^+$ stage. Thus pairing of SLC to μHC appears still possible in the absence of Roquin1/2 proteins and differentiation to $\lambda5^-$ $Ig\mu^+$ pre B cells can occur, but at a dramatically reduced rate with reduced levels of μHC. Yet, molecular events in the context of pre-BCR signaling events are certainly affected by loss of both alleles of Roquin1 and 2, respectively. This phenotype is similar but less pronounced in $Mb1^{cre/+}$ $Rc3h1^{F/F}$-$2^{F/wt}$ mice (Fig. 16A, 16B). Moreover, I investigated the consequences of ablation of Roquin1 and 2 on expression of Ig light chain proteins and λ5 in bone marrow B cell subsets (Fig. 17). Regulation of λ5 expression and its downregulation in intracellular IgL chain $(Ig\kappa)^+$ pro/pre B cells of $Mb1^{cre/+}$ $Rc3h1^{F/F}$-$2^{F/F}$ and $Mb1^{cre/+}$ $Rc3h1^{F/F}$-$2^{F/wt}$ mice remains intact as determined by absence of intracellular $\lambda5^+$ $Ig\kappa^+$ pro/pre B cells (Fig. 17A, 17B). Despite the massive percent reduction of intracellular $Ig\kappa^+$ or $\lambda5^-$ $Ig\kappa^+$ double-deficient pro/pre B cells, intracellular $Ig\kappa^+$ pro/pre and immature B cells are also present in $Mb1^{cre/+}$ $Rc3h1^{F/F}$-$2^{F/F}$ mice in contrast to $Mb1^{cre/cre}$ mice (Fig. 17B, 17C). Whereas the vast majority of Roquin1/2-deficient pro/pre B cells fails to express Igκ, Igλ expression levels in these cells are similar to those controls (Fig. S5A). Furthermore, in contrast to $Mb1^{cre/cre}$ mice, Roquin1/2-deficient immature B cells exist and about 50% of these cells are intracellular $Ig\kappa^+$, which is significantly less compared to immature B cells with one allele of Roquin2 left (Fig. 17C). The population of intracellular $Ig\kappa^+$ immature B cells is reduced 43-fold compared to controls (Fig. 17C), yet intracellular expression levels of Igκ protein is not changed in these cells (Fig. 17D). Subsequently, I analyzed light chain surface expression on immature B cells (Fig. 18). The percentage of Roquin1/2-deficient surface $Ig\kappa^+$ immature B cells is significantly reduced, whereas the percentage of surface $Ig\lambda^+$ immature B cells (Fig. 18B) or intracellular expression of Igλ protein in immature B cells of $Mb1^{cre/+}$ $Rc3h1^{F/F}$-$2^{F/F}$ mice (Fig. S5A).

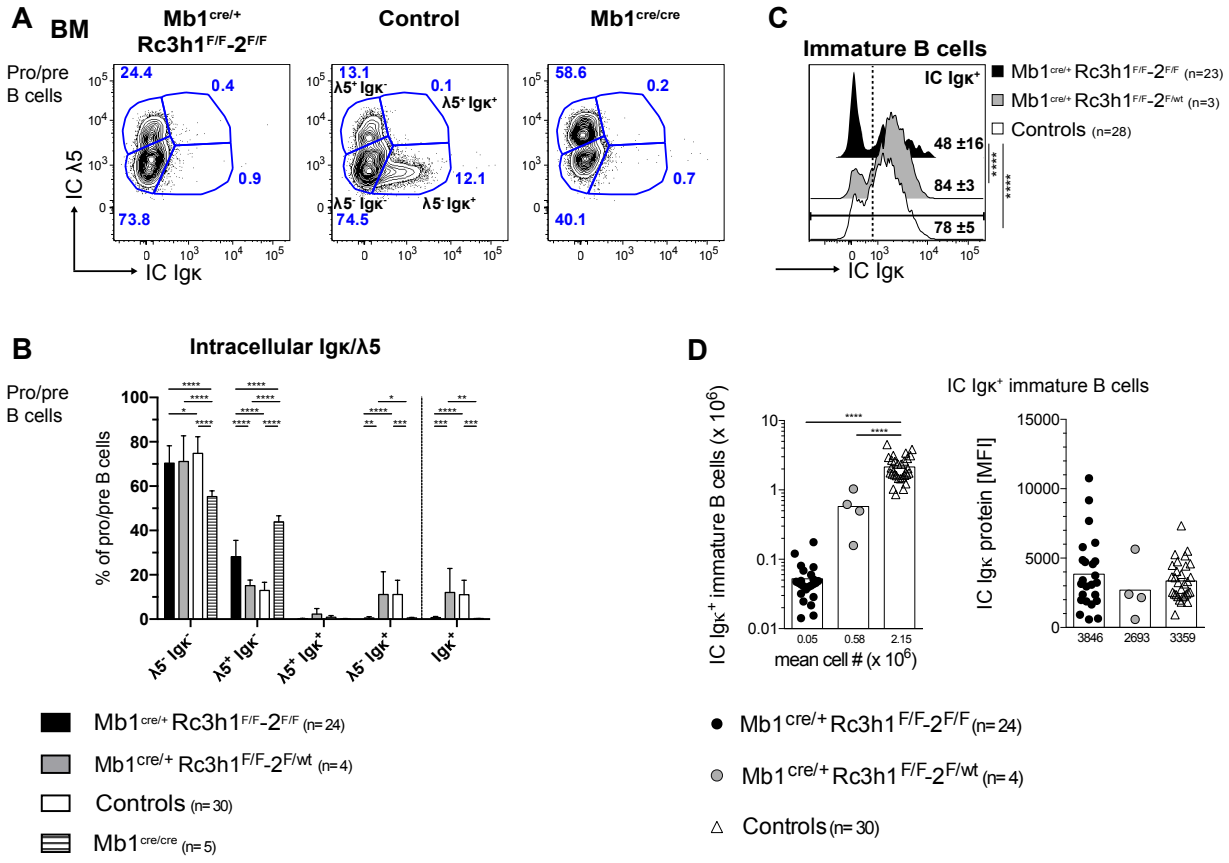

Figure 17: Analysis of intracellular expression of Igκ in bone marrow B cells.
(A) Representative flow cytometric analysis of ($B220^{lo}$ IgM^-) pro/pre B cells stained intracellularly (IC) for λ5 and Igκ as used in (B) is shown. (B) Percentages of respective subsets of pro/pre B cells. $Igκ^+$ denotes total Igκ IC positive pro/pre B cells independent of λ5 IC expression (not shown in A), as indicated by the dotted line. (C) Representative histogram of immature B cells stained (IC) for Igκ expression, numbers are median percentages with standard deviation and significances. (D) Number of IC $Igκ^+$ immature B cells and bar chart representation of IC Igκ protein expression in $Igκ^+$ immature B cells. Immature B cells $B220^{int}$ IgM^+. MFI: median fluorescence intensity. Bars represent means and error bars standard deviation. ****$p \leq 0.0001$, ***$p \leq 0.001$, **$p \leq 0.01$, *$p \leq 0.05$, (B) 2way ANOVA with Tukey test applied or (C, D) ANOVA.

Strikingly, the percentage of surface $Igκ^+$ immature B cells is not altered in immature B cells that express at least one allele of Roquin proteins (Fig. 18B). However, as a consequence of severly reduced numbers of immature B cells are the percentages of $Igκ^+$ and $Igλ^+$immature B cells among total bone marrow cells was well as the total numbers of $Igκ^+$ and $Igλ^+$ immature B cells significantly reduced upon ablation of both alleles of Roquin1 compared to controls (Fig. 18B).

Rc3h2-deficiency does not alter cytoplasmic expression of Igμ, Igκ (Fig. S5B-S5E) or Igλ (data not shown) in bone marrow B cells, nor does it change intracellular protein levels of Igκ or Igλ in splenic B cells (Fig. S5F). However, percentages and total cell numbers of $Igκ^+$ as well as $Igλ^+$ splenic B cells are reduced in $Mb1^{cre/+}$ $Rc3h2^{F/F}$ mice (Fig. S6). This tendency was also observed in IgD^{lo} IgM^{hi} B cells of $Mb1^{cre/+}$ $Rc3h2^{F/F}$ mice (Fig. S6).

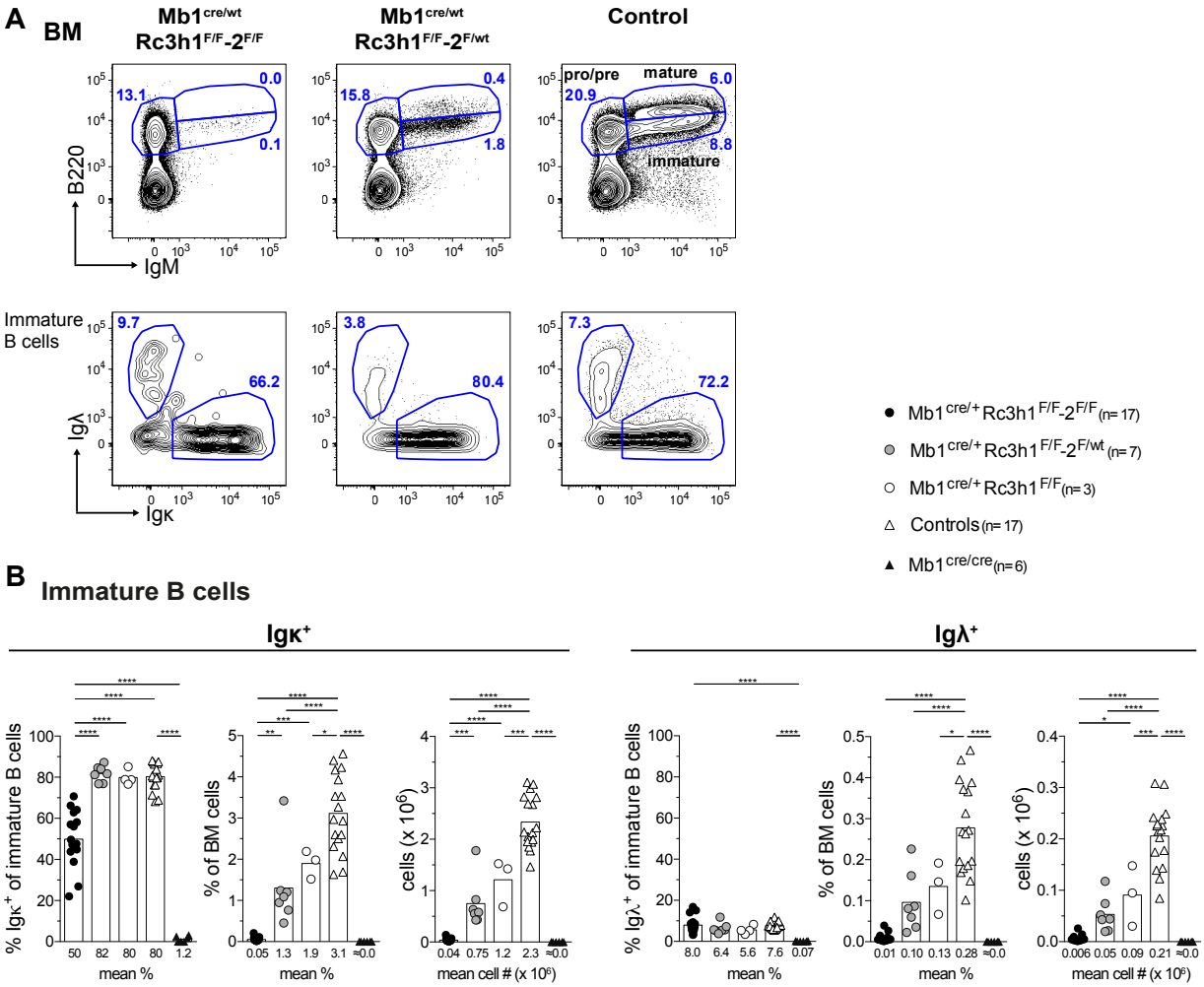

Figure 18: Analysis of surface expression of Igκ and Igλ (Igλ1, 2 and 3) on bone marrow B cells of Mb1$^{cre/+}$ Rc3h1$^{F/F}$-2$^{F/F}$, Mb1$^{cre/+}$ Rc3h1$^{F/F}$-2$^{F/wt}$ and Mb1$^{cre/+}$ Rc3h1$^{F/F}$ mice.

(A) Representative flow cytometric analysis of bone marrow (BM) B cells illustrating gating for surface Igκ$^+$ and Igλ$^+$ immature B cells. (B) Percentages of surface Igκ$^+$ or Igλ$^+$ immature B cells, percentage of Igκ$^+$ or Igλ$^+$ immature B cells of viable cells of BM and their total cell numbers (#). Numbers below graphs and bars show mean values. Calculated cell numbers of < 100 were rounded to 0 and denoted as 0.0. ****p ≤ 0.0001, ***p ≤ 0.001, **p ≤ 0.01, *p ≤ 0.05, ANOVA. Significances for Mb1$^{cre/cre}$ versus Mb1$^{cre/+}$ Rc3h1$^{F/F}$-2$^{F/wt}$ and versus Mb1$^{cre/+}$ Rc3h1$^{F/F}$ are not shown.

Collectively these experiments suggest an important role of Roquin1 for correct expression of Igμ, Igκ and Igλ and/or signaling events mediated by pre-BCR or BCR in bone marrow B cells. Roquin2 has a partially substituting role for normal expression of heavy and light chain as well as for Igκ and Igλ expression on splenic B cells.

1.5 Severly reduced levels of mediators of IL-7R and pre-BCR signaling in Roquin1/2 double-deficient large pre B cells

Having established that the pre-BCR can form in Roquin1/2 double-deficient pre B cells, I investigated the consequences of Roquin1/2 ablation on the protein levels of key molecules of pre-BCR and IL-7R signaling, two fundamental pathways for the transition of pro B into pre B and subsequently into immature B cells [60, 67]. The IL-7R is composed of IL-7Rα and the common γ chain. IL-7R signaling is pivotal for proliferation of pro B and large pre B cells [60]. Strikingly, the surface levels of IL-7Rα are significantly lower on large pre B cells of $Mb1^{cre/+}$ $Rc3h1^{F/F}$-$2^{F/F}$ and $Mb1^{cre/+}$ $Rc3h1^{F/F}$-$2^{F/wt}$ mice compared to controls but not on late pro B of these mouse strains (Fig. 19A, 19B). A significantly reduced percentage of Roquin1/2-deficient large pre B cells express high surface levels of IL-7Rα (IL-$7R\alpha^{hi}$) (Fig. 19A). Furthermore, the number of large pre B cells that express high surface levels of IL-7Rα are significantly reduced in $Mb1^{cre/+}$ $Rc3h1^{F/F}$-$2^{F/F}$ mice (Fig. 19A, 19C), suggesting that proliferative deficiencies at the large pre B cell stage might contribute to the observed block in these mice. In order to investigate if this defect in maintaining high surface levels of IL-7Rα is specific to cells that have ablated Roquin1 and 2, I examined IL-7Rα expression on bone marrow B cells of $Mb1^{cre/+}$ $Rc3h1^{F/F}$-$2^{F/F}$ $R26^{CARStopFL}$ mice (Fig. 19D-19F). Remarkably, there are CAR^{+} double-deficient large and small pre B cells that express high surface levels of IL-7Rα (Fig. 19D, 19E), indicating that complete loss all Roquin alleles does not completelly prohibit IL-7Rα expression. However, the amount of IL-7Rα protein expressed is significantly lower on CAR^{+} large pre B cells of $Mb1^{cre/+}$ $Rc3h1^{F/F}$-$2^{F/F}$ $R26^{CARStopFL}$ and $Mb1^{cre/+}$ $Rc3h1^{F/F}$-$2^{F/wt}$ $R26^{CARStopFL}$ mice (Fig. 19F). Protein surface levels of IL-7Rα are not changed on large pre B cells of $Mb1^{cre/+}$ $Rc3h2^{F/F}$ mice (Fig. S7A), which is in line with the unaltered bone marrow B cell development in these mice.

Upregulation of CXCR4 surface levels, the chemokine receptor for CXCL12, on large pre B cells is essential for their migration towards CXCL12-expressing stromal cells, thereby attenuating IL-7R signaling and inducing Ig light chain rearrangement and ensuing differentiation into small pre B cells [78, 80]. Remarkably, fewer Roquin1/2 double-deficient large pre B cells upregulate CXCR4 surface protein levels and those that express high surface levels ($CXCR4^{hi}$ cells) fail to upregulate expression to the level on control large pre B cells, suggesting ensuing migratory defects (Fig. 20A, 20B). In addition to this protein level reduction on pre B cells, there is a severe decrease in cell numbers of $CXCR4^{hi}$ large pre B cells and ensuing stages in $Mb1^{cre/+}$ $Rc3h1^{F/F}$-$2^{F/F}$ (Fig. 20A, 20C). Egress from the bone

marrow requires a reduction of CXCR4 surface levels on immature B cells compared to small pre B cells. This was observed on control and Roquin1/2-deficient cells (Fig. 20A) and also the number of $CXCR4^{hi}$ cells declines in the immature B cell subset in $Mb1^{cre/+}$ $Rc3h1^{F/F}$-$2^{F/F}$ and control mice (Fig. 20C). Upregulation of CXCR4 surface levels through pre-BCR signaling is mediated by transcription factors IRF4 and IRF8, simultaneous to induction of IgL rearrangement [79, 247]. A similar percent of Roquin1/2-deficient small pre B cells compared to controls upregulate IRF4 protein expression to high levels ($IRF4^{hi}$ cells) (Fig. 21A). Noteworthy, intracellular levels of IRF4 are higher in double-deficient $IRF4^{hi}$ late pro B cells compared to controls (Fig. 21B).

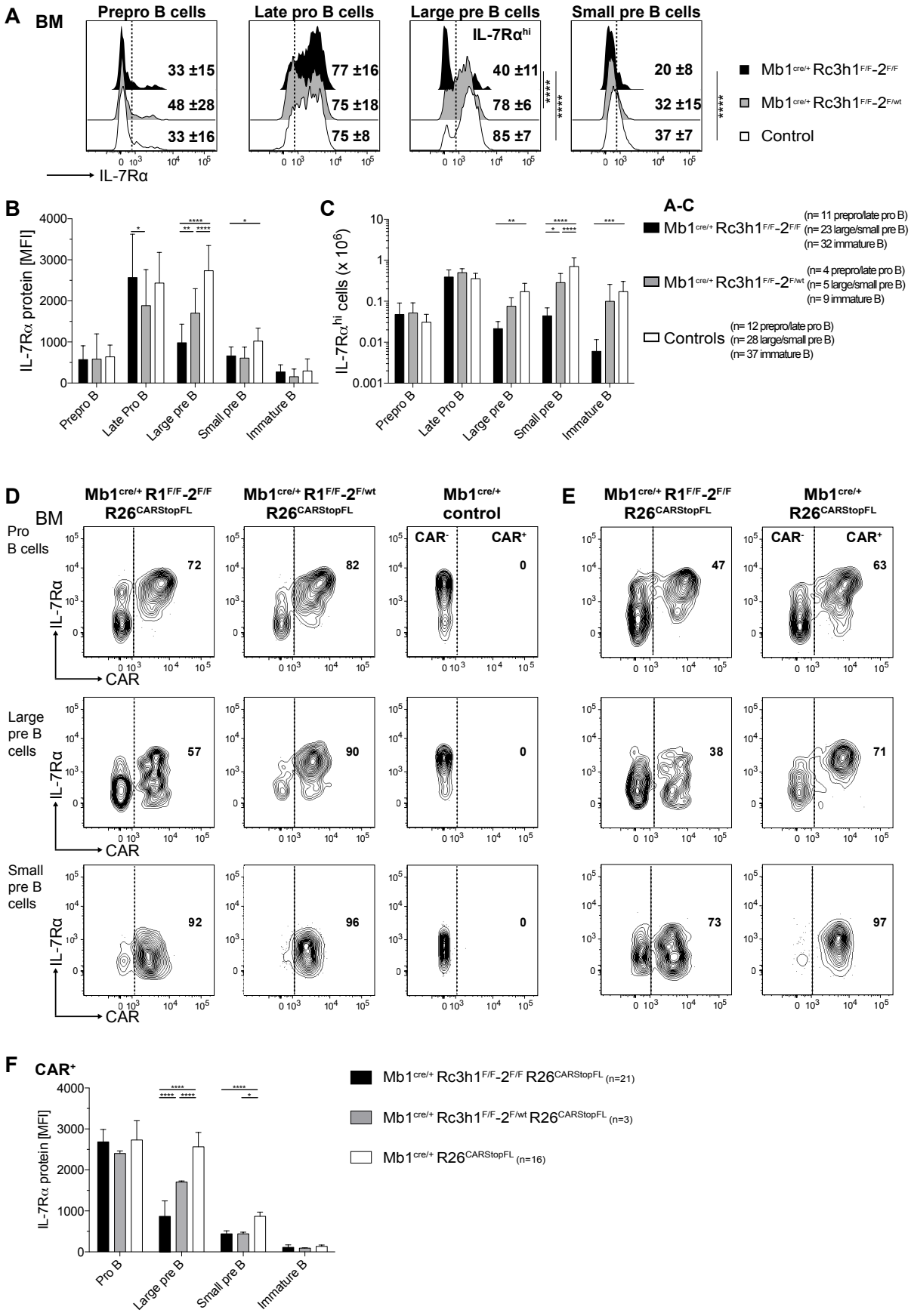

Figure 19: Large pre B cells of Mb1$^{cre/+}$ Rc3h1$^{F/F}$-2$^{F/F}$ and Mb1$^{cre/+}$ Rc3h1$^{F/F}$-2$^{F/wt}$ mice do not maintain high IL-7Rα surface levels, but Roquin1/2-deficient IL-7Rα^{hi} large pre B cells exist. *(Continued on next page)*

(A) Representative cytometry histograms illustrating surface IL-7Rα expression on indicated bone marrow (BM) B cell populations. Percentages of cells expressing high levels of IL-Rα (IL-7Rα^{hi}), based on IL-7Rα expression on large pre B cells, are indicated. Mean percentages with standard deviation and significances are indicated. (B) Bar chart representation of IL-7Rα protein expression on the surface of indicated bone marrow (BM) B cell populations. (C) Total number of IL-7Rα^{hi} cells in the indicated BM cell populations. (D) and (E) Representative flow cytometry plots illustrating surface IL-7Rα expression versus surface CAR expression, which was employed for (F), on indicated bone marrow (BM) B cell populations in the three experimental genotypes, as no experiment comprising all three experimental genotypes was performed. Absence of CAR expression on cells devoid of the R26^{CARStopFL} allele is illustrated (D). Cre-mediated recombination has occured in CAR^{+} cells. (F) Bar chart representation of IL-7Rα surface protein expression on indicated CAR^{+} B cell populations in the bone marrow. Gated B cell subsets: prepro B CD19^{-} B220^{lo} c-kit^{+} CD25^{-} IgD^{-} IgM^{-}; late pro B CD19^{+} B220^{lo} c-kit^{+} CD25^{-} IgD^{-} IgM^{-}; pro B B220^{lo} c-kit^{+} CD25^{-} IgD^{-} IgM^{-}; large pre B B220^{lo} c-kit^{-} CD25^{+} IgD^{-} IgM^{-} FSC^{hi}; small pre B B220^{lo} c-kit^{-} CD25^{+} IgD^{-} IgM^{-} FSC^{lo}; immature B B220^{int} IgM^{+} R: Rc3h; MFI: median fluorescence intensity. Bars represent means and error bars standard deviation. ****p ≤ 0.0001, ***p ≤ 0.001, **p ≤ 0.01, *p ≤ 0.05, 2way ANOVA with Tukey test applied.

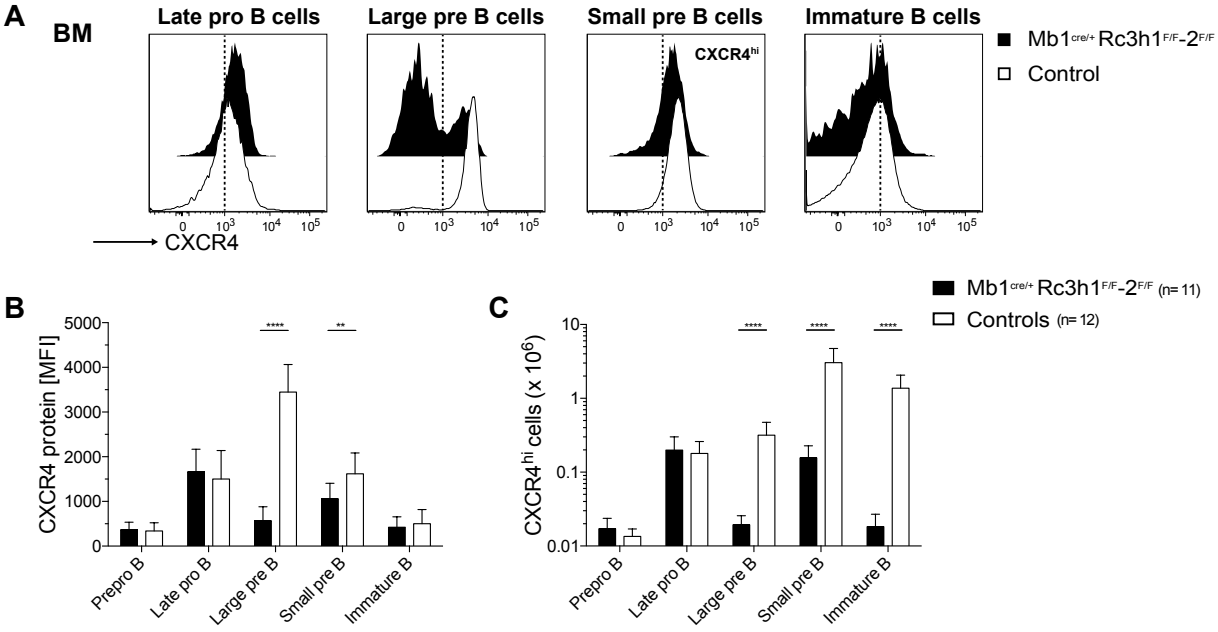

Figure 20: Large pre B cells of Mb1$^{cre/+}$ Rc3h1$^{F/F}$-2$^{F/F}$ mice do not upregulate CXCR4.

(A) Representative cytometry histograms depicting surface CXCR4 expression on indicated bone marrow (BM) B cell populations and percentage of cells expressing high surface levels of CXCR4 (designated CXCR4^{hi}), based on large pre B cells. Percentages with standard deviation and significances are shown. (B) Bar chart representation of CXCR4 protein expression on the surface of CXCR4^{hi} cells among indicated bone marrow (BM) B cells populations. (C) Total number of CXCR4^{hi} cells in the indicated BM cell populations. Bars represent means and error bars standard deviation. Gated B cell subsets: prepro B CD19^{-} B220^{lo} c-kit^{+} CD25^{-} IgD^{-} IgM^{-}; late pro B CD19^{+} B220^{lo} c-kit^{+} CD25^{-} IgD^{-} IgM^{-}; large pre B B220^{lo} c-kit^{-} CD25^{+} IgD^{-} IgM^{-} FSC^{hi}; small pre B B220^{lo} c-kit^{-} CD25^{+} IgD^{-} IgM^{-} FSC^{lo}; immature B B220^{lo} IgM^{+}. MFI: median fluorescence intensity. Bars depict mean values and error bars standard deviation. ****p ≤ 0.0001, **p ≤ 0.01, multiple t tests with Holm-Sidak method applied.

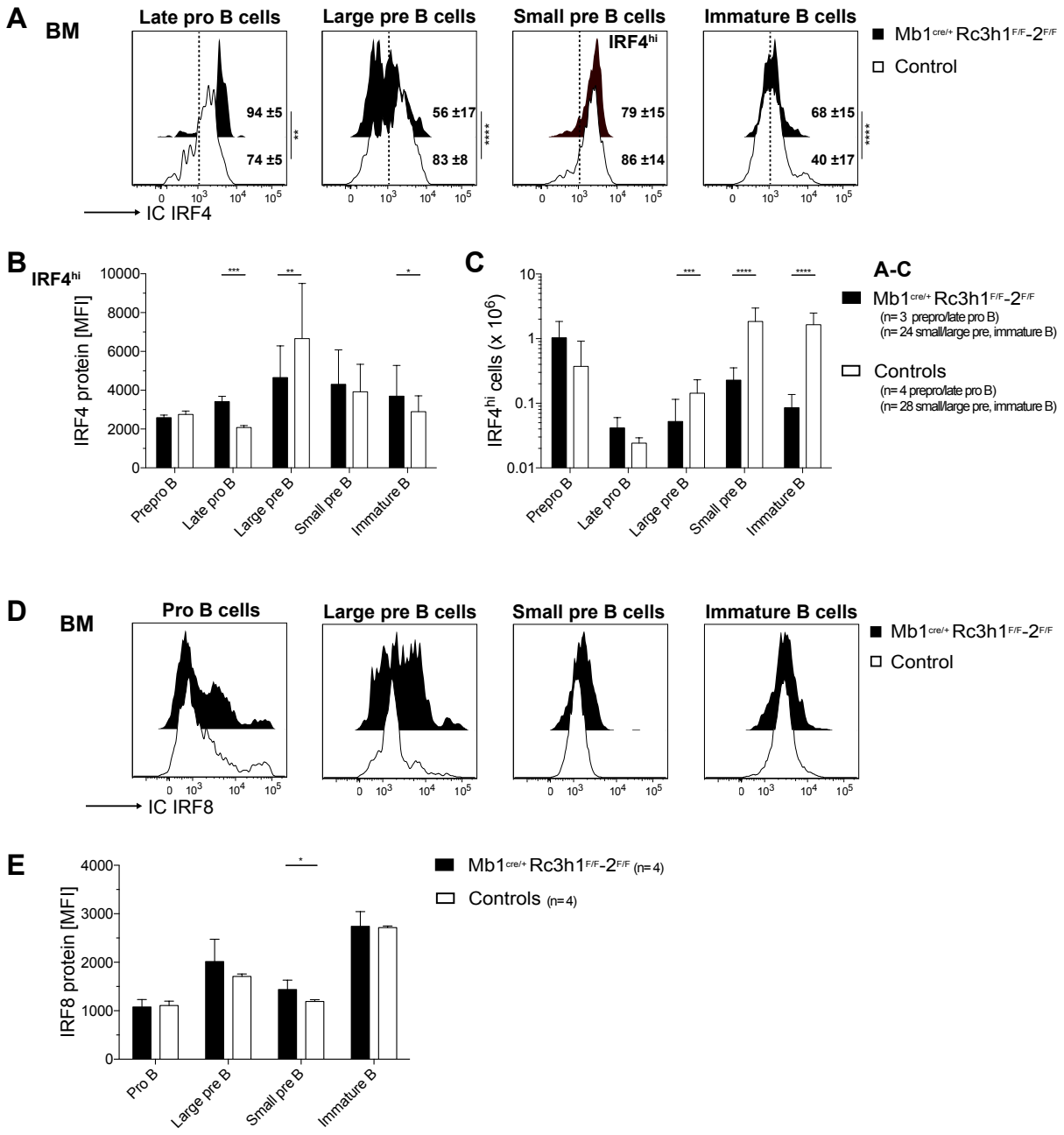

Figure 21: Deregulation of IRF4 levels in bone marrow B cells of Mb1$^{cre/+}$ Rc3h1$^{F/F}$-2$^{F/F}$, while IRF8 levels remain largely unchanged in Mb1$^{cre/+}$ Rc3h1$^{F/F}$-2$^{F/F}$.

(A) Representative flow cytometric analysis illustrating intracellular (IC) IRF4 expression in indicated BM B cell subsets and designation of cells expressing high intracellular IRF4 protein levels (IRF4^{hi}) based on small pre B cells. Shown are mean percentages with standard deviation and significant differences. (B) Bar chart representation of IC IRF4 levels in IRF4^{hi} B cells as determined by flow cytometry. (C) Total cell number of IRF4^{hi} B cells within the indicated B cell subsets. (D) Representative cytometry histograms depicting IC IRF8 expression in specified BM B cell populations. (E) Bar chart representation of flow cytometry-determined IC IRF8 levels in indicated BM cell populations. Gated B cell subsets: prepro B CD19^{-} B220^{lo} c-kit^{+} CD25^{-} IgD^{-} IgM^{-}; late pro B CD19^{+} B220^{lo} c-kit^{+} CD25^{-} IgD^{-} IgM^{-}; pro B B220^{lo} c-kit^{+} CD25^{-} IgD^{-} IgM^{-}; large pre B B220^{lo} c-kit^{-} CD25^{+} IgD^{-} IgM^{-} FSC^{hi}; small pre B B220^{lo} c-kit^{-} CD25^{+} IgD^{-} IgM^{-} FSC^{lo}; immature B B220^{int} IgM^{+}. BM: bone marrow; MFI: median fluorescence intensity. Bars depict mean values and error bars standard deviation. ****p ≤ 0.0001, ***p ≤ 0.001 **p ≤ 0.01, *p ≤ 0.05, multiple t tests with Holm-Sidak method applied.

In contrast large pre B cells of these mice do not upregulate IRF4 as efficiently as control large pre B cells (Fig. 21A). IRF4^{hi} large pre B cells of Mb1$^{cre/+}$ Rc3h1$^{F/F}$-2$^{F/F}$ mice express significantly less IRF4 (Fig. 21B), while the IRF4 level in all double-deficient large pre B cells is approximately 50% of that of control large pre B cells (data not shown). Hence, the reduced IRF4 levels in double-deficient large large pre B cells result from significantly fewer cells expressing high levels of IRF4 (IRF4^{hi} cells) (Fig. 21A, 21C). Furthermore, percent of IRF4^{hi} cells and IRF4 levels in IRF4^{hi} cells remain higher in Roquin1/2-deficient immature B cells compared to controls (Fig. 21A, 21B). IRF8 protein expression levels on the other hand are generally unaltered in Roquin1/2-deficient bone marrow B cells, except for a marginal upregulation of IRF8 in small pre B cells of Mb1$^{cre/+}$ Rc3h1$^{F/F}$-2$^{F/F}$ mice (Fig. 21D, 21E). IRF4 and IRF8 signaling arrests proliferation of pre B cells by activating expression of Ikaros and Aiolos [248]. The Aiolos expression pattern of Roquin1/2-deficient pre B cells mirrors IRF4 levels (Fig. 22A) with regard to the percent of large and small B cells expressing high intracellular protein levels of Aiolos (Aiolos^{hi}).

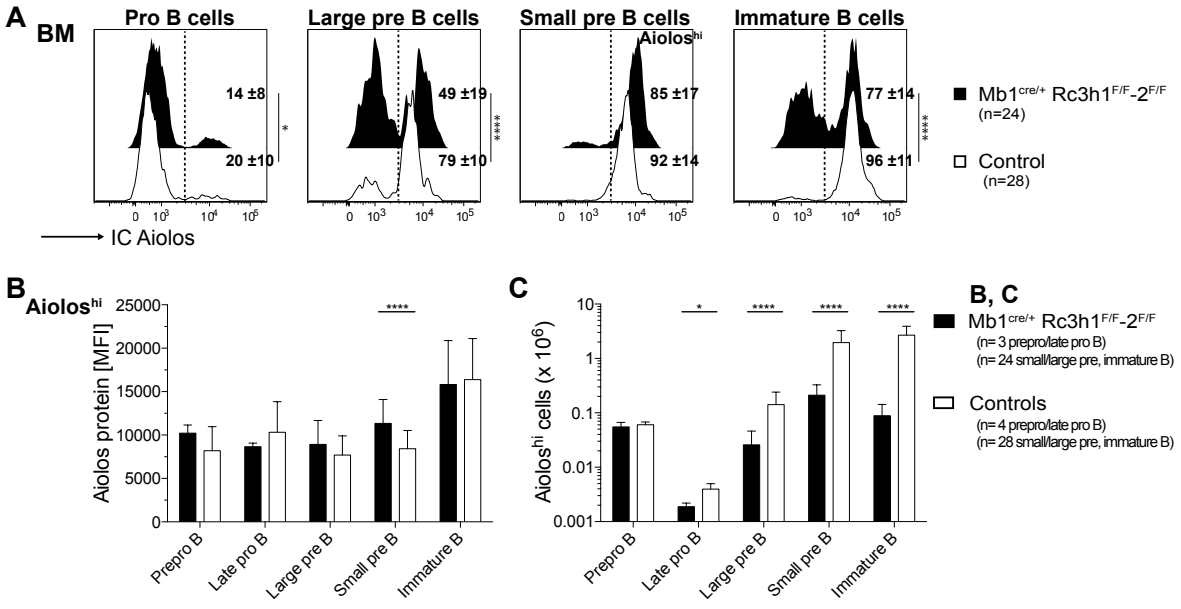

Figure 22: Severe reduction of Aiolos^{hi} level-expressing Roquin1/2-deficient large pre B and ensuing B cell stages.

(A) Representative flow cytometric histogram analysis displaying intracellular (IC) Aiolos expression in indicated BM B cell subsets and mean percentage with standard deviation of cells expressing high intracellular levels of Aiolos (Aiolos^{hi} cells) based on Aiolos expression in small pre B cells. (B) Bar chart representation of IC Aiolos protein levels in Aiolos^{hi} cells of respective B cell subset, as determined by flow cytometry. (C) Total numbers of Aiolos^{hi} BM B cells in indicated subsets. Gated B cell subsets: prepro B CD19^{-} B220^{lo} c-kit^{+} CD25^{-} IgD^{-} IgM^{-}; late pro B CD19^{+} B220^{lo} c-kit^{+} CD25^{-} IgD^{-} IgM^{-}; pro B B220^{lo} c-kit^{+} CD25^{-} IgD^{-} IgM^{-}; large pre B B220^{lo} c-kit^{-} CD25^{+} IgD^{-} IgM^{-} FSC^{hi}; small pre B B220^{lo} c-kit^{-} CD25^{+} IgD^{-} IgM^{-} FSC^{lo}; immature B B220^{lo} IgD^{-} IgM^{+}. BM: bone marrow. MFI: median fluorescence intensity. Bars depict mean values and error bars standard deviation. ****$p \leq 0.0001$, *$p \leq 0.05$, multiple t tests with Holm-Sidak method applied.

Surprisingly, Aiolos levels in Aiolos^{hi} double-deficient small pre B cells are increased compared to controls (Fig. 22A, 22B). Given the general dramatic decrease in B cell numbers in absence of Roquin1/2 proteins, the cell numbers of every pre B cell subset and of immature B cells, which show high intracellular expression of Aiolos (Aiolos^{hi} cells), is significantly lower in Mb1$^{cre/+}$ Rc3h1$^{F/F}$-2$^{F/F}$ mice (Fig. 22C). However, these numbers correlate to the cell numbers of IRF4^{hi} pre and immature double-deficient B cells (Fig. 21C). Functional pre-BCR signaling inhibits activation of AKT and thereby induces nuclear translocation of FOXO1, which initiates BCL6 transcription [67]. BCL6 is essential for survival of pre B cells carrying a functional Igμ [65, 68]. Therefore, I quantified intracellular BCL6 to determine whether defective Igμ expression affects BCL6 levels in bone marrow B cells (Fig. 23). Overall BCL6 expression varies strongly in the populations analyzed, however relative expression of BCL6 is higher in late pro B cells and ensuing developmental stages in Mb1$^{cre/+}$ Rc3h1$^{F/F}$-2$^{F/F}$ mice (Fig. 23). IRF4, Aiolos, and BCL6 protein levels are unaltered in bone marrow B cell subsets of Mb1$^{cre/+}$ Rc3h2$^{F/F}$ mice reflecting the normal B cell development in these mice (Fig. S7B-S7D).

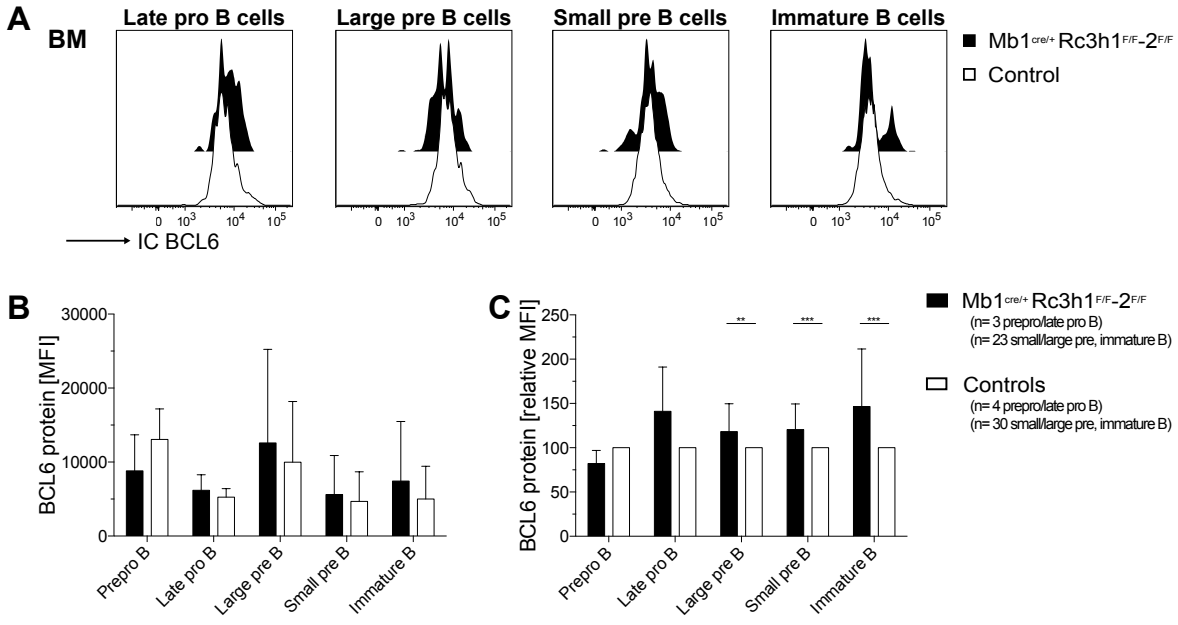

Figure 23: Relative increase of BCL6 protein levels in late pro to immature B cells of Mb1$^{cre/+}$ Rc3h1$^{F/F}$-2$^{F/F}$ mice.

(A) Representative cytometry histograms illustrating intracellular (IC) BCL6 expression in specified BM B cell populations. (B) Bar chart representation of IC BCL6 levels as determined by flow cytometry in referred BM cell populations. (C) IC BCL6 expression levels normalized to respective control values. Gated B cell subsets: prepro B CD19$^-$ B220^{lo} c-kit$^+$ CD25$^-$ IgD$^-$ IgM$^-$; late pro B CD19$^+$ B220^{lo} c-kit$^+$ CD25$^-$ IgD$^-$ IgM$^-$; large pre B B220^{lo} c-kit$^-$ CD25$^+$ IgD$^-$ IgM$^-$ FSC^{hi}; small pre B B220^{lo} c-kit$^-$ CD25$^+$ IgD$^-$ IgM$^-$ FSC^{lo}; immature B B220$^+$ IgD$^-$ IgM$^+$. MFI: median fluorescence intensity. Bars depict mean values and error bars standard deviation. ***p ≤ 0.001, **p ≤ 0.01, multiple t tests with Holm-Sidak method applied.

Proximal pre-BCR signaling requires the tyrosine kinases SYK and to some extent ZAP70 [249]. In order to investigate if the defects in the development of Roquin1/2-deficient pre B cells are caused by impaired pre-BCR signaling, I examined ZAP70 expression in bone marrow B cells populations (Fig. 24). Surprisingly, while intracellular ZAP70 protein levels decline in control B cells from pro/pre B cell to the immature B cell stage, in Mb1$^{cre/+}$ Rc3h1$^{F/F}$-2$^{F/F}$ mice they remain constant (Fig. 24B, 24C).

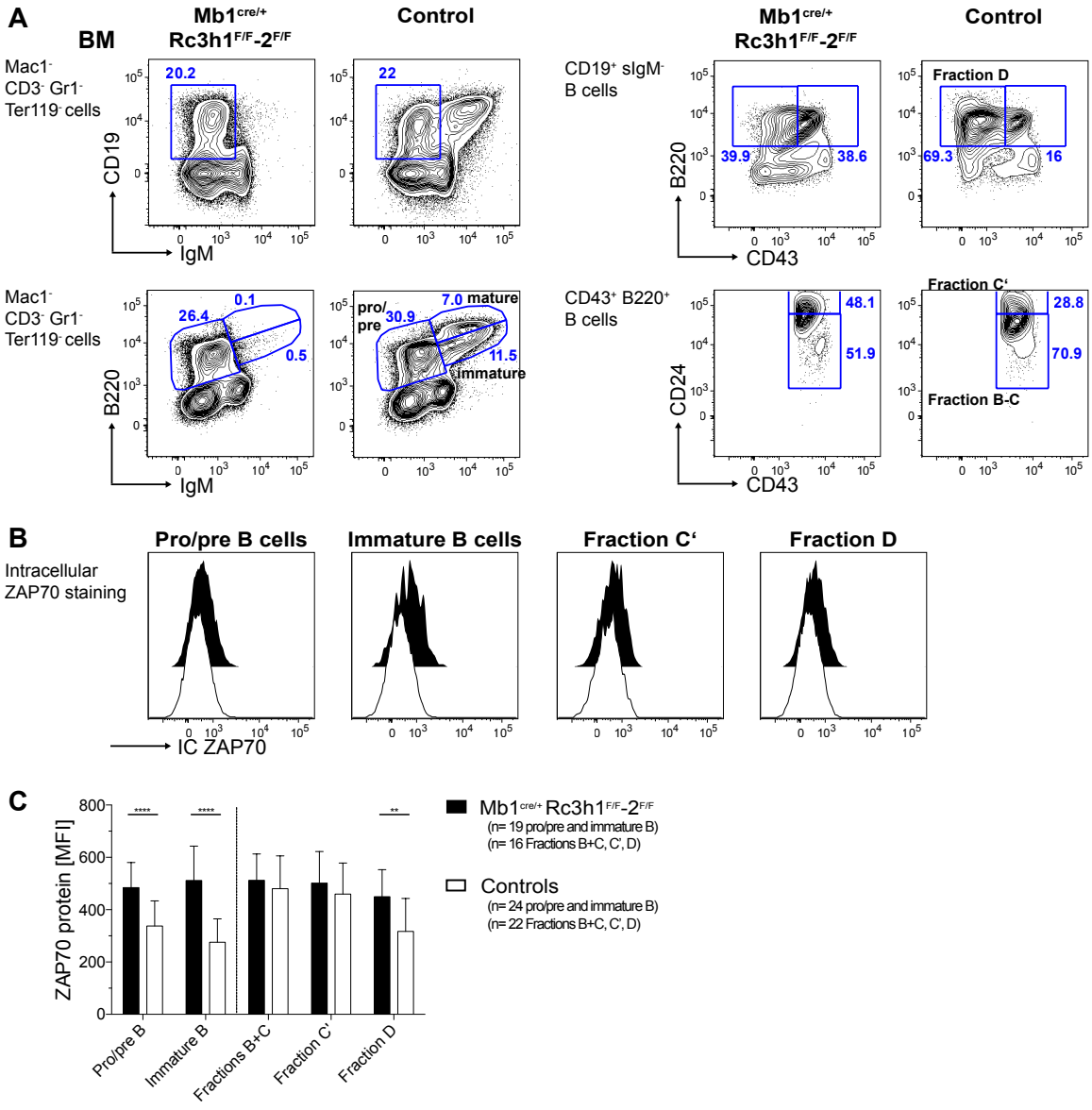

Figure 24: Intracellular protein levels of ZAP70 are increased in pro/pre B and immature B cells in Mb1$^{cre/+}$ Rc3h1$^{F/F}$-2$^{F/F}$ mice.

(A) Representative flow cytometric analysis illustrating gating scheme for Hardy Fractions B and C (B+C), C' and D, pro/pre and immature B cells in bone marrow (BM) for intracellular (IC) detection of ZAP70. (B) Representative cytometry histograms illustrating IC ZAP70 expression in specified B cell populations. (C) Bar chart representation of IC ZAP70 protein levels as analyzed by flow cytometry in designated B cell subsets. MFI: median fluorescence intensity. Bars depict mean values and error bars standard deviation. ****$p \leq 0.0001$, **$p \leq 0.01$, multiple t tests with Holm-Sidak method applied.

Whereas ZAP70 expression is unaltered in double-deficient cells of Hardy Fractions B to C or C', which are cycling large pre B cells, but is lower in cells in Hardy Fraction D (Fig. 24B, 24C). Hardy Fraction D comprises small pre B cells, which in $Mb1^{cre/+}$ $Rc3h1^{F/F}$-$2^{F/F}$ mice retain higher ZAP70 levels compared to control cells (Fig. 24B, 24C).

Collectively, my results indicate that many mediators of pre-BCR and IL-7R signaling are expressed at overall significant lower levels in Roquin1/2 double-deficient large pre B lymphocytes indicating defective signaling and an important role of Roquin proteins in the regulation of the affected pathways.

1.6 The arrest at the pro to pre B cell transition in $Mb1^{cre/+}$ $Rc3h1^{F/F}$-$2^{F/F}$ mice appears independent of cell survival

Based on the specific block at the late pro to large pre B cell transition combined with the multiple deregulated mediators of signaling at these developmental stages, I aimed to analyze the contribution of survival to this phenotype. Furthermore, the rate of *in vivo* cell death among pre B cells has been estimated to be in the range of 50 to 75% underlining its significant contribution to shaping the B cell compartment [250-252]. In a first step, I quantified intracellular levels of the pro-apoptotic BH3 family member Bim in *ex vivo* isolated bone marrow B cells (Fig. 25).

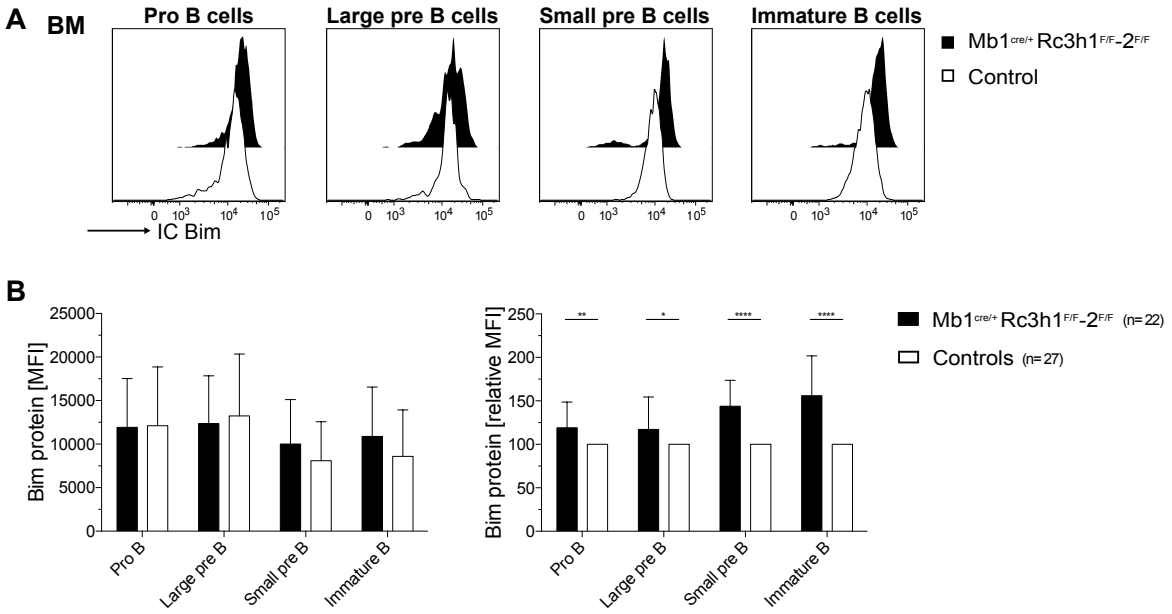

Figure 25: Bone marrow B cell populations of $Mb1^{cre/+}$ $Rc3h1^{F/F}$-$2^{F/F}$ mice have increased intracellular Bim levels relative to control B cells.

(A) Representative histograms depicting flow cytometric analysis of IC Bim protein levels in *ex vivo* isolated bone marrow cells. *(Continued on next page)*

(B) Bar charts displaying IC Bim protein levels as analyzed by flow cytometry and (right) normalized to levels in corresponding control populations. Gated B cell subsets: pro B B220^{lo} c-kit^{+} CD25^{-} IgD^{-} IgM^{-}; large pre B B220^{lo} c-kit^{-} CD25^{+} IgD^{-} IgM^{-} FSC^{hi}; small pre B B220^{lo} c-kit^{-} CD25^{+} IgD^{-} IgM^{-} FSC^{lo}; immature B B220^{+} IgD^{-} IgM^{+}. MFI: median fluorescence intensity, BM: bone marrow. Bars depict mean values and error bars standard deviation. ****p ≤ 0.0001, **p ≤ 0.01, *p ≤ 0.05, multiple t tests with Holm-Sidak method applied.

High inter-experimental variations in Bim levels complicated the analysis. Yet, normalization of Bim levels of Roquin1/2 double-deficient pro, large and small pre and immature B cell stages to their respective controls reveals a general upregulation of Bim in double-deficient bone marrow B cells (Fig. 25B, 25C). Further evaluation of apoptosis in *ex vivo* isolated bone marrow cells by AnnexinV staining indicates no dramatic changes of apoptosis in pro or pre B cell populations of Mb1$^{cre/+}$ Rc3h1$^{F/F}$-2$^{F/F}$ mice (Fig. 26A, 26B).

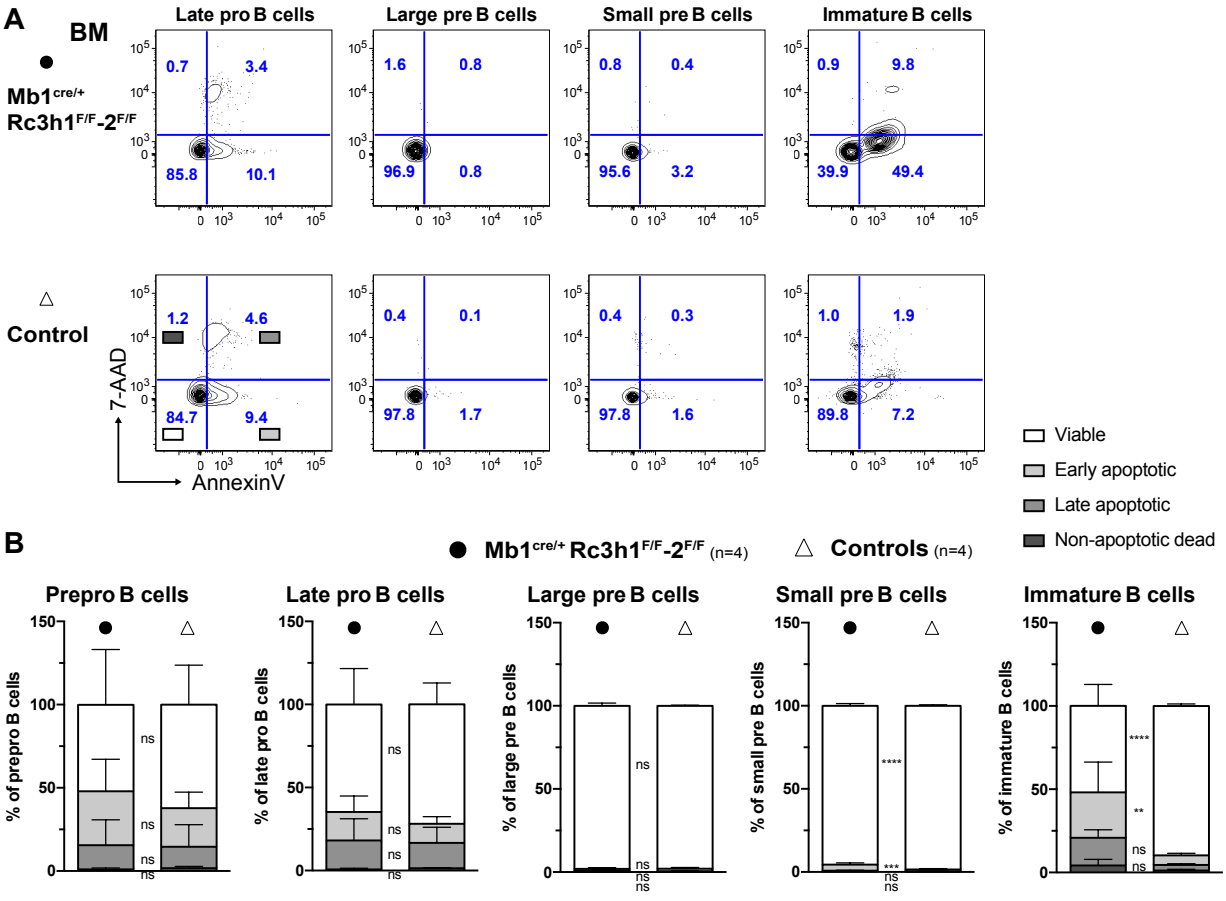

Figure 26: Analyses of apoptosis by surface binding of AnnexinV on bone marrow B cells in Mb1$^{cre/+}$ Rc3h1$^{F/F}$-2$^{F/F}$ mice.

(A) Representative flow cytometry plots of Annexin V/7-AAD staining on indicated bone marrow (BM) B cell populations. (B) Stacked bar charts displaying percentage of viable, early apoptotic, late apoptotic and non apoptotic dead cells within designated BM B cell populations as measured by flow cytometry in *ex vivo* cells and significance is indicated following the same order. Gated B cell subsets: prepro B CD19^{-} B220^{lo} c-kit^{+} CD25^{-} IgD^{-} IgM^{-}; late pro B CD19^{+} B220^{lo} c-kit^{+} CD25^{-} IgD^{-} IgM^{-}; large pre B B220^{lo} c-kit^{-} CD25^{+} IgD^{-} IgM^{-} FSC^{hi}; small pre B B220^{lo} c-kit^{-} CD25^{+} IgD^{-} IgM^{-} FSC^{lo}; immature B B220^{int} IgM^{+}. *(Continued on next page)*

Viable Annexin V^- 7-AAD^-; early apoptotic Annexin V^+ 7-AAD^-, late apoptotic Annexin V^+ 7-AAD^+, non-apoptotic dead Annexin V^- 7-AAD^+. Bars depict mean values and error bars standard deviation. ****$p \leq 0.0001$, ***$p \leq 0.001$, **$p \leq 0.01$, ns non-significant, unpaired t test.

However, the fraction of viable Roquin1/2 double-deficient immature B cells is strikingly reduced compared to controls indicating a possible role of immature B cell apoptosis in the near absence of peripheral Roquin1/2-deficient B cells (Fig. 26B). To further corroborate this result, I investigated caspase activation in *ex vivo* isolated bone marrow B cell subsets (Fig. 27). There is a slight but significant decrease of viable Roquin 1/2 double-deficient large and small pre B cells that is even more pronounced at the immature B cell stage. The ratio of viable immature B cells is approximately 30% lower in $Mb1^{cre/+}$ $Rc3h1^{F/F}$-$2^{F/F}$ mice (Fig. 27B), confirming the AnnexinV staining result on immature B cells and further supporting the hypothesis that apoptotic cell death may contribute to the reduced immature B cells numbers in bone marrow and the near absence of transitional splenic B cells in the $Mb1^{cre/+}$ $Rc3h1^{F/F}$-$2^{F/F}$ mouse line. As expected, apoptosis is only marginaly altered in bone marrow B cell populations of $Mb1^{cre/+}$ $Rc3h2^{F/F}$ mice as analyzed by caspase activation in *ex vivo* cells (Fig. S8A, S8B) despite a relative increase of intracellular Bim in Roquin2-deficient early bone marrow B cell populations (Fig. S8C).

In conclusion, apoptosis does not contribute to the striking reduction of pre B cells in $Mb1^{cre/+}$ $Rc3h1^{F/F}$-$2^{F/F}$ mice, but programmed cell death might play an important role in final cessation of development at the immature B cell stage and therefore it may prevent exit of B cells from the bone marrow into the periphery in these mice.

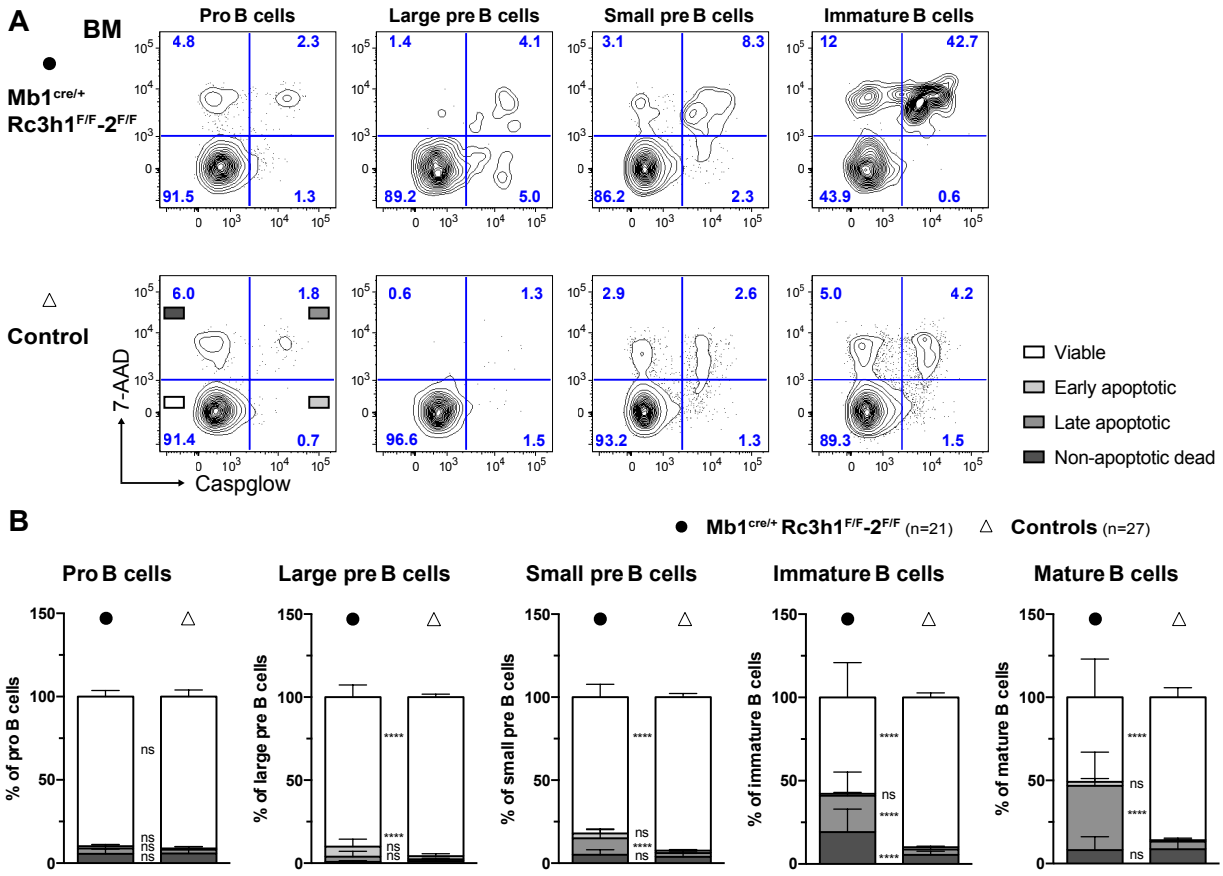

Figure 27: Reduced fractions of viable cells among pre, immature and mature bone marrow B cell populations in Mb1$^{cre/+}$ Rc3h1$^{F/F}$-2$^{F/F}$ mice.

For staining active caspases (caspglow stain), *ex vivo* bone marrow (BM) cells were cultured for 1h *in vitro*. (A) Representative flow cytometric analysis of caspglow and 7-AAD staining on indicated BM B cell populations. (B) Quantification of percentages of viable, early apoptotic, late apoptotic and non-apoptotic dead cells with respective analysis of significance of BM cell subsets as determined by flow cytometry in *ex vivo* cells shown as stacked bar charts. Gated B cell subsets: pro B B220^{lo} c-kit^{+} CD25^{-} IgD^{-} IgM^{-}; large pre B B220^{lo} c-kit^{-} CD25^{+} IgD^{-} IgM^{-} FSC^{hi}; small pre B B220^{lo} c-kit^{-} CD25^{+} IgD^{-} IgM^{-} FSC^{lo}; immature B B220^{+} IgD^{-} IgM^{+}; mature B B220^{+} IgD^{+}. Viable caspglow^{-} 7-AAD^{-}; early apoptotic caspglow^{+} 7-AAD^{-}, late apoptotic caspglow^{+} 7-AAD^{+}, non-apoptotic dead caspglow^{-} 7-AAD^{+}. Bars represent mean values and error bars standard deviation. ****p ≤ 0.0001, ns non-significant, unpaired t test.

1.7 Defective proliferation of large pre B cells may contribute to the observed developmental arrest in Mb1$^{cre/+}$ Rc3h1$^{F/F}$-2$^{F/F}$ mice

In light of the broadly unchanged cell death in pro or pre B cells of Mb1$^{cre/+}$ Rc3h1$^{F/F}$-2$^{F/F}$ mice, I evaluated the consequences of Roquin1 and 2 ablation on the proliferative capacities of bone marrow B cells as a possible mechanism for the immense reduction of large pre B cells and subsequent B cell developmental stages. As aforementioned, massive proliferation of large pre B cells following successful pre-BCR assembly is a fundamental feature of B cell lymphopoiesis in the bone marrow.

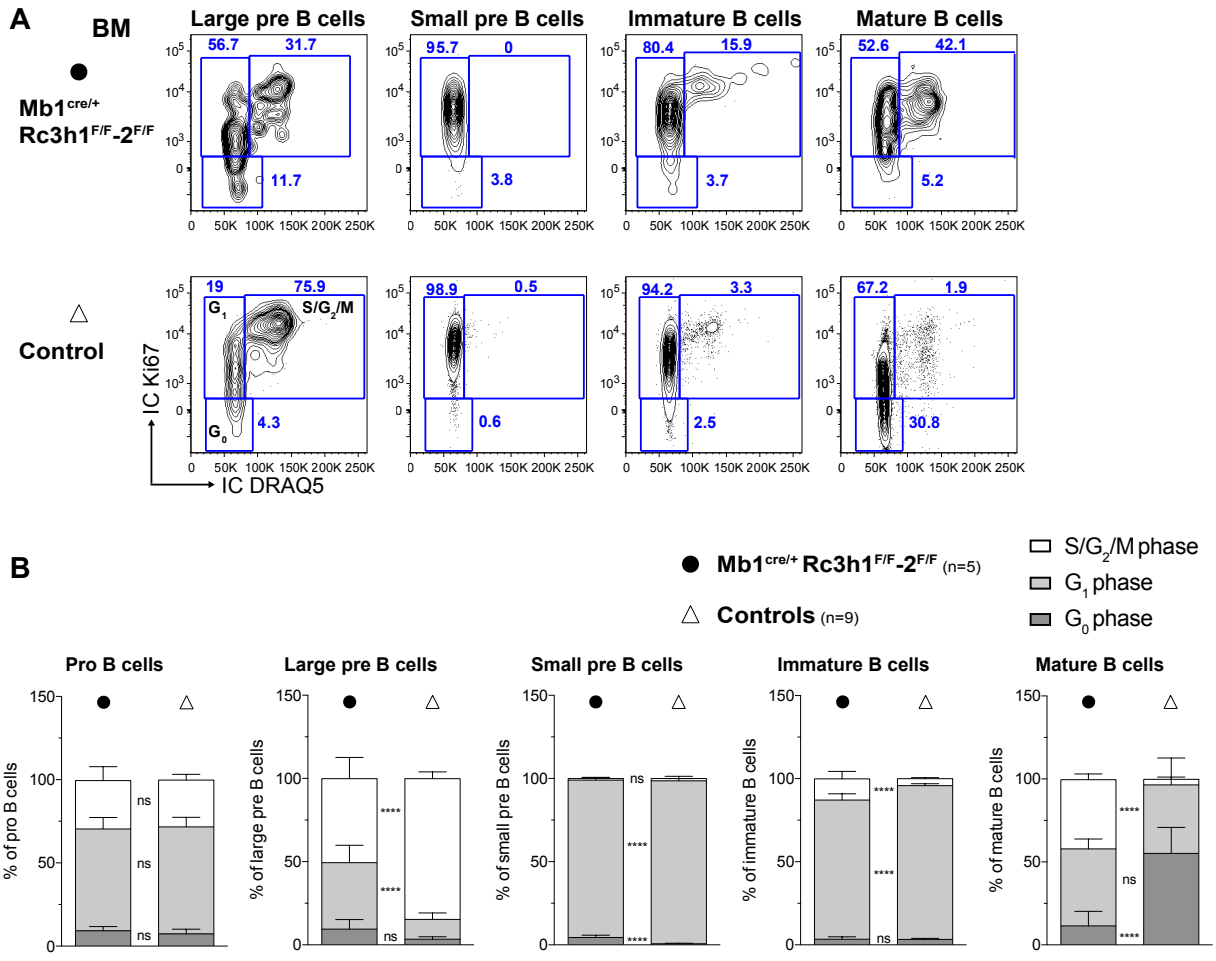

Figure 28: Strinking reduction of large pre B cells in S/G_2/M phase in Mb1$^{cre/+}$ Rc3h1$^{F/F}$-2$^{F/F}$ mice.
(A) Representative flow cytometry plots and histograms of stated BM B cell populations illustrating gating and analysis strategy. Ki67 expression is only deteced in active cell cycle phases (G_1, S, G_2 and M) phase [253] and DRAQ5 intercalates DNA [254]. (B) Percentages of indicated B cell populations in cell cycle phases. Pro B cells B B220^{lo} c-kit^{+} CD25^{-} IgD^{-} IgM^{-}; G_0 phase Ki67^{-} DRAQ5^{lo}; G_1 phase Ki67^{+} DRAQ5^{lo}; S/G_2/M phase Ki67^{+} DRAQ5^{hi}. BM: bone marrow. Bars represent mean values and error bars standard deviation. ****p ≤ 0.0001, ns non-significant, unpaired t test.

The strongly reduced number of Roquin1/2-deficient large pre B cells that express high surface levels of IL-7Rα (Fig. 19A, 19B) suggested impaired proliferative capacities of these cells. Remarkably, analysis of cell cycle stages of *ex vivo* isolated bone marrow B cell subsets demonstrates that a significantly smaller proportion of Roquin1/2 double-deficient large pre B cells enters the proliferative S/G_2/M phases of the cell cycle (50% in dKO vs 80% in controls), while a significantly increased ratio remains in the G_1 phase (Fig. 28). In an interesting contrast, this is reversed in immature and mature B cells of Mb1$^{cre/+}$ Rc3h1$^{F/F}$-2$^{F/F}$ mice in which a higher proportion is detected in S/G_2/M phases of the cell cycle (Fig. 28B). This observation is noteworthy, as control immature B cells are almost exclusively in G_1 phase while control mature B cells are to a major extent in the resting G_0 phase (Fig. 28B). DRAQ5 based *ex vivo* flow cytometry analysis of cell cycle stages allows the discrimination

of S phase versus G_2/M phase. This analysis demonstrates that proportion of Roquin1/2-deficient large pre B cells in S phase is reduced by a factor of 2 compared to controls (Fig. S9). In contrast, an increased ratio of cells in S and G_2/M phases can be detected in immature and mature recirculating B cell populations in $Mb1^{cre/+}$ $Rc3h1^{F/F}$-$2^{F/F}$ mice (Fig. S9). This likely represents homeostatic proliferation in response to the severe B cell deficiency in these mice.

I next combined analysis of cell cycle phases with assessment of intracellular expression of IRF4. High IRF4 levels were shown to be essential for withdrawal of pre B cells from the cell cycle [69]. In an initial experiment, I compared expression of IRF4 in combined $G_{0/1}$ phases and in the proliferative S/G_2/M phases (Fig. 29). Strikingly, IRF4 protein levels differ only slightly between small pre B cells of $Mb1^{cre/+}$ $Rc3h1^{F/F}$-$2^{F/F}$ mice and controls in $G_{0/1}$ phases. However, the IRF4 level in double-deficient large and small pre B cells in S/G_2/M phases is reduced to 50% of wild type levels as a result of fewer cells expressing high IRF4 levels (Fig. 29A), possibly indicating a failure of these $IRF4^{lo}$ cycling large pre B cells to terminate proliferation and start Ig light chain rearrangement in double-deficient small pre B cells (Fig. 29A). Interestingly, this ratio is reversed at the immature B cell stage with double-deficient immature B cells in S/G_2/M phases having twofold increased IRF4 levels compared to controls. These elevated IRF4 levels in immature B cells from $Mb1^{cre/+}$ $Rc3h1^{F/F}$-$2^{F/F}$ mice, potentially suggest non-resolved, open light chain gene loci in these immature B cells [255].

Furthermore, I investigated proliferative capacities *in vivo* by employing BrdU incorporation studies. $Mb1^{cre/+}$ $Rc3h1^{F/F}$-$2^{F/F}$ and control mice were injected with BrdU and incorporation in B cells assessed 4, 18 and 30h post-injection (Fig. 30, 31). Noteably, 50mg of intraperitoneally injected BrdU per kg mouse body weight (50mg/kg) has been shown to remain available for incorporation into newly synthesized DNA for ca. 90 min. [256]. In these experiments, during the BrdU pulse, BrdU is incorporated into the DNA of proliferating cells, in early B cell development, therefore into large pre B cells. $BrdU^+$ pre B cells then differentiate into small pre B cells, which do not divide (Fig. 28A) and therefore retain the BrdU label.

As expected from the *ex vivo* analyses, the percentage of proliferating $BrdU^+$ large pre B cells is strongly and significantly reduced in $Mb1^{cre/+}$ $Rc3h1^{F/F}$-$2^{F/F}$ mice 4h after BrdU injection (Fig. 30, 31). In control mice, the proportion of $BrdU^+$ cell then decreases over time, probably reflecting the differentiation of $BrdU^-$ pro B cells into proliferating large pre B cells in the absence of BrdU.

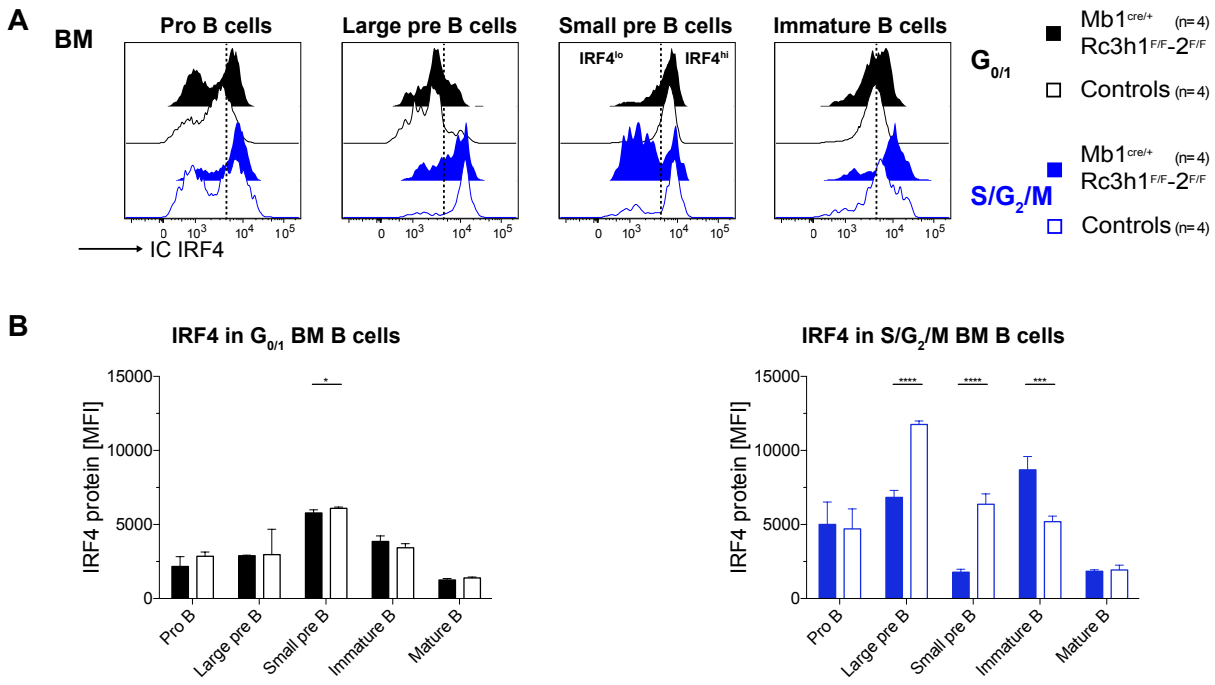

Figure 29: Intracellular levels of IRF4 in $G_{0/1}$ and S/G_2 cell cycle phase of bone marrow B cells in $Mb1^{cre/+}$ $Rc3h1^{F/F}$-$2^{F/F}$ mice.

(A) Representative flow cytometry histograms of stated bone marrow (BM) B cell populations illustrating intracellular (IC) IRF4 staining and determination of $IRF4^{lo}$ and $IRF4^{hi}$ cells among respective populations at either $G_{0/1}$ or $S/G_2/M$ as based on IRF4 expression in $S/G_2/M$ phase control small pre B cells. (B) Bar chart representations of IC IRF4 protein levels as analyzed by flow cytometry in given B cell subsets in $G_{0/1}$ (left) versus S/G_2 (right) cell cycle stages. Colors of cell cycle stages ($G_{0/1}$ in black vs S/G_2 phases in blue) in histograms correspond to colors in bar graphs. Cell cycle stages were defined as shown in Fig. S9, gated B cell subsets: pro B $B220^{lo}$ $c\text{-}kit^{+}$ $CD25^{-}$ IgD^{-} IgM^{-}; large pre B $B220^{lo}$ $c\text{-}kit^{-}$ $CD25^{+}$ IgD^{-} IgM^{-} FSC^{hi}; small pre B $B220^{lo}$ $c\text{-}kit^{-}$ $CD25^{+}$ IgD^{-} IgM^{-} FSC^{lo}; immature B $B220^{+}$ IgD^{-} IgM^{+}; MFI: median flourescence intensity. Bars depict mean values and error bars standard deviation. ****$p \leq 0.0001$, ***$p \leq 0.001$, *$p \leq 0.05$, multiple t tests with Holm-Sidak method applied.

In contrast, in Roquin1/2-deficient large pre B cells the proportion of $BrdU^{+}$ cells remains stable over 26h. The appearance of $BrdU^{+}$ small pre B cells occurs with a minor delay 18h post BrdU injection in the absence of Roquin1/2 proteins (Fig. 31). This difference in percentage of $BrdU^{+}$ small pre B cells increases 30h post injection (Fig. 31), underscoring a deficit of Roquin1/2-deficient large pre B cells to differentiate normally in small pre B cells. The situation in immature and mature B cells is complicated by the fact that both of these populations are actively dividing in $Mb1^{cre/+}$ $Rc3h1^{F/F}$-$2^{F/F}$ as opposed to in control mice (Fig. 28). Correspondingly, there is a significantly higher proportion of $BrdU^{+}$ immature B cells in $Mb1^{cre/+}$ $Rc3h1^{F/F}$-$2^{F/F}$ mice as compared to respective wild type controls, already 4 hours post BrdU injection. This suggests that Roquin1/2-deficient $BrdU^{+}$ immature and mature B cells are at least partially arising due to active division of these cells. In contrast $BrdU^{+}$ immature control B cells are almost exclusively arising from the differentiation of $BrdU^{+}$ pre B cells over time (Fig. 31).

In conclusion, both *ex vivo* and *in vivo* analyses demonstrate that the markedly decreased proliferative capabilities of Roquin1/2 double-deficient large pre B cells likely contribute to the developmental arrest at the pro to pre B transition in $Mb1^{cre/+}$ $Rc3h1^{F/F}$-$2^{F/F}$ mice. However, decrease proliferation does suffice to explain the near complete absence of immature B cells. Moreover, Roquin1/2 double-deficient immature B cells display a higher proliferative capacity *ex vivo* and *in vivo*.

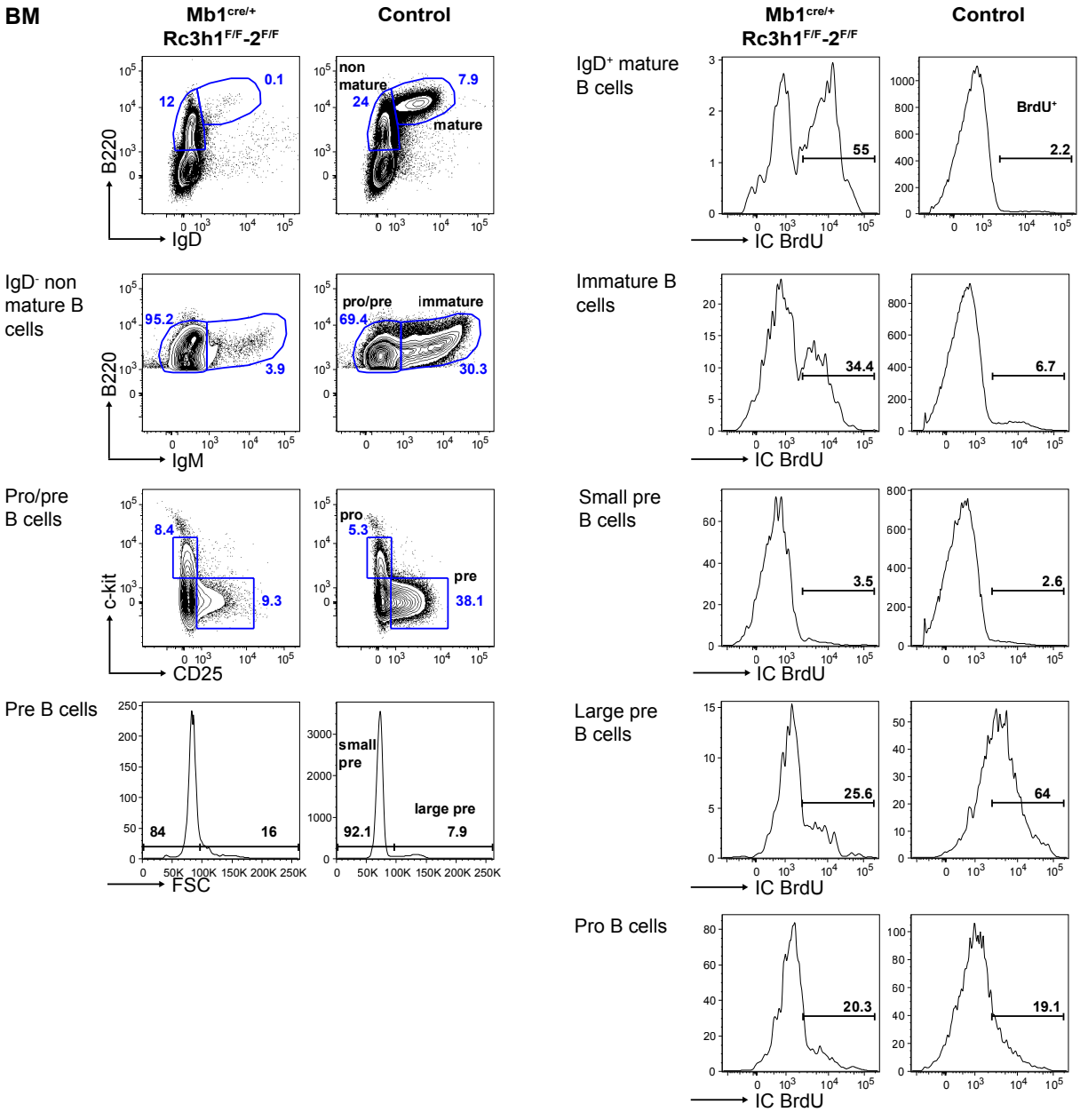

Figure 30: Analysis of *in vivo* BrdU incorporation into the DNA in bone marrow B cell populations of $Mb1^{cre/+}$ $Rc3h1^{F/F}$-$2^{F/F}$ mice.

Representative flow cytometry plots of designated bone marrow (BM) B cell populations 4h post injection illustrating intracellular detection of BRDU incorporation and gating strategies post BrdU injection. BrdU was injected into mice intraperitoneally and incorporation analyzed *ex vivo* 4, 18 and 32h later. The black bar characterizes $BrdU^+$ cells.

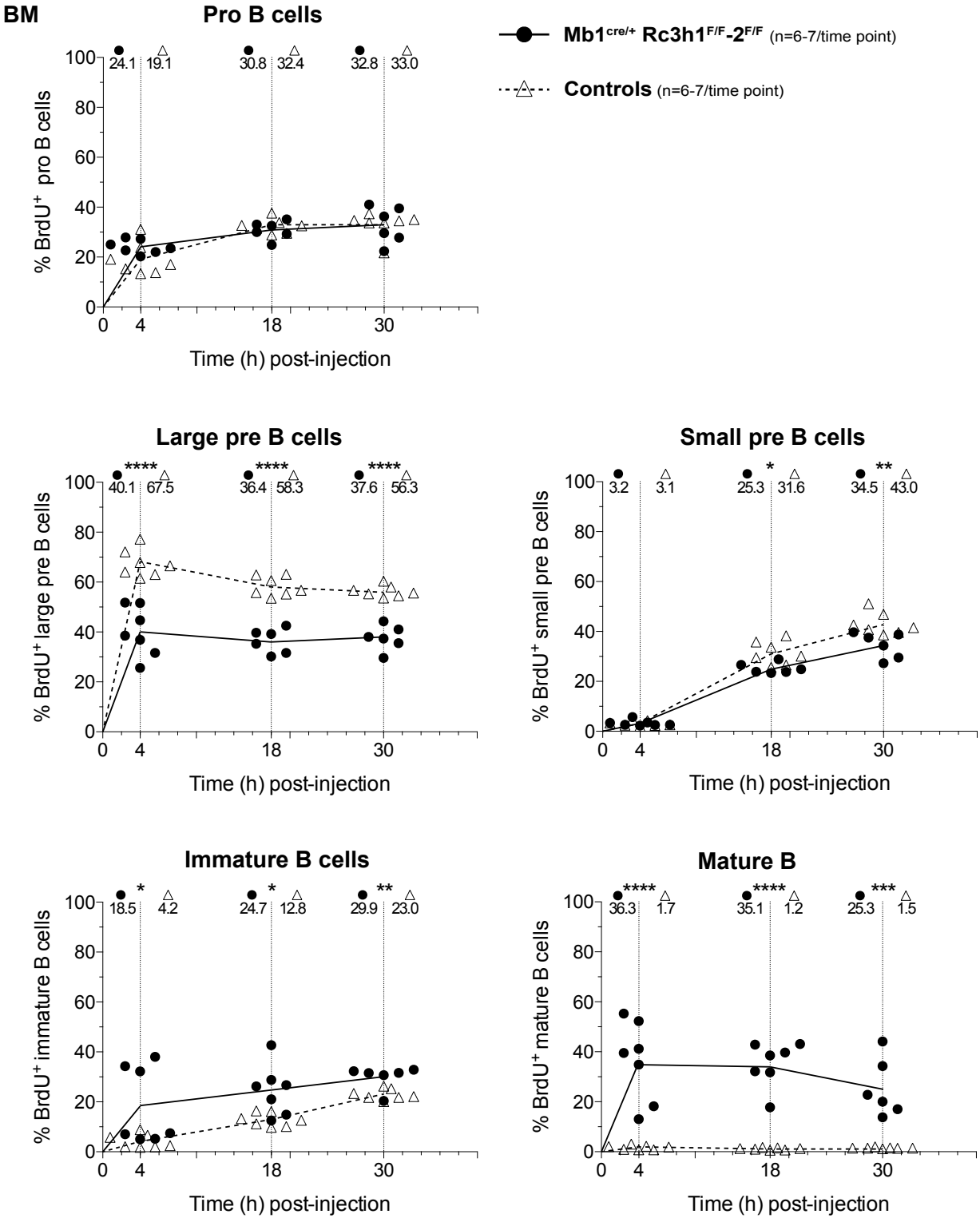

Figure 31: BrdU incorporation *in vivo* into the DNA is strongly impaired in large pre B cells of Mb1$^{cre/+}$ Rc3h1$^{F/F}$-2$^{F/F}$ mice.

2mg BrdU (80mg/kg body weight, assuming a mouse weight of 25g) was injected intraperitoneally 30, 18 and 4h prior to analysis of indicated B cell populations. Gating for BrdU$^+$ cells was performed as shown in Fig. 30. Mean values for each time point are given left (for Mb1$^{cre/+}$ Rc3h1$^{F/F}$-2$^{F/F}$) and right (for controls) of the dotted, vertical line and were connected by a straight line (for Mb1$^{cre/+}$ Rc3h1$^{F/F}$-2$^{F/F}$) or a dashed line (for controls) as trend lines. ****$p \leq 0.0001$, **$p \leq 0.01$, *$p \leq 0.05$, unpaired t test.

1.8 Extrinsic effects in T cells and myeloid cells of $Mb1^{cre/+}$ $Rc3h1^{F/F}$-$2^{F/F}$, $Mb1^{cre/+}$ $Rc3h1^{F/F}$-$2^{F/wt}$ and $Mb1^{cre/+}$ $Rc3h1^{F/F}$ mice

Roquin1-deficiency in individual cell-types, amongst them B cells [212], can have severe cell-extrinsic effects on various other immune cell populations. Therefore, I set out to elucidate the B cell-extrinsic effects that might be associated with the severe and yet different B cell-intrinsic phenotypes in $Mb1^{cre/+}$ $Rc3h1^{F/F}$-$2^{F/F}$, $Mb1^{cre/+}$ $Rc3h1^{F/F}$-$2^{F/wt}$ and $Mb1^{cre/+}$ $Rc3h1^{F/F}$ mice. I also aimed at elucidating extrinsic effects in these mouse strains. Percentages of splenic T cell subsets of $Mb1^{cre/+}$ $Rc3h1^{F/F}$-$2^{F/F}$ mice resemble those of $Mb1^{cre/cre}$ mice with the exception of the $CD4^+$ $CD25^+$ T cell compartment, which contains the pool of regulatory T (T_{reg}) cells. The population of $CD4^+$ $CD25^+$ T cell is significantly increased in percentage and total cell number in the former strain compared to $Mb1^{cre/cre}$ mice (Fig. S10). As this was the only clear difference within T cell subsets between these strains in bone marrow, spleen or thymus (data not shown), I focused on splenic T cell subsets in $Mb1^{cre/+}$ $Rc3h1^{F/F}$-$2^{F/wt}$ and $Mb1^{cre/+}$ $Rc3h1^{F/F}$ mice.

Compared to controls, the spleens of these two mouse strains are increased in weight and cellularity (Fig. 8). The percentage and total number of T cells are increased in both strains, as are $CD4^+$ T cells and $CD4^+$ $CD25^+$ T cells. Noteably, the percent increase in this T_{reg}-containing compartment is twofold in both mouse strains. There is only a slight tendency of percent and cell number increase of the $CD8^+$ T cell pool in the two strains (Fig. S10). Remarkably, in $Mb1^{cre/+}$ $Rc3h1^{F/F}$-$2^{F/wt}$ and $Mb1^{cre/+}$ $Rc3h1^{F/F}$ mice, central memory-like and effector memory-like $CD4^+$ T cells are significantly expanded with regard to percentage and total cell numbers (Fig. 32). This effect is less pronounced for the respective $CD8^+$ T cell subsets. In the $Mb1^{cre/+}$ $Rc3h1^{F/F}$-$2^{F/wt}$ mouse line, there is a trend towards an increase in percentage and total cell number increase of central memory-like $CD8^+$ T cells, while effector memory-like $CD8^+$ T cells are significantly increased in this strain. In $Mb1^{cre/+}$ $Rc3h1^{F/F}$ mice, naive and central memory-like $CD8^+$ T cell populations are not altered, however the pool of effector memory-like $CD8^+$ T cells is significantly enlarged in percentage and total cell number (Fig. 32).

Surprisingly, there is an increase in percentage of $CD4^+$, $CD8^+$ and also overall T cells in $Mb1^{cre/+}$ $Rc3h2^{F/F}$ mice (Fig. S11), whereas differences in cell numbers did not reach significance. Remarkably, within the $CD4^+$ T cell population, the effector memory-like subset is not altered, while the percentages of naive and central memory-like $CD4^+$ are expanded. Furthermore, there is a significantly larger proportion of naive $CD4^+$ and $CD8^+$ T cells, while

effector memory-like and central memory-like are essentially not changed in Mb1$^{cre/+}$ Rc3h2$^{F/F}$ mice (Fig. S11). Splenic NKT cell numbers were also investigated, yet no difference was observed (data not shown). As the myeloid cell compartment is significantly affected by CD19cre-mediated deletion of Roquin1 [212], I next aimed to elucidate the consequences of Roquin1 and/or 2 ablation on the splenic myeloid cell compartment in Mb1$^{cre/+}$ Rc3h1$^{F/F}$-2$^{F/F}$, Mb1$^{cre/+}$ Rc3h1$^{F/F}$-2$^{F/wt}$ and Mb1$^{cre/+}$ Rc3h1$^{F/F}$ mice (Fig. S12). The percentages of every myeloid cell population analysed are increased in Mb1$^{cre/+}$ Rc3h1$^{F/F}$-2$^{F/F}$ mice (Fig. S12B). Percentages of dendritic cells are unaltered in Mb1$^{cre/+}$ Rc3h1$^{F/F}$-2$^{F/wt}$ and Mb1$^{cre/+}$ Rc3h1$^{F/F}$ mice compared to controls (Fig. S12B).

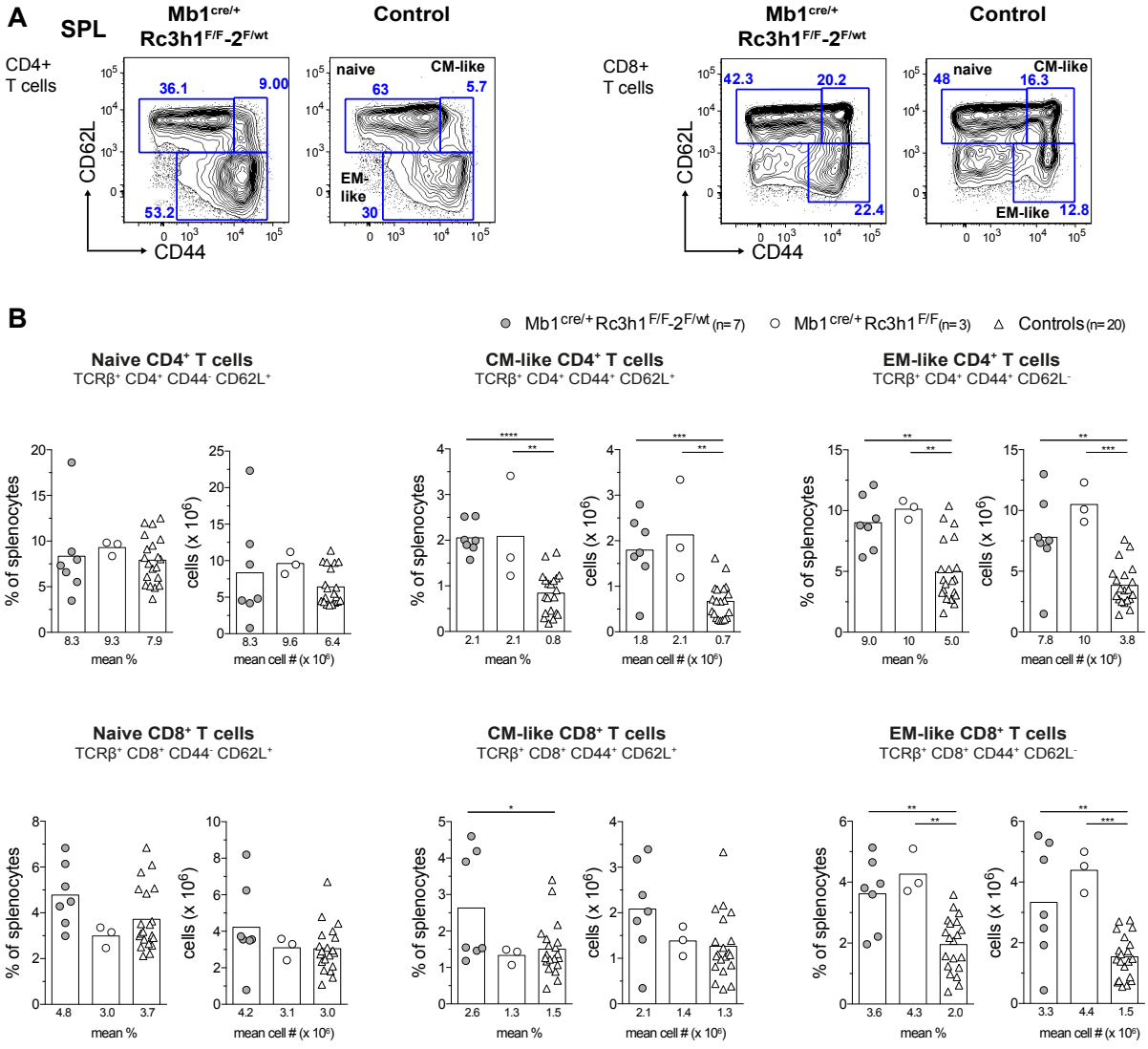

Figure 32: Effector memory-like T cells in CD4$^+$ and CD8$^+$ subsets are expanded in the spleen of Mb1$^{cre/+}$ Rc3h1$^{F/F}$-2$^{F/wt}$ and Mb1$^{cre/+}$ Rc3h1$^{F/F}$ mice.

(A) Representative flow cytometry plots depicting the gating strategy for splenic (SPL) CD4$^+$ and CD8$^+$ T cell subsets. T cell subsets as indicated in (B). (B) Percentages of designated T cell subsets among total splenocytes and total subset cell numbers as analyzed by flow cytometry. Numbers below graphs and bars represent mean percentages or cell numbers (#). ****p ≤ 0.0001, ***p ≤ 0.001, **p ≤ 0.01, *p ≤ 0.05, ANOVA.

There is an increase in percentages and cell numbers of eosinophils in $Mb1^{cre/+}$ $Rc3h1^{F/F}$-$2^{F/wt}$ and $Mb1^{cre/+}$ $Rc3h1^{F/F}$ mice as was observed in $CD19^{cre/+}$ $Rc3h1^{F/F}$ mice (Fig. S12B) [212], yet the differences in $Mb1^{cre/+}$ $Rc3h1^{F/F}$ mice did not reach significance. Similarly, there is a tendency of increased populations of monocytes/macrophage and neutrophils in $Mb1^{cre/+}$ $Rc3h1^{F/F}$-$2^{F/wt}$ mice (Fig. S12B). Unexpectedly, there is a distinguishable population of $Gr1^{+}$ monocytes or macrophages in $Mb1^{cre/+}$ $Rc3h1^{F/F}$-$2^{F/F}$, $Mb1^{cre/+}$ $Rc3h1^{F/F}$-$2^{F/wt}$ and $Mb1^{cre/+}$ $Rc3h1^{F/F}$ mice (Fig. S12A), which is absent in $Mb1^{cre/+}$ $Rc3h2^{F/F}$ mice (Fig. S13). However, the percentage of classical dendritic cells is significantly increased, while neutrophils and activated monocytes and macrophages are reduced in percent in this mouse strain (Fig. S13). However, differences in cell numbers did not reach significance (Fig. S13).

Furthermore, the near absence of B cells leads to a paucity in plasma cells and antibody production. Secreted IgE is loaded onto mast cells, which results in upregulation of FceRI on the mast cell surface and transient cellular activation. Therefore, I investigated the cellularity and surface phenotype of serosal mast cells in the peritoneal cavity of $Mb1^{cre/+}$ $Rc3h1^{F/F}$-$2^{F/F}$ mice (Fig. 33A, 33B). As expected, mast cells in $Mb1^{cre/+}$ $Rc3h1^{F/F}$-$2^{F/F}$ mice displayed nearly no bound IgE on their surface, while FceRI surface levels are surprisingly not increased and remain unchanged on control mast cells (Fig. 33C). FcγRIIB, a negative regulator of proliferation [257], shows a tendency for lower expression levels on mast cells of $Mb1^{cre/+}$ $Rc3h1^{F/F}$-$2^{F/F}$ mice. Additionally, the surface protein levels of IL-33R, the receptor for the alarmin IL-33 [258, 259], are significantly reduced on these mast cells.

In conclusion, the observed changes in splenic cellularity in $Mb1^{cre/+}$ $Rc3h1^{F/F}$-$2^{F/wt}$ and $Mb1^{cre/+}$ $Rc3h1^{F/F}$ mice originate to some extent from expansion of primarily $CD4^{+}$ memory-like cells and partly $CD8^{+}$ effector memory-like cells but not to any major extent from changes in myeloid populations. Remarkably cell-extrinsic effects of Mb1cre-mediate ablation of Roquin1 or Roquin2 differ, while the T cell compartment appears hyperactivated upon ablation of Roquin1, Roquin2 ablation appears to result in hypoactivation of the T cells. Furthermore, B cell-specific Roquin1 and 2 ablation results in different effects on the myeloid compartment.

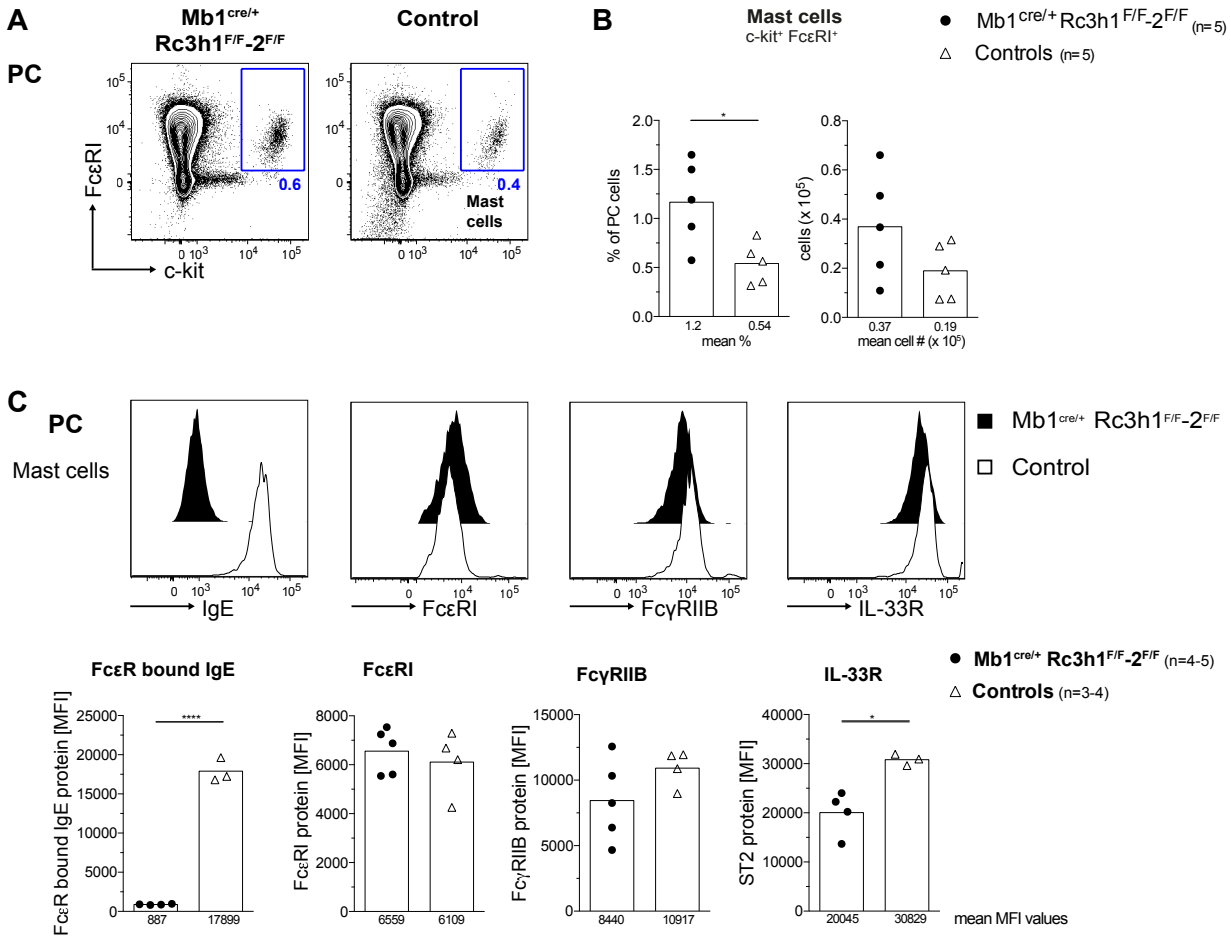

Figure 33: Analysis of peritoneal cavity mast cells in Mb1$^{cre/+}$ Rc3h1$^{F/F}$-2$^{F/F}$ mice.
(A) Representative plots illustrating gating for mast cells in peritoneal cavity (PC). (B) Percentages of mast cells of total PC cells and total cell numbers (#) as determined by flow cytometry. (C) (Top) Representative flow cytometry plots of PC mast cells depicting surface expression of FcεR-bound IgE, FcεRI, FcγRII and IL-33R. (Bottom) FcεR-bound IgE, FcεRI, FcγRIIB and IL-33R cell surface protein levels on mast cells as determined by flow cytometry. Numbers below graphs and bars show mean values. ****p ≤ 0.0001, *p ≤ 0.05, unpaired t test.

1.9 A pre-rearranged IgH knock-in (IgH^{MOG}) rescues the development of pre B cells and partially rescues the immature and mature recirculating B cell pool in Mb1$^{cre/+}$ Rc3h1$^{F/F}$-2$^{F/F}$ IgH^{MOG} mice

Considering the strikingly reduced intracellular protein levels of μHC, I interrogated if defects in V_HDJ_H rearrangement and heavy chain expression are the underlying reason for the developmental arrest of Roquin1/2-deficient B cells at the pro to pre B cell transition as well as the reason for the changes observed in mediators of signaling downstream of the pre-BCR. To this end, I decided to evaluate whether expression of a pre-rearranged heavy chain can rescue some of the developmental defects observed in the B cell lineage of Mb1$^{cre/+}$ Rc3h1$^{F/F}$-2$^{F/F}$ mice. For this purpose, I employed the IgH^{MOG} heavy chain knock-in allele [226].

IgH^{MOG} knock-in B cells have intact allelic exclusion and can undergo class-switch recombination (CSR) and somatic hypermuation (SHM) in the germinal center reaction. Furthermore, despite specificity of the heavy chain for the myelin oligodendrocyte glycoprotein (MOG), there are no self-reactive antibodies produced in IgH^{MOG} transgenic mice [226, 260, 261]. As detailed analyses of $Mb1^{cre/+}$ $Rc3h1^{F/F}$-$2^{F/F}$ mice up to one year of age revealed no difference in the phenotype described here compared to 8-20 week old mice, I decided to maintain this 8-20 week age span for all experiments based on Mb1cre-mediated ablation of Roquin1/2 proteins.

First, I analyzed bone marrow B cell lymphopoiesis in $Mb1^{cre/+}$ $Rc3h1^{F/F}$-$2^{F/F}$ IgH^{MOG} mice (Fig. 34). The overall bone marrow B cell number is not altered, but the percentage (data not shown) and total cell number of pro B cells of both $Mb1^{cre/+}$ $Rc3h1^{F/F}$-$2^{F/F}$ IgH^{MOG} and IgH^{MOG} control mice are reduced compared to mice without heavy chain insertion. This stems from a nearly complete absence of late pro B cells, the developmental stage when V_HDJ_H recombination is being (Fig. 34). Likewise, there is a trend towards lower percentage and cell numbers in small pre B cells of these genotypes (Fig. 34) This observation underlines the innocuousness of the BCR encoded by the IgH^{MOG} allele, as pro and pre B cell can transit quicker through these developmental stages if no self-reactive BCRs are expressed [57, 255]. In accordance with this result, the percentage and total cell numbers of large pre B cells are not altered in $Mb1^{cre/+}$ $Rc3h1^{F/F}$-$2^{F/F}$ IgH^{MOG} mice (Fig. 34). However, at the small pre B cell stage, when Ig light chain rearrangement occurs, percentage and total cell number are reduced in $Mb1^{cre/+}$ $Rc3h1^{F/F}$-$2^{F/F}$ IgH^{MOG} mice compared to IgH^{MOG} and wt controls, although the difference is only significant compared to the wt controls. Furthermore, percentage and total cell number of immature B cells in $Mb1^{cre/+}$ $Rc3h1^{F/F}$-$2^{F/F}$ IgH^{MOG} mice are even lower than in IgH^{MOG} mice, which are also reduced compared to control mice (Fig. 34). Incompatility of the IgH^{MOG} heavy chain with certain light chains may result in the lower numbers of IgH^{MOG}-transgenic immature B cells compared to controls (Fig. 34). Nevertheless, the percentage and number of mature B cells in IgH^{MOG} mice are unaltered compared to control mice, while they are strikingly decreased in $Mb1^{cre/+}$ $Rc3h1^{F/F}$-$2^{F/F}$ IgH^{MOG} mice (Fig. 34).

In summary, analysis of bone marrow B cell numbers indicates that a pre-rearranged μHC rescues pre B cell development, but does not reconstitute immature and mature recirculating B cell numbers to wild type levels in $Mb1^{cre/+}$ $Rc3h1^{F/F}$-$2^{F/F}$ IgH^{MOG} mice.

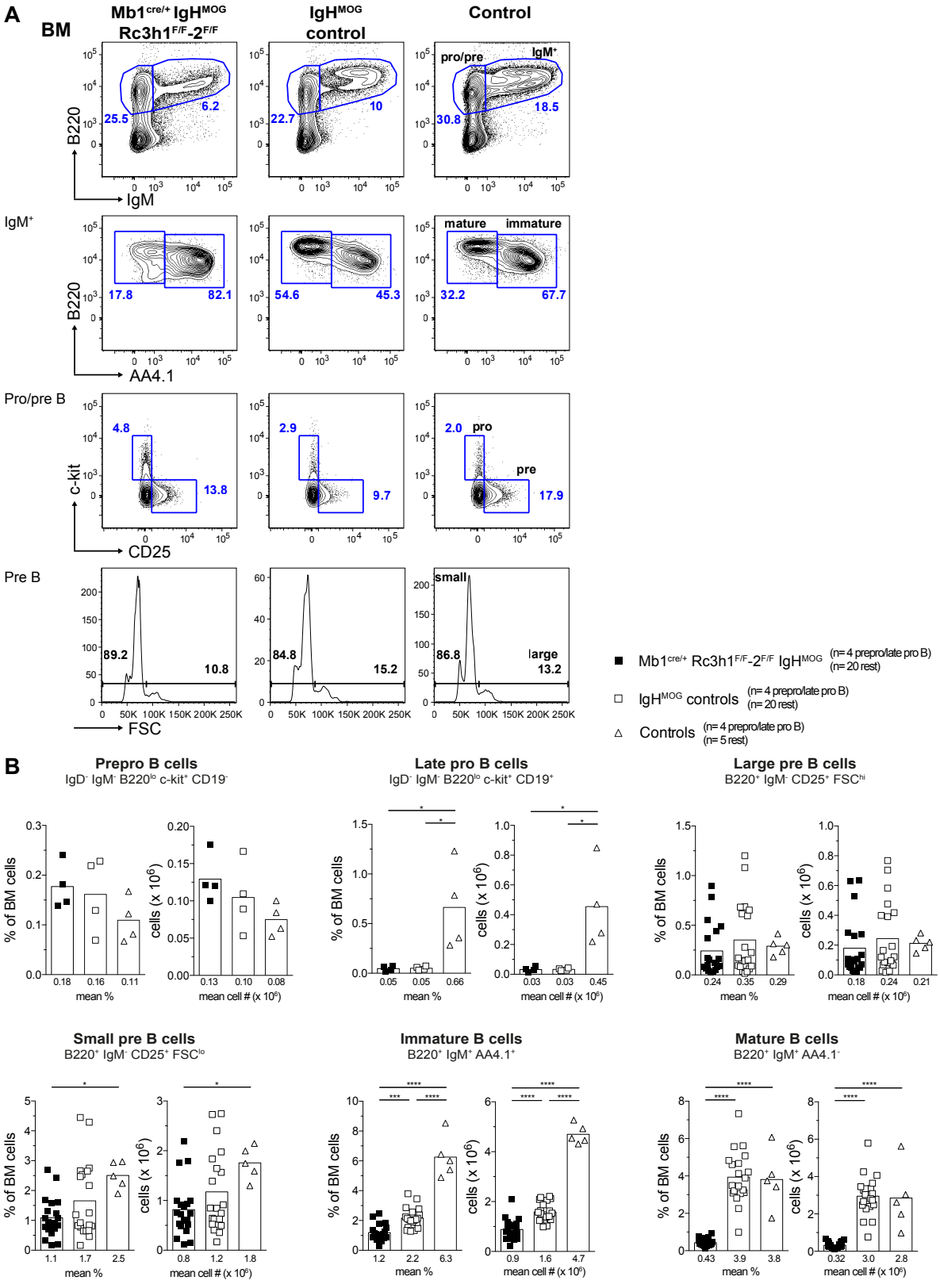

Figure 34: The pre B cell compartment is, but immature and mature bone marrow B cell populations are not rescued in Mb1$^{cre/+}$ Rc3h1$^{F/F}$-2$^{F/F}$ IgH^{MOG} mice.

(A) Representative flow cytometry plots of indicated bone marrow (BM) B cell subsets illustrating the employed gating strategies. (B) Percentages of respective B cell subsets of total BM cells and total subset cell numbers as determined by flow cytometry. Mb1$^{cre/+}$ and wild type mice (collectively refered to as controls) were used as controls for comparison of Mb1^{cre} based experiments if not otherwise mentioned. Numbers below graphs and bars represent mean percentages and cell numbers (#). ****p ≤ 0.0001, ***p ≤ 0.001, *p ≤ 0.05, ANOVA.

1.10 B cells populate secondary lymphoid organs with very divergent efficiencies in Mb1^{cre} Rc3h1$^{F/F}$-2$^{F/F}$ IgH^{MOG} mice and show a defect in peripheral development

The spleen weight of Mb1$^{cre/+}$ Rc3h1$^{F/F}$-2$^{F/F}$ IgH^{MOG} mice is significantly increased (Fig. 35A), although the total cell count of splenocytes is not changed. There are splenic Roquin1/2-deficient IgH^{MOG} B cells, yet their percentage and total cell count are significantly reduced by over two fold (Fig. 35B, 35C). The immature/transitional splenic B cell pool of Mb1$^{cre/+}$ Rc3h1$^{F/F}$-2$^{F/F}$ IgH^{MOG} mice matches that of IgH^{MOG} control mice in percent and cell number, while the Roquin1/2-deficient IgH^{MOG} mature splenic B cell compartment is three fold reduced with regard to percentage and total cell count compared to both control mouse strains (Fig. 35C). To further delineate the developmental stage at which splenic B cells of Mb1$^{cre/+}$ Rc3h1$^{F/F}$-2$^{F/F}$ IgH^{MOG} mice accumulate, I further characterized transitional B cell stages within the AA4.1^{-} immature/transitional compartment as well as follicular and marginal zone B cell subsets of the mature AA4.1^{-} B220^{+} B cell pool (Fig. 36). Numbers and percentages of transitional T1 B cells are not reduced.

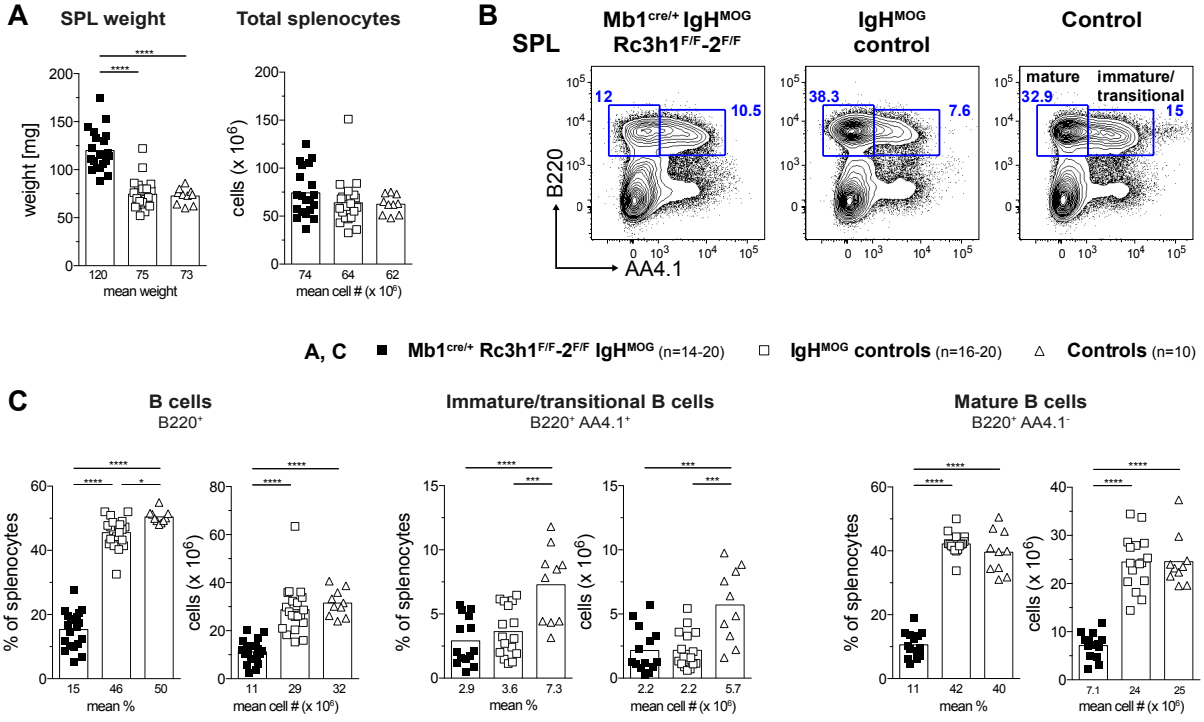

Figure 35: Spleens of Mb1$^{cre/+}$ Rc3h1$^{F/F}$-2$^{F/F}$ IgH^{MOG} mice are enlarged, but B cell numbers are reduced.
(A) SPL weight and total number of splenocytes. (B) Representative flow cytometric analysis of splenic (SPL) B cells showing the employed gating scheme. (C) Percentages of respective B cell subsets of total SPL cells and total subset cell numbers as determined by flow cytometry. Numbers below graphs and bars show mean percentages and cell numbers (#). ****p ≤ 0.0001, ***p ≤ 0.001, *p ≤ 0.05, ANOVA.

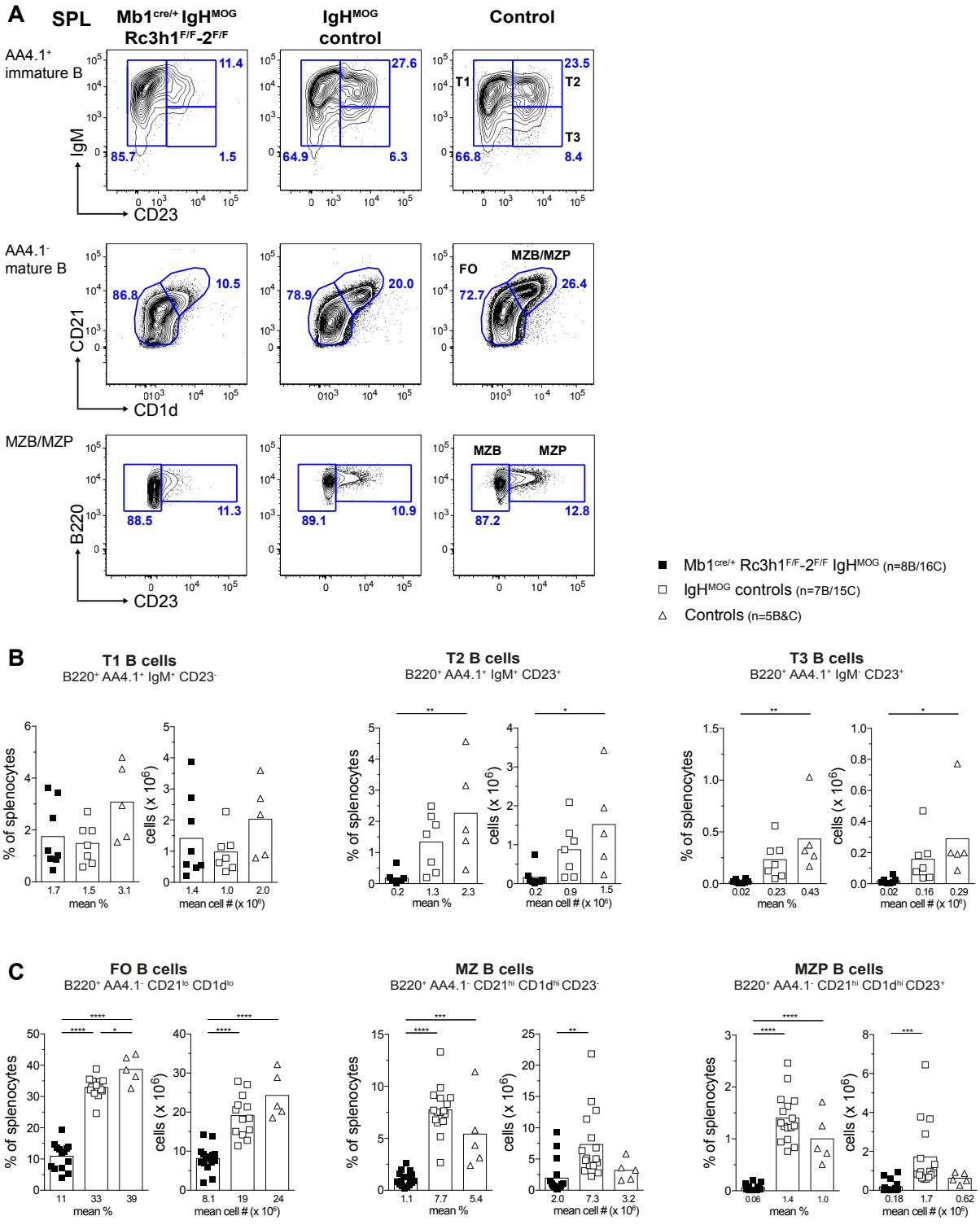

Figure 36: Mb1$^{cre/+}$ Rc3h1$^{F/F}$-2$^{F/F}$ IgH^{MOG} splenic B cell development is arrested between transitional stages 1 and 2.

(A) Representative flow cytometric analysis of splenic (SPL) B cells illustrating the gating strategy. (B, C) Percentages of respective AA4.1^{+} immature or AA4.1^{-} mature (B, C) B cell subsets of total SPL cells and total subset cell numbers as determined by flow cytometry. T: transitional; FO: follicular; MZB/MZP: mature and marginal zone precursor; MZB or MZ B: mature marginal zone; MZP: marginal zone precursor. Numbers below graphs and bars represent mean percentages and cell numbers (#). ****p ≤ 0.0001, ***p ≤ 0.001, **p ≤ 0.01, *p ≤ 0.05, ANOVA.

Yet, as described previously for $Mb1^{cre/+}$ $Rc3h1^{F/F}$-$2^{F/F}$ mice, there is a clear deficit of development at the T1 to T2 transition in $Mb1^{cre/+}$ $Rc3h1^{F/F}$-$2^{F/F}$ IgH^{MOG} mice as reflected by the reduced cell numbers and percentages of T2 and T3 in both strains (Fig. 36B). Furthermore, follicular, marginal zone and marginal zone precursor populations are all significantly reduced in $Mb1^{cre/+}$ $Rc3h1^{F/F}$-$2^{F/F}$ IgH^{MOG} mice (Fig. 36C), although this flow cytometric analysis was complicated by the deregulated expression pattern of the employed surface markers CD21, CD1d and CD23 (Fig. 36A).

Classification of transitional stages as well as MZ precursor B cell relies on CD23-based gating. As I noticed an unusual CD23 expression pattern among splenic B cell populations in $Mb1^{cre/+}$ $Rc3h1^{F/F}$-$2^{F/F}$ IgH^{MOG} mice (Fig. 36), I quantified CD23 surface expression (Fig. 34A). This analysis demonstrated that CD23 is downregulated on all splenic B cell populations of $Mb1^{cre/+}$ $Rc3h1^{F/F}$-$2^{F/F}$ IgH^{MOG} mice, except for marginal zone B cells (Fig. 37). Accordingly, the stated percentages and total cell numbers of splenic B cell populations could be biased (Fig. 36).

Preliminary data in the Schmidt-Supprian laboratory suggested that Roquin proteins could regulate CD24 surface expression on mast cells. The GPI-anchored surface receptor CD24 promotes apoptosis in pro and pre B cells plays a role in cell adhesion. Additionally its expression levels decline with progressing B cell maturation [262, 263], with the exception of marginal zone B cells. Evaluation of surface CD24 levels on splenic B cell populations of $Mb1^{cre/+}$ $Rc3h1^{F/F}$-$2^{F/F}$ IgH^{MOG} mice showed very specific and significant higher expression levels on all mature splenic B cell populations, further substantiating Roquin-mediated regulation of CD24 or indicating a function in apoptosis of mature double-deficient B cells (Fig. 37B).

Furthermore, the general developmental arrest at the T1 to T2 transition was supported also independently of CD23 staining (Fig. 38A). The described impairment of B cell development past the transitional T1 stage in $Mb1^{cre/+}$ $Rc3h1^{F/F}$-$2^{F/F}$ IgH^{MOG} mice is underlined by the almost unchanged population of the more immature IgD^{lo} IgM^{hi} B cell compartment in contrast to the almost absent more mature IgD^{hi} IgM^{lo} B cells in this mouse line in comparison to control mice (Fig. 38A). Strikingly, the cell number of the more mature IgD^{hi} IgM^{lo} B cell subset was shown to comprise only a fourth of the cell number of the $B220^{+}$ $AA4.1^{-}$ mature B cell subset (Fig. 36, 38A). Subsequent analysis of B220 surface expression on $B220^{+}$ $AA4.1^{+}$ immature and $B220^{+}$ $AA4.1^{-}$ mature B demonstrated significantly lower relative expression of B220 on $B220^{+}$ $AA4.1^{-}$ mature B cells in $Mb1^{cre/+}$ $Rc3h1^{F/F}$-$2^{F/F}$ IgH^{MOG} mice compared to IgH^{MOG} wild type control mice (Fig. 38B).

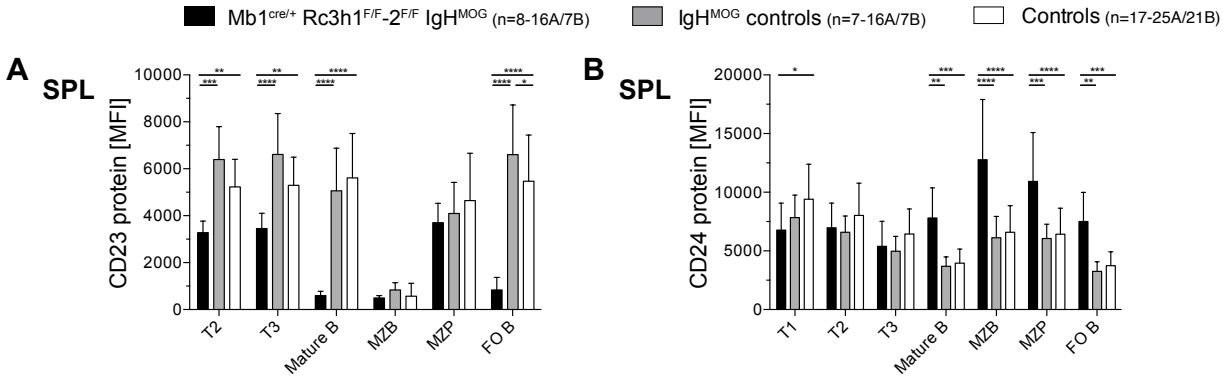

Figure 37: Surface CD23 levels are reduced on splenic B cells of Mb1$^{cre/+}$ Rc3h1$^{F/F}$-2$^{F/F}$ IgH^{MOG} mice, while CD24 surface levels are increased on mature splenic B cell populations of these mice.
Bar chart representation of surface expression levels of CD23 (A) and CD24 (B) as determined by flow cytometry on indicated B cell populations. Gated B cell subsets: immature B B220^{+} AA4.1^{+}; Transitional 1 (T1) B220^{+} AA4.1^{+} CD23^{-} IgM^{+}; T2 B220^{+} AA4.1^{+} CD23^{+} IgM^{+}; T3 B220^{+}AA4.1^{+}CD23^{+} IgM^{-}; Mature B B220^{+} AA4.1^{-}; mature MZ B cells (MZB) B220^{+} AA4.1^{-} CD1d^{hi} CD21^{hi} CD23^{lo}; MZ precursors (MZP) B220^{+} AA4.1^{-} CD1d^{hi} CD21^{hi} CD23^{hi}; follicular (FO) B B220^{+} AA4.1^{-} CD1d^{int} CD21^{int}. SPL: spleen; MFI: median fluorescence intensity. Bars represent mean values and error bars standard deviation. ****p ≤ 0.0001, ***p ≤ 0.001, **p ≤ 0.01, *p ≤ 0.05, 2way ANOVA with Tukey test applied.

This suggests that the splenic B220^{+} AA4.1^{-} mature B cell pool of Mb1$^{cre/+}$ Rc3h1$^{F/F}$-2$^{F/F}$ IgH^{MOG} mice contains reasonably more B1 B cells. Likewise, the B cell compartment in the peritoneum, altogether missing in Mb1$^{cre/+}$ Rc3h1$^{F/F}$-2$^{F/F}$ mice, is rescued and entirely composed of B1b cells in Mb1$^{cre/+}$ Rc3h1$^{F/F}$-2$^{F/F}$ IgH^{MOG} mice (Fig. 39B). It is noteworthy, that the B1 cell compartment in the spleen of Mb1$^{cre/+}$ Rc3h1$^{F/F}$-2$^{F/F}$ IgH^{MOG} mice is significantly increased in percent and in total cell number, which is caused by a five fold increase of the B1b cell pool, while the splenic B1a subset is not changed compared to IgH^{MOG} controls and reduced compared to wt controls (Fig. 39A). In addition, the remarkable deficiency of truly mature peripheral B cells in Mb1$^{cre/+}$ Rc3h1$^{F/F}$-2$^{F/F}$ IgH^{MOG} mice is emphasized by the almost entire absence of Peyer's patches on the small intestines of these mice (data not shown) as well as the significantly reduced percentage of germinal center B cells in the spleen and in the GALT (mLN and PP) (Fig. S14).

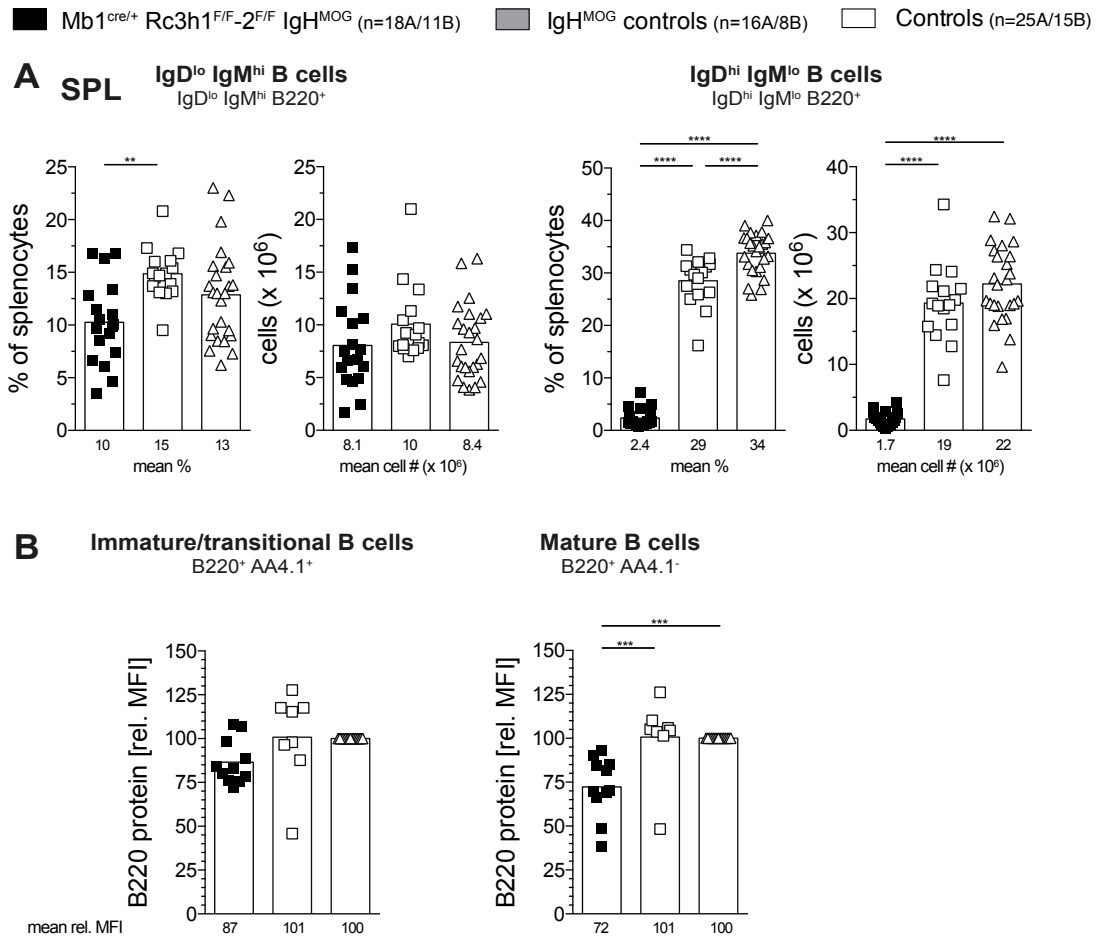

Figure 38: IgD^{hi} IgM^{lo} B cell reflects mature B2 cells in Mb1$^{cre/+}$ Rc3h1$^{F/F}$-2$^{F/F}$ IgH^{MOG} mice.
(A) Percentages of stated B cell subsets of total splenic (SPL) cells and total subset cell numbers as determined by flow cytometry. (B) Bar chart representation of surface expression levels of B220 on AA4.1^{+} immature/transitional and AA4.1^{-} mature splenic as determined by flow cytometry on indicated B cell populations. Numbers below graphs and bars show mean values. ****p ≤ 0.0001, ***p ≤ 0.001, **p ≤ 0.01, ANOVA.

In conclusion, Mb1$^{cre/+}$ Rc3h1$^{F/F}$-2$^{F/F}$ IgH^{MOG} mice can develop splenic B cells, which however are mainly arrested at the T1 to T2 transition and essentially fail to develop into mature IgD expressing peripheral B cells. The absence of functional mature B cells is mirrored by near complete absence of splenic or GALT germinal center B cells. Furthermore, CD23 surface levels on splenic B cells appear to depend on Roquin proteins while the data indicates that Roquin1 and 2 repress CD24 expression levels in mature B cell subsets with CD24 potentially being a Roquin target. Unexpectedly, B1 cell development in the spleen and peritoneal cavity is rescued in these mice due to an unexpected, massive increase of B1b cells.

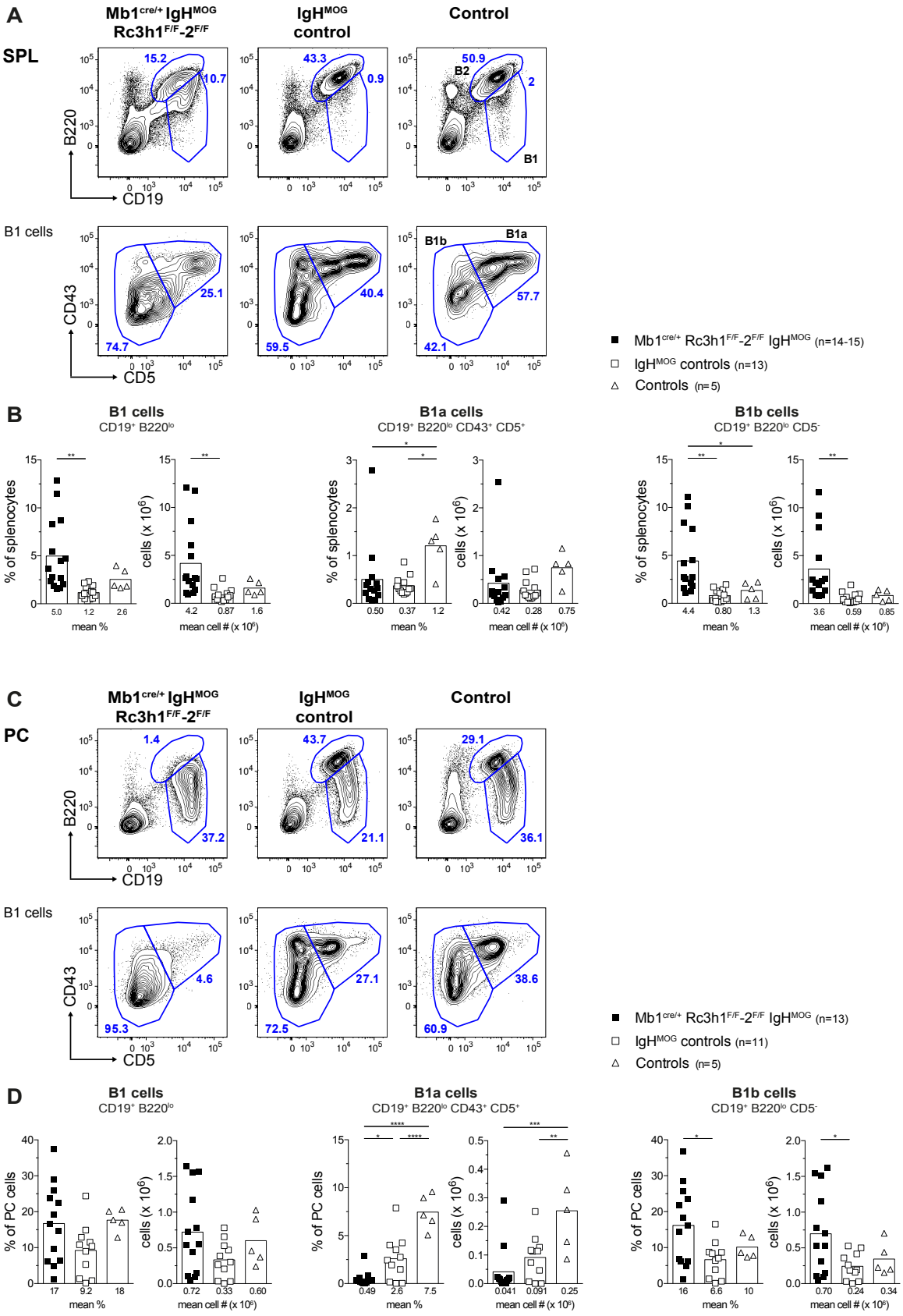

Figure 39: Expansion of B1b cells in spleen and peritoneal cavity of Mb1$^{cre/+}$ Rc3h1$^{F/F}$-2$^{F/F}$ IgH^{MOG} mice.
(A, C) Representative flow cytometry analyses of SPL/PC B cells illustrating the gating scheme. (B, D) Percentages of respective B1 cell populations of total SPL/PC (B, D) cells and total subset cell numbers as determined by flow cytometry. SPL: spleen; PC: peritoneal cavity. Numbers below graphs and bars represent mean percentages and cell numbers (#). ****p ≤ 0.0001, **p ≤ 0.001 **p ≤ 0.01, *p ≤ 0.05, ANOVA.

1.11 Bone marrow immature B and successive B cell stages use almost exclusively IgH^{MOG} in $Mb1^{cre/+}$ $Rc3h1^{F/F}$-$2^{F/F}$ IgH^{MOG} mice

Endogenous or transgenic heavy chain usage in naive B cells in IgH^{MOG} mice can be determined by flow cytometric analysis of IgH allotypes, as the IgH^{MOG} allele has a Igμ allotype a (IgM^a), while μ chains of the second endogenous C57BL/6 allele have the IgM^b allotype (Fig. 40) [226].

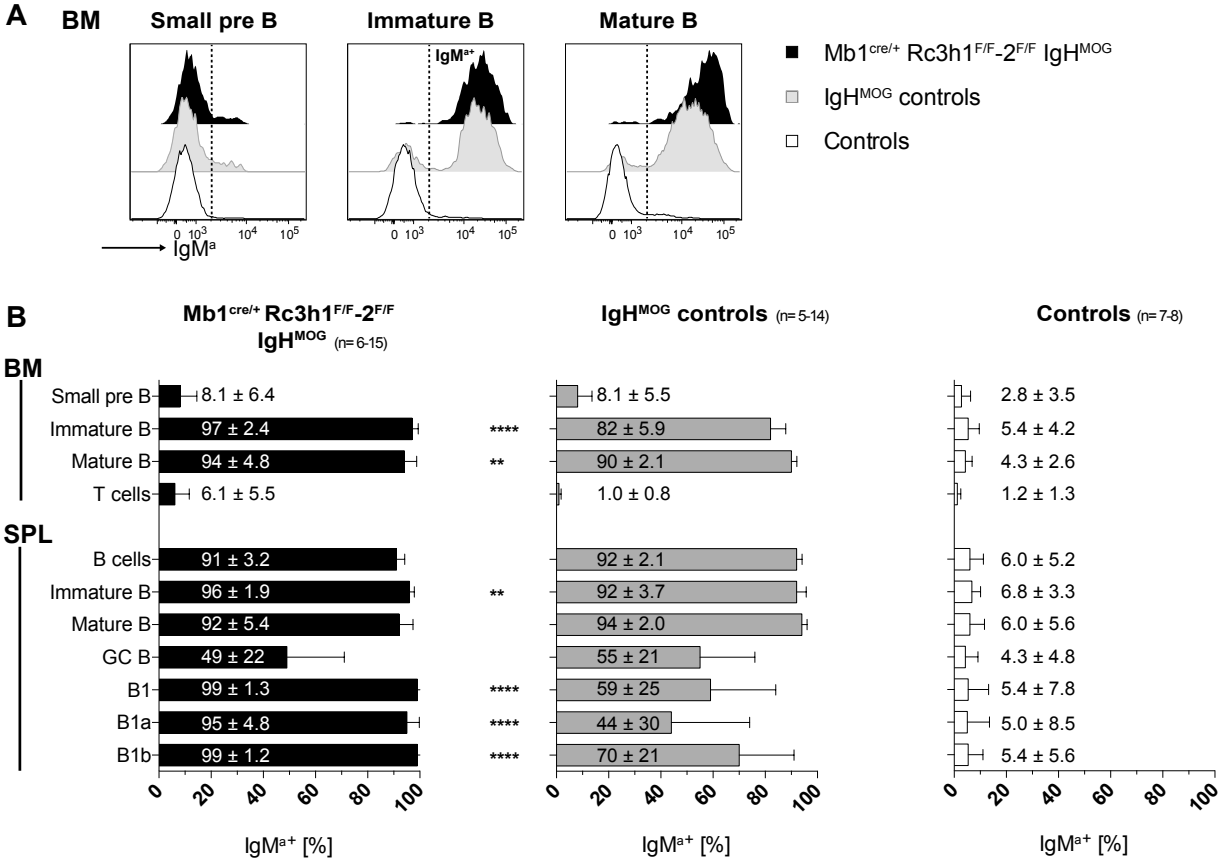

Figure 40: Immature B cells in the bone marrow and splenic B1 cell populations of $Mb1^{cre/+}$ $Rc3h1^{F/F}$-$2^{F/F}$ IgH^{MOG} mice express almost exclusively IgM^a.

(A) Representative flow cytometry histograms depicting surface staining of IgM^a on designated BM B cell populations. Cells expressing IgM^a (IgM^{a+}) are indicated. The positive signal in controls represents background staining. (B) Percentages of IgM^a-positive (IgM^{a+}) B and T cell subsets among the respective subsets. Black * represent significant differences between cell populations from $Mb1^{cre/+}$ $Rc3h1^{F/F}$-$2^{F/F}$ IgH^{MOG} and IgH^{MOG} controls. B cell subset gating: BM small pre B $B220^{lo}$ IgD^- IgM^- c-kit^- $CD25^+$ FSC^{lo}, immature B $B220^+$ IgD^- IgM^+; mature B $B220^+$ IgD^+; SPL B cells $B220^+$; immature B $B220^+$ $AA4.1^+$; mature B $B220^+$ $AA4.1^-$; GC B $B220^+$ $CD19^+$ PNA^+ Fas^+ $CD38^{lo}$; B1 $CD19^+$ $B220^{lo}$; B1a $CD19^+$ $B220^{lo}$ $CD43^+$ $CD5^+$, B1a $CD19^+$ $B220^{lo}$ $CD5^-$. BM: bone marrow; SPL: spleen; GC: germinal center. Bars represent means and error bars standard deviation. ****$p \leq 0.0001$, **$p \leq 0.01$, ANOVA.

Therefore, IgM^a surface positive (IgM^{a+}) B cells express the IgH^{MOG} knock-in allele. Almost all, and thereby significantly more, immature and mature B cells in the bone marrow of $Mb1^{cre/+}$ $Rc3h1^{F/F}$-$2^{F/F}$ IgH^{MOG} mice are IgM^{a+} compared to IgH^{MOG} control mice. In addition, there is near exclusive IgH^{MOG} usage also in splenic immature and mature B cells of the experimental mice. Interestingly, essentially all splenic and peritoneal cavity B1 cell populations in $Mb1^{cre/+}$ $Rc3h1^{F/F}$-$2^{F/F}$ IgH^{MOG} mice were found to use IgH^{MOG} which is significantly more as compared to IgH^{MOG} controls (Fig. 40, S15).
In summary, the bone marrow and peripheral B cell populations present in $Mb1^{cre/+}$ $Rc3h1^{F/F}$-$2^{F/F}$ IgH^{MOG}, which are absent in $Mb1^{cre/+}$ $Rc3h1^{F/F}$-$2^{F/F}$ mice, rely nearly exclusively on the IgH^{MOG} allele. Therefore, development of mature Roquin1/2-deficient B cells is only possible in the context of IgH^{MOG} expression and these cells nearly exclusively develop into B1b cells.

1.12 Intracellular Igμ levels are restored in bone marrow B cell populations, but Igκ expression is reduced in splenic B cells of $Mb1^{cre/+}$ $Rc3h1^{F/F}$-$2^{F/F}$ IgH^{MOG} mice

To analyse the expression of the inserted IgH^{MOG} heavy chain during B cell development, I investigated whether the IgH^{MOG} allele could restore proper intracellular expression of Igμ in the different bone marrow B cell populations. Additionally, I characterized light chain usage in bone marrow and splenic B cell subsets in these mice (Fig. 41). The cells numbers in populations defined by Igμ and λ5 expression in $Mb1^{cre/+}$ $Rc3h1^{F/F}$-$2^{F/F}$ IgH^{MOG} pro/pre B cells is not altered compared to respective IgH^{MOG} control cells with the exception of the number of $Igμ^-$ $λ5^-$ pro/pre B cells indicating that Roquin1/2-deficiency might accelerate transition through this developmental phase on a IgH^{MOG} background even further (Fig. 41). The percentages of intracellular $Igμ^+$ are significantly increased in all pro, pre and immature B cells populations investigated and match the level of relevant controls in mature recirculating B cells (Fig. 41B).

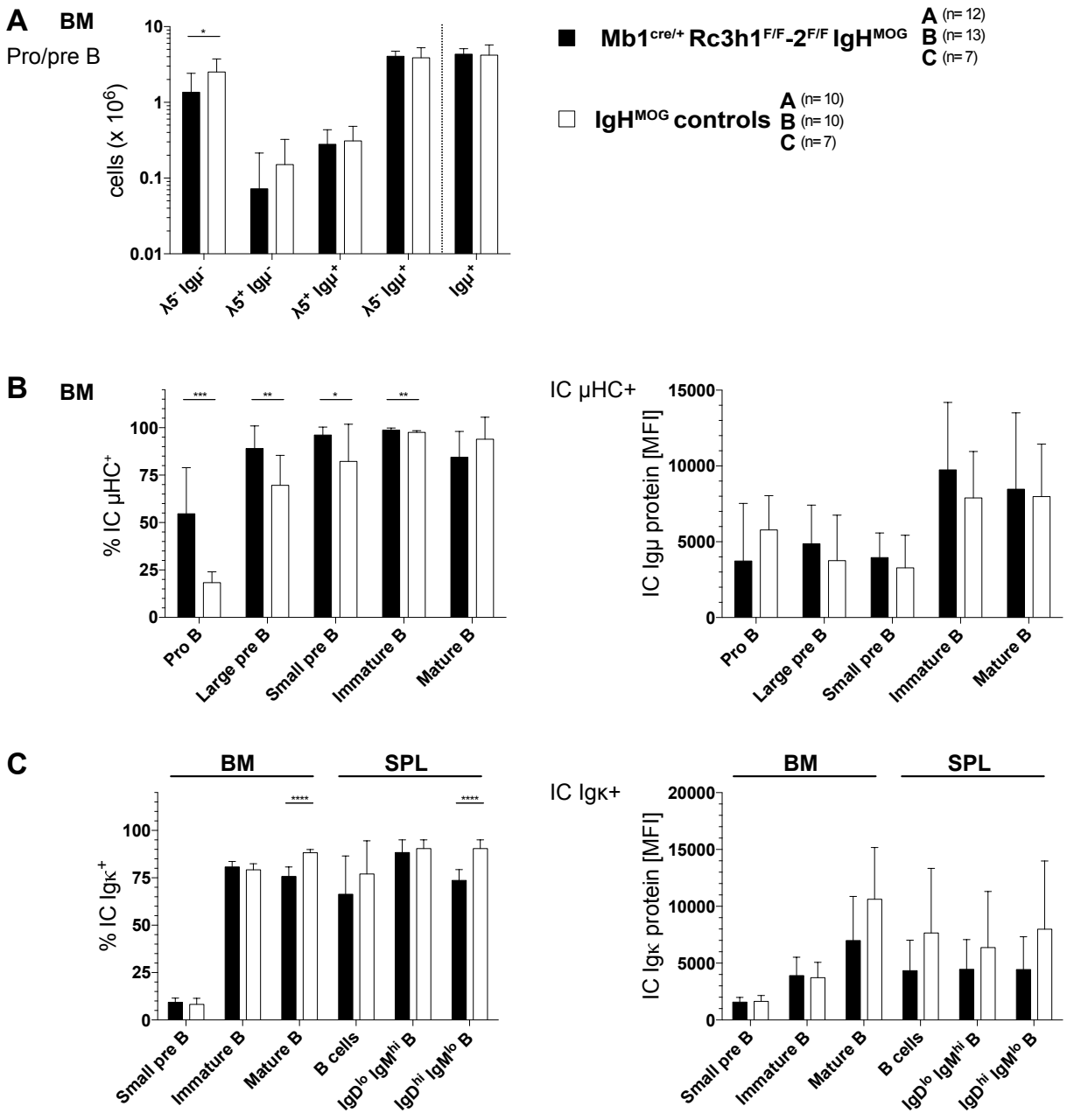

Figure 41: Analyses of intracellular expression of Igμ and Igκ in bone marrow and splenic B cell populations of Mb1$^{cre/+}$ Rc3h1$^{F/F}$-2$^{F/F}$ IgH^{MOG} and control mice.

(A) Bar chart depicting analysis of subsets of the pro/pre B cell compartment based on intracellular (IC) expression of μHC/Igμ and λ5. Igμ$^+$ marks total IC IgM$^+$ pro/pre B cells independent of IC λ5 as indicated by the dotted line. (B) Flow cytometric determination of percentage of μHC$^+$ bone marrow (BM) B cell populations (left) and Igμ protein levels in μHC$^+$ B cell populations (right). The antibody employed for IgM detection binds to Ig heavy (IgH) chain, thus detects expression of only IgH chain in pro and most pre B cells. (C) Flow cytometric determination of percentage of Igκ$^+$ BM and splenic (SPL) B cell populations (left) and Igκ protein levels in Igκ$^+$ B cell populations (right). μHC: μ heavy chain; Igμ: Intracellular IgM; IC: intracellular; MFI: median fluorescence intensity. Bars represent means and error bars standard deviation. ****p ≤ 0.0001, ***p ≤ 0.001, **p ≤ 0.01, *p ≤ 0.05, multiple t test with Holm-Sidak method applied.

Additionally, Igμ protein levels are unaltered in every μHC^{+} bone marrow B cell population of $Mb1^{cre/+}$ $Rc3h1^{F/F}$-$2^{F/F}$ IgH^{MOG} compared to IgH^{MOG} control mice. Remarkably, the percentage of intracellular $Ig\kappa^{+}$ splenic IgD^{hi} IgM^{lo} and mature recirculating bone marrow $Mb1^{cre/+}$ $Rc3h1^{F/F}$-$2^{F/F}$ IgH^{MOG} B cells are significantly reduced compared to IgH^{MOG} controls (Fig. 41C). Intracellular Igκ expression levels in $Ig\kappa^{+}$ bone marrow and splenic B cell populations are unaltered (Fig. 41C).

I further validated this result by flow cytometric analysis of cells expression Igκ and Igλ on their surface (Fig. S16). The percentage and total cell numbers of $Ig\kappa^{+}$ and $Ig\lambda^{+}$ immature B cells are not changed in $Mb1^{cre/+}$ $Rc3h1^{F/F}$-$2^{F/F}$ IgH^{MOG} compared to IgH^{MOG} controls. The percentage and total cell number of $Ig\kappa^{+}$ and $Ig\lambda^{+}$ mature recirculating B cells in the bone marrow (Fig. S16B) and splenic B cells (data not shown) of $Mb1^{cre/+}$ $Rc3h1^{F/F}$-$2^{F/F}$ IgH^{MOG} mice are significantly decreased. There is also no detectable change in the ratio of Igκ over Igλ usage between immature and mature B cells. This observation indicates that the deficiency of intracellular Igκ expression (Fig. 41C) does not originate from an exhaustion of the Igκ locus by light chain editing which would result in an increase of Igλ surface usage, but rather a general deficiency in light chain expression in $Mb1^{cre/+}$ $Rc3h1^{F/F}$-$2^{F/F}$ IgH^{MOG} mice.

In summary, the IgH^{MOG} allele restores expression of Igμ to at least control levels, yet tends to rush early pro B cells through development, while intracellular light chain expression is still impaired compared to controls in $Mb1^{cre/+}$ $Rc3h1^{F/F}$-$2^{F/F}$ IgH^{MOG} mice.

1.13 The rescue of pre B cell development in $Mb1^{cre/+}$ $Rc3h1^{F/F}$-$2^{F/F}$ IgH^{MOG} mice is reflected by rescued IL-7Rα and IRF4 expression, apoptosis and proliferation

To investigate the underlying reason for the rescued pre B cell compartment in $Mb1^{cre/+}$ $Rc3h1^{F/F}$-$2^{F/F}$ IgH^{MOG} mice, I performed analysis of IL-7Rα surface expression and proliferative capabilities of bone marrow B cells in these mice (Fig. 42). Remarkably, the percent of IL-$7R\alpha^{hi}$ pro and pre $Mb1^{cre/+}$ $Rc3h1^{F/F}$-$2^{F/F}$ IgH^{MOG} B cells are unchanged compared to IgH^{MOG} controls, but are significantly lower than control B cells (Fig. 42A). Likewise, IL-7Rα protein surface levels are almost 50% lower in the two IgH^{MOG} transgenic mouse strains compared to wild type controls (Fig. 42B). Moreover, IL-$7R\alpha^{hi}$ cell numbers of the pro, pre and immature B cell subset are strongly reduced in IgH^{MOG} transgenic Roquin1/2 deficient and control mice compared to wild type controls (Fig. 42C).

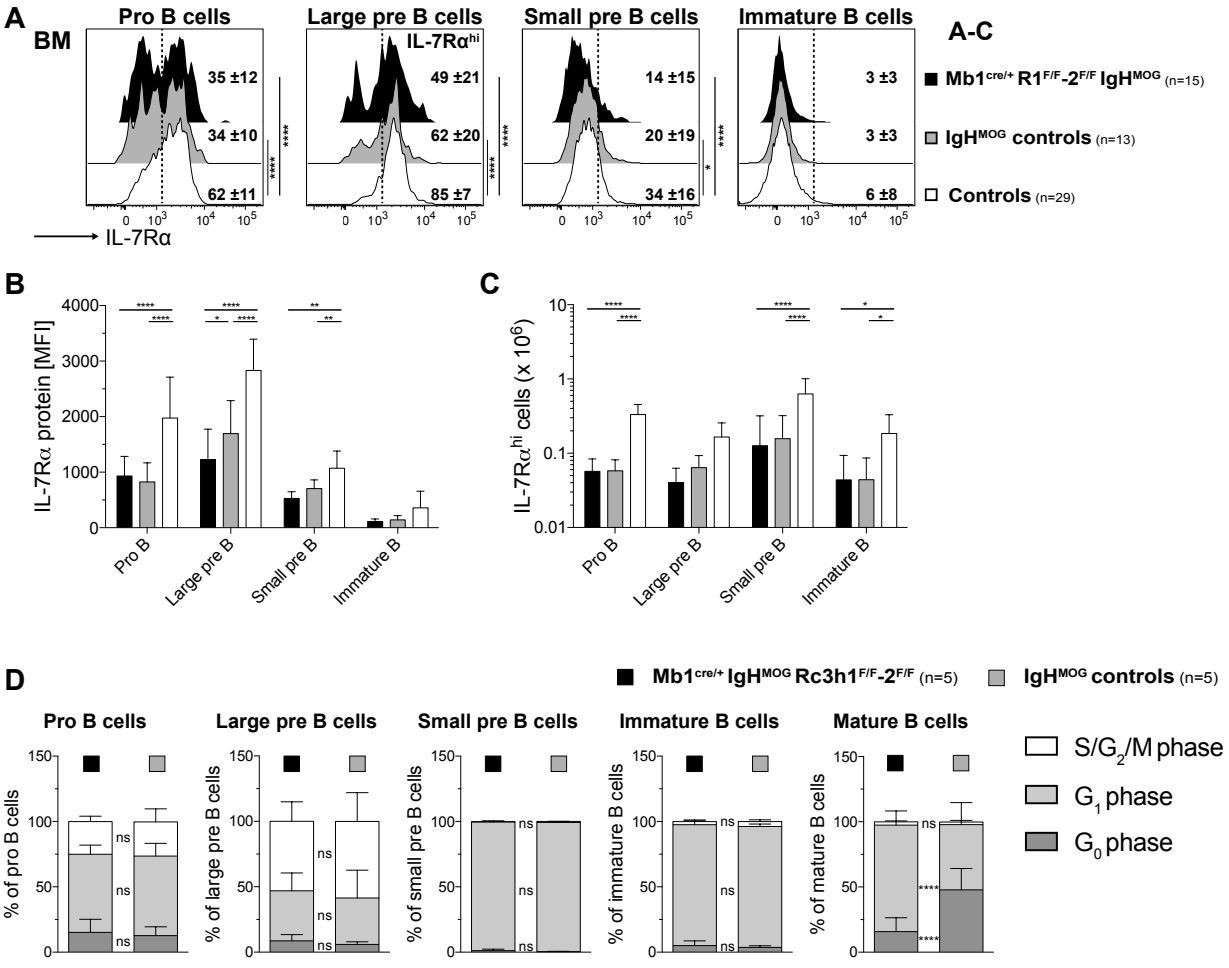

Figure 42: IgH^{MOG} transgenic Roquin1/2-deficient and control pro and pre B cells develop independent of IL-R7α-driven proliferation.

Data on IL-7Rα expression in control B cell populations contains data shown in Fig. 19 to allow comparison of IL-7Rα in IgH^{MOG} transgenic B cells compared to wild type controls. (A) Representative cytometry histograms illustrating surface IL-7Rα expression on indicated bone marrow (BM) B cell populations. Percentages of cells expressing high levels of IL-Rα (IL-7Rα^{hi}), based on IL-7Rα expression on large pre B cells, are indicated. Mean percentages with standard deviation and significances are indicated. (B) Bar chart representation of IL-7Rα protein expression on the surface of indicated bone marrow (BM) B cell populations. (C) Total number of IL-7Rα^{hi} cells in the indicated BM cell populations. (D) Quantification of percentages of designated B cell populations in different cell cycle phases. Cell cycle phases were distinguished as in Fig. 28, briefly: G_0 phase (dark grey) Ki67$^-$ DRAQ5^{lo}; G_1 phase (light grey) Ki67$^+$ DRAQ5^{lo}; S/G_2/M phase (white) Ki67$^+$ DRAQ5^{hi}. Flow cytometric analysis was performed as in Fig. 28. Gated B cell subsets: pro B B220^{lo} c-kit$^+$ CD25$^-$ IgD$^-$ IgM$^-$; large pre B B220^{lo} c-kit$^-$ CD25$^+$ IgD$^-$ IgM$^-$ FSC^{hi}; small pre B B220^{lo} c-kit$^-$ CD25$^+$ IgD$^-$ IgM$^-$ FSC^{lo}; immature B B220^{int} IgM$^+$; Bars represent means and error bars standard deviation. BM: bone marrow; MFI: median fluorescence intensity. ****p ≤ 0.0001, **p ≤ 0.01, *p ≤ 0.05, (A-C) 2way ANOVA with Tukey test applied; (D) unpaired t test, ns: non significant.

The IL-7Rα data (Fig. 42A-42C) indicated that presence of the IgH^{MOG} allele renders pro and pre B cells independent of IL-7Rα mediated proliferation. To corroborate the finding, I performed cell cycle analysis of bone marrow B cells to investigate their proliferative capabilites (Fig. 42D). Remarkably, the percentage of large pre B cells of IgH^{MOG} and Mb1$^{cre/+}$ Rc3h1$^{F/F}$-2$^{F/F}$ mice in the proliferative S/G_2/M phase are approximately 50%, similar

to Roquin1/2-deficient large pre B cells (Fig. 28). Importantly, no pronounced difference in proliferation was observed in *ex vivo* isolated cells in pro to immature B cell stages between the $Mb1^{cre/+}$ $Rc3h1^{F/F}$-$2^{F/F}$ IgH^{MOG} and the IgH^{MOG} control strain (Fig. 42D). Interestingly, as was observed before in the few detected Roquin1/2-deficient mature recirculating B cells (Fig. 28), the ratio of cells in G_0 phase is also significantly lower in mature B cells of $Mb1^{cre/+}$ $Rc3h1^{F/F}$-$2^{F/F}$ IgH^{MOG} mice (Fig. 42D). Therefore, IgH^{MOG} Roquin1/2-deficient and control transgenic pro and pre B cells appear to develop largely autonomous of IL-7Rα-mediated proliferation. Next, I monitored IRF4, Aiolos and ZAP70 expression and apoptosis in experimental and control IgH^{MOG} mice, to assess whether the observed differences are a direct consequence of Roquin1/2-deficiency or more indirectly connected to the block in B cell development. I quantified intracellular IRF4 expression, which is essential for light chain expression in B cells (Fig. 43A-43C) [264]. In contrast to $Mb1^{cre/+}$ $Rc3h1^{F/F}$-$2^{F/F}$ mice, percentage of $IRF4^{hi}$ cells and IRF4 levels in $Mb1^{cre/+}$ $Rc3h1^{F/F}$-$2^{F/F}$ IgH^{MOG} mice do not decrease in large pre B cells compared to relevant IgH^{MOG} controls, which correlates with the rescued numbers of large pre B cells. As shown before, IRF4 levels in immature B cells of the $Mb1^{cre/+}$ $Rc3h1^{F/F}$-$2^{F/F}$ IgH^{MOG} genotype are not increased, further underlining a general IRF4 independent defect in expression of Ig light chain as opposed to ongoing receptor editing similar to the explanation for the lower intracellular Igκ levels in mature B cells (Fig. 41). In addition, the observed developmental impairment of B cells in $Mb1^{cre/+}$ $Rc3h1^{F/F}$-$2^{F/F}$ IgH^{MOG} mice appears to be independent of Aiolos, since percentages of $Aiolos^{hi}$ bone marrow B cells and Aiolos levels in $Aiolos^{hi}$ bone marrow B cells of these mice resemble that of IgH^{MOG} controls (Fig. 43D-43F). Similar data were obtained for BCL6 (data not shown). Interestingly, ZAP70 intracellular expression is increased in mature B cells of the experimental $Mb1^{cre/+}$ $Rc3h1^{F/F}$-$2^{F/F}$ IgH^{MOG} mice (Fig. 43G), similar as in pro/pre and immature B cells of $Mb1^{cre/+}$ $Rc3h1^{F/F}$-$2^{F/F}$ (Fig. 24). As ZAP70 protein levels decline during development, this could reflect defective maturation of Roquin1/2-deficient IgH^{MOG} immature and mature B cells. This deregulated ZAP70 expression unlikely stems from mature B1, as preliminary data did not indicate increased cell numbers of B1 cells in the bone marrow of $Mb1^{cre/+}$ $Rc3h1^{F/F}$-$2^{F/F}$ IgH^{MOG} mice (data not shown).

Furthermore, it is unlikely that increased apoptosis has a major role in the reduced immature B cell numbers in $Mb1^{cre/+}$ $Rc3h1^{F/F}$-$2^{F/F}$ IgH^{MOG} mice, as the proportion of viable *ex vivo* isolated immature B cells in these mice is only slightly reduced (Fig. S17) and in general not affected in other bone marrow B cell populations.

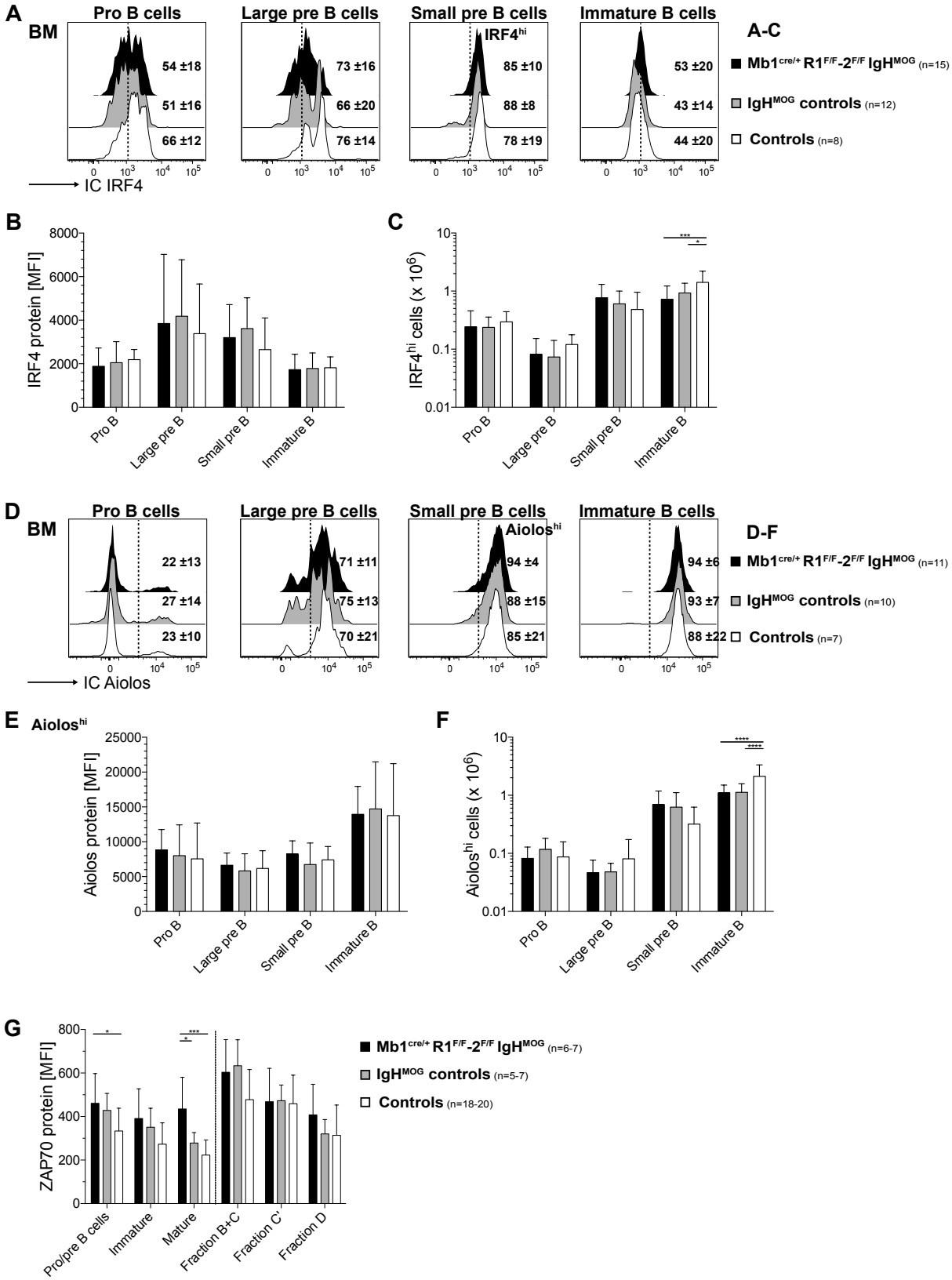

Figure 43: Analysis of intracellular levels of Aiolos, IRF4 and ZAP70 in bone marrow B cell populations of Mb1$^{cre/+}$ Rc3h1$^{F/F}$-2$^{F/F}$ IgH^{MOG} mice.

(A) Representative flow cytometry histograms of stated bone marrow (BM) B cell populations illustrating intracellular (IC) IRF4 expression in indicated BM B cell subset and mean percentage with standard deviation of cells expressing high intracellular levels of IRF4 (IRF4^{hi} cells) based on IRF4 expression in small pre B cells. *(Continued on next page)*

(B) Bar chart representation of IC IRF4 protein levels in respective B cell subset, as determined by flow cytometry. (C) Total numbers of IRF4^{hi} BM B cells in indicated subsets. (D) Representative flow cytometry histograms of stated bone marrow (BM) B cell populations illustrating intracellular (IC) Aiolos expression in indicated BM B cell subset and mean percentage with standard deviation of cells expressing high intracellular levels of Aiolos (Aiolos^{hi} cells). Aiolos^{hi} cell determination is based on Aiolos expression in small pre B cells. (E) Bar chart representation of IC Aiolos protein levels in Aiolos^{hi} cells of respective B cell subset, as determined by flow cytometry. (F) Total numbers of Aiolos^{hi} BM B cells in indicated subsets. (G) Bar chart representation of IC expression levels ZAP70 as determined by flow cytometry on indicated BM B cell populations, data used for wild type controls include data employed in controls of Fig. 24 to allow comparison to wild type controls. Gated B cell subsets: Gated B cell subsets: pro/pre B B220^{lo} IgM^{-}, pro B B220^{lo} c-kit^{+} CD25^{-} IgD^{-} IgM^{-}; large pre B B220^{lo} c-kit^{-} CD25^{+} IgD^{-} IgM^{-} FSC^{hi}; small pre B B220^{lo} c-kit^{-} CD25^{+} IgD^{-} IgM^{-} FSC^{lo}; immature B B220^{int} IgD^{-} IgM^{+} (D-F)/B220^{int} IgM^{-} (A-C&G), mature B B220^{+} IgD^{+} (D-F)/ B220^{+} IgM^{+} (A-C&G), Fraction B+C B220^{+} CD43^{+} CD24^{-}; Fraction C' B220^{+} CD43^{+} CD24^{+}; Fraction D B220^{+} CD43^{-} CD19^{+} IgM^{-}; Bars represent means and error bars standard deviation. R: Rc3h; IC: intracellular; BM: bone marrow; MFI: median fluorescence intensity. Bars represent mean values and error bars standard deviation. ****p ≤ 0.0001, ***p ≤ 0.001, *p ≤ 0.05, 2way ANOVA with Tukey test applied.

Approximately 75% of immature B cells were classified as viable in Mb1$^{cre/+}$ Rc3h1$^{F/F}$-2$^{F/F}$ IgH^{MOG} mice, while this was the case for only 50% of the even lower immature B cells numbers in the Mb1$^{cre/+}$ Rc3h1$^{F/F}$-2$^{F/F}$ strain (Fig. 27). In the Mb1$^{cre/+}$ Rc3h1$^{F/F}$-2$^{F/F}$ IgH^{MOG} mouse strain, intracellular Bim levels are also not changed in any bone marrow B cell subset compared to IgH^{MOG} controls (data not shown).

Taken together, the IgH^{MOG} insertion rescues nearly all aspects of Roquin1/2-deficient B cell development up to the immature B cell stage, which are independent of IL-7R signaling and proliferation, such as IRF4 and Aiolos protein levels or apoptotic cell death. The IgH^{MOG} allele, appears to render developing pro and pre B cells largely independent of IL-7R-mediated proliferation. This likely allows Roquin1/2-deficient IgH^{MOG} transgenic pro and pre B cells to develop into small and immature pre B cells, despite their impairment in IL-7R signaling, such as upregulation of IL-7Rα protein levels and proliferation.

1.14 Expansion of T cells but not myeloid cells in the Mb1$^{cre/+}$ Rc3h1$^{F/F}$-2$^{F/F}$ IgH^{MOG} mouse line

Since the spleens of Mb1$^{cre/+}$ Rc3h1$^{F/F}$-2$^{F/F}$ IgH^{MOG} mice are significantly heavier than control spleens and splenocyte numbers in these mice are not altered, despite a significant reduction of B cell numbers, I investigated cell-extrinsic effects of Roquin1/2-deficient B cells on the T cell and myeloid cell compartments in the spleen. There is a general increase of the splenic T cell compartment, including CD4^{+}, CD8^{+} and also double negative subsets (data not shown), in percentage and total cell number (Fig. S18A) Moreover, the T_{reg}-containing pool of CD4^{+} CD25^{+} T cells, the CD69^{+} activated T cell subset and CD4^{+} and CD8^{+} naive, effector

memory-like and central memory-like subsets are increased in percent (Fig. S18B) and thus also in cell numbers (data not shown) in this strain. However, there is no change in percentage or total cell number (data not shown) of myeloid cell populations, except for the $Gr1^+$ monocyte and macrophage population, which is also increased in $Mb1^{cre/+}$ $Rc3h1^{F/F}$-$2^{F/F}$ IgH^{MOG} mice (Fig. S19). Hence, the splenic B cells of $Mb1^{cre/+}$ $Rc3h1^{F/F}$-$2^{F/F}$ IgH^{MOG} mice appear to unspecifically increase the entire T cell compartment, but lack effects on myeloid cells, that were observed in $Mb1^{cre/+}$ $Rc3h1^{F/F}$-$2^{F/F}$ mice.

1.15 The developmental arrest in Roquin1/2-deficient bone marrow B cells is largely independent of Ig heavy and light chain rearrangements

In light of the striking defects in Ig light chain (IgL) expression in splenic B cells of $Mb1^{cre/+}$ $Rc3h1^{F/F}$-$2^{F/F}$ mice and the developmental impairment in bone marrow B cells of this strain, I aimed at investigating if Roquin1 and 2 might play a role in IgL somatic rearrangement or expression and if this might be the cause of the developmental arrest of Roquin1/2-deficient B cells following the late pro B cell stage. The near absence of IgL chain expression in pro/pre B cells and the strong reduction of intracellular $Ig\kappa^+$ immature B cells in Roquin1/2-deficient B cells (Fig. 17) indicated either an inability to undergo somatic rearrangement of the IgL loci or a severe block in differentiation before Igκ recombination. Noteably, there are a significant number of Roquin1/2-deficient pro/pre B cells, which express μHC (Fig. 15, 16). To accomplish this goal, I employed the $IgL^{D23\kappa}$ light chain knock-in allele [28, 243] to generate $Mb1^{cre/+}$ $Rc3h1^{F/F}$-$2^{F/F}$ $IgL^{D23\kappa}$ and $Mb1^{cre/+}$ $Rc3h1^{F/F}$-$2^{F/F}$ IgH^{MOG} $IgL^{D23\kappa}$ mice. The combination of these strains allows analyzing if Roquin1/2-deficiency results in a developmental arrest due to defects in rearrangement of heavy and light chain, light chain alone or a yet unknown defect independent of somatic rearrangement.

The overall bone marrow cell count is not altered in any of the above mice compared to controls (data not shown). Strikingly, expression of the D23κ light chain did not lead to any rescue in the development of small pre B, immature and mature B cells in Roquin1/2-deficiency compared to controls (Fig. 44A, 44B, S20), indicating that lack of IgL chain expression is not the cause of the developmental defect. Furthermore, percentage and total cell numbers of immature and mature recirculating B cells are significantly reduced in $Mb1^{cre/+}$ $Rc3h1^{F/F}$-$2^{F/F}$ IgH^{MOG} $IgL^{D23\kappa}$ mice compared to IgH^{MOG} $IgL^{D23\kappa}$ controls (Fig. 44A, 44B). The bone marrow B cell compartments of $Mb1^{cre/+}$ $Rc3h1^{F/F}$-$2^{F/F}$ IgH^{MOG} $IgL^{D23\kappa}$ and $Mb1^{cre/+}$ $Rc3h1^{F/F}$-$2^{F/F}$ IgH^{MOG} mice appear very similar with regard to immature and mature

B cell pools, except that there is an approximately twofold increase in immature B cell numbers in the heavy and light chain insertion mice compared to the heavy chain only insertion mice (Fig. 34, 44). This may for instrance result from either more efficient pairing of IgH^{MOG} μHC to the D23κ IgL chain in contrast to paring of IgH^{MOG} to recombined endogenous IgL chain or of an even further accelerated transition through bone marrow B cell development leading to more B cells that have incomplete Roquin1 or 2 ablation. This might more likely be an indication for an enhanced formation of functional, innoccuous BCRs on immature B cells of $Mb1^{cre/+}$ $Rc3h1^{F/F}$-$2^{F/F}$ IgH^{MOG} $IgL^{D23κ}$ mice as also the number of immature IgH^{MOG} $IgL^{D23κ}$ control B cells is almost 2.5fold higher than that of IgH^{MOG} control B cells (Fig. 34, 44).

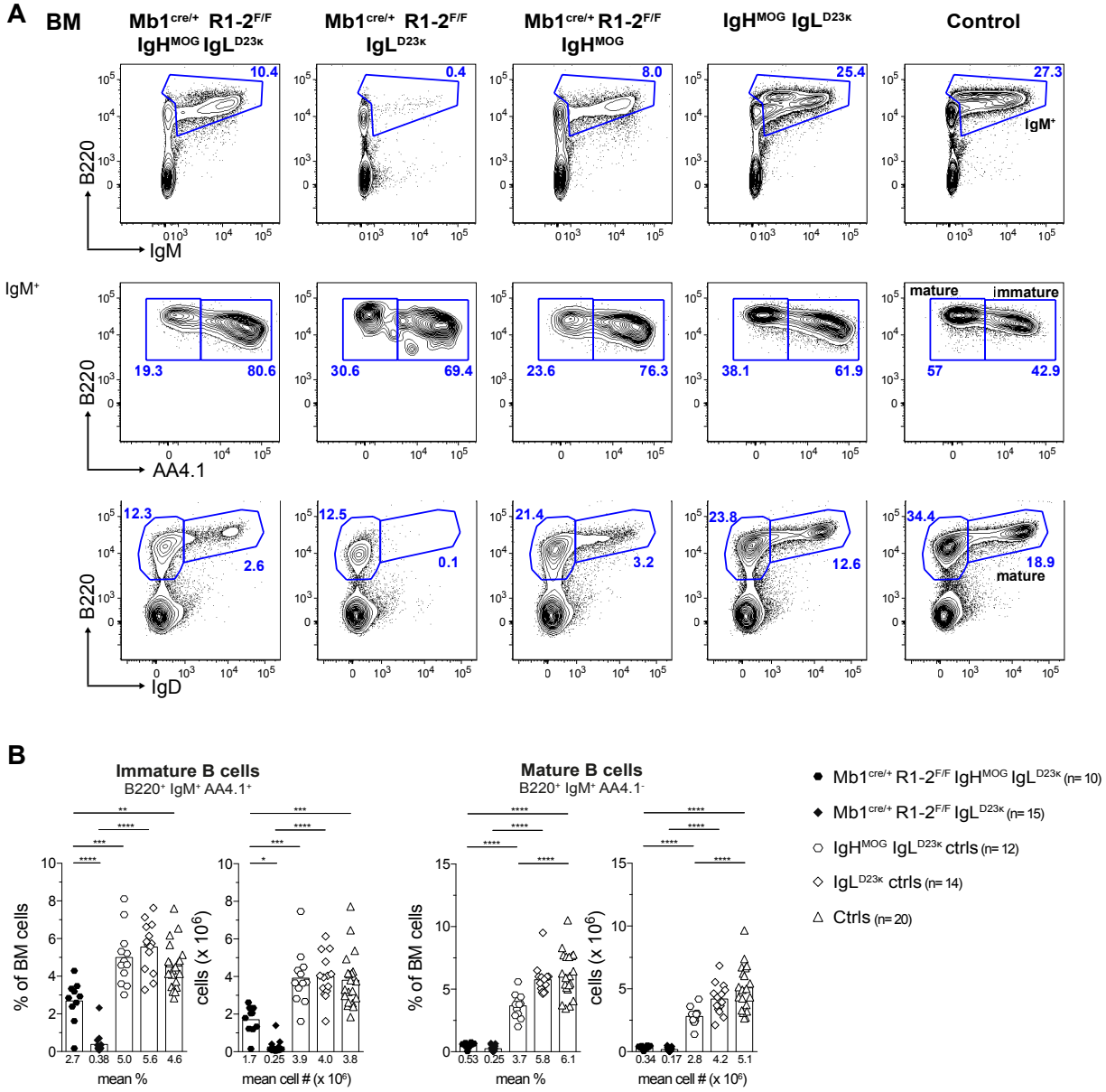

Figure 44: Immature and mature bone marrow B cell populations in Mb1$^{cre/+}$ Rc3h1-2$^{F/F}$ IgH^{MOG} IgL^{D23κ} and Mb1$^{cre/+}$ Rc3h1-2$^{F/F}$ IgL^{D23κ} mice.

(A) Representative flow cytometry plots illustrating the gating strategy for bone marrow (BM) B cells and highlighting the similarity of B cell populations of Mb1$^{cre/+}$ IgH^{MOG} IgL^{D23κ} R1-2$^{F/F}$ with those of Mb1$^{cre/+}$ R1-2$^{F/F}$ IgH^{MOG} mice, R: Rc3h. (B) Percentages of respective B cell subsets of total BM cells and total subset cell numbers as determined by flow cytometry. The genotypes represented in the bar charts differ from (A). Ctrls: controls; R: Rc3h. Numbers below graphs and bars show mean values. ****p ≤ 0.0001, ***p ≤ 0.001, **p ≤ 0.01, *p ≤ 0.05, ANOVA. Significances for Mb1$^{cre/+}$ R1-2$^{F/F}$ IgH^{MOG} IgL^{D23κ} and IgH^{MOG} IgL^{D23κ} ctrls versus IgL^{D23κ} ctrls and Mb1$^{cre/+}$ R1-2$^{F/F}$ IgL^{D23κ} versus IgH^{MOG} IgL^{D23κ} ctrls and ctrls are not shown.

The presence of pre-rearranged heavy and light chains essentially leads to skipping of pro and pre B cell stages in Mb1$^{cre/+}$ Rc3h1$^{F/F}$-2$^{F/F}$ IgH^{MOG} IgL^{D23κ} and IgH^{MOG} IgL^{D23κ} mice alike, as indicated by the significantl lower cell numbers of pro and pre B cells from both strains compared to controls, which is not observed in Mb1$^{cre/+}$ Rc3h1$^{F/F}$-2$^{F/F}$ IgH^{MOG} mice (Fig. S20, 34).

Likewise, the presence of a pre-rearranged light chain in pre B cells of the $Mb1^{cre/+}$ $Rc3h1^{F/F}$-$2^{F/F}$ $IgL^{D23\kappa}$ mouse line or the $IgL^{D23\kappa}$ control genotype significantly reduces the number of pre B cells in comparison to those of controls. The total cell number of pre B cells in $Mb1^{cre/+}$ $Rc3h1^{F/F}$-$2^{F/F}$ $IgL^{D23\kappa}$ mice compared to $IgL^{D23\kappa}$ controls is significantly reduced, suggesting the presence of a developmental block in the pre B cell stages, as aforementioned.

Next, I analyzed peripheral B cell subsets in these experimental mice. Interestingly, $Mb1^{cre/+}$ $Rc3h1^{F/F}$-$2^{F/F}$ IgH^{MOG} $IgL^{D23\kappa}$ mice have significantly enlarged spleens and increased splenocyte counts (Fig. S21A). Yet the percentage and number of total splenic B cells is significantly reduced in the $Mb1^{cre/+}$ $Rc3h1^{F/F}$-$2^{F/F}$ IgH^{MOG} $IgL^{D23\kappa}$ strain compared to IgH^{MOG} $IgL^{D23\kappa}$ mice, emanating from immense reduction of percentage and cell number of mature splenic B cells (Fig. S21, data not shown). This is reminiscent of the phenotype observed in the spleens of $Mb1^{cre/+}$ $Rc3h1^{F/F}$-$2^{F/F}$ IgH^{MOG} mice (Fig. 35, 38). However, the difference in cell numbers determined for mature B $Mb1^{cre/+}$ $Rc3h1^{F/F}$-$2^{F/F}$ IgH^{MOG} $IgL^{D23\kappa}$ B cells based on AA4.1 is only twofold that determined by IgD^{hi} IgM^{lo} staining (Fig. S21), indicating that the described splenic B1b expasion in $Mb1^{cre/+}$ $Rc3h1^{F/F}$-$2^{F/F}$ IgH^{MOG} mice is reduced by expression of the D23κ light chain.

Likewise, in $Mb1^{cre/+}$ $Rc3h1^{F/F}$-$2^{F/F}$ IgH^{MOG} $IgL^{D23\kappa}$ mice, transitional/immature B cell numbers decline strongly from T1 to T2 stage as in $Mb1^{cre/+}$ $Rc3h1^{F/F}$-$2^{F/F}$ IgH^{MOG} mice (Fig. 36, S22) Moreover, the mature splenic B cell compartment in the $Mb1^{cre/+}$ $Rc3h1^{F/F}$-$2^{F/F}$ IgH^{MOG} $IgL^{D23\kappa}$ mouse strain resembles that of $Mb1^{cre/+}$ $Rc3h1^{F/F}$-$2^{F/F}$ IgH^{MOG} mice (Fig. S14) with regard to the absence of germinal center B cells in spleen (Fig. S22), mesenteric lymph nodes and Peyer's patches (data not shown). In addition, as in the $Mb1^{cre/+}$ $Rc3h1^{F/F}$-$2^{F/F}$ IgH^{MOG} strain, B1b cell percentage and total cell numbers in spleen and peritoneal cavity of $Mb1^{cre/+}$ $Rc3h1^{F/F}$-$2^{F/F}$ IgH^{MOG} $IgL^{D23\kappa}$ mice are rescued, while B1a cells are not rescued (Fig. S23), resembling the phenotype of $Mb1^{cre/+}$ $Rc3h1^{F/F}$-$2^{F/F}$ IgH^{MOG} mice. However, the B1b cell expansion is not as pronounced in the Roquin1/2-deficient heavy and light chain insertion B lineage compared to the heavy chain insertion B lineage only (Fig. 39). This indicates that other light chains than D23κ favor B1b cell development in combination with IgH^{MOG}.

Total splenocytes and splenic B cells in $Mb1^{cre/+}$ $Rc3h1^{F/F}$-$2^{F/F}$ $IgL^{D23\kappa}$ mice recapitulate the observations made in the $Mb1^{cre/+}$ $Rc3h1^{F/F}$-$2^{F/F}$ mouse strain (Fig. 44, S21-S23, data not shown). Similarly, there are no splenic or peritoneal cavity B1 cells in $Mb1^{cre/+}$ $Rc3h1^{F/F}$-$2^{F/F}$ $IgL^{D23\kappa}$ mice (Fig. S23). In conclusion, it appears that a pre-rearranged heavy and light chain, despite further increasing the number of immature bone marrow B cells in $Mb1^{cre/+}$ $Rc3h1^{F/F}$-$2^{F/F}$ IgH^{MOG} $IgL^{D23\kappa}$ mice do not rescue B cell development to wild type levels as the number

of mature recirculating B cells is still dramatically decreased (Fig. 44). Furthermore, splenic and GALT B cell populations are not reconstituted, more pronouncedly in this mouse line than in the $Mb1^{cre/+}$ $Rc3h1^{F/F}$-$2^{F/F}$ IgH^{MOG} genotype with a very strong developmental hindrance from transitional T1 to T2 stage.

Taken together with the data obtained in the $Mb1^{cre/+}$ $Rc3h1^{F/F}$-$2^{F/F}$ $IgL^{D23\kappa}$ strain, the developmental arrest in $Mb1^{cre/+}$ $Rc3h1^{F/F}$-$2^{F/F}$ mice appears to be independent of somatic rearrangement of Ig heavy and light chain provided that μHC (from the IgH^{MOG} allele) and Igκ (from the $IgL^{D23\kappa}$ allele) are correctly expressed and can efficiently pair in $Mb1^{cre/+}$ $Rc3h1^{F/F}$-$2^{F/F}$ IgH^{MOG} $IgL^{D23\kappa}$ mice.

1.16 Igκ light chain is expressed in B cells of $IgL^{D23\kappa}$ transgenic mice and can pair with IgH^{MOG}

The decreased cell numbers and percentages of pre B cells in $IgL^{D23\kappa}$ control mice compared to wild type controls suggest that a majority of developing pre B cells in $IgL^{D23\kappa}$ transgenic mice bypasses this developmental step by expressing the pre-rearranged Igκ light chain. Moreover, it remained possible that the observed reduced percentages of μHC^{+} pro/pre B cells and the respective reduction in $\lambda5^{-}$ $Ig\kappa^{+}$ pro/pre B cells of $Mb1^{cre/+}$ $Rc3h1^{F/F}$-$2^{F/F}$ mice stem from a defect in light chain expression (Fig. 15, 16). To answer these questions, Igμ and Igκ intracellular expression was quantified in bone marrow and splenic B cell subsets in the $Mb1^{cre/+}$ $Rc3h1^{F/F}$-$2^{F/F}$ $IgL^{D23\kappa}$ and $IgL^{D23\kappa}$ strains (Fig. 45) Interestingly, an intracellular $\lambda5^{+}$ $Ig\kappa^{+}$ pro/pre B cell subset is clearly distinguishable in $Mb1^{cre/+}$ $Rc3h1^{F/F}$-$2^{F/F}$ $IgL^{D23\kappa}$ mice (Fig. 45A). The percentage of this population is significantly increased in $Mb1^{cre/+}$ $Rc3h1^{F/F}$-$2^{F/F}$ $IgL^{D23\kappa}$ mice compared to $IgL^{D23\kappa}$ controls (Fig. 45B). In contrast, the intracellular $\lambda5^{-}$ $Ig\kappa^{+}$ pro/pre B cell population is significantly reduced in $Mb1^{cre/+}$ $Rc3h1^{F/F}$-$2^{F/F}$ $IgL^{D23\kappa}$ mice (Fig. 45B). The overall proportion of intracellular $Ig\kappa^{+}$ pro/pre B cells is not altered between $Mb1^{cre/+}$ $Rc3h1^{F/F}$-$2^{F/F}$ $IgL^{D23\kappa}$ and $IgL^{D23\kappa}$ control mice. Therefore, there is a clear block at the $\lambda5^{+}$ $Ig\kappa^{+}$ to $\lambda5^{-}$ $Ig\kappa^{+}$ transition in absence of Roquin1/2 proteins in D23κ light chain insertion mice. It is noteworthy that intracellular Igμ expression is significantly reduced in $\lambda5^{+}$ $Ig\kappa^{+}$ pro/pre B cells of $Mb1^{cre/+}$ $Rc3h1^{F/F}$-$2^{F/F}$ $IgL^{D23\kappa}$ compared to the relevant $IgL^{D23\kappa}$ controls (Fig. 45C).

Moreover, I quantified intracellular Igκ expression in $Ig\kappa^{+}$ bone marrow and splenic B cell populations (Fig. 45D, 45E). The percentage of $Ig\kappa^{+}$ and the intracellular Igκ levels are not altered in pre to immature bone marrow B cell populations of $Mb1^{cre/+}$ $Rc3h1^{F/F}$-$2^{F/F}$ $IgL^{D23\kappa}$

compared to $IgL^{D23\kappa}$ mice (Fig. 45D, 45E), but both are significantly decreased in the few generated mature recirculating bone marrow B cells and mature splenic IgD^{hi} IgM^{lo} B cells (Fig. 45D, 45E). This demonstrates that despite presence of Igκ light chain, Igμ heavy chain levels are reduced. Hence the reduction in Igμ heavy chain levels observed in pre B cells of $Mb1^{cre/+}$ $Rc3h1^{F/F}$-$2^{F/F}$ mice is unlikely caused by destabilization of Igμ protein resulting from absence of IgL chain protein for binding.

I performed identical analyses in $Mb1^{cre/+}$ $Rc3h1^{F/F}$-$2^{F/F}$ IgH^{MOG} $IgL^{D23\kappa}$ mice in which the $\lambda5^+$ $Ig\kappa^+$ pro/pre B subset is clearly distinguishable (Fig. 46), yet remarkably reduced compared to $Mb1^{cre/+}$ $Rc3h1^{F/F}$-$2^{F/F}$ $IgL^{D23\kappa}$ mice. Furthermore, as stated before for $Mb1^{cre/+}$ $Rc3h1^{F/F}$-$2^{F/F}$ $IgL^{D23\kappa}$ mice, the ratio of $\lambda5^-$ $Ig\kappa^+$ pro/pre B is reduced compared to IgH^{MOG} $IgL^{D23\kappa}$ controls (Fig. 46A, 46B). It is noteworthy that intracellular expression levels of Igμ in the $\lambda5^+$ $Ig\kappa^+$ as well as the $\lambda5^+$ $Ig\kappa^+$ pro/pre B cell populations tends to be even increased in experimental mice (Fig. 46C) as well as in all bone marrow B cell populations of the $Mb1^{cre/+}$ $Rc3h1^{F/F}$-$2^{F/F}$ IgH^{MOG} $IgL^{D23\kappa}$ mouse strain (data not shown). Quantification of intracellular Igκ in $Ig\kappa^+$ bone marrow and splenic B cell populations of these mice yielded a result similar to the analysis in $Mb1^{cre/+}$ $Rc3h1^{F/F}$-$2^{F/F}$ $IgL^{D23\kappa}$ mice, except that differences in percent of $Ig\kappa^+$ cells and Igκ levels in these cells in splenic IgD^{hi} IgM^{lo} B cells and mature recirculating bone marrow B cells of $Mb1^{cre/+}$ $Rc3h1^{F/F}$-$2^{F/F}$ IgH^{MOG} $IgL^{D23\kappa}$ are less pronounced (Fig. 46D, 46E).

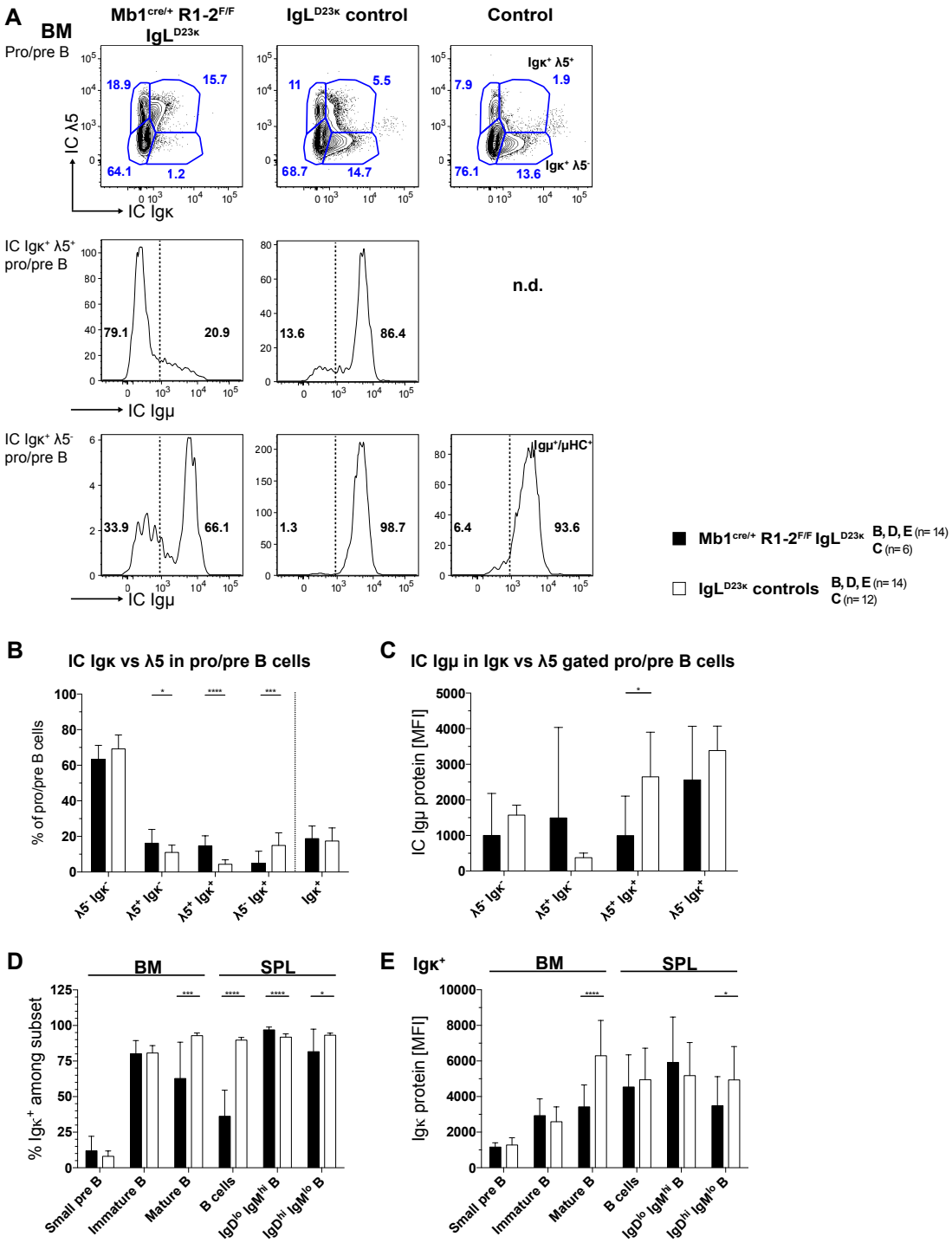

Figure 45: Analysis of intracellullar Igμ and Igκ expression in bone marrow and splenic B cell subsets of Mb1$^{cre/+}$ Rc3h1-2$^{F/F}$ IgL^{D23κ} mice.

(A) Representative flow cytometry plots illustrating the gating strategies for pro/pre (B220^{lo} IgD^{-} IgM^{-}) B cells. (B) Bar chart depicting analysis of the pro/pre B cell compartment based on IC expression of Igκ and λ5. Igκ^{+} marks percentage of IC Igκ^{+} pro/pre B cells independent of IC λ5 expression. (C) Flow cytometric determination of IC protein expression of μHC/Igμ in the discriminated (B) pro/pre B cell subset. (D) Determination of percentage of IC Igκ^{+} among stated BM (left) or SPL (right) B cell populations as analyzed by flow cytometry and (E) IC Igκ protein levels in these Igκ^{+} cells. Gated B cell subsets: small pre B B220^{lo} c-kit^{-} CD25^{+} IgD^{-} IgM^{-} FSC^{lo}; immature B B220^{int} IgD^{-} IgM^{+}, mature B B220^{+} IgD^{+}, B cells B220^{+}, IgD^{lo} IgM^{hi} and IgD^{hi} IgM^{lo} B cells. R: Rc3h; Igμ: intracellular IgM; IC: intracellular; n.d.: not depicted; MFI: median fluorescence intensity; BM: bone marrow; SPL: spleen. Bars represent means and error bars standard deviation. ****p ≤ 0.0001, ***p ≤ 0.001, *p ≤ 0.05, multiple t tests with Holm-Sidak method applied.

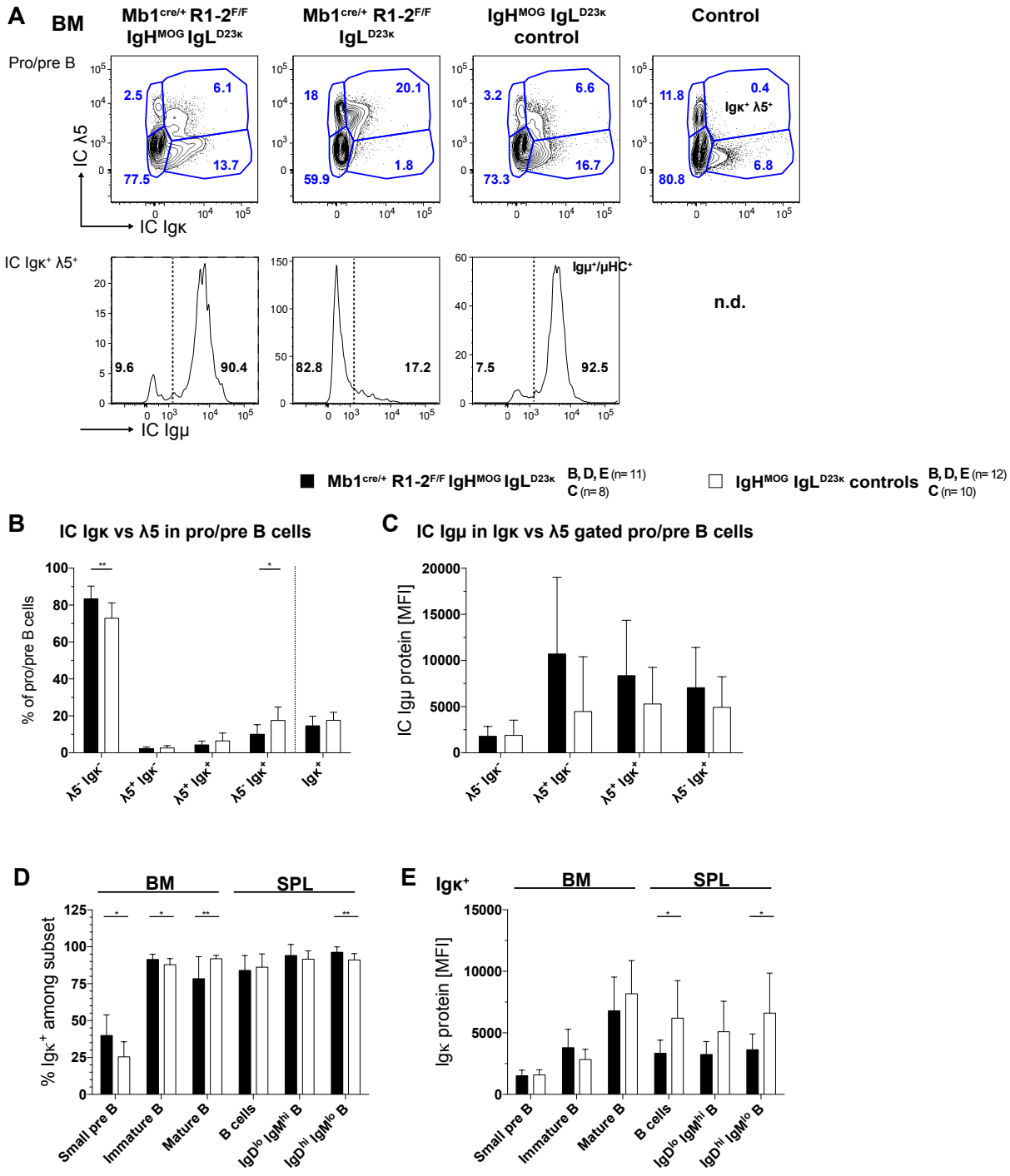

Figure 46: Analysis of intracellular Igμ and Igκ expression in bone marrow and splenic B cell subsets of Mb1$^{cre/+}$ Rc3h1-2$^{F/F}$ IgH^{MOG} IgL^{D23κ} mice.

Similar analysis performed as in Fig. 45. (A) Representative flow cytometry plots illustrating the gating for pro/pre (B220^{lo} IgD^{-} IgM^{-}) B cells. (B) Bar chart depicting analysis of the pro/pre B cell compartment based on IC expression of Igκ and λ5. Igκ^{+} marks percentage of IC Igκ^{+} pro/pre B cells independent of IC λ5 expression. (C) Flow cytometric determination of IC protein expression of μHC/Igμ in the discriminated (B) pro/pre B cell subset. (D) Determination of percentage of IC Igκ^{+} among stated BM (left) or SPL (right) B cell populations as analyzed by flow cytometry and (E) IC Igκ protein levels in these Igκ^{+} cells. Gated B cell subsets: small pre B B220^{lo} c-kit^{-} CD25^{+} IgD^{-} IgM^{-} FSC^{lo}; immature B B220^{int} IgD^{-} IgM^{+}, mature B B220^{+} IgD^{+}, B cells B220^{+}, IgD^{lo} IgM^{hi} and IgD^{hi} IgM^{lo} B cells. R: Rc3h; Igμ: intracellular IgM; n.d.: not depicted; IC: intracellular; MFI: median fluorescence intensity; BM: bone marrow; SPL: spleen. Bars represent means and error bars standard deviation. **p ≤ 0.01, *p ≤ 0.05, multiple t tests with Holm-Sidak method applied.

Efficient pairing of IgH^{MOG} heavy chain and $IgL^{D23\kappa}$ light chain in B cells of $Mb1^{cre/+}$ $Rc3h1^{F/F}$-$2^{F/F}$ IgH^{MOG} $IgL^{D23\kappa}$ was confirmed by surface staining for Igκ and Igλ (Fig. 47A). Mature recirculating B cells of these mice express almost exclusively Igκ, most likely originating from the $IgL^{D23\kappa}$ allele, while in the relevant $Mb1^{cre/+}$ $Rc3h1^{F/F}$-$2^{F/F}$ IgH^{MOG} controls a significant fraction expresses Igλ on the cell surface (Fig. 47A). This is consistend with the observed phenotype that pre B cell development appears accelerated by the pre-rearranged $IgL^{D23\kappa}$ allele in $Mb1^{cre/+}$ $Rc3h1^{F/F}$-$2^{F/F}$ IgH^{MOG} $IgL^{D23\kappa}$ compared to $Mb1^{cre/+}$ $Rc3h1^{F/F}$-$2^{F/F}$ IgH^{MOG} mice (Fig. 34, S20). The same was observed for immature B cells of $Mb1^{cre/+}$ $Rc3h1^{F/F}$-$2^{F/F}$ IgH^{MOG} $IgL^{D23\kappa}$ and $Mb1^{cre/+}$ $Rc3h1^{F/F}$-$2^{F/F}$ IgH^{MOG} mouse lines (Fig. 34, 41). Moreover, cell numbers of $Ig\lambda^{+}$ immature B cells in the $IgL^{D23\kappa}$ transgenic IgH^{MOG} $IgL^{D23\kappa}$ and $IgL^{D23\kappa}$ mouse lines tend to be reduced compared to wild type controls, which is not the case for $Ig\kappa^{+}$ immature B cells in these mice, indicating a bias for Igκ usage independent of IgH^{MOG} or endogenous heavy chain usage (Fig. 47B).

Interestingly, there is a peculiar population of Igκ/λ double positive ($Ig\kappa^{+}$ $Ig\lambda^{+}$) mature recirculating B cells in the bone marrow (Fig. 47A) and more mature IgD^{hi} IgM^{lo} splenic B cell pool (data not shown) in the IgH^{MOG} $IgL^{D23\kappa}$ control mouse. As it has been shown that $IgL^{D23\kappa}$-driven Igκ expression occurs in the presence of an Igκ locus closed by recombination to the recombining sequence, which deletes the C_κ gene segment (Fig. 1) [28, 265] and co-expression of a MOG-specific Ig heavy and light chain cause ongoing receptor editing [226], I aimed to investigate if receptor editing by secondary rearrangements might be the cause of this Igκ/λ double positive population. Downregulation of the BCR as well as IRF4 upregulation are hallmarks of receptor editing [28, 255, 266]. However, I neither found IgM surface expression levels (Fig. 44, data not shown) to be reduced nor intracellular IRF4 levels to be increased in pro, pre or immature B cells of IgH^{MOG} $IgL^{D23\kappa}$ mice compared to $IgL^{D23\kappa}$ and wild type control mice (Fig. 48). Therefore, these Igκ/λ double positive B cells appear due to a yet unknown reason. The quantification of intracellular IRF4 levels strongly highlights the similarity of IgH^{MOG} containing Roquin1/2-deficient B cells and the Roquin1/2-deficient genotypes without IgH^{MOG} (Fig. 48). Additionally, IgH^{MOG} inserted pre B cells exhibit (Fig. 48) a tendency of higher IRF4 levels compared to those with D23κ inserted (Fig. 48). This observation further supports the conclusion that insertion of D23κ allows the pre B cells to transition quicker to the immature B cell stage compared to IgH^{MOG} only inserted pre B cells, which must successfully recombine IgL. Strikingly, IRF4 levels in IgH^{MOG} inserted Roquin1/2-deficient and wild type pro, pre and immature B cells are near identical, further supporting the conclusion of partial IgH^{MOG}-mediated rescue (Fig. 48). Remarkably, IRF4

levels in Roquin1/2-deficient pro, pre and immature B cells are very similar irrespective if they have the D23κ allele inserted or not (Fig. 48).

In conclusion, lack of an $IgL^{D23\kappa}$-specific antibody prohibited specific staining of Ig light chain derived from this allele, yet appearance of a novel cytoplasmic $\lambda5^+$ $Ig\kappa^+$ pro/pre B cell population suggests efficient expression of transgene-derived κ light chain. Moreover, I provide evidence for successful pairing of IgH^{MOG} heavy chain and $IgL^{D23\kappa}$ light chain suggesting that despite formation of a BCR on the cell surface of immature B cells of $Mb1^{cre/+}$ $Rc3h1^{F/F}$-$2^{F/F}$ IgH^{MOG} $IgL^{D23\kappa}$ mice, B cell lymphopoiesis is not rescued and the developmental pro to pre B cell block observed upon Mb1cre-mediated deletion of Roquin1 and 2 is independent of Igμ or Igκ/λ rearrangement and (pre-)BCR expression.

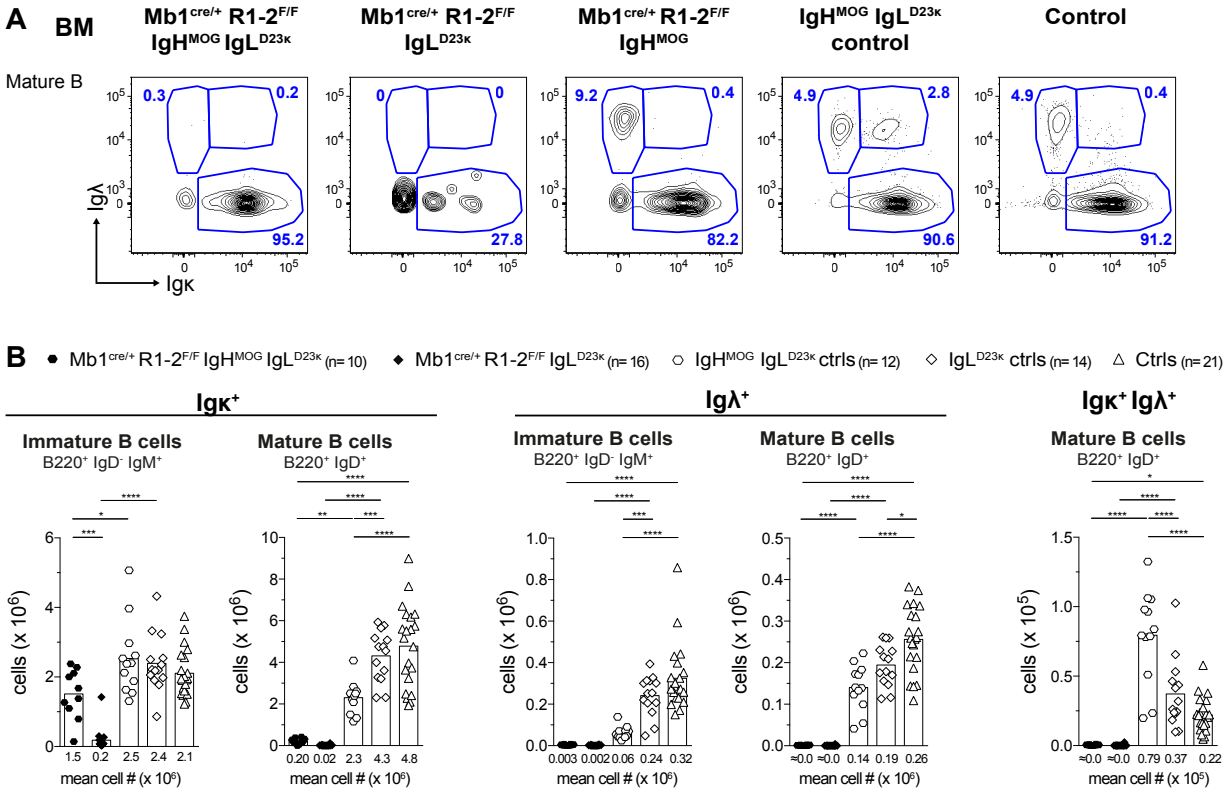

Figure 47: Analysis of surface expression of Igκ and Igλ on BM B cells of $Mb1^{cre/+}$ $Rc3h1\text{-}2^{F/F}$ IgH^{MOG} $IgL^{D23\kappa}$ and $Mb1^{cre/+}$ $Rc3h1\text{-}2^{F/F}$ $IgL^{D23\kappa}$ mice.

(A) Representative flow cytometric analysis of mature, recirculating ($B220^+$ IgD^+) bone marrow (BM) B cells. (B) Total cell numbers of immature/mature Igκ-positive ($Ig\kappa^+$) or Igλ-positive ($Ig\lambda^+$) or double positive ($Ig\kappa^+$ $Ig\lambda^+$) B cells. R: Rc3h. The genotypes displayed in the bar charts differ from (A). Numbers below graphs and bars indicate mean cell numbers (#). ****$p \leq 0.0001$, ***$p \leq 0.001$, **$p \leq 0.01$, *$p \leq 0.05$, ANOVA. Calculated cell numbers of < 1000 were rounded to 0 and denoted as ≈0.0. Significances for $Mb1^{cre/+}$ $R1\text{-}2^{F/F}$ IgH^{MOG} $IgL^{D23\kappa}$ versus $IgL^{D23\kappa}$ ctrls and $Mb1^{cre/+}$ $R1\text{-}2^{F/F}$ $IgL^{D23\kappa}$ versus IgH^{MOG} $IgL^{D23\kappa}$ ctrls and ctrls are not shown.

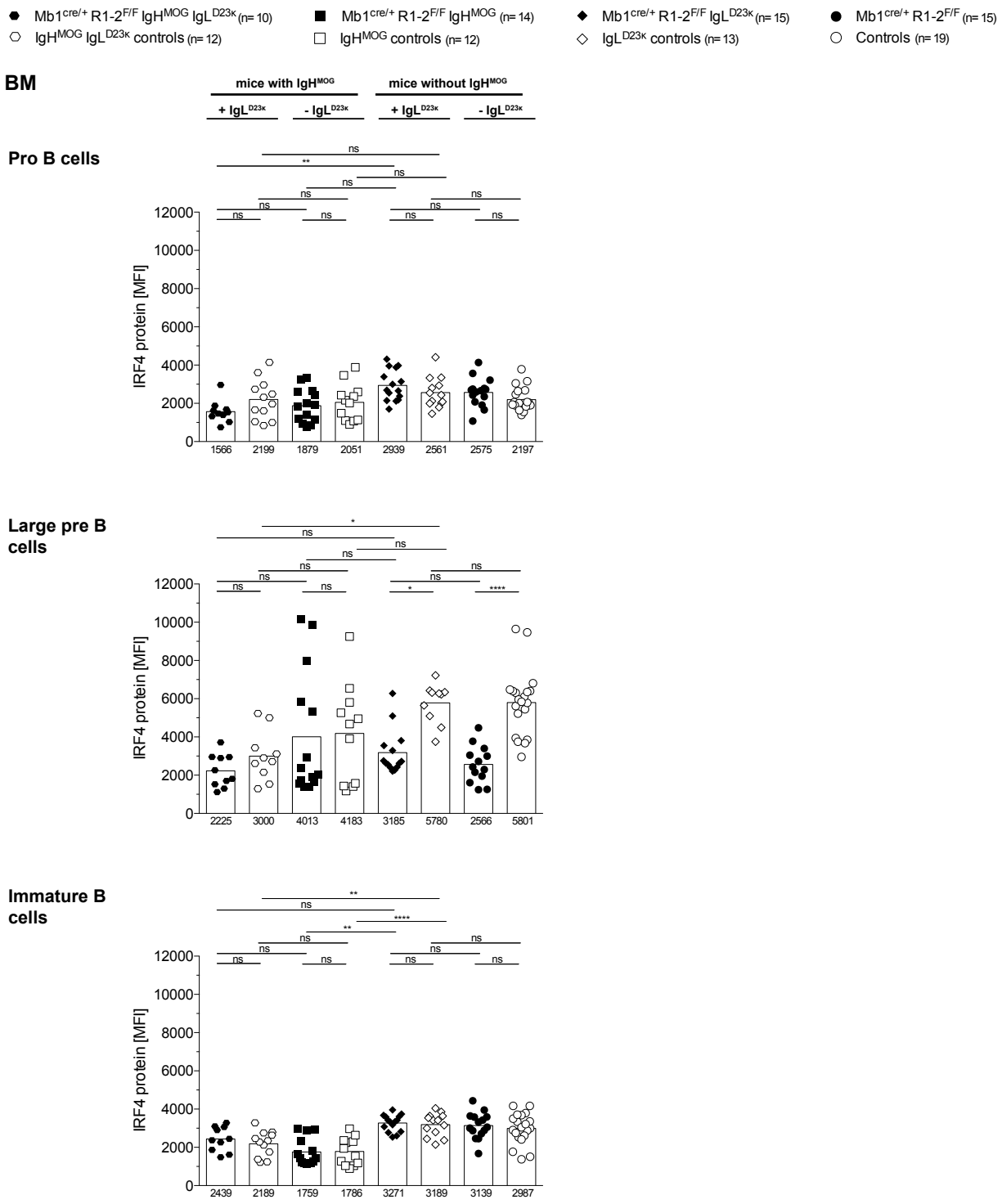

Figure 48: Analysis of intracellular IRF4 levels in bone marrow B cell populations of Mb1$^{cre/+}$ Rc3h1-2$^{F/F}$, Mb1$^{cre/+}$ Rc3h1-2$^{F/F}$ IgL^{D23κ}, Mb1$^{cre/+}$ Rc3h1-2$^{F/F}$ IgH^{MOG} and Mb1$^{cre/+}$ Rc3h1-2$^{F/F}$ IgH^{MOG} IgL^{D23κ} mice.

Bar chart representation of IC IRF4 levels as determined by flow cytometry in indicated BM B cell populations. Bars and numbers below bars represent mean MFI values and error bars standard deviation. All significances determined are shown. Mouse grouping based on insertion of IgH^{MOG} or not and additional insertion of IgL^{D23κ} (+IgL^{D23κ}) or not (-IgL^{D23κ}) are grouped as stated on top. Values for data points of Mb1$^{cre/+}$ Rc3h1-2$^{F/F}$ IgH^{MOG} and IgH^{MOG} ctrl are the sames as used for Fig. 43. B cell subset gating: Pro B B220^{lo} IgD^{-} IgM^{-} ckit^{+} CD25^{-}; Large pre B B220^{lo} IgD^{-} IgM^{-} ckit^{-} CD25^{+} FSC^{hi}; Immature B B220^{+} IgD^{-} IgM^{+}. BM: bone marrow; MFI: median flourescence intensity; IC: intracellular; R: Rc3h. Numbers below bars indicate mean MFI values. ****p ≤ 0.0001, **p ≤ 0.01, *p ≤ 0.05, ns non-significant, ANOVA.

1.17 Loss of immature and mature bone marrow B cells in Mb1$^{cre/+}$ Rc3h1$^{F/F}$-2$^{F/F}$ IgH^{MOG} IgL$^{D23\kappa}$ and Mb1$^{cre/+}$ Rc3h1$^{F/F}$-2$^{F/F}$ IgL$^{D23\kappa}$ mouse lines is mostly independent of apoptosis and proliferation

Subsequently, I aimed to dissect the role of apoptosis and proliferation in the hindered development of bone marrow B cells in Mb1$^{cre/+}$ Rc3h1$^{F/F}$-2$^{F/F}$ IgH^{MOG} IgL$^{D23\kappa}$ and Mb1$^{cre/+}$ Rc3h1$^{F/F}$-2$^{F/F}$ IgL$^{D23\kappa}$ mice. As expected the ratios of viable B cells of the individual subsets in Mb1$^{cre/+}$ Rc3h1$^{F/F}$-2$^{F/F}$ IgH^{MOG} IgL$^{D23\kappa}$ mice do not differ much from those of IgH^{MOG} IgL$^{D23\kappa}$ control (Fig. S24A) or Mb1$^{cre/+}$ Rc3h1$^{F/F}$-2$^{F/F}$ IgH^{MOG} mice (data not shown), except for the fraction of viable small pre B cells, which is strongly decreased in the former mouse line. However, this decreased viability of small pre B cells is unlikely to have strong consequences as the total cell number of small pre B cells is very low in Mb1$^{cre/+}$ Rc3h1$^{F/F}$-2$^{F/F}$ IgH^{MOG} IgL$^{D23\kappa}$ mice (Fig. S20). Similarly, survival of bone marrow B cell populations is hardly altered in Mb1$^{cre/+}$ Rc3h1$^{F/F}$-2$^{F/F}$ IgL$^{D23\kappa}$ mice compared to IgL$^{D23\kappa}$ control mice (Fig. 24B) or Mb1$^{cre/+}$ Rc3h1$^{F/F}$-2$^{F/F}$ mice (data not shown), except for a significant decrease in the percentage of viable immature B cells, which however affects only a very small total cell number (Fig. 44). Moreover, quantification of Bim levels in bone marrow B cells of Mb1$^{cre/+}$ Rc3h1$^{F/F}$-2$^{F/F}$ IgH^{MOG} IgL$^{D23\kappa}$ in relation to IgH^{MOG} IgL$^{D23\kappa}$ mice showed no significant differences (data not shown).

IL-7Rα expression levels on bone marrow B cells of Mb1$^{cre/+}$ Rc3h1$^{F/F}$-2$^{F/F}$ IgH^{MOG} IgL$^{D23\kappa}$ mice recapitulated that of Mb1$^{cre/+}$ Rc3h1$^{F/F}$-2$^{F/F}$ IgH^{MOG} mice, while IL-7Rα levels in the Mb1$^{cre/+}$ Rc3h1$^{F/F}$-2$^{F/F}$ IgL$^{D23\kappa}$ mice phenocopied that of the Mb1$^{cre/+}$ Rc3h1$^{F/F}$-2$^{F/F}$ genotype (data not shown). There is a significant, but small increase of the proportion of immature B cells of Mb1$^{cre/+}$ Rc3h1$^{F/F}$-2$^{F/F}$ IgH^{MOG} IgL$^{D23\kappa}$ mice in the proliferative S/G_2/M-phase compared to IgH^{MOG} IgL$^{D23\kappa}$ (Fig. S25A) or Mb1$^{cre/+}$ Rc3h1$^{F/F}$-2$^{F/F}$ IgH^{MOG} mice (data not shown). Likewise, mature recirculating B cells in the Mb1$^{cre/+}$ Rc3h1$^{F/F}$-2$^{F/F}$ IgH^{MOG} IgL$^{D23\kappa}$ and Mb1$^{cre/+}$ Rc3h1$^{F/F}$-2$^{F/F}$ IgL$^{D23\kappa}$ mouse strains were demonstrated to have a higher ratio of cells in S/G_2/M-phase in comparison to IgH^{MOG} IgL$^{D23\kappa}$ or IgL$^{D23\kappa}$ mice, respectively (Fig. S25A). However the loss of immature and mature recirculating bone marrow B cells in Mb1$^{cre/+}$ Rc3h1$^{F/F}$-2$^{F/F}$ IgH^{MOG} IgL$^{D23\kappa}$ and Mb1$^{cre/+}$ Rc3h1$^{F/F}$-2$^{F/F}$ IgL$^{D23\kappa}$ mice appears to a large part independent of increased apoptosis and defects in proliferation.

1.18 Altered extrinsic effects in T and myeloid populations in presence of $IgL^{D23\kappa}$ in $Mb1^{cre/+}$ $Rc3h1^{F/F}$-$2^{F/F}$ IgH^{MOG} $IgL^{D23\kappa}$ and $Mb1^{cre/+}$ $Rc3h1^{F/F}$-$2^{F/F}$ $IgL^{D23\kappa}$ mice

Unexpectedly, despite an increase in splenic B cells numbers, there is no change with regard to percentage in the T cell compartment in the $Mb1^{cre/+}$ $Rc3h1^{F/F}$-$2^{F/F}$ IgH^{MOG} $IgL^{D23\kappa}$ mouse line compared to IgH^{MOG} $IgL^{D23\kappa}$ controls (Fig. S26). Due to the increase in total splenic cell numbers some T cell populations are significantly increased in cell numbers, such as $CD4^+$ and the T_{reg}-containing $CD4^+$ $CD25^+$ T cell pool (Fig. S26). Moreover, the striking increases observed in the splenic T cell compartment of $Mb1^{cre/+}$ $Rc3h1^{F/F}$-$2^{F/F}$ IgH^{MOG} mice are altogether reduced (Fig. S18). Surprisingly, all splenic T cell populations investigated in mice of the $Mb1^{cre/+}$ $Rc3h1^{F/F}$-$2^{F/F}$ $IgL^{D23\kappa}$ genotype are significantly increased in percentage in comparison to $IgL^{D23\kappa}$ controls (Fig. S26) and also show a trend of elevated percentages compared to $Mb1^{cre/+}$ $Rc3h1^{F/F}$-$2^{F/F}$ IgH^{MOG} $IgL^{D23\kappa}$ mice.

Next, I analyzed splenic myeloid cell populations. Plasmacytoid dendritic cells as well as activated monocytes and macrophages are increased in percentage in the $Mb1^{cre/+}$ $Rc3h1^{F/F}$-$2^{F/F}$ IgH^{MOG} $IgL^{D23\kappa}$ mouse line compared to IgH^{MOG} $IgL^{D23\kappa}$ controls (Fig. S27). Furthermore, percentages of myeloid cell populations are in general elevated in $Mb1^{cre/+}$ $Rc3h1^{F/F}$-$2^{F/F}$ IgH^{MOG} $IgL^{D23\kappa}$ mice in comparison to the $Mb1^{cre/+}$ $Rc3h1^{F/F}$-$2^{F/F}$ IgH^{MOG} mouse line. Likewise, all myeloid cell subsets are expanded percentagewise in the $Mb1^{cre/+}$ $Rc3h1^{F/F}$-$2^{F/F}$ $IgL^{D23\kappa}$ mouse line compared to $IgL^{D23\kappa}$ controls (Fig. S27).

Summary of the most important findings of part 1

Collectively, Mb1cre-mediated deletion of Roquin1 and 2 has revealed a novel and unexpected role of both proteins in early B cell development in the bone marrow. Roquin1 and 2 have important functions at the pre-BCR checkpoint largely independent of μHC expression or formation of a pre-BCR/BCR. The indications presented in this thesis point towards a contribution of Roquin1 and 2 to normal IL-7R and (pre-)BCR signaling and downstream effects mediated by these pathways such as expansion of the large pre B cell pool by proliferation.

2. Roquin proteins regulate the maturation, activation and differentiation of peripheral B cells

2.1 B cells of CD19$^{cre/+}$ Rc3h1$^{F/F}$-2$^{F/F}$ mice do not show signs of a developmental block in the bone marrow

In addition to investigating the role of Roquin1 and 2 in early B cell development, I also studied their role in splenic B cell development and peripheral B cell physiology. To this end, I used the CD19cre knock-in mouse strain (cre: inserted / +: wild type), which expresses cre recombinase under endogenous control of the B cell-confined CD19 locus [224, 225]. Recombination efficiency of loxP flanked alleles by CD19cre has been shown to be 75-80% in bone marrow and above 90% in splenic B cells, thus reflecting the fact that CD19cre-mediated deletion is a continuous process resulting in complete deletion in mature B cells [225, 238, 267]. The experiments employing CD19cre-mediated Roquin1 and 2 deletion were performed in 8-16 weeks old experimental and CD19$^{cre/+}$ control mice. An Rc3h1-2$^{F/F}$ nomenclature is used for CD19cre-based experiments to reflect the fact that every experiment was aimed at deleting all four alleles of Roquin1 and 2, unlike in the initial Mb1cre experiments.

Mice of the CD19$^{cre/+}$ Rc3h1-2$^{F/F}$ strain developed normally and no changes in weight or total cell number of bone marrow cells were noted (Fig. 49A). As CD19 expression, and hence CD19cre activity, starts at the pro B cell stage, unexpectedly the number of pro B cells is significantly increased, while total numbers of pre or immature B cells remain unchanged (Fig. 49B, 49C). This observation was surprising in the context of the Mb1cre-mediated developmental block upon deletion of both Roquin paralogs. However, the total number of mature recirculating B cells is strongly decreased in CD19$^{cre/+}$ Rc3h1-2$^{F/F}$ mice. Yet, very significantly and in contrast to the Mb1cre experiments, a population of mature recirculating B cells is generated in this strain.

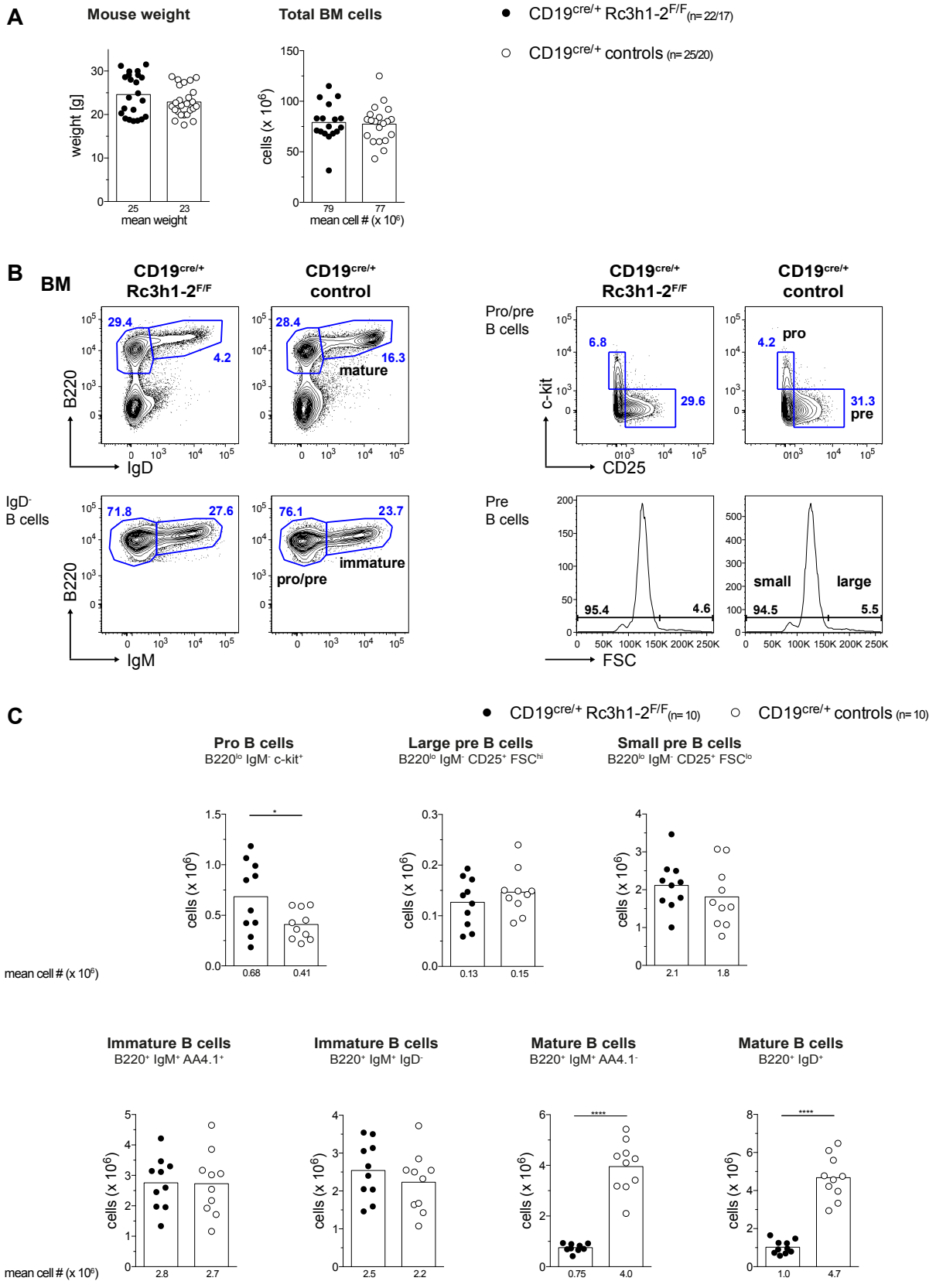

Figure 49: Minute mature recirculating B cells numbers in CD19$^{cre/+}$ Rc3h1-2$^{F/F}$ mice.
(A) Mouse weight and total number of bone marrow cells. (B) Representative flow cytometry plots illustrating the gating strategies for bone marrow B cell populations. (C) Total bone marrow B cell subset numbers as determined by flow cytometry. #: numbers; BM: bone marrow. Numbers below graphs and bars show mean values. ****p ≤ 0.0001, *p ≤ 0.05, paired t test.

2.2 Maturation defect of splenic B cells and reduction of B1a cells in CD19$^{cre/+}$ Rc3h1$^{F/F}$-2$^{F/F}$ mice

As the number of mature recirculating B cells in the bone marrow is strongly reduced in experimental mice, I further investigated naive peripheral B cell stages. Surprisingly, the spleens of these mice are significantly heavier and contain more splenocytes (Fig. 50A). However, percentage and total splenic B cell numbers are reduced. There is no alteration in splenic immature/transitional B cells, but percentage and total cell number of the mature B cell subsets are reduced in the CD19$^{cre/+}$ Rc3h1-2$^{F/F}$ mouse line (Fig. 50B, 50C). Similarly, the number of the immature splenic B cell population as defined by IgD^{lo} IgM^{hi} expression is not altered, while the cell number of the more mature IgD^{hi} IgM^{lo} B cells is strongly reduced (Fig. 51). Remarkably, the AA4.1^{-} mature B cell numbers are twofold higher than the IgD^{hi} IgM^{lo} mature B cell numbers, indicating that similar to Mb1$^{cre/+}$ Rc3h1$^{F/F}$-2$^{F/F}$ IgH^{MOG} mice, AA4.1^{-} mature splenic B cells in CD19$^{cre/+}$ Rc3h1-2$^{F/F}$ comprise a significant ratio of B1 cells (Fig. 51).

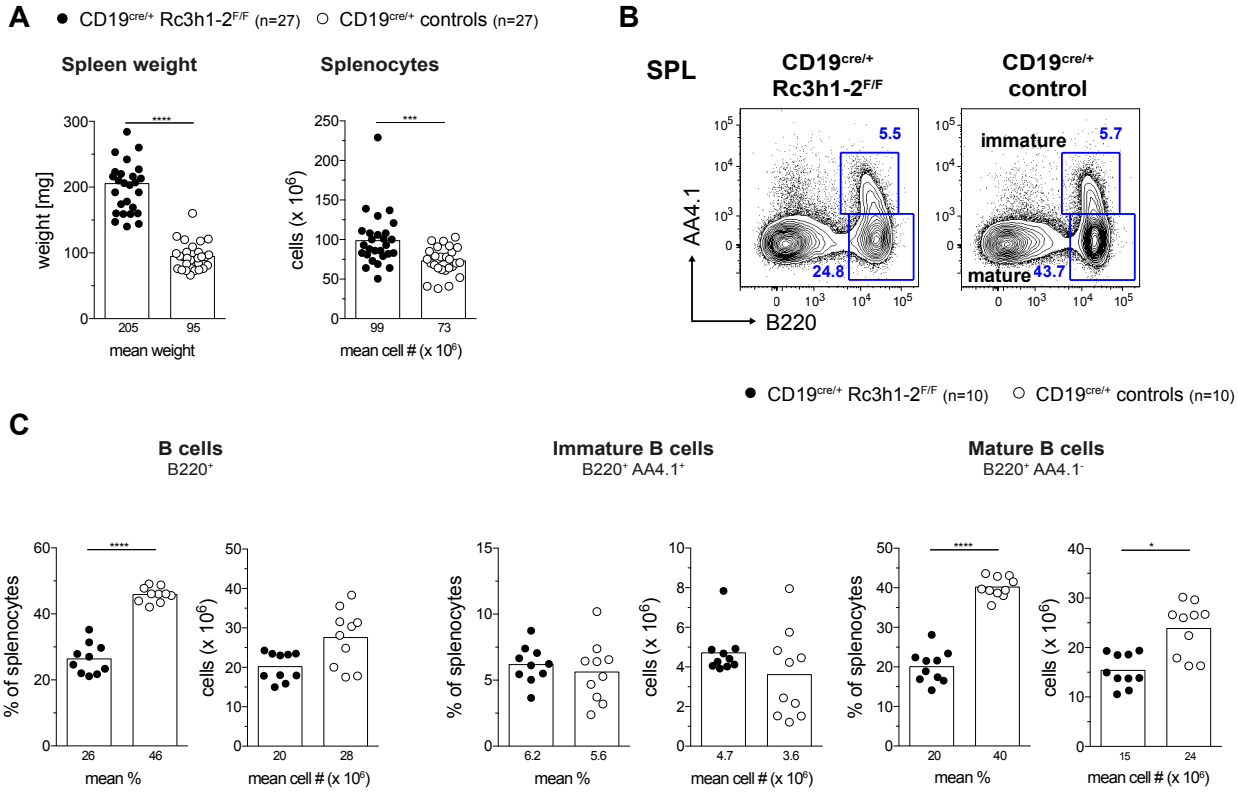

Figure 50: CD19$^{cre/+}$ Rc3h1-2$^{F/F}$ mice have an enlarged spleen, but a reduction in mature splenic B cells.
(A) Spleen weight and absolute number of splenocytes. (B) Representative flow cytometry analysis depicting gating scheme of splenic (SPL) B cells. (C) Percentage of stated SPL B cell populations among total splenocytes and total subset cell numbers as determined by flow cytometry. SPL: spleen. Numbers below graphs and bars represent mean percentages and cell numbers (#). ****p ≤ 0.0001, ***p ≤ 0.001, *p ≤ 0.05, paired t test.

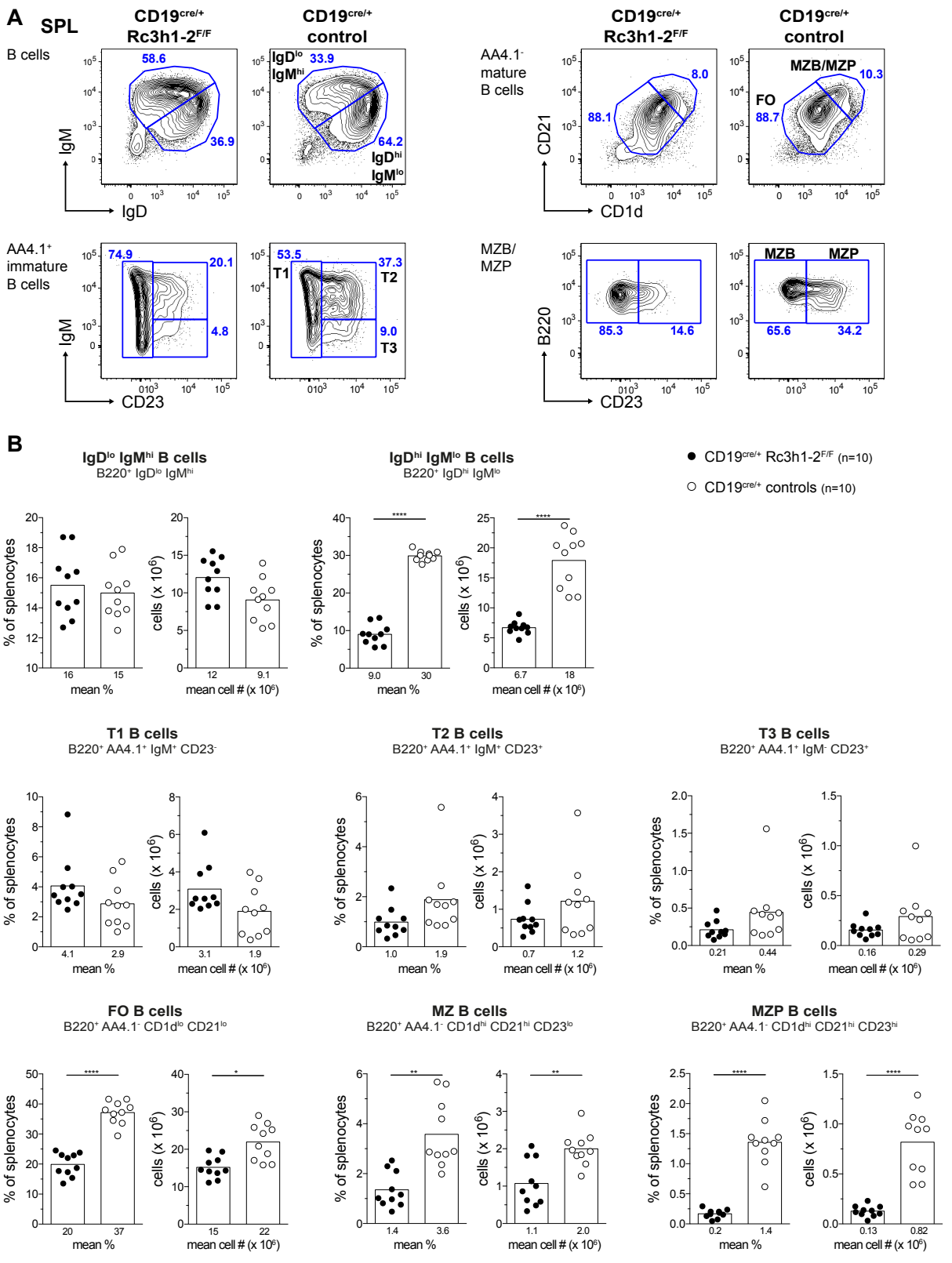

Figure 51: Reduction of splenic B cell population sizes post the T1 stage in CD19$^{cre/+}$ Rc3h1-2$^{F/F}$ mice.
(A) Representative flow cytometric analysis illustrating the gating strategy for splenic B cells. (B) Total splenic (SPL) subset B cell numbers as determined by flow cytometry. T1: transitional 1; T2: transitional 2, T3: transitional T3; FO: follicular, MZB/MZ B: mature marginal zone; MZP: marginal zone precursor. SPL: spleen. Numbers below graphs and bars show mean percentages and cell numbers (#). ****p ≤ 0.0001, **p ≤ 0.01, *p ≤ 0.05, paired t test.

However, within the immature/transitional B cell subset, there is a trend for increased percentages and cell numbers of transitional T1 B cells, whereas percentages and numbers of T2 and T3 B cells are decreased in $CD19^{cre/+}$ $Rc3h1\text{-}2^{F/F}$ mice (Fig. 51) Within the mature compartment, the percentages and cell numbers of follicular, marginal zone and marginal zone precursors are significantly reduced. In line with previous experiments, I observed a similar deregulation of the surface markers CD21, CD1d and CD23 on splenic B cells of $CD19^{cre/+}$ $Rc3h1\text{-}2^{F/F}$ mice (Fig. 51A) as noted for $Mb1^{cre/+}$ $Rc3h1^{F/F}$ $\text{-}2^{F/F}$ IgH^{MOG} mice (Fig. 36).

As indicated by the twofold higher numbers of $AA4.1^{-}$ mature B cells compared to IgD^{hi} IgM^{lo} B cell numbers, the percentage and cell number of the splenic B1 cell pool is significantly increased in $CD19^{cre/+}$ $Rc3h1\text{-}2^{F/F}$ mice. There is a reduction of the splenic B1a population in percentage and cell number, whereas the B1b pool is significantly and strongly increased in percent and cell number (Fig. 52) culminating in the overall increase of the splenic B1 compartment. Similarly, the peritoneal cavity B1a subset is significantly decreased in percentage and cell number, while the B1b population is increased resulting in an overall increase of the B1 cell population in the peritoneal cavity (Fig. 52).

Thus, the B1 cell compartment in spleen and peritoneal cavity of $CD19^{cre/+}$ $Rc3h1\text{-}2^{F/F}$ mice (Fig. 52) resembles that of the $Mb1^{cre/+}$ $Rc3h1^{F/F}$ $\text{-}2^{F/F}$ IgH^{MOG} mouse strain (Fig. 39). The numbers of Peyer's patches as well as the number of cells per Peyer's patch are significantly reduced in the $CD19^{cre/+}$ $Rc3h1\text{-}2^{F/F}$ mouse strain (Fig. S28A), which I have similarly observed for Peyer's patches of $Mb1^{cre/+}$ $Rc3h1^{F/F}$ $\text{-}2^{F/wt}$ mice (Fig. 13).

In conclusion, splenic B cells of $CD19^{cre/+}$ $Rc3h1\text{-}2^{F/F}$ mice show a strong reduction in mature recirculating B cells in the bone marrow and in mature IgDlo splenic B cells. Detected phenotypes in this strain resemble those described before in the different Mb1cre models. This suggests that the later onset of recombination of loxP-flanked Rc3h1 and 2 alleles in the CD19cre model allows B cell development in the bone marrow to occur. However, loss of Roquin proteins at a later time point eventually cause similar maturation defects as observed in $Mb1^{cre/+}$ $Rc3h1^{F/F}$ $\text{-}2^{F/F}$ IgH^{MOG} mice: Roquin1/2-deficient B lineage cells cannot differentiate into mature recirculating bone marrow B cells, mature IgD^{hi} IgM^{lo} splenic B cells and B1a cells in spleen and peritoneal cavity. Interestingly, both genetic models also point to an inhibitory role for Roquin proteins in controlling the expansion of B1b cells in spleen and peritoneal cavity.

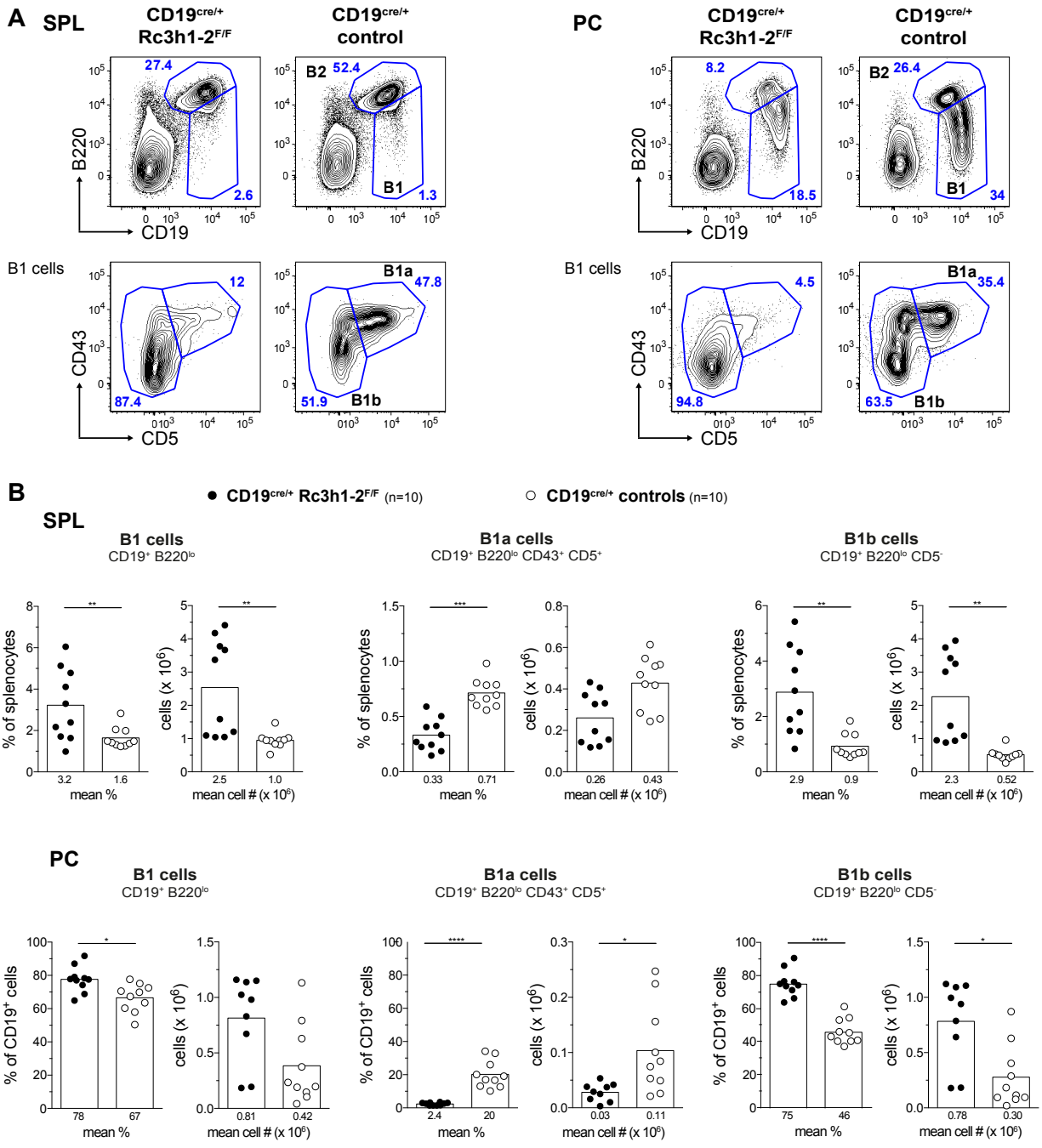

Figure 52: Splenic and peritoneal cavity B1 cell populations are increased in CD19$^{cre/+}$ Rc3h1-2$^{F/F}$ mice resulting from increased B1b cell compartments, wheres B1a subsets are reduced.

(A) Representative flow cytometric analysis depicting the gating strategy for B1 cells. (B) Percentage of indicated SPL/PC B cell populations among total SPL/PC cells and total subset cell numbers as determined by flow cytometry. SPL: spleen; PC: peritoneal cavity. Numbers below graphs and bars indicate mean values. ****p ≤ 0.0001, ***p ≤ 0.001, **p ≤ 0.01, *p ≤ 0.05, paired t test.

2.3 Evidence for counterselection of Roquin1/2-ablated mature splenic B cells in CD19$^{cre/+}$ Rc3h1$^{F/F}$-2$^{F/F}$ mice

Subsequently, I further investigated the striking maturation inability of Roquin1/2 ablated splenic B cells. To this end, I performed qRT-PCR analysis to quantify *Rc3h1* and *2* mRNA in flow-cytometry purified mature follicular and marginal zone B cell subsets (Fig. 53)

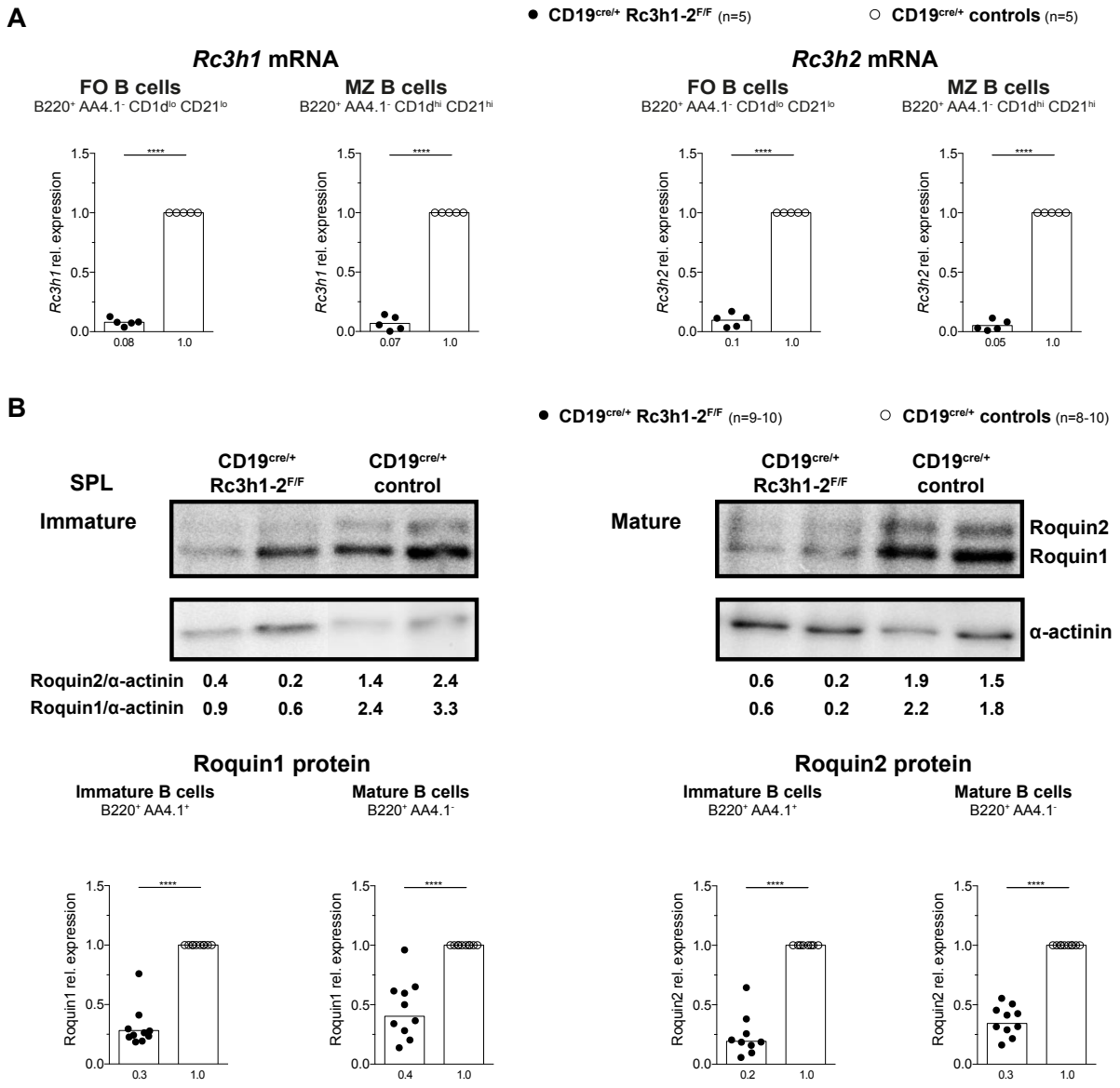

Figure 53: Efficient recombination of *Rc3h1* and *2* alleles in mature B cell populations of CD19$^{cre/+}$ Rc3h1-2$^{F/F}$ mice and reduction of Roquin1 and 2 protein levels in immature und mature B cell subsets.
(A) Follicular and marginal zone splenic B cell subsets were purified as stated below the respective subset by flow cytometry. Measured *Rc3h1-2* mRNA levels were normalized to PBGD and resulting relative gene expression compared to CD19$^{cre/+}$ controls is depicted. (B) (Top) Immature and mature splenic B cells were purified by flow cytometry. Representative Western blot analyses of two samples for each CD19$^{cre/+}$ Rc3h1-2$^{F/F}$ and CD19$^{cre/+}$ controls with quantified ratios of Roquin1 or 2 expression relative to α-actinin. *(Continued on next page)*

(Bottom) Roquin1 and 2 expression was quantified relative to α-actinin and expression normalized to $CD19^{cre/+}$ controls. SPL: spleen. Number below graphs and bars are mean values (A) or geometric means (B). ****$p \leq 0.0001$, unpaired t test.

I calculated *Rc3h1* and *2* mRNA levels in these mature populations from the $CD19^{cre/+}$ Rc3h1-$2^{F/F}$ genotype to correspond to 5-10% of the levels in $CD19^{cre/+}$ controls. To more direcly monitor Roquin1/2-deficiency at the protein levels, I quantified the relative protein expression of Roquin1 and 2 by Western blot in FACS purified immature and mature splenic B cells (Fig. 53B). The protein levels of Roquin1 and 2 normalized to a-actinin increase in double-deficient mature B cells compared to immature B cells. This in in contrast to the recombination efficiency of CD19cre, which increases from immature to mature B cells in the absence of selective pressures [238]. Therefore, this result indicates ongoing counterselection against Roquin1/2-deficient B cells. Analyses of Roquin1 protein levels compared to Roquin2 revealed an approximately 3fold higher expression in immature and 2.5fold higher expression in mature splenic B cells from $CD19^{cre/+}$ mice (data not shown). To further evaluate selection process by an additional method, I again employed the R26/CAG-CARΔ1^{StopF} ($R26^{CARStopFL}$) allele. The increase of pro B cell numbers (Fig. 49) correlates with a significantly lower surface expression of CAR on late pro B cells of $CD19^{cre/+}$ Rc3h1-$2^{F/F}$ $R26^{CARStopFL}$ mice (Fig. 54). This expression pattern might reflect early counterselective pressure in Roquin1/2-ablated late pro B cells. However, there is no increase in proliferation of *ex vivo* isolated pro B cells of $CD19^{cre/+}$ Rc3h1-$2^{F/F}$ that could explain this increase in pro B cell numbers (Fig. S28B). As expected from the protein quantification (Fig. 53B), while CAR surface expression does not differ on immature splenic B cells, it is significantly lower on mature splenic B cells and mature recirculating bone marrow B cells of $CD19^{cre/+}$ Rc3h1-$2^{F/F}$ $R26^{CARStopFL}$ mice (Fig. 54). Mature recirculating B cells of experimental mice show a significantly increased proliferative capacity as judged by the ratio of cells in G_1 and $S/G_2/M$ phases potentially as a consequence of homeostatic proliferation in response to the low number of mature B cells in the bone marrow (Fig. S28B). Taken together, Roquin1 and 2 protein levels and CAR surface expression together with the data on indicate that Roquin1/2-deficient mature B cells have a competitive disadvantage in $CD19^{cre/+}$ Rc3h1-$2^{F/F}$ $R26^{CARStopFL}$ mice.

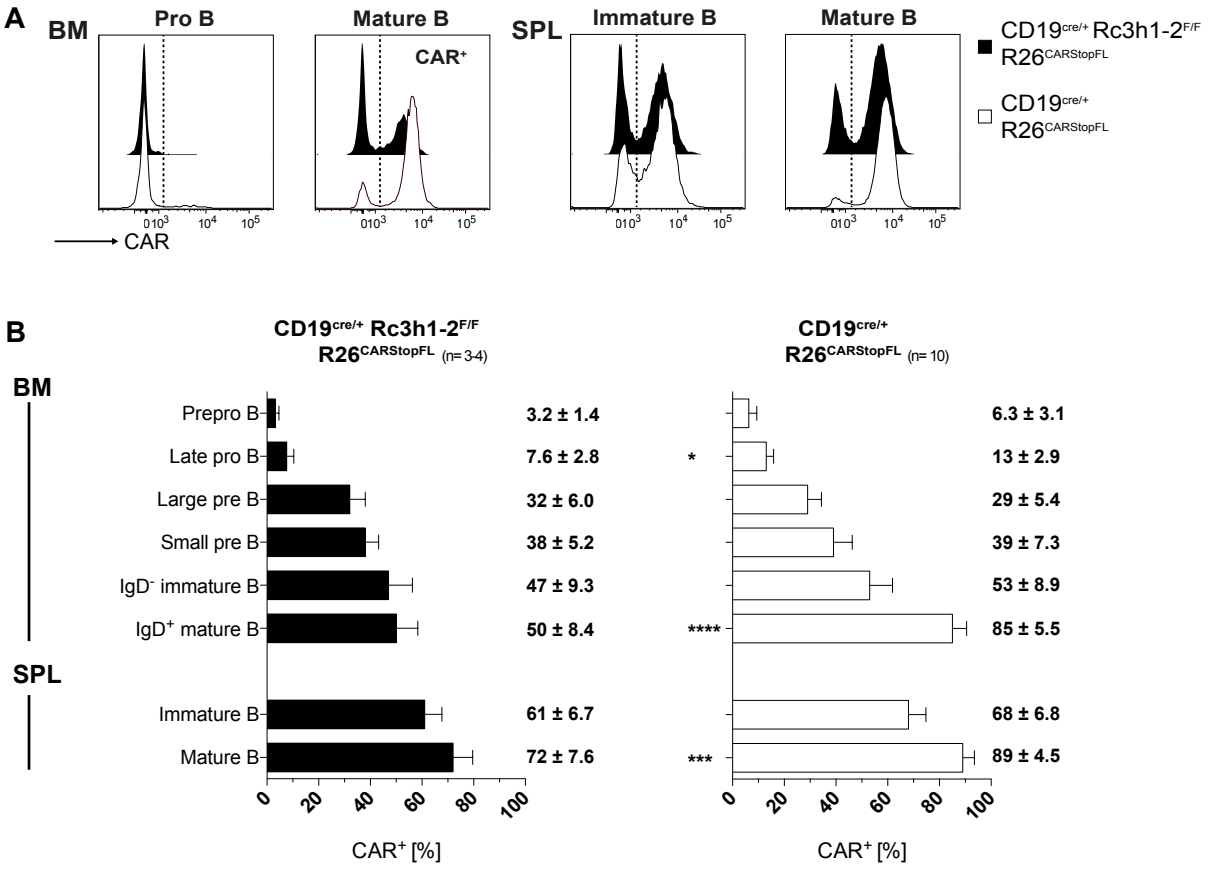

Figure 54: Counterselection of *Rc3h1/2-deficient* mature B cells in CD19$^{cre/+}$ Rc3h1-2$^{F/F}$ R26^{CARStopFL} reporter mice.

(A) Representative flow cytometric analysis of cell surface expression on indicated bone marrow and splenic B cell subsets of the CAR reporter after CD19^{cre}-mediated deletion. The dotted line in the histograms denotes CAR expression (CAR$^+$). (B) Percentages of CAR$^+$ B cells among the respective B cell subsets in bone marrow (BM) and spleen (SPL). CAR signal in the respective B cell populations in wild type and CD19$^{cre/+}$ mice was always < 1% (data not shown). Gated B cell subsets: BM - Prepro B B220^{lo} IgD$^-$ IgM$^-$ ckit$^+$ CD25$^-$ CD19$^-$; Late pro B B220^{lo} IgD$^-$ IgM$^-$ ckit$^+$ CD25$^-$ CD19$^+$; Pro B B220^{lo} IgD$^-$ IgM$^-$ ckit$^+$ CD25$^-$; Large pre B B220^{lo} IgD$^-$ IgM$^-$ ckit$^-$ CD25$^+$ FSC^{hi}; Small pre B B220^{lo} IgD$^-$ IgM$^-$ ckit$^-$ CD25$^+$ FSC^{lo}; Immature B B220$^+$ IgD$^-$ IgM$^+$; Mature B B220$^+$ IgD$^+$; SPL - Immature B B220$^+$ AA4.1$^+$; Mature B B220$^+$ AA4.1$^-$. Bars represent mean values and error bars standard deviation. ****p ≤ 0.0001, ***p ≤ 0.001, *p ≤ 0.05, unpaired t test.

2.4 Shifted ratios of Igκ and Igλ light chain usage with progressing maturation of Roquin1/2-deficient B cells

Since the pro to pre B cell transition appeared unaltered in CD19$^{cre/+}$ Rc3h1-2$^{F/F}$ mice, I investigated if Ig light chain expression is affected in bone marrow B cells in this mouse line (Fig. 55). While the number of surface Igκ$^+$ or Igλ$^+$ immature B cells is unaltered, there are significantly fewer Igκ$^+$ or Igλ$^+$ mature recirculating B cells (Fig. 55B). Strikingly, the number of Igκ$^+$ mature recirculating B cells is reduced to about 11% of the cell number in CD19$^{cre/+}$ controls, whereas the cell number of Igλ$^+$ mature B cells is reduced to only 28%

(Fig. 55B). Subsequently, I analyzed the ratio of Igκ to Igλ usage in splenic B cells (Fig. 55A, 55C). As expected, there is a significant change towards an increased Igλ usage in splenic B cells with a concomitant decrease in Igκ usage from the rather immature IgD^{lo} IgM^{hi} B cells to the more mature IgD^{hi} IgM^{lo} B cells and also mature recirculating B cells in the bone marrow (Fig. 55C) of the $CD19^{cre/+}$ $Rc3h1\text{-}2^{F/F}$ mouse strain. This shift from Igκ to Igλ usage was also observed in the total $B220^{+}$ splenic B cell population.

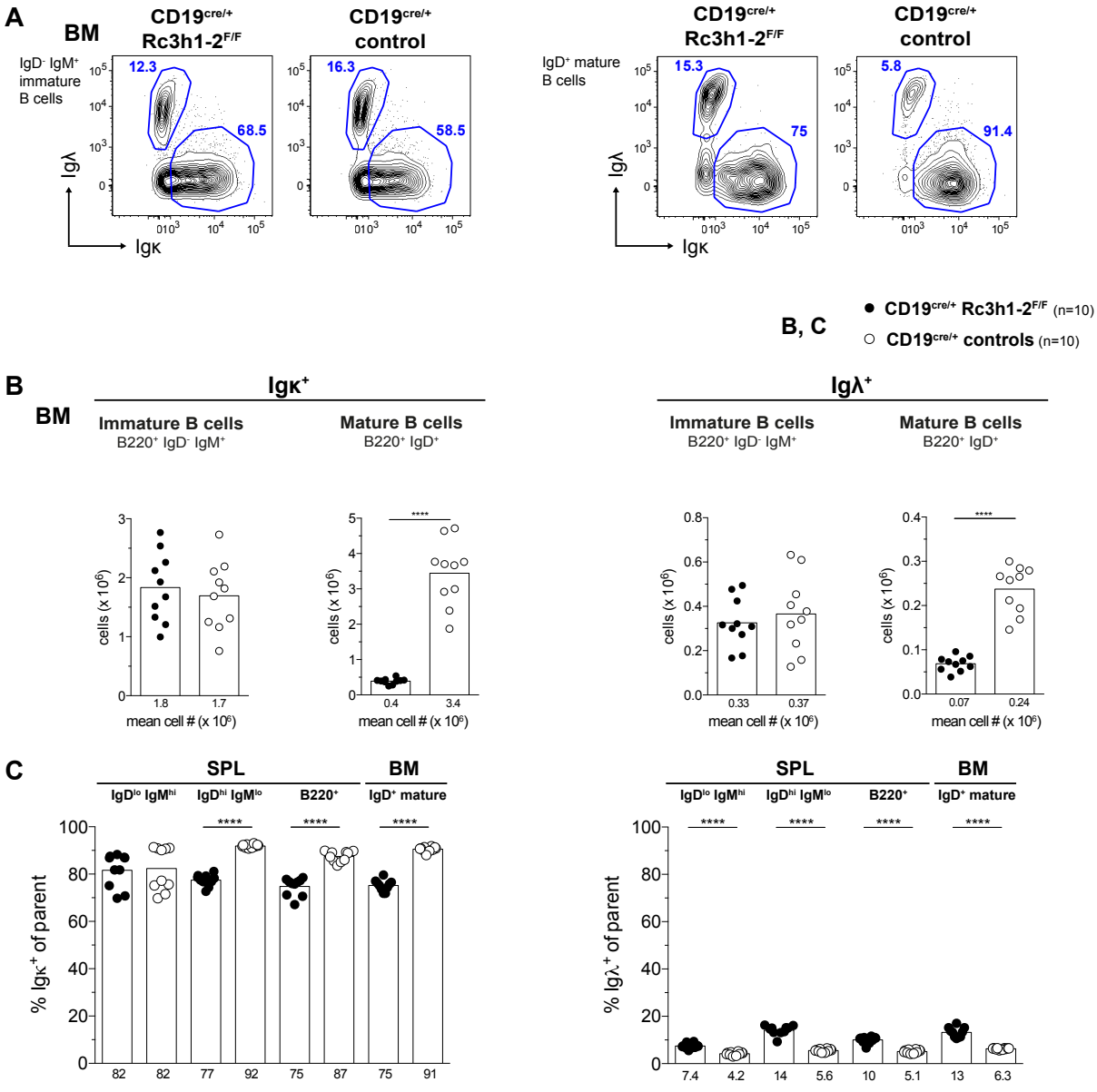

Figure 55: Shifted ratio of Igκ versus Igλ expression on splenic B and mature B cells in the bone marrow of $CD19^{cre/+}$ $Rc3h1\text{-}2^{F/F}$ mice.

(A) Representative flow cytometry analysisof Igκ versus Igλ (λ1, 2 and 3) expression on bone marrow (BM) B cells. (B) Total cell numbers of Igκ- or Igλ-expressing immature and mature recirculating BM cells. (C) Bar chart representation of percentages determined by flow cytometry of Igκ (left) or Igλ (right) positive BM or spleen (SPL) B cells among parent population as stated. Gated B cell subsets: BM - immature B $B220^{+}$ IgD^{-} IgM^{+}, mature B $B220^{+}$ IgD, SPL - B cells $B220^{+}$, IgM^{hi} IgD^{lo} and IgM^{lo} IgD^{hi} B cells. Numbers below graphs and bars show mean values. ****$p \leq 0.0001$, paired t test.

In conclusion, the shift in ratios of Igκ and Igλ light chain usage with progressing maturation in splenic B cells of CD19$^{cre/+}$ Rc3h1-2$^{F/F}$ mice is indicative of superior survival and/or expansion of Roquin1/2-deficient Igλ^{+} compared to Igκ^{+} mature B cells. Alternatively, secondary rearrangements could occur in immature and mature splenic B cells [268].

2.5 *Ex vivo* verification of potential direct and indirect Roquin targets in splenic B cells of CD19$^{cre/+}$ Rc3h1$^{F/F}$-2$^{F/F}$ mice

Since CD23 surface levels are downregulated on splenic B cells of the Mb1$^{cre/+}$ Rc3h1$^{F/F}$-2$^{F/F}$ IgH^{MOG} mouse strain, whereas CD24 surface levels are significantly increased on mature B cells of this strain (Fig. 37), I quantified CD23 and CD24 surface levels on splenic B cells of CD19$^{cre/+}$ Rc3h1-2$^{F/F}$ mice (Fig. 56A, 56B). Flow cytometric analysis confirmed the downregulation of CD23 on all splenic B cell populations investigated, particularly on follicular B cells. CD24 surface expression levels are significantly increased on mature splenic B cell populations in CD19$^{cre/+}$ Rc3h1-2$^{F/F}$ mice (Fig. 56B), confirming the relevance of Roquin1 and 2 in the regulation of CD23 and CD24.

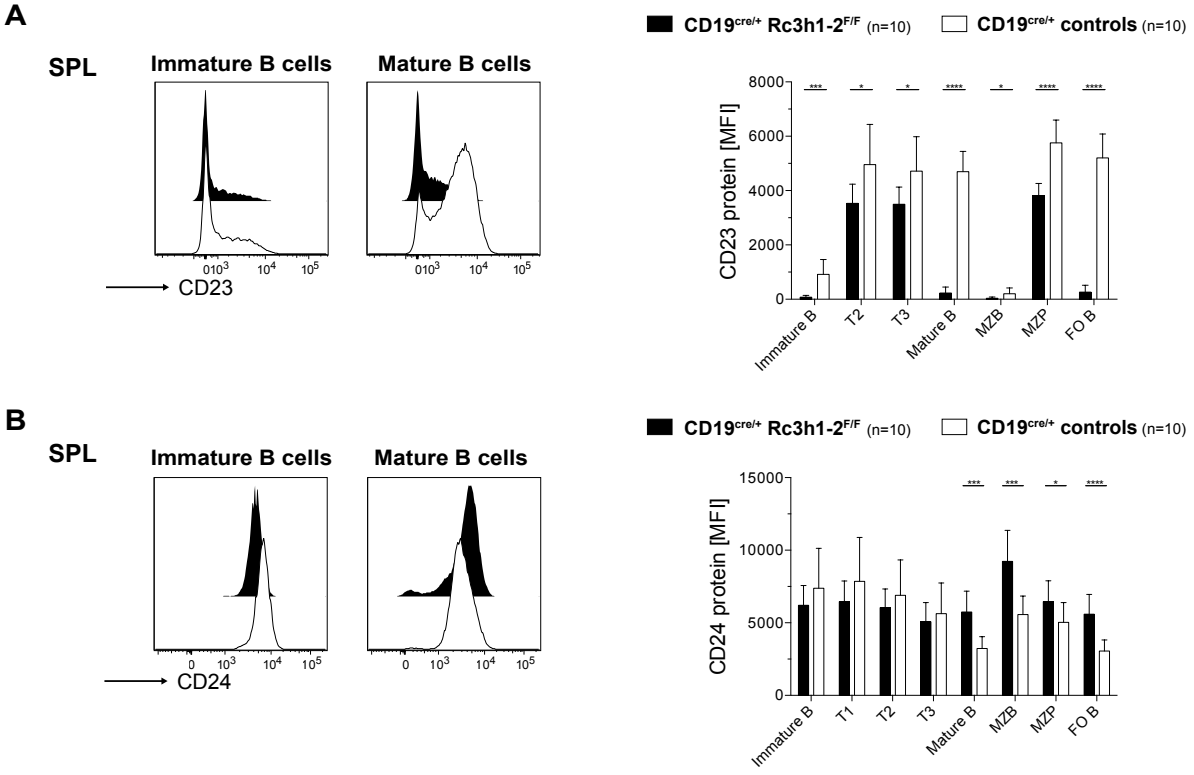

Figure 56: Reduced CD23 surface levels on splenic B cells and enhanced CD24 surface levels on mature splenic B cells in CD19$^{cre/+}$ Rc3h1-2$^{F/F}$ mice.
(A left) Representative flow cytometry histogram showing CD23 surface expression on designated splenic (SPL) B cell subsets. *(Continued on next page)*

(A right) Bar chart representation of CD23 surface levels on indicated B cell populations as measured by flow cytometry. (B left) Representative flow cytometry analysis depicting determination of CD24 surface expression on stated splenic B cells. (B right) Bar chart represenation of CD24 surface levels as analyzed by flow cytometry on designated B cell popoulations. Immature B $B220^{+}$ $AA4.1^{+}$; $CD23^{-}$ IgM^{-} B cells $B220^{+}$ $AA4.1^{+}$ $CD23^{-}$ IgM^{-}; Transitional 1 (T1) $B220^{+}$ $AA4.1^{+}$ $CD23^{-}$ IgM^{+}; T2 $B220^{+}$ $AA4.1^{+}$ $CD23^{+}$ IgM^{+}; T3 $B220^{+}$ $AA4.1^{+}$ $CD23^{+}$ IgM^{-}; Mature B $B220^{+}$ $AA4.1^{-}$; Marginal zone B cells (MZB) $B220^{+}$ $AA4.1^{-}$ $CD1d^{hi}$ $CD21^{hi}$ $CD23^{lo}$; MZ precursors (MZP) $B220^{+}$ $AA4.1^{-}$ $CD1d^{hi}$ $CD21^{hi}$ $CD23^{hi}$; follicular (FO) B $B220^{+}$ $AA4.1^{-}$ $CD1d^{int}$ $CD21^{int}$. MFI: median fluorescence intensity. Bars represent mean values and error bars standard deviation. ****$p \leq 0.0001$, ***$p \leq 0.001$, *$p \leq 0.05$, unpaired t test.

The altered CD23 expression levels could result in biased percentages and cell numbers of splenic B cells which were calculated partially based on CD23 expression (Fig. 51). Yet the general statement on the impairment of maturation holds true as it is supported by the ratio of IgD^{lo} IgM^{hi} to IgD^{hi} IgM^{lo} B cells (Fig. 51).

Previous work by Leppek and colleagues has established the relevance of Roquin in binding and repression of TNFα [196]. I therefore aimed to test whether Roquin1 and 2 play a role in the regulation of TNFα in splenic B cells. As intracellular levels of cytokines, such as TNFα, are low in *ex vivo* cells due to their secretory nature, their concentration can be enriched by culturing the cells in the presence of Brefeldin A (BFA), an inhibitor of the secretory pathway [269]. This procedure enables intracellular flow cytometry-based detection of cytokines. Interestingly, the percentages of various unstimulated (BFA only) *ex vivo* isolated Roquin1/2-ablated B cell populations that stain positive for TNFα are significantly increased (Fig. 57A, 57B). Moreover, the MFI of TNF, correlating to intracellular levels of TNFα, in unstimulated B cells are slightly, yet significantly increased (Fig. 57A, 57C). I do not observe an increase in percentage of $TNF\alpha^{+}$ Roquin1/2-deficient B cells in Phorbol 12-myristate 13-acetate (PMA) and Ionomycin-stimulated (PMA/Iono/BFA) *ex vivo* isolated B cells (Fig. 57A, 57B), but the increase TNF MFI is also observed in stimulated *ex vivo* isolated B cells (Fig. 57C). As expected, *ex vivo* isolated T cells express TNFα only after stimulation. To my surprise, while about 50% of control T cells express cytolasmic TNFα, there is less than 30% and thus significantly fewer $TNF\alpha^{+}$ T cells from $CD19^{cre/+}$ $Rc3h1\text{-}2^{F/F}$ mice which also express lower levels of TNFα (Fig. 57B, 57C). The increase of TNFα in unstimulated Roquin1/2-deficient B cells does not result in altered serum levels of TNFα in untreated $CD19^{cre/+}$ $Rc3h1\text{-}2^{F/F}$ mice (Fig. 57D), suggesting that *in vivo* Roquin proteins do play a rather small role in the regulation of serum TNFα in the absence of an external stimulus.

IL-6 can be secreted by nearly every cell type of the immune system and critically shapes the mature B cell compartment as well as the post-activation development of B cells [270]. IL-6 mRNA is degraded following binding of the endonuclease Regnase-1 (Zc3h12a) to a

stemloop motif in its 3'UTR [271] and repression of *IL-6* mRNA following Roquin binding has been shown *in vitro* [207]. As there is an overlap in Regnase and Roquin target motifs [201], I wanted to investigate if Roquin1 and 2 play a role in the regulation of IL-6 by B cells *in vivo* (Fig. 58).

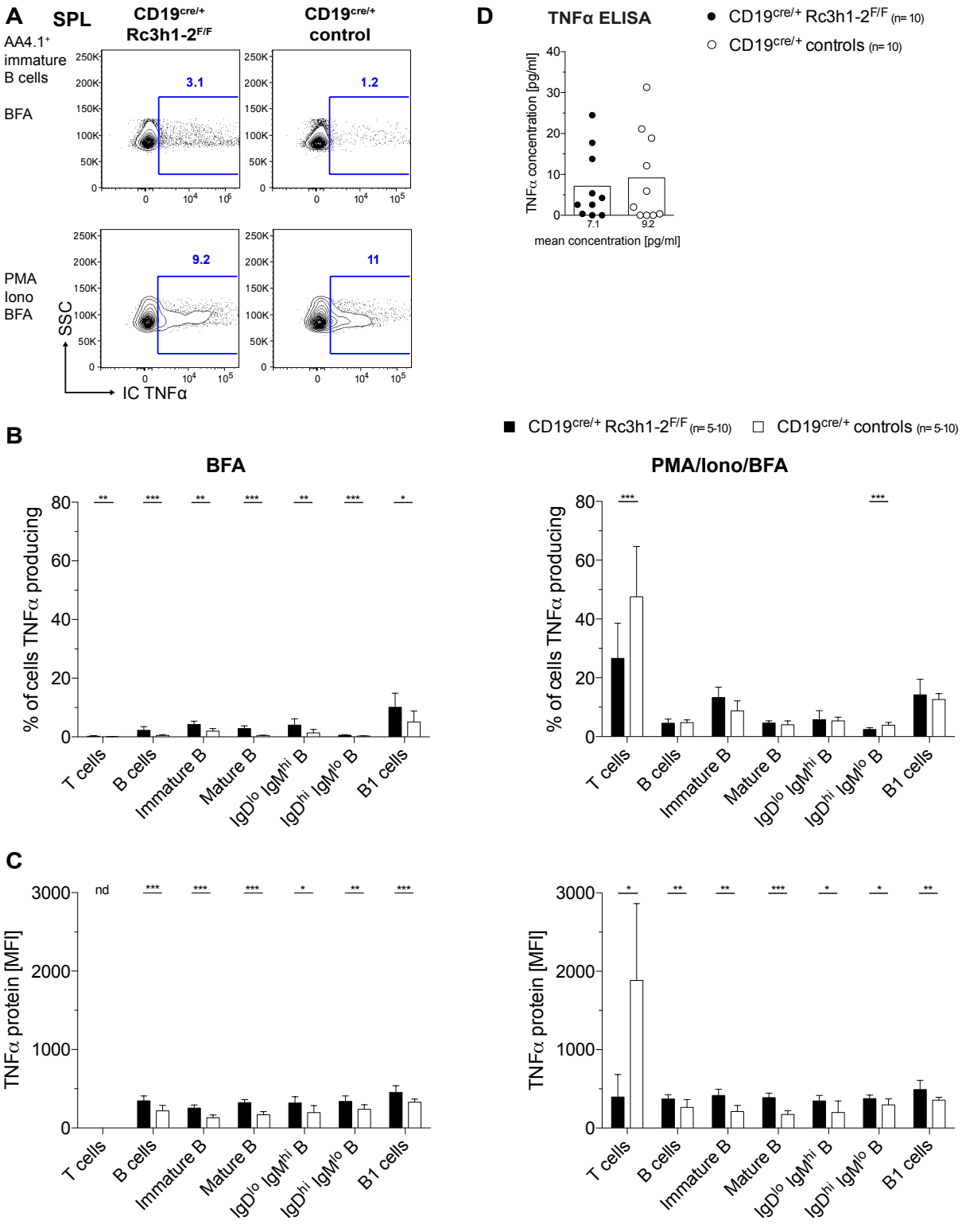

Legend on the next page

Figure 57 (previous page): Investigation of TNFα expression in B cell subsets of CD19$^{cre/+}$ Rc3h1-2$^{F/F}$ mice. For analyses depicted in (A), (B) and (C) *ex vivo* splenocytes were stimulated for 4-6h in Brefeldin A (BFA) or BFA, Phorbol 12-myristate 13-acetate (PMA) and Ionomycin (Iono). (A) Representative flow cytometry analysis depicting intracellular gating strategy for TNFα-producing cells. (B) Percentage of TNFα-producing cells among indicated cell population after stimulation with BFA only (left) or with BFA, PMA and Iono (right) as determined by flow cytometry. (C) Bar chart representation of intracellular TNFα protein levels as analyzed by flow cytometry after BFA (left) or BFA, PMA and Iono (right) treatment in the indicated lymphocyte populations. (D) Serum titer of TNFα as determined by ELISA. T cells TCRβ$^+$; B cells B220$^+$; Immature B B220$^+$ AA4.1$^+$; Mature B B220$^+$ AA4.1$^-$; B1 cells CD19$^+$ B220^{lo}. SPL: spleen; MFI: median fluorescence intensity; nd: not detected. Bars represent mean values and error bars standard deviation. ***p ≤ 0.001, **p ≤ 0.01, *p ≤ 0.05, unpaired t test.

There is a significant increase in the percentage of intracellular IL-6$^+$ unstimulated (BFA), mature splenic *ex vivo* isolated B cells from CD19$^{cre/+}$ Rc3h1-2$^{F/F}$ mice and a trend for an increase in immature B cells (Fig. 58A, 58B). Quantification of intracellular IL-6 levels in total lymphocyte populations showed a significant increase in mature B cells and a tendency for an increase in immature B cells. Similarly, after stimulation (PMA/Iono/BFA) the ratio of IL-6$^+$ Roquin1/2-deficient immature B cells is significantly higher (Fig. 58B). However, the overall intracellular IL-6 levels are approximately similar between stimulated and unstimulated cells for every analyzed B cell population (Fig. 58C), indicating that IL-6 induction after stimulation with PMA and Iono was not very efficient. Moreover, the observed marginal changes in IL-6 producing cells as well as total IL-6 levels suggest Roquin proteins play only a minor role in the regulation of IL-6 expression in B cells. Accordingly, there are no changes in the IL-6 serum levels of untreated CD19$^{cre/+}$ Rc3h1-2$^{F/F}$ mice (Fig. 58D).

In addition to deregulated CD23 and CD24 surface levels, splenic Roquin1/2 double-deficient B cells express significantly higher surface levels of the high affinity IL-2 receptor chain CD25, also a marker of proliferation (Fig. 59A). To investigate the surface phenotpe of activated Roquin1/2-deficient B cells further, I analyzed various cell surface activation markers on purified B cells, both unstimulated and upon over night stimulation with different B cell mitogens (Fig. 59B). As expected, the surface levels of CD25, CD69, CD80, CD86 and MHC class II are significantly higher on unstimulated B cells of CD19$^{cre/+}$ Rc3h1-2$^{F/F}$ mice, reinforcing the concept of a general hyperactivation of Roquin1/2-deficient B cells. Remarkably, CD25 generally upregulated to a lesser extent upon stimulation in double-deficient compared to control B cells. Moreover, CD25, CD69 and CD86 are significantly less upregulated after stimulation through the BCR (αIgM), whereas CD80 is significantly more upregulated on B cells of CD19$^{cre/+}$ Rc3h1-2$^{F/F}$ mice following stimulation via the BCR (Fig. 59B).

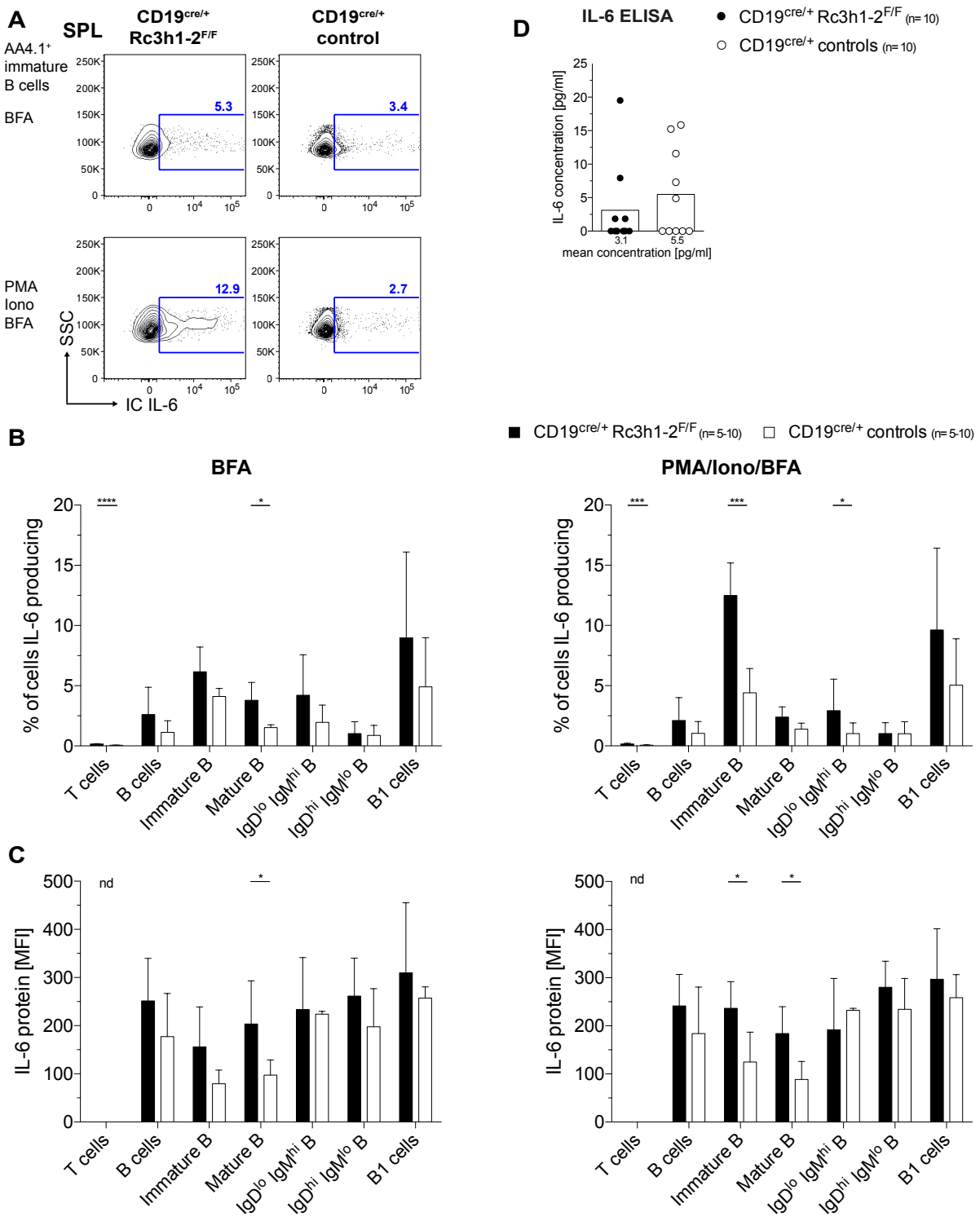

Figure 58: Analysis of IL-6 expression in B cell subsets of CD19$^{cre/+}$ Rc3h1-2$^{F/F}$ mice.
For analyses depicted in (A) and (B) *ex vivo* splenocytes were cultured for 4-6h in BFA or PMA, Iono and BFA. (A) Representative flow cytometry plots of IC IL-6-expressing cells. (B) Flow cytometrically determined proportion of IL-6-producing cells as percentage of cell population indicated after stimulation with BFA only (left) or with BFA, PMA and Iono (right). (C) Bar chart representation of intracellular IL-6 protein levels as analyzed by flow cytometry after BFA (left) or BFA, PMA and Iono (right) treatment in the indicated lymphocyte populations. (D) Serum titer of IL-6 as determined by ELISA. T cells TCRβ$^+$; B cells B220$^+$; Immature B B220$^+$ AA4.1$^+$; Mature B B220$^+$ AA4.1$^-$; B1 cells CD19$^+$ B220^{lo}. SPL: spleen; MFI: median fluorescence intensity; nd: not detected. Bars represent mean values and error bars standard deviation. ****p ≤ 0.0001, ***p ≤ 0.001, *p ≤ 0.05, unpaired t test.

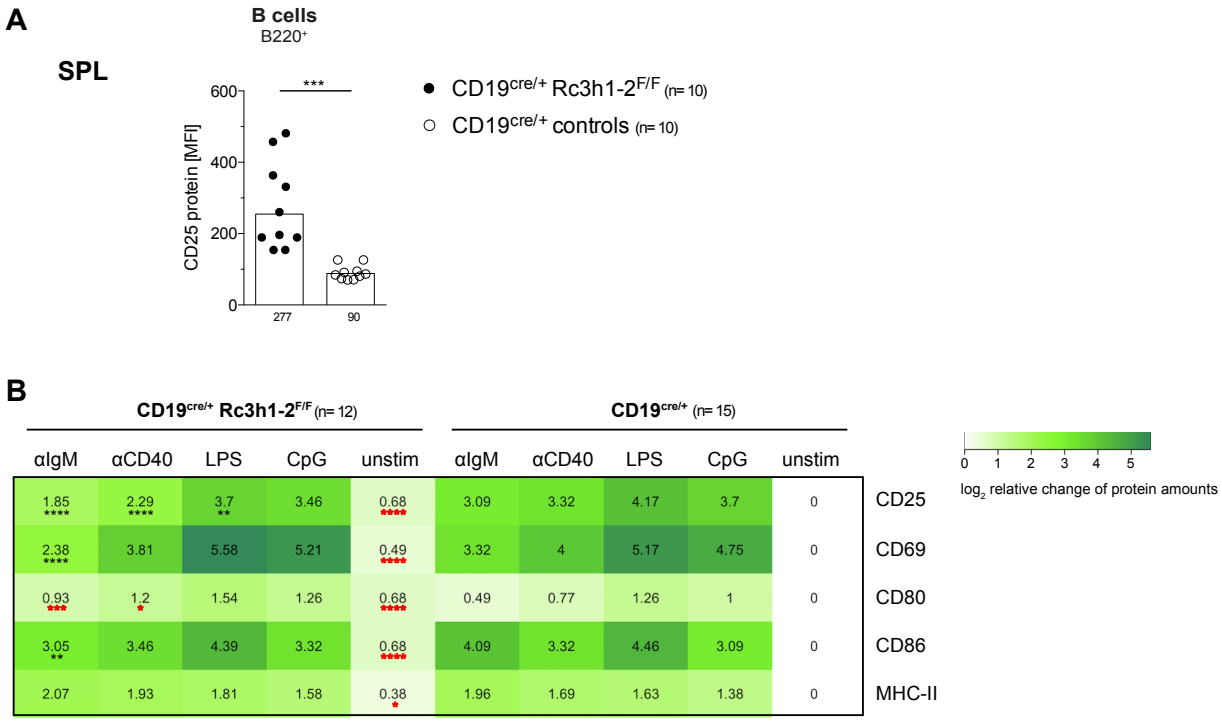

Figure 59: Regulation of activation cell surface markers on B cell purified from CD19$^{cre/+}$ Rc3h1-2$^{F/F}$ and control mice.

(A) Surface expression levels of CD25 on splenic *ex vivo* B cells as determined by flow cytometry. (B) Heatmap representation of log_2-transformed values of geometric means of relative changes of activation marker protein amounts for CD19$^{cre/+}$ Rc3h1-2$^{F/F}$ mice and CD19$^{cre/+}$ controls. Levels of indicated activation markers were assessed by flow cytometry after over night stimulation with stated stimuli in MACS-isolated splenic B cells and normalized to unstimulated (unstim) CD19$^{cre/+}$controls. SPL: spleen; MFI: median fluorescence intensity. Bars and numbers below graph represent mean values. ****p ≤ 0.0001, ***p ≤ 0.001, **p ≤ 0.01, *p ≤ 0.05, unpaired t test. Red * indicate a significantly increased upregulation in B cells of CD19$^{cre/+}$ Rc3h1-2$^{F/F}$ mice compared to controls while black * mark a significantly reduced upregulation in these B cells.

In conclusion, unstimulated naive B cells isolated ex vivo from CD19$^{cre/+}$ Rc3h1-2$^{F/F}$ mice appear to be hyperactivated including increased surface expression of prototypical activation markers such as CD69, MHC-II, CD80 and CD86 as well as increased TNFα production. However, upon stimulation most of the hyperactivated status is lost and in part turns into a hypoactivated status, especially upon BCR stimulation.

2.6 Increased T cell and myeloid compartments in the spleens of CD19$^{cre/+}$ Rc3h1$^{F/F}$-2$^{F/F}$ mice

In line with the hypothesis of cell-extrinsic effects mediated by hyperactive Roquin1/2-deficient B cells the numbers of CD69^{+} T cells are significantly increased in CD19$^{cre/+}$ Rc3h1-2$^{F/F}$ mice (Fig. S29). Moreover, percentages and absolute numbers of naive CD4^{+} and CD8^{+} T cells are significantly reduced while those of CD4^{+} and CD8^{+} effector memory-like T cells are significantly increased. The T_{reg} cell-containing CD4^{+} CD25^{+} T cell is also expanded in this mouse line. Furthermore, I analyzed the myeloid compartment (Fig. S30). All splenic myeloid populations are strongly increased in percentage and cell number (Fig. S30A). Furthermore, as observed in Mb1$^{cre/+}$ Rc3h1$^{F/F}$ -2$^{F/F}$ mice, there is a trend for an increase of the total cell number of peritoneal mast cells (Fig. S30B) stemming from an increased cellularity of the peritoneal cavity in CD19$^{cre/+}$ Rc3h1-2$^{F/F}$ mice.

Summary of the most important findings of part 2

In conclusion, later onset of Roquin1 and 2 ablation in the CD19cre-based experiments compared to the Mb1cre-based experiments, leads to significant production of splenic B cells in the former. This shows, that in absence of a complete block in B cell development at the pre B and immature B cell stages, Roquin1/2-deficient mature B cells can be produced. Yet, peripheral B cells in CD19$^{cre/+}$ Rc3h1-2$^{F/F}$ mice have a clear maturation defect and Roquin1/2-deficient mature B cells are counterselected. Furthermore, peripheral Roquin1/2-deficient B cells appear hyperactivated in the absence of stimulation and these cells shown signs of altered BCR signaling.

3. Unraveling structural principles of mRNA binding by Roquin proteins

3.1 Structural analysis of ROQ, a novel RNA-binding domain

The second focus of my thesis, the structural characterization of Roquin-mediated mRNA binding, was initiated and yielded exciting new insights before various other groups reported the structure, essentially ending our own efforts [188, 197, 205-208]. The entire data on crystallization as well as the figures on peptide structures presented in this thesis were generated by Dr. Christian Benda, a research fellow in the group of Prof. Dr. Elena Conti. I performed all the molecular cloning and cellular validation analyses. I would like to acknowledge this joint effort in the subsequent part of my thesis. In addition, the premature termination of the project is the reason for the absence of a table containing collected data and refinement statistics.

Since the ROQ domain in the first description of Roquin1 was predicted exclusively on the basis of sequence conservation and the original experiments to analyze Roquin-mediated binding did not exclude involvement of additional parts of the protein, we wanted to biochemically and functionally investigate the RNA binding domain of murine Roquin1 [161, 165, 192].

Based on interspecies homology of the ROQ domain sequence various different domain boundaries were suggested (Fig. 60A) [161, 165, 192]. To delineate the structural boundaries of the RNA-binding domain of Roquin1 we performed subtilisin-mediated, limited proteolysis of different constructs expressing the ROQ domain. Proteolysis performed on constructs N-term1 and N-term2 reproducibly yielded a stable protein fragment spanning amino acids 174-326 (ROQ). Subsequently, we solved the crystal structure of the ROQ domain to a resolution of 1.6Å (Fig. 60B left). Potential interaction with the negatively charged phosphate backbone of RNA substrates is indicated by the presence of a positively charged surface grove (Fig. 60B right). Moreover, a structural winged helix (WH) motif covering amino acids K259 to S265, reminiscent of winged helix-turn-helix proteins such as the RING ubiquitin ligase cullin and other proteins, was uncovered (Fig. 60B left) [272].

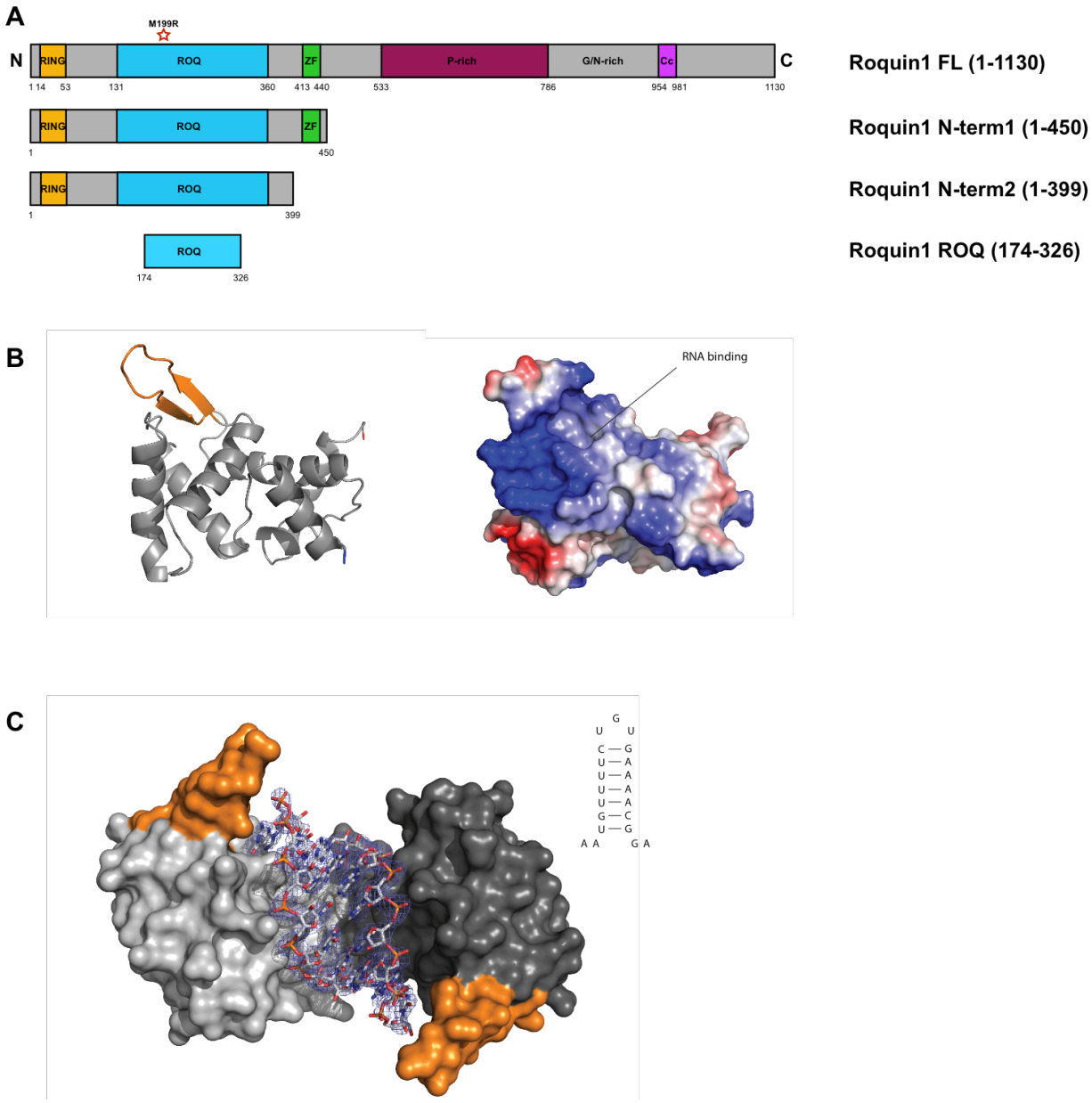

Figure 60: The ROQ domain suffices for binding CDE RNA.
I performed design and cloning of expression constructs for structural analyses (A). The entire crystallization and structure analysis was performed by Dr. Christian Benda (B, C). (A) (Roquin1 FL) and the three variations in length (N-term1, N-term2, ROQ) used for this study as defined from limited proteolysis. The boundaries of the novel ROQ domain are stated as they were defined by interspecies homology at the beginning of our investigations [196]. ZF: zinc finger; P rich: proline-rich sequence; G/N-rich: glycine/asparagine-rich sequence; Cc: coiled-coil region. Numbers state length in amino acids (aa). (B left) The crystal structure of the ROQ domain (aa 175-321) of mouse Roquin1 was solved at 1.6Å resolution. This domain folds into a helical core (gray), which weakly resembles armadillo repeats, and a beta-hairpin protrusion (orange). (Ribbon representation with N- and C-terminus colored blue and red, respectively). (B right) Electrostatic surface potential mapped on the ROQ domain (same orientation as on the left) revealing a positively charged surface patch that could be shown to be involved in RNA binding. (C) The crystal structure of the ROQ domain bound to the constitutive decay element (CDE) P2-L2 stem-loop RNA of TNFα (insert) was solved at 3.3Å resolution. The structure shows how the CDE RNA (orange stick model, shown with its electron density map) folds into a stem-loop (previously shown by [196]) and is recognized and bound between two copies of the ROQ domain (light and dark gray).

We aimed at qualitatively assessing binding of this ROQ core structure to the TNFα CDE [196]. To this end, we crystallized the CDE in complex with the ROQ domain and solved the structure to a resolution of 3.3Å (Fig. 60C). Strikingly the asymmetric unit contained dimeric ROQ bound to the CDE (the binding site was later termed A site in [207]. Results of preparative gel filtration analyses of the subtilisin-digested constructs N-term1 or N-term2 in presence or absence of CDE-RNA combined with the dimeric state in the asymmetric unit of the crystals generated in both scenarios suggest that the ROQ domain may harbor the potential to form homodimers (data not shown). However, analytical size exclusion chromatography (SEC) performed independently on undigested construct N-term1 in the group of Dr. Sabine Suppman in the core facility of the Max-Planck-Institute suggested a monomeric state of Roquin1 in solution (data not shown).

The general hairpin structure of the CDE of TNFα was confirmed (Fig. 60C). Recognition of the CDE by the ROQ domain occurs mainly via sequence-independent contacts to RNA bases or the sugar-phosphate backbone. In this structure, the 5' half of the CDE is coordinated via interactions of S238, K239 and T240 with the phosphate backbone, whereas Q247, Y250 and R251 appear to coordinate the RNA via base-interaction. Additionally, L217 appears to be an essential amino acid in the interface between the two units of the dimer. Interestingly, our analysis did not reveal the position and binding of the CDE triloop structure (Fig. 60C), yet the prominent position of the "wing" residues (K259-S265) suggested them as promising interactors of the loop. Overall, the structure of the apoenzyme (Fig. 60B) is very similar to that of the RNA-ROQ complex. A search for structural homology of similar folds demonstrated that the ROQ domain constitutes a novel RNA-binding fold. The ROQ construct alone contains a functional ROQ domain sufficient for structure-specific binding of the TNFα CDE that occurs largely irrespective of the nucleotide sequence.

A larger ROQ fragment termed structure 2, in complex with the CDE was also obtained upon limited proteolysis of N-term2 in complex with the RNA (Fig. 61). Structure 2 covers approximately amino acids 100 to 321 and was solved at a resolution of 3.3Å. Interestingly, the CDE was bound at a different site (termed B site in [207]) compared to the ROQ construct in structure 1. Superposition of structure 1 and 2 demonstrates that structure 2 comprises structure 1. Moreover, the novel B site is composed in parts by C-terminal helices present in structure 1 and a set of N-terminal helices new in structure 2 including S315 and S319. Preliminary analysis suggested that while recognition of the CDE RNA in the A site is specific for a stemloop structure, dsRNA is recognized in the B site. This part of the project

was discontinued upon publication of a series of papers describing both A and B site in detail [197, 203, 205-207].

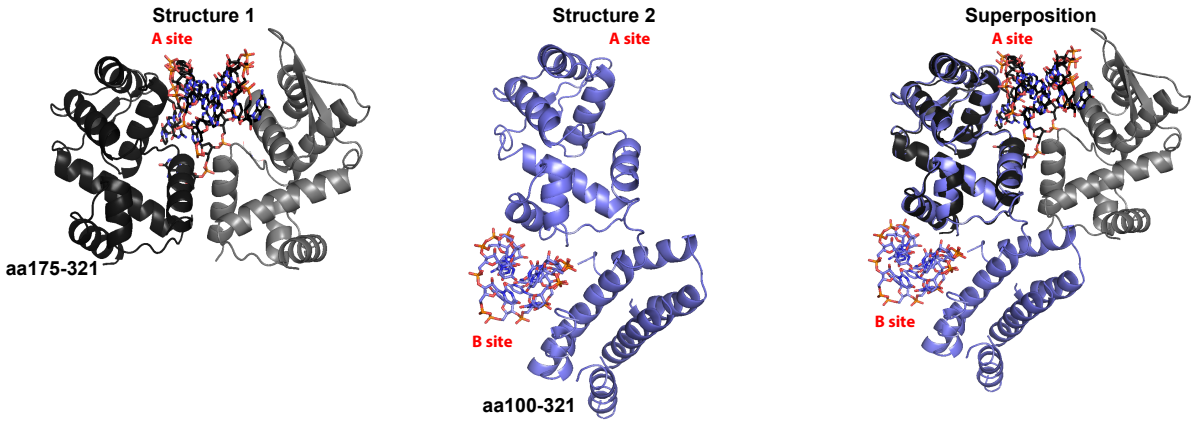

Figure 61: The ROQ domain comprises two separate RNA-binding sites.
Structure 1 (aa 175-321) as shown in Fig. 60 and structure 2 (aa 100-321) solved at 3.3 Å resolution both in complex with constitutive decay element (CDE) stem-loop RNA (orange). The additional N-terminal helical domain contained in structure 2 was found to coordinate CDE dsRNA together with a helical domain shown in structure 1 revealing a novel RNA binding site absent in structure 1. The two binding sites for RNA were termed A site or B site, respectively [207]. Superposition of the two structures illustrates the site of the additional N-terminal domain of structure 2 as well as the relative location of the two sites and interaction in coordinating RNA.

3.2 Mutational analysis of the ROQ-RNA interaction

Subsequently to analysis of structure 1, we performed mutational analysis of the CDE-ROQ interaction to investigate the importance of single contact sites of protein and RNA. In initial experiments, we knocked-out Roquin1 and 2 in murine mast cells and subsequently virally complemented the cells with wild type or mutated Roquin1 co-expressing GFP protein (Fig. 62). Protein expression of ROQ-mutants compared to ROQ-wild type (wt) was indirectly assessed by means of GFP levels, which was at least equal to wt (data not shown). We monitored Roquin1 mRNA degradation capacity by measuring normalized changes of the mRNA targets *Nfκid*, which had previously been shown to carry even 2 CDE motifs in its 3'UTR [196], and EBV-induced gene 3 (EBI3), which Dr. Klaus Heger, a colleague in the Schmidt-Supprian laboratory, had identified as a novel Roquin target in mast cells (Fig. 62).

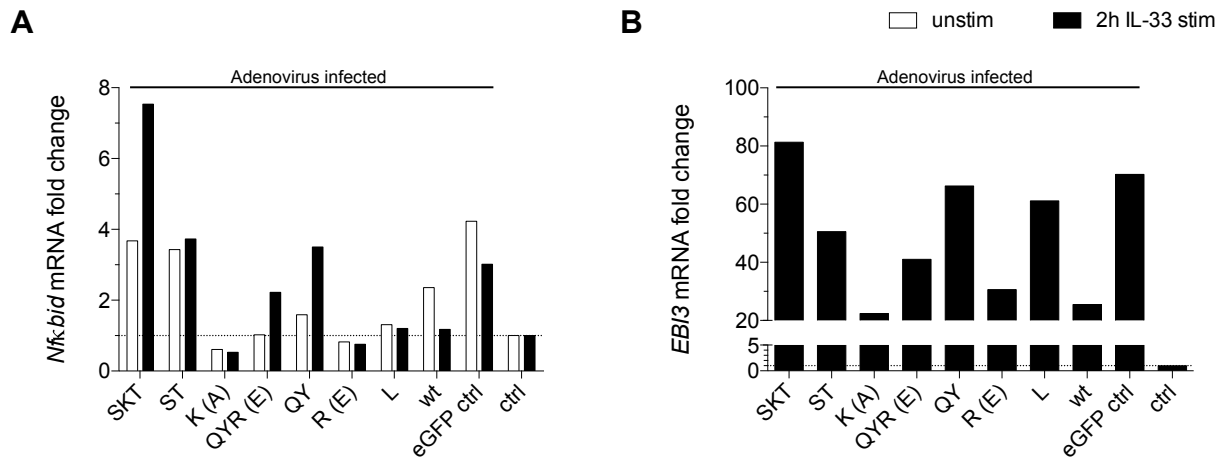

Figure 62: Mutational structure-function analysis of mouse Roquin1 in murine mast cells.
Kitcre$^{ERT2/+}$ Rc3h1-2$^{F/F}$ CAR$^{StopFL/StopFL}$ mast cells were generated and treated as described [228]. Briefly, after culture for 4d in 4-hydroxy tamoxifen (4-OHT) to induce Cre activity resulting in ablation of Rc3h1 and 2 and expression of the Coxsackie Adenovirus receptor (CAR) on the cell surface, mast cells were cultured for 3 days in 4-OHT free media. Next, 10 x 10^6 mast cells were infected with adenoviruses transducing Roquin1/2 deficient mast cells with different Roquin1 mutants and wild type Roquin at a multiplicity of infection (MOI) of 100. The employed adenoviruses co-expressed GFP from an internal ribosomal entry site (IRES). Two days after infection GFP positive mast cells were flow cytometrically purified and either left unstimulated (unstim) or stimulated for 2h with 10ng/ml IL-33 (2h IL-33 stim) before RNA was prepared. GFP MFIs of ROQ-mutants transduced matched at least the MFI of ROQ-wt (data not shown). mRNA levels of (A) *Nfκbid* and (B) *EBI3* were determined and normalized to Roquin1/2-deficient non-infected control mast cells (ctrl). The following Roquin mutants were transduced: SKT S238A K239E T240A; ST S238A T240A; K (A) K239A; QYR (E) Q247A Y250A R251E; QY Q247A Y250A; R (E) R251E; L L217Y; wt wt Roquin1; eGFP ctrl eGFP only control; MFI median fluorescence intensity, GFP green fluorescent protein.

Additionally, we quantified changes of target mRNAs following IL-33 stimulation to potentially identify changes in dependence on certain protein-RNA contacts. Interestingly, mutants S238A K239A T240A (SKT) and S238A T240A (ST) lost their repressional capacity of *Nfκid* mRNA already in the unstimulated setup and are therefore very likely to contribute to the binding of RNA in site A (Fig. 62). Following stimulation, mRNA levels of *Nfκid* and EBI3 increased even further for SKT, potentially indicating a role of K239 in improving binding and decay of targets. The Q247A Y250A R251E (QYR) and Q247A Y250A (QY) failed to repress *Nfκid* and EBI3 mRNA only after stimulation, with higher mRNA levels for the QY mutant, possibly indicating that reversing the charge through the R251E mutation results in improved coordination over an H_2O molecule in the QYR compared to the QY mutant.

Moreover, we generated a cell culture reporter system for application in Roquin1/2-loxP-flanked or-ablated mouse embryonic fibroblasts (MEFs) (Fig. 63A). In this reporter system, the fluorescent proteins eGFP and Neptune are expressed from the same construct, but from independent promoters and eGFP expression was generated to be regulable by action of

Roquin proteins by inserting the wild type *Nfκid* tandem CDE or a mutated version 3' of the eGFP coding sequence. In an initial experiment, we generated Roquin1-2$^{F/F}$ MEFs carrying wt and mutated *Nfκid* reporter constructs. We then ablated Roquin1 and 2 in these MEFs by His-TAT-NLS-Cre (HTNC) treatment and measured eGFP and Neptune levels. We could clearly demonstrate regulation of the wt reporter by Roquin proteins (Fig. 63B). Upon ablation of Roquin1 and 2 by HTNC the geometric mean of the ratio of eGFP to Neptune expression strikingly increased. Surprisingly, also the mutated reporter displayed some degree of regulation by Roquin1 and 2, albeit at a reduced level (Fig. 63B), possibly due to the remaining three proximal basepairs in each stem of the CDE. Having shown that in this reporter system eGFP expression can be tightly regulated by Roquin, we tested lentiviral complementation of Roquin1/2-deficient MEFs. The lentiviruses used place expression of the gene of interest under control of the 5x upstream activating sequence (5xUAS). Therefore, in our setup expression of wild type Roquin or Roquin mutants could be induced by the addition of 4-hydroxy tamoxifen (4-OHT), inducing nuclear translocation of GEV16 and ensuing induction of transcription from the 5xUAS promoter [234, 235]. However, in parallel experiments we observed that the lentiviral gene of interest is not induced in all treated cells that carry the lentivirus. In a pilot experiment, induction of wild type-ROQ expressing Roquin but not induction of a S238A K239E T240A Q247A Y250A R251E-ROQ expressing mutant resulted in eGFP repression in some of the wt *Nfκid* reporter MEFs (Fig. 63C). We also observed downregulation of eGFP levels in some of the MEFs containing the mutated *Nfκid* reporter system, similar to the previous result (Fig. 63B). The partial effects of Roquin regulated eGFP in the reporter MEFs are most likely due to the incomplete induction of wild type and mutant Roquin proteins by our inducible lentiviral system. Although strongly suggestive, our experiments do not formally establish that binding of Roquin to RNAs is required for post-transcriptional regulation of the employed read-outs, as we did not perform electromobility shift assay (EMSA) analyses.

Summary of the most important findings of part 3

In summary, we made many novel observations regarding the RNA-binding ROQ domain in terms of novel structural fold, structural motifs contained, mode of binding, stem loop RNA in site A and dsRNA in site B, as well as the suspected amino acids involved in these interactions. Our findings were confirmed and extended by the published ROQ structures. Furthermore we evaluated Roquin1/2 mediated regulation of EBI3 providing evidence for its regulation by Roquin proteins.

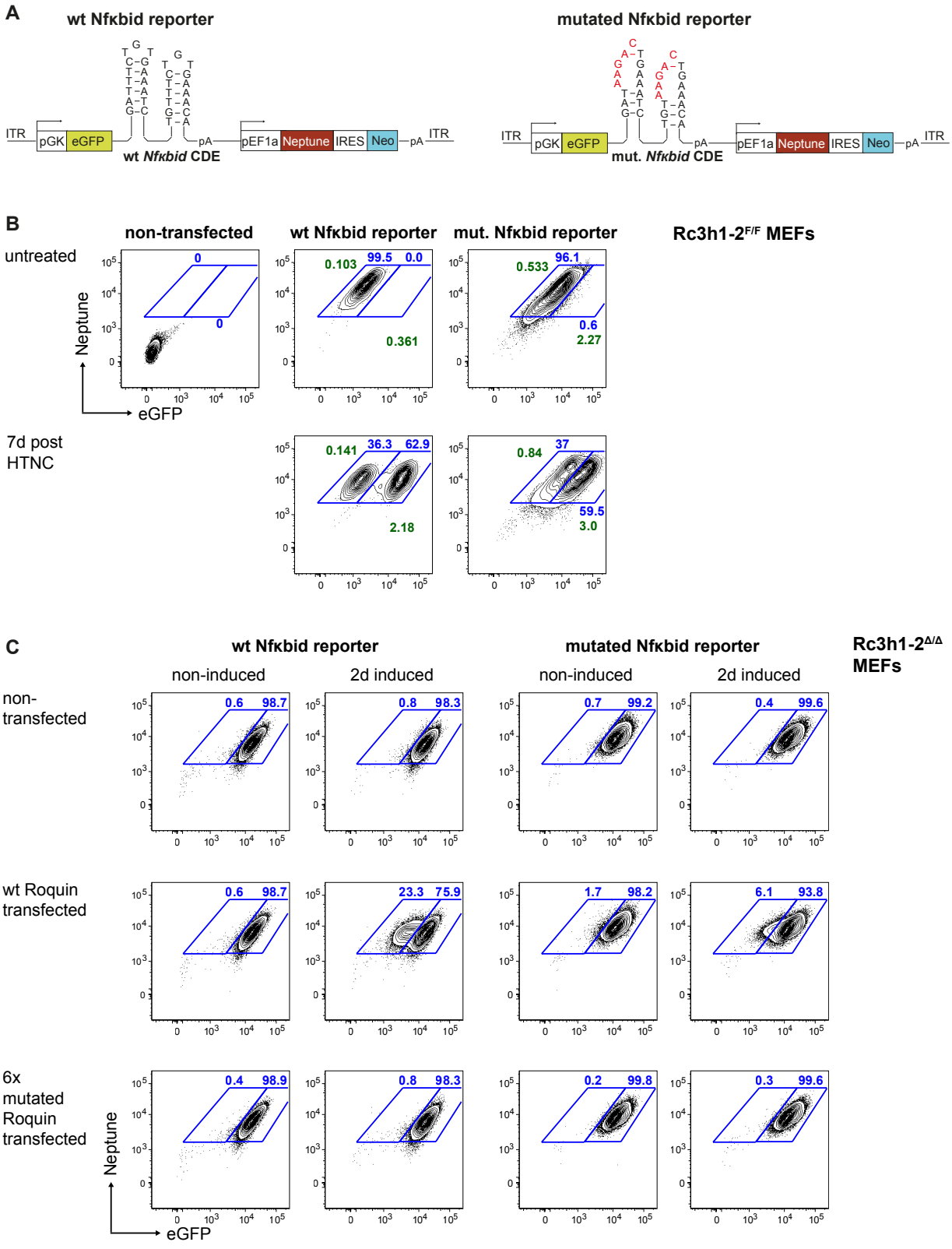

Figure 63: Functional study of mouse Roquin1 and 2 emplyoing a Roquin-regulable reporter in murine endothelial fibroblasts (MEFs).

(A) Schematics of the cloned Roquin-regulable reporter in which a part of the 3'UTR of *Nfκbid*, the only mouse mRNA described [196] to contain a tandem constitutive decay element (CDE), was cloned 3' of eGFP. Hence eGFP protein expression is under control of CDE-based regulating factors such as Roquin1 and 2. Two versions of the reporter were cloned, one with the *Nfκbid* wt CDE sequence and one in which essential bases (highlighted in red, [196]) for Roquin mediated repression were mutated. *(Continued on next page)*

Neptune, a second fluorescent protein, is expressed independently of eGFP from the same construct without regulatory 3' UTR. MEFs with ITR-mediated stable integration of the reporter were generated by co-transfection of PiggyBac transposase and selected with neomycin. (B) Representative flow cytometric analysis of an experiment testing regulability of eGFP expression in the described setup. Rc3h1-2$^{F/F}$ MEFs carrying either no reporter (non-transfected), the wt reporter or the mutated reporter were treated with HTNC to induce Rc3h1-2 ablation and thus reduction of Roquin1/2-mediated repression of eGFP. eGFP versus Neptune expression was analyzed 7d post treatment by flow cytometry. Numbers in green represent the geometric mean of the MFI ratios of eGFP to Neptune in the respective gates. Cells that remain low in eGFP protein levels most likely still contain Roquin proteins. (C) Flow cytometry-based pilot experiment for reintroduction of mutated Roquin1 into reporter-expressing Rc3h1-2$^{\Delta/\Delta}$ MEFs. MEFs were infected with lentiviruses allowing 4-OHT-induced expression of Roquin1 mutants. 4-OHT treatment induced nuclear localization of GEV16, which resulted in transcription of Roquin1 driven by a 5xUAS promoter. Wt or 6x mutated Roquin1 (S238A K239E T240A Q247A Y250A R251E) were transduced. 2d after Roquin1 induction eGFP versus Neptune expression was determined. ITR inverted terminal repeats; UTR untranslated region; HTNC His-TAT-NLS-Cre; Δ ablated, 4-OHT: 4-hydroxy tamoxifen, 5xUAS: 5x upstream activating sequence.

V. Discussion

Most of the previous work on the function of the RNA-binding proteins Roquin1 and 2 in the immune system has focused on their role in T lymphocyte differentiation and function either by T cell-specific ablation studies or analyses of the Roquin1 mutant *sanroque* mouse strain. In my PhD thesis, I present the first extensive *in vivo* analyses of the role of Roquin1 and 2 during B cell development (Part 1.) and during maturation and activation (Part 2.) by loss-of-function studies. Moreover, I demonstrate my own efforts at investigating the structure of the RNA-binding ROQ domain and unraveling novel RNA targets to further enhance our understanding of the importance of post-transcriptional gene regulation in B cell immunology (Part 3.).

1. Roquin family proteins are central regulators of B cell lymphopoiesis in the bone marrow and early B cell physiology

Graded loss of Roquin alleles impairs or blocks B cell lmyphopoiesis at different developmental time points. Emerging evidence has highlighted that transcriptional networks, which integrate external cues, do not suffice to orchestrate proper B cell development on their own and that at least miRNA-dependent post-transcriptional gene regulatory mechanisms play essential roles [227, 273, 274]. When work on this study commenced, ICOS was the only relevant validated *in vivo* target of the mRNA binding protein Roquin1, resulting from work in the *sanroque* mouse strain [161, 162, 166, 275], mechanistic *in vitro* studies [165, 192], systemic Roquin1 ablation or specific ablation of Roquin1 in T cells, B cells and the entire hematopoietic immune system [212]. Evidence steming from the *sanroque* mouse in which the autoimmune phenotype had been rescued by selective ablation of T_{FH} cell development indicated roles of Roquin proteins outside of the T cell compartment. In fact, specific ablation of Roquin1 in B cells using CD19cre, a Cre-knock-in mouse strain ideally suited to address the function of conditional alleles in mature B cells [238], resulted in increased splenic B cell numbers. On the other hand, ablation of Roquin1 in hematopoietic precursor cells led to reduced B cell development in the bone marrow [212].

Hence, I reasoned that specific ablation of Roquin1 in early development employing Mb1cre should yield a definitive picture of the function of Roquin1 in early B cell lymphopoiesis. Moreover, the striking degree of conservation of the N-terminal part, which harbors the E3 ubiquitin ligase function as well as the novel RNA-binding ROQ domain, of Roquin1 in its paralog Roquin2 as well as the cytoplasmic localization of both paralogs [192, 202] strongly argued for redundant functions between Roquin1 and Roquin2. Hence, I investigated how graded inactivation of Roquin alleles affects early B cell development. Strikingly, loss of both alleles of Roquin2 has no obvious effect on B cell development in the bone marrow. On the other hand inactivation of both Roquin1 alleles impaired the pre to immature B cell transition, whereas additional ablation of one Roquin2 allele reduced the transit of pro to pre B cells. Strikingly, B cell-specific complete knockout of Roquin1/2 culminates in a developmental block at the pre B cell stage. Noteably, I also repeatedly failed to obtain IL-7 dependent (IL-7d) B cell lines of $Mb1^{cre/+}$ $Rc3h1^{F/F}$-$2^{F/F}$ mice in contrast to the generation of IL-7d B cell lines from control mice (data not shown). Moreover, deficiencies of other mediators of B cell development, resulting in a similar block at pro to pre B cell transition, permitted the generation of IL-7d B cell lines [276]. I speculate that the striking inability of Roquin1/2-deficient large pre B cells to maintain high surface levels of IL-7Rα may be related to this inability through preventing the extensive proliferation required for emergence of immortalized cells. In constrast, cell numbers of prepro B cells in $Mb1^{cre/+}$ $Rc3h1^{F/F}$-$2^{F/F}$ mice and pro B cell numbers in the $CD19^{cre/+}$ Rc3h1-$2^{F/F}$ mouse line are increased at the onset of Cre-mediated Roquin1/2-ablation (Fig. 6, 49). Surprisingly, in both cases I did not observe an increase in survival or in proliferation in the respective subsets. Furthermore IL-7Rα expression is not changed at any pro B cell stage in $Mb1^{cre/+}$ $Rc3h1^{F/F}$-$2^{F/F}$ mice (Fig. 19). A similar developmental defect in pro to pre B cell transition was observed in mice with Mb1cre-mediated ablation of Jun activation domain-binding protein 1 (JAB1) ($Mb1^{cre/+}$ $JAB1^{F/F}$) [277]. JAB1 deneddylates and thereby regulates cullin-based ubiquitin-dependent protein degradation [277]. Likewise, a lack of proliferation was observed following IL-7 stimulation of rescued, Bcl2 transgenic pro B cells from $Mb1^{cre/+}$ $JAB1^{F/F}$ mice [277].

In addition to showing the functional consequences of Roquin1-ablation in conjunction with additional ablation of Roquin2 alleles in this thesis, I also demonstrated B cell specific roles for Roquin2. Mice with systemic knockout of Roquin2 were investigated with regard to total splenic $B220^{+}$ B cell numbers, which did not show significant differences [191]. I show here that the number of mature recirculating B cells in the bone marrow of $Mb1^{cre/+}$ $Rc3h2^{F/F}$ mice (Fig. S2) are significantly reduced. Moreover, the splenic B cell population in these mice

tends to be reduced (Fig. S3). The milder effects of Roquin2 compared to Roquin1 deficiency might relate to their respective protein amounts, as Roquin2 is significantly lower expressed in the spleen compared to Roquin1 [191].

Relevance of highly efficient Mb1cre-mediated deletion of *Rc3h1/2 genes*. The early onset and very high efficiency of *Rc3h1/2* ablation in $Mb1^{cre/+}$ $Rc3h1^{F/F}$-$2^{F/F}$ mice appears essential for uncovering the specific block between the pro and pre B cell stages. The high efficiency of ablation already in pro B cells, which is essentially identical with that in pre B cells, indicates that inactivation of *Rc3h1/2* alleles already occurs in $CD19^{-}$ prepro B cells (Fig. 14A). The near absence of Roquin1/2-deficient B cells post the immature stage (Fig. 7, Fig. 8) correlates with levels of non-recombined, intact *Rc3h1 & 2* mRNA remaining stably low in double-deficient immature B cells compared to pre B cell stage (Fig. 14A). This indicates most remaining pre B cells have inactivated all four alleles of Roquin1/2 in $Mb1^{cre/+}$ $Rc3h1^{F/F}$-$2^{F/F}$ mice and counterselected Roquin-expressing cells cannot expand. This result in conjunction with the significantly lower percentage of CAR^{+} double-deficient large but not small pre B cells, compared to control large pre B cells (Fig. 14C, 14D), indicates specific deficits at the large pre B cell stage, characterized by pre-BCR signals.

Reduced CAR surface staining on Roquin1/2 double-deficient pro, immature, mature and especially large pre B cells compared to controls (Fig. 14B), indicate negative selection at these developmental stages. As potentially 18% of pre B cells retain one allele of either *Rc3h1 or 2* together with the potential absence of negative selection at the small pre B cell stage (discussed below), I cannot formally exclude that 18% of small pre and ensuing B cell stages, which I have analyzed, still expressed residual' amounts of Roquin proteins. However, B cell development ceases at the immature B cell stage in $Mb1^{cre/+}$ $Rc3h1^{F/F}$-$2^{F/F}$ mice, but B cells that retain one allele of Roquin2 ($Mb1^{cre/+}$ $Rc3h1^{F/F}$-$2^{F/wt}$ mice) can develop into subsequent stages (Fig. 7, 8). This indicates that on-going very efficient Cre-mediated recombination eventually inactivates all present conditional Roquin alleles. It is remarkable that the small pre B cell stage, the stage when neither the pre-BCR nor the BCR are expressed on the surface, is the only stage at which CAR expression is not reduced in bone marrow B cell subsets of $Mb1^{cre/+}$ $Rc3h1^{F/F}$-$2^{F/F}$ $R26^{CARStopFL}$ compared to controls (Fig. 14C, 14D). One could envision many explanations for this observation. For instance, CAR^{+} small pre B cells have not co-ablated all alleles of *Rc3h1 & 2* or recombination is on-going in double-deficient small pre B cells, a stage at which they are not subject to negative selection as indicated by unchanged CAR expression (Fig. 14C, 14D). Alternatively, double-deficient CAR^{+} small pre B cells become stalled at this developmental stage and cannot develop into immature B cells or the

negative selection pressure against Roquin1/2-deficient B cells is very specific to pro, large pre and immature B cell stages, whereas those cells that have developed into small pre B cells have escaped this negative selection. It seems even possible that the higher percentage of CAR expressing cells of double-deficient small pre B cells in contrast to double-deficient large pre B cells might also indicate a selective advantage. However, I consider the last possibility rather unlikely, as I did not observe a strong advantage with regard to proliferation or viability (Fig. 26-28) in double-deficient small pre B cells and the percentage of Roquin1/2-deficient small pre B cell numbers compared to control small pre B cell numbers is lower than for large pre B cells (Number of large and small pre B cells in $Mb1^{cre/+}$ $Rc3h1^{F/F}$-$2^{F/F}$ mice is 25% (large pre B) and 10% (small pre B) of that in control mice) (Fig. 6).

Double-deficient large pre B cells exhibit many defects around the pre-BCR checkpoint including IL-7Rα expression (Fig. 19), proliferation (Fig. 28, 30, 31) and upregulation of IRF4, an essential transcription factor for exit of the cell cycle and initiation of IgL rearrangement [278]. Therefore, I suppose that the observed CAR expression on large and small pre B cells indicates that there is counterselection of double-deficient large pre B cells, which is absent or reduced at the small pre B cell stage. Moreover, as Roquin1/2-deficient B cells fail to develop past the immature B cell stage (Fig. 7, 8), reduced CAR expression at the immature B cell stage on double-deficient B cells might indicate a subsequent checkpoint. This checkpoint would involve surface expression of the BCR and associated signaling pathways and at this checkpoint the development of Roquin1/2-deficient B cells finally ceases completely, potentially due to apoptotis (Fig. 26, 27). This interpretation is supported by the observation that also in $CD19^{cre/+}$ Rc3h1-$2^{F/F}$ mice there is an impaired development subsequent to the immature B cell stage (Fig. 49, 54).

CAR expression is more reduced on FO and GC B cells compared to the innate-like B cells in spleen and peritoneal cavity of $Mb1^{cre/+}$ $Rc3h1^{F/F}$-$2^{F/wt}$ $R26^{CARStopFL}$ compared to control mice (Fig. S4). B2 and B1 B cells differ in their requirement for certain signaling pathways, such as IL-7 and BAFF induced signaling [95] that are differentially required for development and maturation. The observed difference in CAR expression levels might therefore reflect a differential sensitivity to the consequences of Roquin1/2 ablation in the precursors of FO, MZ or B1 B cells. Alternatively, the ratio of *Rc3h1/2*-incompletely ablated CAR^+ cells might be higher in innate-like B cell subsets. Yet, the precise underlying reason(s) remain to be investigated.

Furthermore, the experiments employing the $R26^{CARStopFL}$-allele clearly established that the phenotype is B cell-intrinsic and does not stem from Mb1cre-mediated recombination in T

cells, as frequencies of CAR^+ T cells tend to be even reduced in $Mb1^{cre/+}$ $Rc3h1^{F/F}$-$2^{F/F}$ $R26^{CARStopFL}$ mice compared to $Mb1^{cre/+}$ $R26^{CARStopFL}$ controls (Fig. S4).

Absence of µHC in Roquin1/2-deficient pre B cells. In this PhD thesis, I clearly show that expression of µHC is defective in pre B cells of $Mb1^{cre/+}$ $Rc3h1^{F/F}$-$2^{F/F}$ mice (Fig. 15, 16), but I do not observe such a reduction of µHC in $B220^{lo}$ $ckit^+$ pro B cells (Fig. 12B, 12C) or in $CD19^+$ late pro B cells (data not shown). This may be due to residual amounts of Roquin1/2 protein sufficient to support initial µHC expression in late pro B cells, which might be degraded and diluted during further developmental stages resulting in defective Igµ expression at the large pre B cell stage. However, to more definitively identify late pro B cells I suggest to include the surface markers CD24 and BP-1 in future analyses.

I considered that Roquin1/2-deficient B cells might have a defect in splicing of the V_HDJ_H exon to the C_H segment exons, which as a direct effect of Roquin proteins would require their nuclear localization [279, 280]. However, as the prerearranged V_HDJ_H exon of the IgH^{MOG} allele, which also requires splicing to the C_H exons, is readily processed and expressed in B cells of $Mb1^{cre/+}$ $Rc3h1^{F/F}$-$2^{F/F}$ IgH^{MOG} mice (Fig. 40), splicing and processing of the µHC pre-mRNA does not seem to be affected.

Furthermore, Roquin has a role in stabilizing the miRNA-RNA-induced silencing complex (RISC) [197, 275]. Thus, one might hypothesize that impaired RISC function could hinder µHC expression, and also be involved with the other deficiencies observed, in Roquin1/2-deficient large pre B cells. Similar to the absence of mature recirculating B cells in the bone marrow of $Mb1^{cre/+}$ $Rc3h1^{F/F}$-$2^{F/F}$ IgH^{MOG} or $Mb1^{cre/+}$ $Rc3h1^{F/F}$-$2^{F/F}$ IgH^{MOG} $IgL^{D23\kappa}$ mice (Fig. 34, 44), insertion of a pre-rearranged IgHEL BCR does not rescue the development of mature recirculating Dicer/miRNA-deficient B cells [227]. Pro B cells deficient for Dicer, the essential enzyme involved in the second miRNA-processing step preceding formation of the RISC, do not exhibit a defect in intracellular µHC expression [227]. To my knowledge, no data on µHC expression in miRNA-deficient pre B cells is available and Roquin1/2-deficient pro B cells exhibit unchanged µHC expression (Fig. 15). Therefore, I cannot exclude the contribution of absent miRNA-mediated gene regulation upon ablation of Roquin paralogs to the developmental block observed.

It remains to be determined if impaired V(D)J recombination is a consequence of ablation of Roquin paralogs, as well as whether V_H usage is affected. Since the IgH^{MOG} allele appears to be able to rescue B cell development at the large pre B cell stage, defects in V_HDJ_H rearrangement might contribute to the developmental defect in $Mb1^{cre/+}$ $Rc3h1^{F/F}$-$2^{F/F}$ mice.

Residual Roquin protein levels in pro B cells of $Mb1^{cre/+}$ $Rc3h1^{F/F}$-$2^{F/F}$ mice might impede analysis of V_HDJ_H recombination in these cells. Therefore, I suggest to investigate V(D)J rearrangement in prepro and pro B cells of $Vav^{cre/+}$ Rc3h1-$2^{F/F}$ mice. Alternatively, a Hoxb8FL cell culture system [281] of Rc3h1-$2^{F/F}$ $R26^{CARStopFL}$ B cell precursors cells could be employed. In such cells Roquin proteins would be completely ablated by treatment with HTNC or a genetically encoded or virally delivered inducible Cre prior to the induction of the B cell fate in vitro and in vivo.

A potential role of Mb1cre-inflicted genotoxycitiy in the phenotype. Recently, a group reported a similar developmental block in mice in which MZB1, an endoplasmatic reticulum (ER)-resident protein specific to B cells, was ablated using Mb1cre [282]. This group observed a striking block in pro to pre B cell transition, massively reduced splenic B cell numbers as well as peritoneal B1 and B2 cell numbers [282]. Genotoxicity of the Mb1cre allele, which was exposed through MZB1-deficiency in this mouse strain was demonstrated to result in increased ER-retainment of the pre-BCR and as a consequence significant reduction of the ratio of surface $\lambda5^+$ μHC^+ cells among $CD19^+$ $B220^+$ bone marrow cells [282]. Therefore, it seemed possible that similar accumulation of Cre-induced toxicity in the absence of Roquin paralagogs results in the intermediate developmental impairments or the block observed in $Mb1^{cre/+}$ $Rc3h1^{F/F}$-$2^{F/F}$, $Mb1^{cre/+}$ $Rc3h1^{F/F}$-$2^{F/wt}$, $Mb1^{cre/+}$ $Rc3h1^{F/F}$ and $Mb1^{cre/+}$ $Rc3h2^{F/F}$ mice (Fig. 6, 7, S2).

However, this mechanism is rather unlikely to be relevant for the pro to pre B cell block in $Mb1^{cre/+}$ $Rc3h1^{F/F}$-$2^{F/F}$ mice for several reasons: First, Roquin paralogs have been shown to localize to the cytoplasm and not to the ER or ribosomes in all cell types analyzed so far [201, 202]. Second, we did observe significant numbers of intracellular $\lambda5^+$ μHC^+ Roquin1/2-deficient pro/pre B cells, indicating that at this intracellular $\lambda5^+$ stage the intracellular µHC expression is not affected (Fig. 16). Third, I did not observe a comparable increase in apoptosis in pro B cells, which was suggested to result from Cre-genotoxicity in the MZB1 mouse model [283]. Fourth, cell numbers of the respective B cell subset in which Cre-mediated recombination is initiated in the Mb1cre model and the CD19cre model are actually increased (Fig. 6, 49). Fifth and most importantly, a pre-rearranged IgH chain, the IgH^{MOG} allele, enabled the generation of significant numbers of immature B cells (Fig. 30), while a similar approach failed in the case of $Mb1^{cre/+}$ $Mzb1^{F/F}$ mice [282]. In this context, it is important to note that the rescue experiments involving the knockin IgH^{MOG} and $IgL^{D23\kappa}$ alleles clearly established that pre-BCR and BCR are not simple retained in the ER as a consequence of ablation of Roquin paralagos. The pre-BCR is capable of signaling in any

post-ER compartment but the ER itself [48], hence ER-retainment of the pre-BCR upon ablation of Roquin1 and 2 should result in completely abrogated pre-BCR signaling. However, Roquin1/2 double-deficient pro and pre B cells readily transit to the immature B cell stage in the presence of IgH^{MOG} (Fig. 34).

Similarly, absence of BCR surface expression significantly reduces tonic as well as BCR engagement-induced signaling, evidenced by impaired PI3K activity, which results in the inability to prevent the FOXO1-dependent transcription of pro-apoptotic genes [284]. Therefore, BCR retainment would likely be reflected by reduced IgM surface levels as well as increased fractions of pro-apoptotic immature and later stage B cells. However, neither in $Mb1^{cre/+}$ $Rc3h1^{F/F}$-$2^{F/F}$ IgH^{MOG} nor in the $CD19^{cre/+}$ Rc3h1-$2^{F/F}$ mice were IgM surface levels reduced on bone marrow immature and splenic transitional B cells (Fig. 34, 36, 47, 49) and the fraction of pro-apoptotic bone marrow immature B cells was not increased (Fig. S17, S24).

IL-7R and pre-BCR signaling is impaired in double-deficient pro and pre B cells. The signaling circuits in pro and pre B cells are organized to ensure dominance of either the pre-BCR or the IL-7R pathway at a given developmental time point. Proliferation in pro and large pre B cells is largely driven by IL-7R signaling [60]. While the IL-7R is presumably functional in Roquin1/2-deficient $CD19^{+}$ late pro B cells, as judged by unaltered surface expression of IL-7Rα (Fig. 19) and normal cell numbers, IL-7Rα surface expression is dramatically reduced in double-deficient large pre B cells. Moreover, expression levels of IL-7Rα are also reduced on large pre B cells of $Mb1^{cre/+}$ $Rc3h1^{F/F}$-$2^{F/wt}$ mice (Fig. 19), in which B cells are also strongly impaired at the transition from pro to pre B cells (Fig. 6). Therefore, it is possible that impaired signaling downstream of the IL-7R causes the very pronounced defect in proliferation of Roquin1/2-deficient large pre B cells (Fig. 28-31). It would be interesting to attempt to rescue the proliferation phenotype by intercrossing a constitutively active form of STAT5A/B, the predominant signaling mediator downstream of IL-7R activation [61] or infect sorted BM B cells with a constitutively active STAT5A/B prior to the generation of IL-7d cell lines to investigate if this rescues B cell development at the large pre B cell stage and proliferation defects. Furthermore, PI3K signaling, which is essential for pre B cell development [285] might be affected by loss of Roquin proteins, maybe through upregulation of PTEN or other PI3K inhibitors. As *in vivo* proliferation of Roquin1/2-deficient pro B cells, which is independent of PI3K signaling [60], is unaltered (Fig. 28), decreased activity of AKT and therefore nuclear retention of FOXO1 may also explain the increased Bim levels upon ablation of Roquin1 and 2 (Fig. 25). Decreased PI3K signaling

would also explain defects in tonic BCR signaling and effects observed in mature B cells of $Mb1^{cre/+}$ $Rc3h1^{F/F}$-$2^{F/F}$ IgH^{MOG} and $CD19^{cre/+}$ Rc3h1-$2^{F/F}$, such as reduction of follicular B cells, loss of marginal zone and reductions in CD23 surface levels [285].

To my surprise, the strong reduction of IL-7Rα expression does not correlate with an increase of classical mediators of pre-BCR signaling at the large pre B cell stage (Fig. 24). SYK and ZAP70 amplify pre-BCR proximal signaling events and mediate phosphorylation and activation of SLP65, the expression of which is induced upon attenuation of IL-7R signaling [59]. ZAP70 expression levels are not increased in Roquin1/2-deficient Hardy fraction C' cells, the large pre B cell stage, but ZAP70 levels are increased in double-deficient pro/pre, Hardy Fraction D (small pre B cells) and immature B cells (Fig. 24). ZAP70 has been shown to support pre B cell development, albeit less efficiently than SYK, and its expression in bone marrow B cells peaks in large pre B cells [249, 286]. Moreover, $SYK^{-/-}$ bone marrow chimeras exhibit a partial block in B cell development with dramatically reduced immature B cell numbers reminiscent of that exhibited in $Mb1^{cre/+}$ $Rc3h1^{F/F}$-$2^{F/F}$ mice [287, 288]. The onset of this block was shown to occur at the Hardy C to C' transition, the transition from late pro B into large pre B cells and additional absence of ZAP70 results in a complete block at this stage [249]. This complete block is not caused by defective synthesis or assembly of the pre-BCR, but is rather a consequence of defective pre-BCR signaling [249, 289]. Moreover, functional ZAP70 is sufficient to promote generation of approximately 10-fold more immature B cells in $Mb1^{cre/+}$ $Syk^{F/F}$ mice compared to $Mb1^{cre/+}$ $Rc3h1^{F/F}$-$2^{F/F}$ mice, with total numbers based on two femurs, whereas the numbers presented in this thesis are based on two femurs and two tibias [289]. Therefore, the deficiency in Roquin1/2 proteins causes a more severe block than the absence of SYK. This supports the notion that in $Mb1^{cre/+}$ $Rc3h1^{F/F}$-$2^{F/F}$ B cells not just signaling downstream of the pre-BCR is affected, but also events before pre-BCR signaling such as V_HDJ_H recombination or IL-7R signaling.

Furthermore, phosphorylated SLP65 is central for mediating many of the differentiation-inducing effects of pre-BCR signaling [63] and its ablation results in a partial block of B cell development at the pre B cell stage with an increased ratio of cycling large B cells versus small pre B cells [290, 291]. Functions of SLP65 serve to cease proliferation and induce IgL rearrangement [246], including suppression of PI3K activity [63] and induction of Ikaros and Aiolos, which repress transcription of c-Myc, cyclin D3 [248], λ5 and V_{preB} [292, 293].

Pre-BCR signaling additionally induces the expression of BCL6, potentially involving interference of SLP65 with JAK3-STAT5 signaling downstream of IL-7R signaling [294], which results in additional repression of c-Myc. Interestingly, *Bcl6* mRNA has been shown to

be expressed at high levels in naive mature B cells [295] and post-transcriptional control of its expression has been suggested [296]. It is tempting to speculate that *Bcl6* mRNA is also expressed in developing pro and pre B cells and is partially regulated by Roquin paralogs, which could explain the relative increase of BCL6 protein levels in double-deficient bone marrow B cells (Fig. 23). Alternatively, Lee and colleagues have shown indirect upregulation of BCL6 levels in T_{FH} and GC B cells in *sanroque* mice as a consequence of increased IFNγ signaling [167]. Moreover, the *Bcl6* promoter in effector T_H1 cells is bound by STAT5 and BCL6 expression is repressed, following strong IL-2 signaling, while in an IL-2^{lo} environment STAT3, FOXO1 and FOXO3a bind and induce *Bcl6* expression [297]. Repression of *Bcl6* expression by STAT5 binding to the *Bcl6* promoter has also been shown in a B cell lymphoma line [298]. Therefore, it can be envisioned that defective IL-7R signaling results in reduced phosphorylated STAT5 levels and hence increased BCL6 levels in late pro and ensuing B cell stages of $Mb1^{cre/+}$ $Rc3h1^{F/F}$-$2^{F/F}$ mice (Fig. 23).

Additionally, SLP65 was demonstrated to induce the expression of IRF4, which activates surface expression of CXCR4 enabling CXCL12-instructed migration and attenuation of IL-7R signaling [79, 299]. In the present study, I show that induction of IRF4 is impaired in Roquin1/2-deficient large pre B cells (Fig. 21), more specifically in proliferating large pre B cells (Fig. 29). Additionally, CXCR4 and Aiolos upregulation are impaired in this subset, whereas relative BCL6 levels are increased (Fig. 20, 22, 23). Defective μHC expression is likely not the major cause of the developmental block in $Mb1^{cre/+}$ $Rc3h1^{F/F}$-$2^{F/F}$ mice, as evidenced by the set of experiments involving the IgH^{MOG} allele. Moreover, expression of SLC components with ensuing formation of the pre-BCR remains functional upon Mb1cre-mediated ablation of Roquin paralogs (Fig. 15, 16). Therefore, an impaired signaling capability downstream of the pre-BCR is likely to be the main cause of the developmental block upon Roquin1/2 ablation.

In addition, IRF4 and IRF8 are important for IgL chain rearrangement as they induce expression of Aiolos and Ikaros as well as mediate accessibility of the IgL chain loci [69, 264]. Strikingly, the ratios of cells expressing high levels of IRF4 are normal in double-deficient small pre B cells and Aiolos protein levels are even increased in Roquin1/2-deficient $Aiolos^{hi}$ small pre B cells is even increased (Fig. 21, 22). However, IgL chains are absent in pro/pre B cells (Fig. 17). As the pre-rearranged $IgL^{D23κ}$ allele does not rescue immature B cell development (Fig. 44), it is important to note that the developmental block in $Mb1^{cre/+}$ $Rc3h1^{F/F}$-$2^{F/F}$ mice is thus independent of IgL expression, also in the $μHC^{+}$ double-deficient pro/pre B cells. As Aiolos levels in small pre B cells of $Mb1^{cre/+}$ $Rc3h1^{F/F}$-$2^{F/F}$ $IgL^{D23κ}$ are

normal (data not shown), I assume that the increased Aiolos levels in double-deficient small pre B cells stem from absence of IgL expression and are thus a cause of the developmental block (Fig. 22).

Taken together, the differentiation of late pro B cells into immature B cells relies initially on IL-7R signaling and afterwards on pre-BCR signaling [60]. Therefore, I propose that the developmental block around the large pre B cell stage in $Mb1^{cre/+}$ $Rc3h1^{F/F}$-$2^{F/F}$ mice is a consequence of consecutive defects in both pathways. Initially it is presumably the result of a defect upstream of SLP65 signaling, as already large pre B cell numbers in this mouse line are strongly reduced and IL-7R signaling and proliferation are dramatically impaired. Subsequently, defective pre-BCR signaling, which fails to induce IRF4, expression of CXCR4, upregulation of Aiolos and IgL chain expression, contributes to the developmental block [42, 60, 67]. I suggest to specifically investigate the signaling capacities of the pre-BCR in Roquin1/2-deficient pre B cells by examining proximal events, such as SYK and SLP65 expression, phosphorylation of SYK, ZAP70 and SLP65 and measuring Ca^{2+} influx. I plan to perform these experiments in an $SLP65^{-/-}$, $RAG2^{-/-}$ and λ5 triple knockout IL-7d pre B cell line transduced with a 4-OHT (tamoxifen)-inducible $SLP65cre^{ERT2}$, a μHC and λ5 [299]. Roquin1/2 paralogs will be inactivated in this cell line employing CRISPR/Cas9 methodology [300].

Additionally, a potential role for apoptosis remains to be investigated *in vivo*. *Ex vivo* analysis of intracellular Bim expression demonstrated relatively increased Bim levels at all stages of B cell development in $Mb1^{cre/+}$ $Rc3h1^{F/F}$-$2^{F/F}$ mice (Fig. 25). However, *ex vivo* analyses of AnnexinV binding to exposed phosphatidylserine and pancaspase activation (Fig. 26, 27) revealed only a possible mild contribution to the defects in pro and pre B cells, but apoptosis seems to contribute more significantly to the absence of double-deficient immature B cells. I suggest analyzing the expression of MCL1, the most important anti-apoptotic BCL2 family member in pro B cells [301, 302], BCL-xL and BCL2, all shown to be expressed in pro B cells [60]. If apoptosis is relevant for the phenotype I describe in this present thesis, it presumably also contributes to the inability of generating IL-7d cell lines from $Mb1^{cre/+}$ $Rc3h1^{F/F}$-$2^{F/F}$ mice. Hence viral transduction of these antiapoptotic genes into primary cells sorted from the bone marrow of this mouse line prior to generation of an IL-7d cell line might help to understand the role of apoptosis in the developmental block.

Possible mechanisms causing the phenotypes observed in Roquin-deficient B cell lineages include defects in ubiquitination or post-transcriptional regulation of mRNA targets. The regulatory roles of RING E3 ubiquitin ligases in B cell development have

primarily been described with respect to apoptosis or proliferation [277, 303, 304]. For example stabilization of p53 in absence of the RNA-binding RING-type E3 ligase Mdm2 [303] or upregulation of apoptosis-inducing FasL on the surface of pro B cells upon Mb1cre-based ablation of JAB1 [277]. The later model shares many phenotypic traits with $Mb1^{cre/+}$ $Rc3h1^{F/F}$-$2^{F/F}$ mice, a block at the pro to pre B cell transition with deficiencies in µHC expression and lack of peripheral B cells, including B1 cells in the spleen [277]. However, the fraction of proliferative active ($S/G_2/M$ phase) residual pre B cells in these mice is significantly increased in contrast to my observations [277]. In this regard, it would be very interesting to investigate the B cell-specific phenotype of the Roquin1/2 ringless mutations (hypothetical "*Bringless*" mice - $Mb1^{cre/+}$ $Rc3h1^{rin/rin}$-$2^{rin/rin}$) [202]). Such experiments could reveal whether or to what extent post-transcriptional regulation of protein stability by K48-linked poly-ubiquitination of target proteins represents a means how Roquin paralogs control B cell development in the bone marrow.

The developmental block observed in $Mb1^{cre/+}$ $Rc3h1^{F/F}$-$2^{F/F}$ is also reminiscent of the recently published Mb1cre-mediated ablation of *Cnot3*, which affects nuclear and cytoplasmic functions mediated by the CCR4-NOT complex [283, 305]. This suggests that the developmental block is rather a function of the absent cytoplasmic post-transcriptional gene regulation function of Roquin proteins, rather than a consequence of a lack of E3 ligase function. mRNA-binding by the NOT component, which comprises CNOT1, CNOT2 and CNOT3, is a requirement for subsequent association of the CCR4 part to form the mammalian CCR4-NOT complex on a specific mRNA [306]. The CCR4-NOT complex was shown to be involved in all facets of the mRNA life cycle, from synthesis to its best-known function in mRNA degradation [307]. $Mb1^{cre/+}$ $Cnot3^{F/F}$ mice show a block at the pre B cell stage with an even earlier onset already at the late pro B cell stage and a more pronounced reduction of immature B cells [283, 305]. Rescue experiments involving the B1-8^{hi} IgH-knockin allele similarly enabled only the generation of CNOT3-deficient immature bone marrow B cells but not of mature recirculating B cells [283, 305]. However, the two reports on CNOT3-deficient B cells differ in the presented underlying cause of the developmental block. Inoue et al. stated increased p53 stability and defective NMD in pro B cells [305], whereas Yang and colleagues reported the absence of important functions of the CCR4-NOT complex performed in conjunction with EBF1 and resulting dysregulated gene expression, including pre-BCR components, as a contributing factor [283]. In the later study, the authors demonstrated a specific interaction of EBF1 with CNOT3 and assembly of the CCR4-NOT complex [283]. Strikingly, the ablation of Cnot3 resulted in down-regulation of EBF1 mRNA and protein

levels as a result of decreased transcription of EBF1 [283]. Similarly, Roquin paralogs were shown to interact with the CNOT1, 2 and 3, but also with CCR4 part of the CCR4-NOT complex in an RNA independent manner [196, 209]. However, it appears less likely that loss of the Roquin-CCR4-NOT complex will result in reduced transcription, as Roquin proteins have so far been described to localize to the cytoplasm [201], whereas EBF1 is a nuclear transcription factor.

This might indicate that the specific increase of IRF4^{hi} late pro B cells and upregulation of protein levels of IRF4, which carries a CDE motif in its 3'UTR [196], in IRF4^{hi} Roquin1/2-deficient late pro B cells (Fig. 21) is the consequence of absent Roquin-mediated regulation of IRF4 mRNA. That this effect is then overridden, when pre-BCR mediated signaling induces further IRF4 expression. IRF4 upregulation was also observed in Roquin1/2-ablated T cells [191], which was thought to result from increased NF-κB activation downstream of upregulated OX40 surface levels rather than IRF4 mRNA representing a potential novel Roquin1/2 target. The specific upregulation at the late pro B cell stage, when NFκB signaling is dispensable [239, 308], underscores that IRF4 mRNA might be directly regulated post-transcriptionally by Roquin paralogs.

Ectopic over-expression of IRF4 in pro B cells at levels similar to those observed in pre B cells results in premature IgL chain expression and annulment of the order of IgH before IgL chain rearrangement [309]. However, I do not observe a premature induction of IgL expression in late pro B cells (Fig. 17, data not shown), despite levels of IRF4 in IRF4^{hi} Roquin1/2-deficient late pro B cells reaching the levels of IRF4 in IRF4^{hi} small pre B control cells (Fig. 21). This further supports the notion that impairments in IgL chain expression are a consequence of the absence of Roquin paralogs.

2. Roquin proteins regulate the maturation, activation and differentiation of peripheral B cells

Roquin paralogs are important for peripheral B cell maturation. As the specific ablation of Roquin paralogs in early B cell development employing Mb1cre results in a complete developmental block, I investigated whether these proteins fulfill an additional essential function in peripheral B cells maturation employing the CD19cre model. B cell development in the bone marrow of CD19$^{cre/+}$ Rc3h1-2$^{F/F}$ mice is not altered (Fig. 49), most likely due to incomplete Cre-mediated recombination and residual mRNA and protein levels in recombined developing B cells. Peripheral B cell maturation is impaired from the T1 to T2 transition

onwards with strong reduction of FO and MZ B cell numbers, which appears more pronounced in MZ B cells and MZP B cells (Fig. 50, 51). In addition, I observed reduced numbers and cellularity of PPs (Fig. S28A). Furthermore, B1a development is nearly absent in spleen and peritoneal cavity, whereas increased B1b cell numbers result in overall elevated B1 cell numbers (Fig. 52). A similar picture, but somewhat less pronounced is seen in $Mb1^{cre/+}$ $Rc3h1^{F/F}$-$2^{F/F}$ IgH^{MOG} mice (Fig. 39). This increased B1b population affected analysis of total $AA4.1^-$ mature B cells numbers in both models (Fig. 35, 50), such that IgD^{hi} IgM^{lo} splenic B cell numbers reflect the real number of mature B cells. Additionally, some of the analyses involving $AA4.1^-$ mature B cell gating, such as analysis of CD23 and CD24 (Fig. 37, 56) might be partially skewed by this phenomenon.

The reduction of MZ and B1a cells might be the consequence of an essential E3 ligase function performed by the RING domain of Roquin paralogs. Both Roquin1 and 2 were shown to pair with the E2 enzyme UBE2N or Ubc13 resulting in K63-linked polyubiquitin chains *in vitro* [203]. The CD19cre-mediated ablation of Ubc13 similarly shows strong reduction of MZ and peripheral $CD5^+$ B1 cell numbers [214]. *Ex vivo* MACS-sorted $B220^+$ B cells from this mouse model proliferate less in response to mitogenic stimuli, but cell death is increased post-stimulation. However, B cells from $CD19^{cre/+}$ $Ubc13^{F/F}$ mice produce less IL-6 48h post CpG stimulation [214]. Although *IL-6* mRNA was shown to be suppressed by Roquin proteins *in vitro* [207], it cannot be excluded that Roquin1/2-mediated K63 ubiquitination supports IL-6 production in B cells. Here, I did not find increased IL-6 serum levels or strongly increased IL-6 production in stimulated MACS-purified B cells in $CD19^{cre/+}$ Rc3h1-$2^{F/F}$ mice (Fig. 58). However, my stimulation experiment should be repeated using LPS, as PMA/Iono stimulation did not result in increased IL-6 production or percentage of IL-6 expressing cells also in the controls (Fig. 58).

The E3 Ubiquitin ligase function of Roquin paralogs might also be specifically relevant for MZ B cell development, that is critically instructed by Notch2 signaling induced by its ligand DL-1 [310]. Notch activation involves ligand induced proteolytic cleavage steps leading to the liberation and nuclear translocation of the cytoplasmic domain of the respective Notch protein. Proteolytic cleavage by γ-secretase, subsequent to endocytosis of Notch receptors, critically depends on monoubiquitination at K1749 [311], by a not yet identified E3 ligase [312]. However, thymocyte development, which requires Notch1 signaling, was not reported to be impaired in *Tringless* mice [202], which would be expected if Roquin proteins were Notch E3 ligases [313]. Yet, homozygosity for the germline $Rc3h1^{rin/rin}$ mutation results in perinathal death [202] due to similar defects as described for homozygous $Rc3h1^{-/-}$ mice

[212], indicating an important function of the RING domain. A detailed study of *Bringless* mice would help greatly in determining the role of the RING domain of Roquin1 and 2 in maturation of B cells in the periphery.

In addition, the weak interaction of Notch2 with DL-1 was shown to be strengthened significantly by lunatic fringe (LNFG) and manic fringe glycosoltransferes [207]. In the Schmidt-Supprian laboratory, we observed Roquin-mediated regulation of LNFG mRNA in the Roquin1/2-devoid mast cell system (Fig. 62, data not shown), which remains to be confirmed for B cells as well as potential functional consequences.

Surface IgM levels are no reliable readout to assess the cause of shifted ratios of Igκ and Igλ light chain usage with progressing maturation in CD19$^{cre/+}$ Rc3h1-2$^{F/F}$ mice. The reason causing the shift in ratios of Igκ and Igλ light chain usage with progressing maturation in splenic B cells of CD19$^{cre/+}$ Rc3h1-2$^{F/F}$ mice remains to be determined. The occurrence of secondary rearrangements in peripheral B cells is controversial [268]. Hence, the informative value of employed experiments, including a potential downregulation of surface IgM on editing cells, must be scrutinized. IgM levels are not downregulated in any of the analyzed B cell populations of the Mb1$^{cre/+}$ Rc3h1$^{F/F}$-2$^{F/F}$ IgH^{MOG} or the CD19$^{cre/+}$ Rc3h1-2$^{F/F}$ mouse strains. In the former model, general deficits of IgL chain rearrangement and expression seem more relevant (Fig. 41), whereas in CD19$^{cre/+}$ Rc3h1-2$^{F/F}$ mice a shift towards increased Igλ usage with B cell maturation was observed (Fig. 55). This shift occurs in the absence of reduced IgM surface expression in the respective populations, but rearrangement status of the IgL loci and IRF4 expression levels remain to be determined. However, it is now realized that IgM surface levels are no clear indication of ongoing BCR receptor editing, as depending on the avidity of the BCR for a self-antigen, surface IgM expression can be down-modulated to levels resembling those in pre B cells [314, 315] or remain similar to normal surface BCR levels [314, 316, 317]. Hence, it remains to be carefully analyzed if the shift in IgL chain usage in peripheral B cells of CD19$^{cre/+}$ Rc3h1-2$^{F/F}$ mice results from receptor editing or more likely from a preferential survival or expansion of Igλ^{+} cells.

Counterselection of Roquin1/2-deficient B cells in CD19$^{cre/+}$ Rc3h1-2$^{F/F}$ mice. My analyses demonstrate that in splenic B cells protein levels of Roquin1 are significantly higher than those of Roquin2 (Fig. 53), which is in accordance with the general expression of Roquin paralogs in the spleen [191]. To my knowledge this is the first description of expression levels of Roquin paralogs in splenic B cells, in which Roquin1 levels are 2.5 to 3fold increased compared to Roquin, which is a smaller difference in expression compared to the 5fold difference observed in T cells [191]. This finding indicates a significant possibility for

Roquin2 to compensate for loss of Roquin1 in splenic B cells, evidenced by the strongly exacerbated effects in double-deficient cells. The relative residual mRNA expression of Rc3h1/2 in mature splenic B cells isolated from $CD19^{cre/+}$ Rc3h1-$2^{F/F}$ mice is low, indicating efficient Cre-mediated recombination of the Rc3h1-$2^{F/F}$ alleles. Increasing residual Roquin1/2 protein levels as well as decreasing CAR surface expression on the other hand strongly indicate continuous negative selection of Roquin1/2-deficient splenic B cells with ongoing B cell maturation and CD19cre-mediated recombination of the conditional alleles (Fig. 53, 54). The on-going counterselection of Roquin1/2-deficient B cells has to be kept in mind when drawing conclusions from experiments with peripheral splenic B cell populations in $CD19^{cre/+}$ Rc3h1-$2^{F/F}$ mice. However, the fact that Roquin1/2 deregulate CD23 and CD24 expression should enable me to specifically identify B cell populations strongly enriched for Roquin1/2-deficient cells.

The consequences of different degrees of Roquin1/2 deficiencies for B cell activation, differentiation and B cell-extrinsic effects. As observed in $CD19^{cre/+}$ Rc3h$1^{F/F}$ mice [212], $Mb1^{cre/+}$ Rc3h$1^{F/F}$ mice have increased ratios of spontaneous GC B cells in spleen and PPs and also $Mb1^{cre/+}$ Rc3h$1^{F/F}$-$2^{F/wt}$ mice still have normal ratios of GC B cells in PPs, despite their developmental defects (Fig. 13). Furthermore, both strains exhibit a deregulated T cell compartment with increased numbers of cells resembling central-memory and effector-memory $CD4^+$ and $CD8^+$ T cells (Fig. 32), as observed in $CD19^{cre/+}$ Rc3h1-$2^{F/F}$ mice (Fig. S29). Splenic B cells from $CD19^{cre/+}$ Rc3h1-$2^{F/F}$ mice display a primed or pre-activated resting state (Fig. 51-53). The development of follicular as well as B1 cells relies on strong BCR signaling [99, 100, 318] and loss of Roquin paralogs presumably results in a hyperactivated state in (antigen-)naive B cells potentially mirroring some effects of strong BCR signaling. It is possible that this increased BCR signaling contributes to the preferential development of FO and B1b B cells in $Mb1^{cre/+}$ Rc3h$1^{F/F}$-$2^{F/F}$ and $CD19^{cre/+}$ Rc3h1-$2^{F/F}$ mice.
Few extensively proliferating cells suffice to nucleate and initiate GC formation [319]. This indicates that proliferative defects of activated FO B cells could have severe consequences for the generation of GCs and GC B cells. It can be imagined that proliferative defects similar to those observed in in large pre B cells of $Mb1^{cre/+}$ Rc3h$1^{F/F}$-$2^{F/F}$ mice, as well as reduced CD25 expression on resting and stimulated Roquin1/2-deficient B cells (Fig. 59A, 59B), contribute to the significantly reduced GC B cell numbers in these mice and defective generation of Peyer's Patches [M. Kober and D. Rieß, data not shown] (Fig. S28A).
The increase of the T_{reg} cell-containing $CD4^+$ $CD25^+$ T cell pool in the $CD19^{cre/+}$ Rc3h1-$2^{F/F}$ mouse strain might prevent systemic inflammation and might have aided in repressing TNFα

production by T cells in the *ex vivo* stimulation of splenocytes (Fig. 57). Therefore, I propose that Roquin paralogs are critical for repressing B cell activation. Graded reduction in Roquin1/2 protein levels first results in a hyperproliferative B cells state as observed in $Mb1^{cre/+}$ $Rc3h1^{F/F}$ mice with additional reduction in protein levels causing developmental and maturation defects. To test this hypothesis I suggest analyzing $CD19^{cre/+}$ $Rc3h1^{F/F}$-$2^{F/wt}$ mice with regard to development and activation status.

Furthermore, it will be interesting to analyze whether MALT1-mediated regulation of Roquin proteins downstream of the BCR plays a role similar to that observed downstream of the TCR in T cells [198, 199]. In that context it should be investigated whether cleaved Roquin fragments might still fulfill a role of target mRNA sponges, as a dominant negative effect was observed *in vitro* by transfection of N-terminal and C-terminal Roquin1 fragments that stabilized a globin-TNFαCDE$_{37nt}$ hybrid mRNA [196]. Moreover, MALT1 has recently been shown to be required in B cells downstream of BCR signaling for initial GC formation potentially involving MALT1-mediated proliferative and survival effects and plasma cell differentiation [320]. It can be imagined that some of the underlying effects are mediated by deregulated Roquin paralogs, which repress expression of the negative regulators of NF-κB signaling A20 and IκBα *in vitro* [209]. As the underlying defects for the hyperactivated resting state as well as the hypoactivated and hypoproliferative state of peripheral $CD19^{cre/+}$ $Rc3h1^{F/F}$-$2^{F/F}$ B cells remain elusive, I hypothesize that defined protein levels of Roquin paralogs ensure regulation of intricate networks of signaling mediators involving NF-κB family members and proliferation for correct peripheral development, activation and post-activation behavior of B cells.

3. Unraveling structural principles of mRNA binding by Roquin proteins

The crystallization and description of the bipartite architecture of Roquin's RNA-binding regions, comprising the novel RNA-binding ROQ domain and the HEPN domains (Fig. 3) [197, 203, 205-208], precluded our efforts to do so. This architecture, the primarily structure-based mode of recognition as well as relevant amino acids for CDE binding in ROQ and HEPN domain were also identified in our structures 1 and 2 (Fig. 60, 61). Surprisingly, almost all groups that have reported a crystal apo structure of the ROQ domain, also showed two copies of the ROQ peptide in the asymmetric unit. Initially it was suggested that Roquin may dimerize through the ROQ domains enabling the binding of different forms of RNA

[206]. Although our gel filtration experiments initially also pointed towards a dimeric state in solution and reported dimer interfaces appear similar [197, 203], our analytical SEC with lower peptide concentrations revealed a monomeric state (data not shown). However, EBI3, which encodes a subunit of the cytokines IL-27, IL-35 and IL-39 [321], a novel target of Roquin-mediated mRNA regulation is described in this thesis (Fig. 63). B cells express the receptor for the immunemodulatory and -suppressive IL-35 [322]. Moreover, infection or activation induced IL-35 secretion by the recently suggested "i35-Breg" B cell subset has been [323]. It is tempting to speculate that uncontrolled EBI3 upregulation and ensuing IL-35 secretion upon stimulation of *ex vivo* purified $CD19^{cre/+}$ $Rc3h1\text{-}2^{F/F}$ B cells (Fig. 59) contributed to the dampened upregulation of activation markers observed. However, it remains to be investigated if EBI3 is a relevant novel target of Roquin proteins in B cells.

The physiological relevance of the dsRNA binding B site has not been clearly analyzed. Furthermore, it was suggested that the ROQ and the ZF domains of Roquin move together in solution [203], and contributions of the ZF domain to RNA binding domains were also demonstrated [165, 209], however no study has looked further into the molecular interaction of ROQ/ZF and RNAs. With the growing number of cis-regulatory motifs present in target mRNAs, which are bound by Roquin proteins [208-210], I propose to investigate if HEPN/ROQ and ROQ/ZF domains cooperatively bind and scan target mRNAs enabling a more effective recognition of target mRNAs. This analysis could potentially explain the different CDEs proposed [196, 208], which were either based on binding affinity or RNA decay efficiency readouts. Also all reports that showed ROQ interaction with CDE mRNA employed mRNAs that were max. 30 nucleotides long and therefore not suited to address the question of a potential involvement of the B site or the ZF domain in cooperative scanning and binding of target mRNA. I speculate that similar to the importance of defined Roquin protein levels for adequate *in vivo* function, mRNA binding and decay efficiency is encoded by different cis-regulatory motifs in target mRNAs and multiple parts of Roquin facilitating binding and degradation of these mRNAs.

Supplemental figures

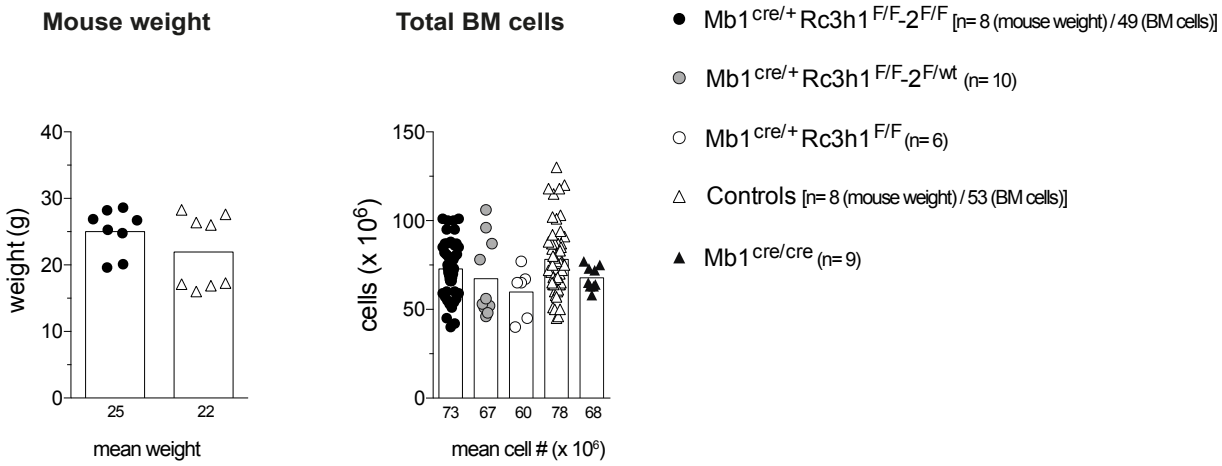

Figure S1: Normal weight of Mb1$^{cre/+}$ Rc3h1$^{F/F}$-2$^{F/F}$ mice and unchanged total bone marrow cell numbers in Mb1$^{cre/+}$ Rc3h1$^{F/F}$-2$^{F/F}$, Mb1$^{cre/+}$ Rc3h1$^{F/F}$-2$^{F/wt}$ and Mb1$^{cre/+}$ Rc3h1$^{F/F}$ mice.
Mouse weight and number (#) of total BM cells. BM: bone marrow. Numbers below graphs and bars indicate mean values.

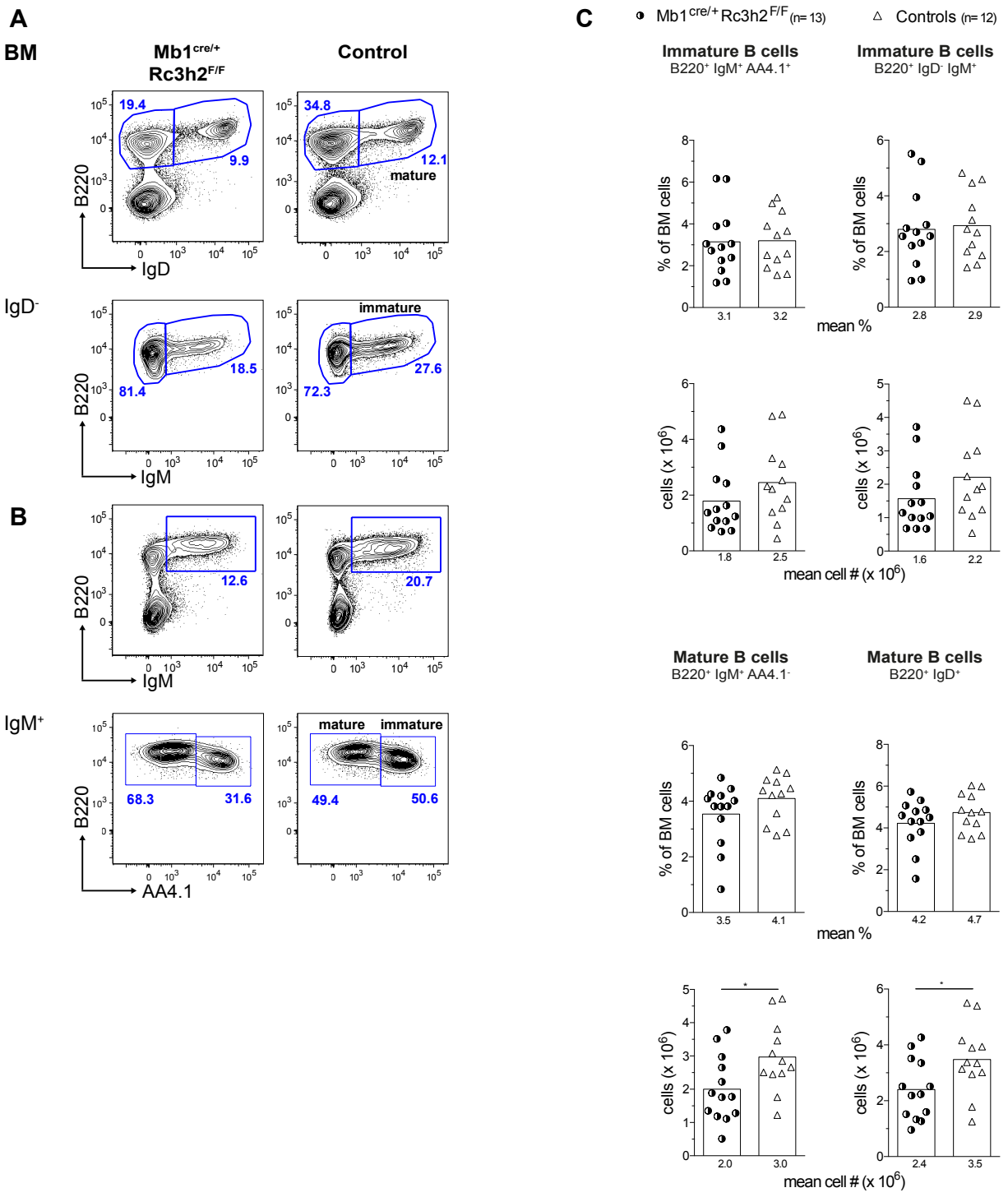

Figure S2: Reduction of mature B cells in the bone marrow of Mb1$^{cre/+}$ Rc3h2$^{F/F}$ mice.
(A) Representative flow cytometry plots of immature and mature bone marrow B cells. (B) Percentages of immature and mature B cells of total BM cells and total immature and mature B cell numbers. BM: bone marrow. Numbers below graphs and bars represent mean values. *p ≤ 0.05, unpaired t test.

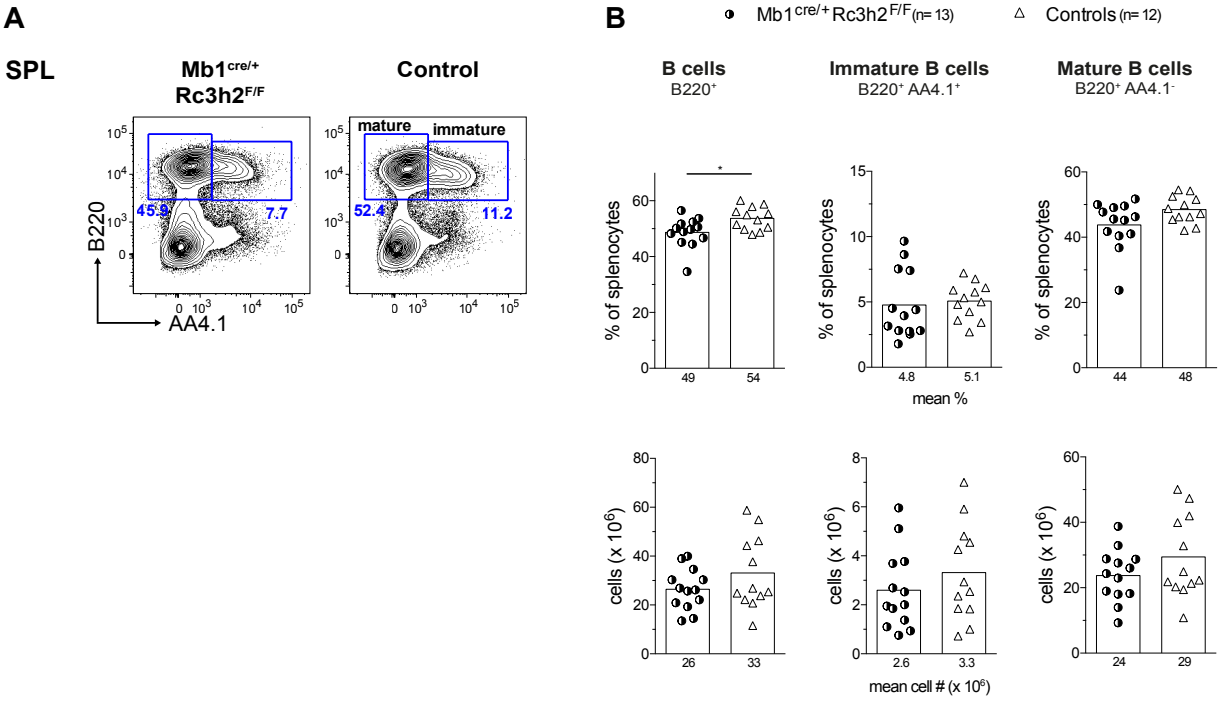

Figure S3: Splenic B cells in Mb1$^{cre/+}$ Rc3h2$^{F/F}$ mice.
(A) Representative flow cytometric analysis and (B) percentages of viable splenic cells and total cell numbers of indicated B cell subsets. SPL: spleen. Numbers below graphs and bars indicate mean percentages and cell numbers (#). *p ≤ 0.05, unpaired t test.

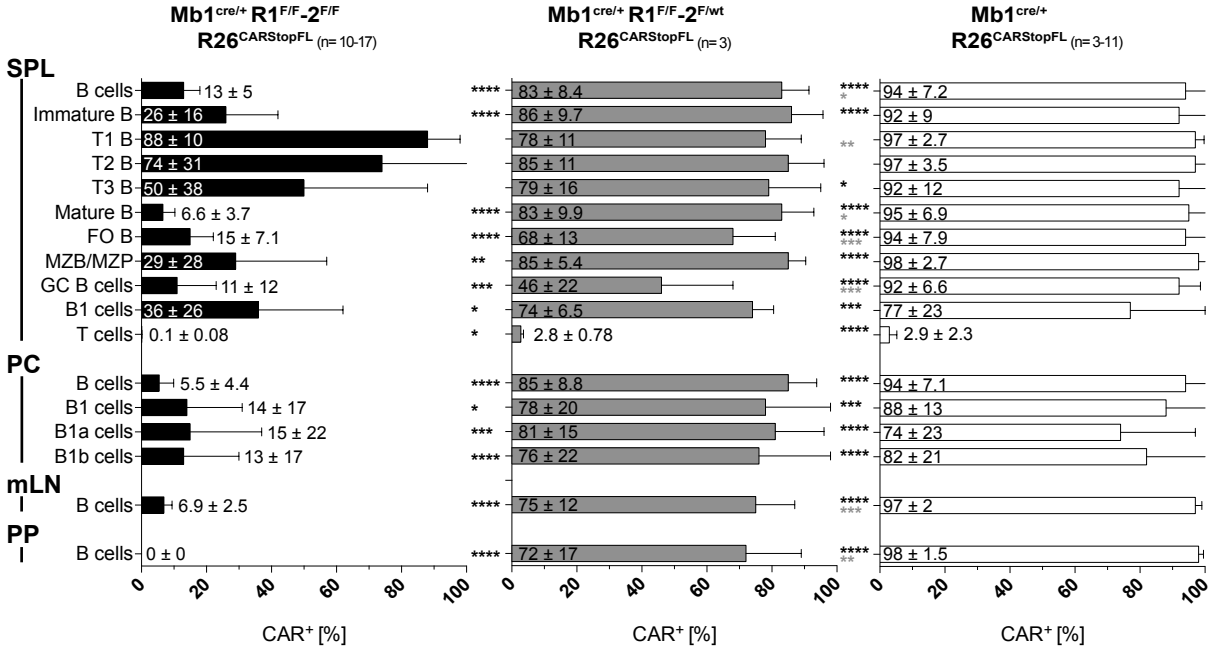

Figure S4: Expression of the R26^{CARStopFL} reporter allele in peripheral B cells and T cells.
Percentages of CAR$^+$ B cells among indicated B and T cell subsets. Specification of CAR$^+$ cells was performed as in Fig. 14. Black * describe significant differences of Mb1$^{cre/+}$ Rc3h1$^{F/F}$-2$^{F/F}$ R26^{CARStopFL} versus Mb1$^{cre/+}$ Rc3h1$^{F/F}$-2$^{F/wt}$ R26^{CARStopFL} or Mb1$^{cre/+}$ R26^{CARStopFL} B cells as designated by position of the *, gray * show significant differences of Mb1$^{cre/+}$ Rc3h1$^{F/F}$-2$^{F/wt}$ R26^{CARStopFL} versus Mb1$^{cre/+}$ R26^{CARStopFL} B cell. CAR signal in the respective cell populations in wild type and Mb1$^{cre/+}$ mice was always < 1% (data not shown). Subset gating: B cells B220$^+$, Immature B B220$^+$ AA4.1$^+$, T1 (transitional T1) B B220$^+$ AA4.1$^+$ CD23$^-$ IgM$^+$, T2 B B220$^+$ AA4.1$^+$ CD23$^+$ IgM$^+$, T3 B B220$^+$ AA4.1$^+$ CD23$^+$ IgM$^-$, Mature B B220$^+$ AA4.1$^-$, FO (follicular) B B220$^+$ AA4.1$^+$ CD1d^{int} CD21^{int}, MZB/MZP (marginal zone and MZ precursor) B220$^+$ AA4.1$^+$ CD1d^{hi} CD21^{hi}, GC (germinal center) B220$^+$ CD19$^+$ PNA$^+$ Fas$^+$ CD38^{lo}, B1 B220^{lo} CD19^{hi}, B1a B220^{lo} CD19^{hi} CD43$^+$ CD5$^+$, B1b B220^{lo} CD19^{hi} CD5$^-$, T cells TCRβ$^+$. Bars represent means and error bars standard deviation. ****p ≤ 0.0001, ***p ≤ 0.001, **p ≤ 0.01, *p ≤ 0.05, 2way ANOVA with Tukey test applied.

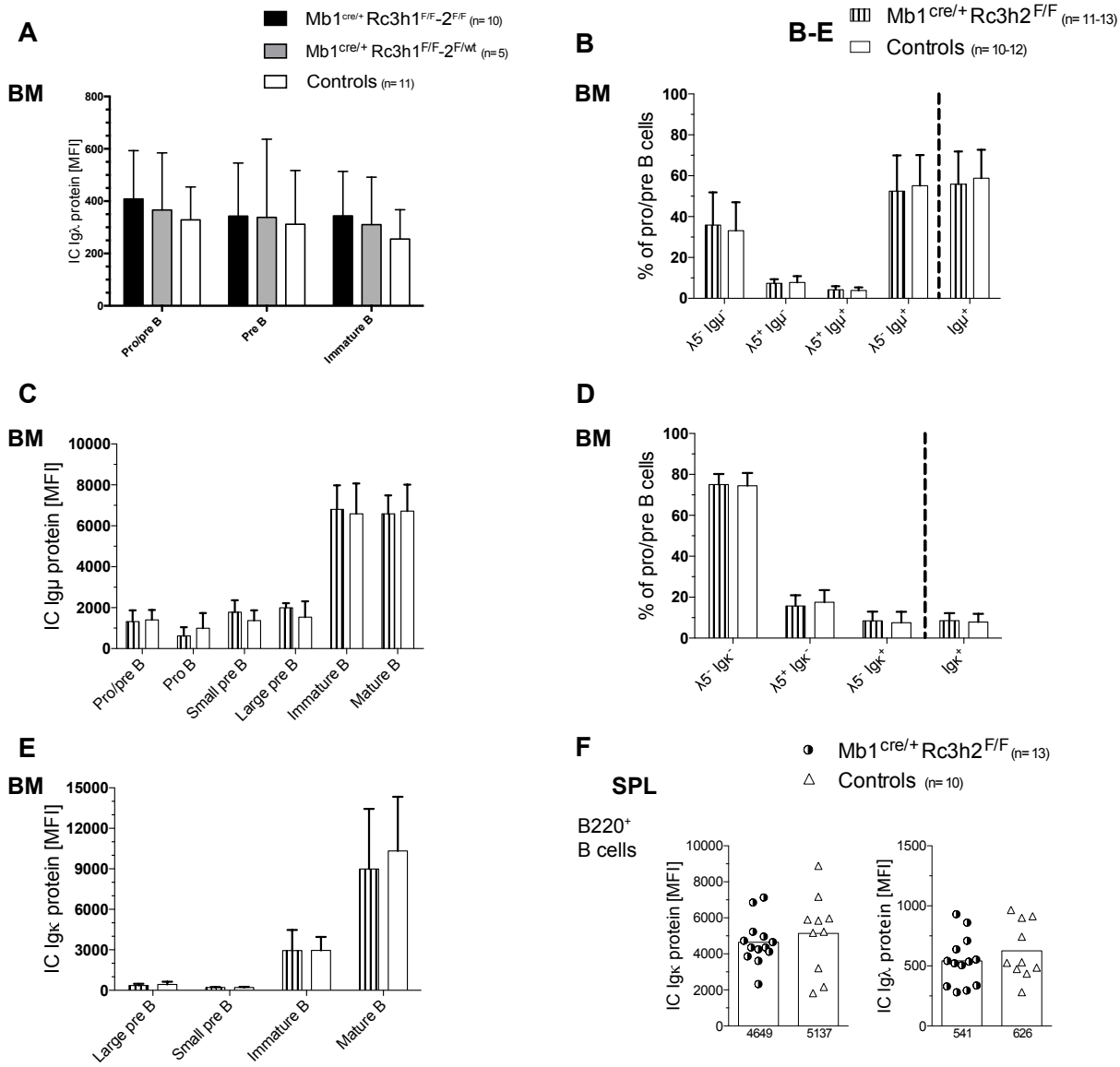

Figure S5: Analysis of intracellular expression of Igμ, Igκ and Igλ in bone marrow and splenic B cells of Mb1$^{cre/+}$ Rc3h1$^{F/F}$-2$^{F/F}$, Mb1$^{cre/+}$ Rc3h1$^{F/F}$-2$^{F/wt}$ and Mb1$^{cre/+}$ Rc3h2$^{F/F}$ mice.

(A) Flow cytometry based quantification of intracellular (IC) expression levels of Igλ (Igλ1, 2 and 3) in indicated bone marrow B cells. (B) Analyses of pro/pre B cells (B220^{lo} IgM^{-}) and pro/pre B cell subgating according to intracellular Igμ and λ5 expression. (C) Flow cytometry based quantification of IC μHC expression in indicated bone marrow B cells. (D) Analyses of pro/pre B cells and their subgating according to intracellular Igκ and λ5 expression. (E) IC protein expression of Igκ in denoted BM B cell populations as measured by flow cytometry. (F) Flow cytometric determination of IC protein expression of Igκ and Igλ (Igλ1, 2 and 3) in B220^{+} splenic B cell. B cell subsets analysed: pro B B220^{lo} IgM^{-} CD25^{-} c-kit^{+}, large pre B B220^{lo} c-kit^{-} CD25^{+} IgD^{-} IgM^{-} FSC^{hi}; small pre B B220^{lo} c-kit^{-} CD25^{+} IgD^{-} IgM^{-} FSC^{lo}; immature B B220^{+} IgD^{-} IgM^{+}. BM: bone marrow; MFI: median fluorescence intensity. Numbers below bars represent mean values and error bars standard deviation. (A) 2way ANOVA with Tukey test applied, (B-E) multiple t tests with Holm-Sidak method applied and unpaired (F) t test.

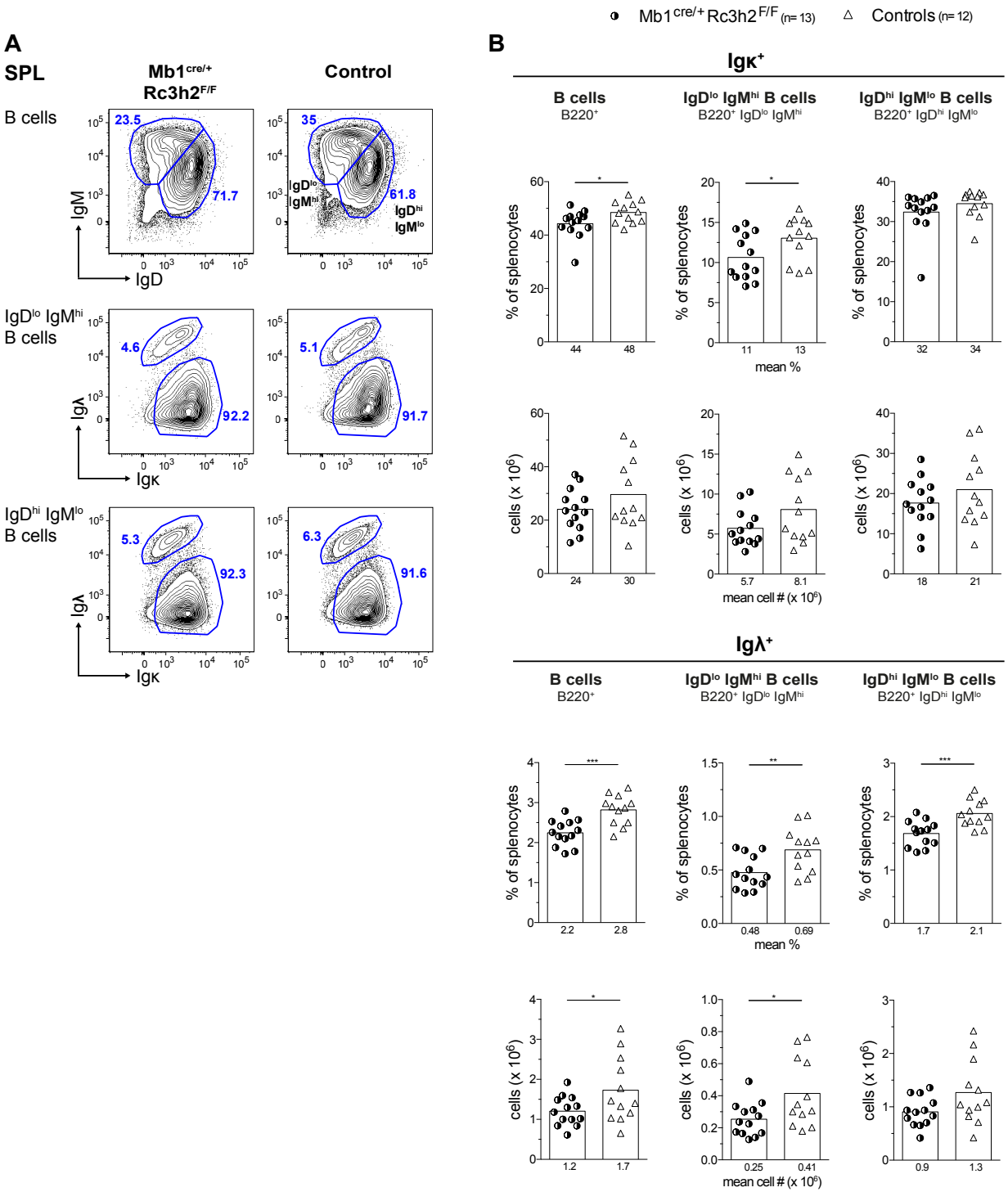

Figure S6: Analysis of surface expression of Igκ and Igλ on splenic B cells of Mb1$^{cre/+}$ Rc3h2$^{F/F}$ mice.
(A) Representative flow cytometric analysis for surface expression of Igκ or Igλ (Igλ1, 2 and 3) on splenic (SPL) B cells. (B) Percentages of indicated B cell subsets among viable splenocytes and total cell numbers (#). SPL: spleen. Numbers below graphs and bars represent mean percentages and cell numbers (#). ***p ≤ 0.001, **p ≤ 0.01, *p ≤ 0.05, unpaired t test.

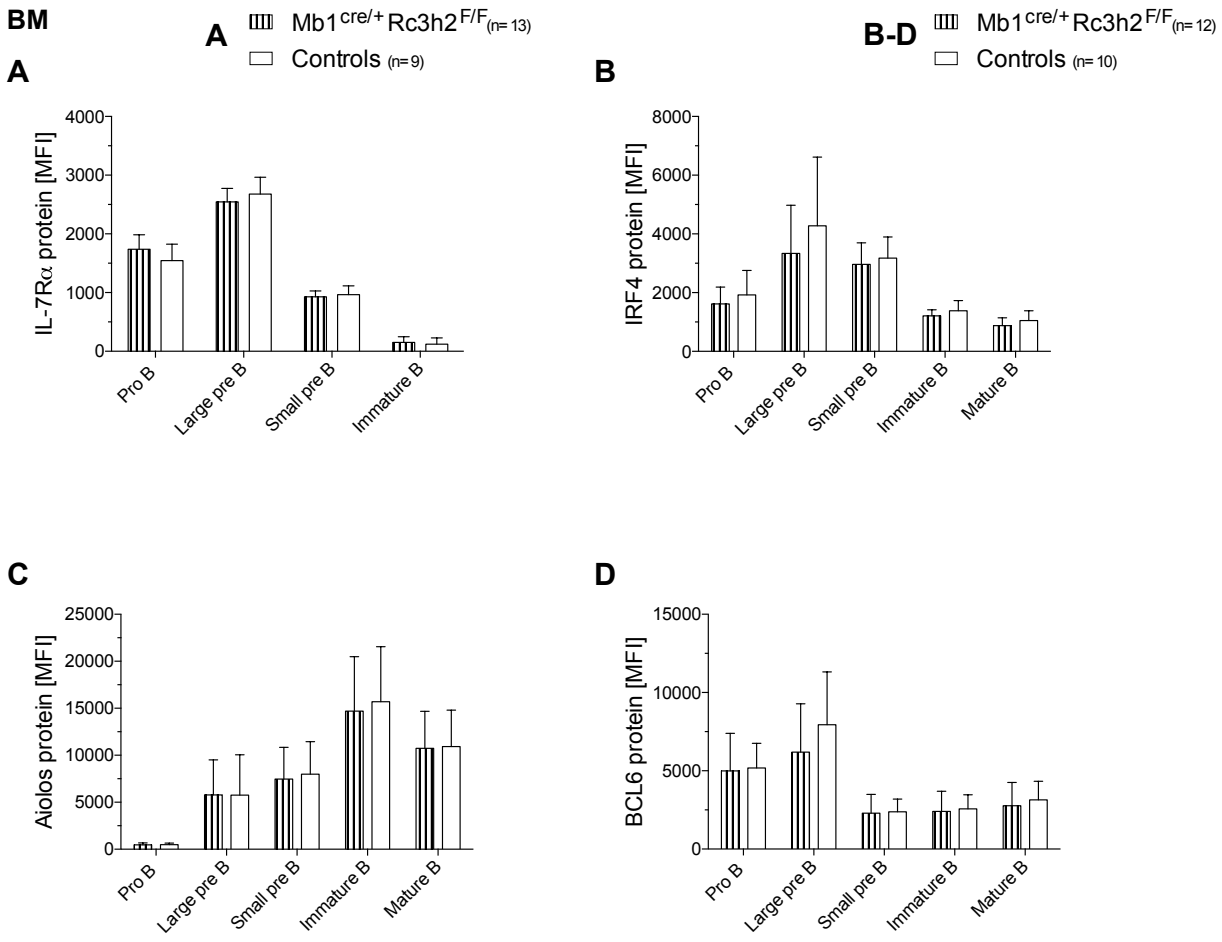

Figure S7: Extracellular IL-7α expression and intracellular levels of IRF4, Aiolos and BCL6 are not altered in Mb1$^{cre/+}$ Rc3h2$^{F/F}$ bone marrow B cell subsets.

(A) Bar chart representation of IL-7Rα protein expression on the surface of indicated bone marrow (BM) B cells populations. (B-D) Bar charts displaying intracellular (IC) levels of (B) IRF4, (C) Aiolos and (D) BCL6 as determined by flow cytometry in designated bone marrow (BM) cells. B cell subsets analysed: pro B B220^{lo} IgM^{-} CD25^{-} c-kit^{+}, large pre B B220^{lo} c-kit^{-} CD25^{+} IgD^{-} IgM^{-} FSC^{hi}; small pre B B220^{lo} c-kit^{-} CD25^{+} IgD^{-} IgM^{-} FSC^{lo}; immature B B220^{+} IgD^{-} IgM^{+}, mature B B220^{hi} IgD^{+}. BM: bone marrow; MFI: median fluorescence intensity. Numbers below bars represent mean values and error bars standard deviation. MFI: median fluorescence intensity. Multiple t tests with Holm-Sidak method applied.

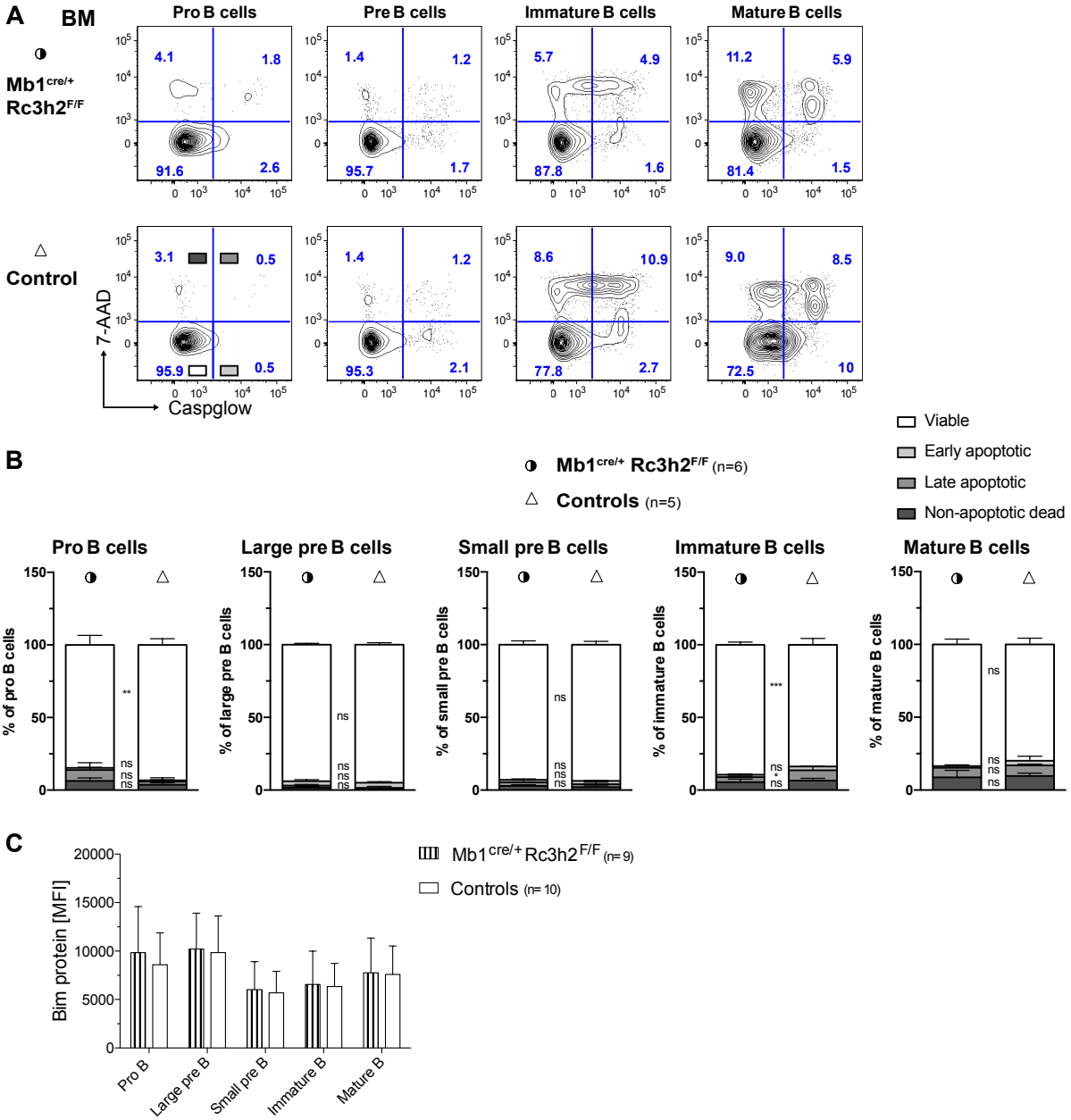

Figure S8: Analyses of active caspases and intracellular Bim levels in bone marrow B cell populations in Mb1$^{cre/+}$ Rc3h2$^{F/F}$ mice.

For staining active caspases (caspglow stain) *ex vivo* BM cells were cultured for 1h *in vitro*. (A) Representative flow cytometry plots illustrating active caspase stain (caspglow) and 7-AAD staining on indicated BM B cell subsets. (B) Stacked bar charts displaying percentages of viable, early apoptotic, late apoptotic and non-apoptotic dead cells within stated BM B cell populations as measured by flow cytometry in *ex vivo* cells with analyses of significance also following this order. Viable caspglow$^-$ 7-AAD$^-$; early apoptotic caspglow$^+$ 7-AAD$^-$, late apoptotic caspglow$^+$ 7-AAD$^+$, non-apoptotic dead caspglow$^-$ 7-AAD$^+$. (C) Bar charts displaying intracellular Bim protein levels normalized to levels in control populations as analyzed by flow cytometry. No significant differences were observed with non-normalized values. B cell subset gating: pro B B220^{lo} IgM$^-$ CD25$^-$ c-kit$^+$, large pre B B220^{lo} c-kit$^-$ CD25$^+$ IgD$^-$ IgM$^-$ FSC^{hi}; small pre B B220^{lo} c-kit$^-$ CD25$^+$ IgD$^-$ IgM$^-$ FSC^{lo}; immature B B220$^+$ IgD$^-$ IgM$^+$, mature B B220^{hi} IgD$^+$. BM: bone marrow. Bars represent mean values and error bars standard deviation. ***p ≤ 0.001, **p ≤ 0.01, *p ≤ 0.05, ns notsignificant, (B) unpaired t test or (C) multiple t test with Holm-Sidak method applied.

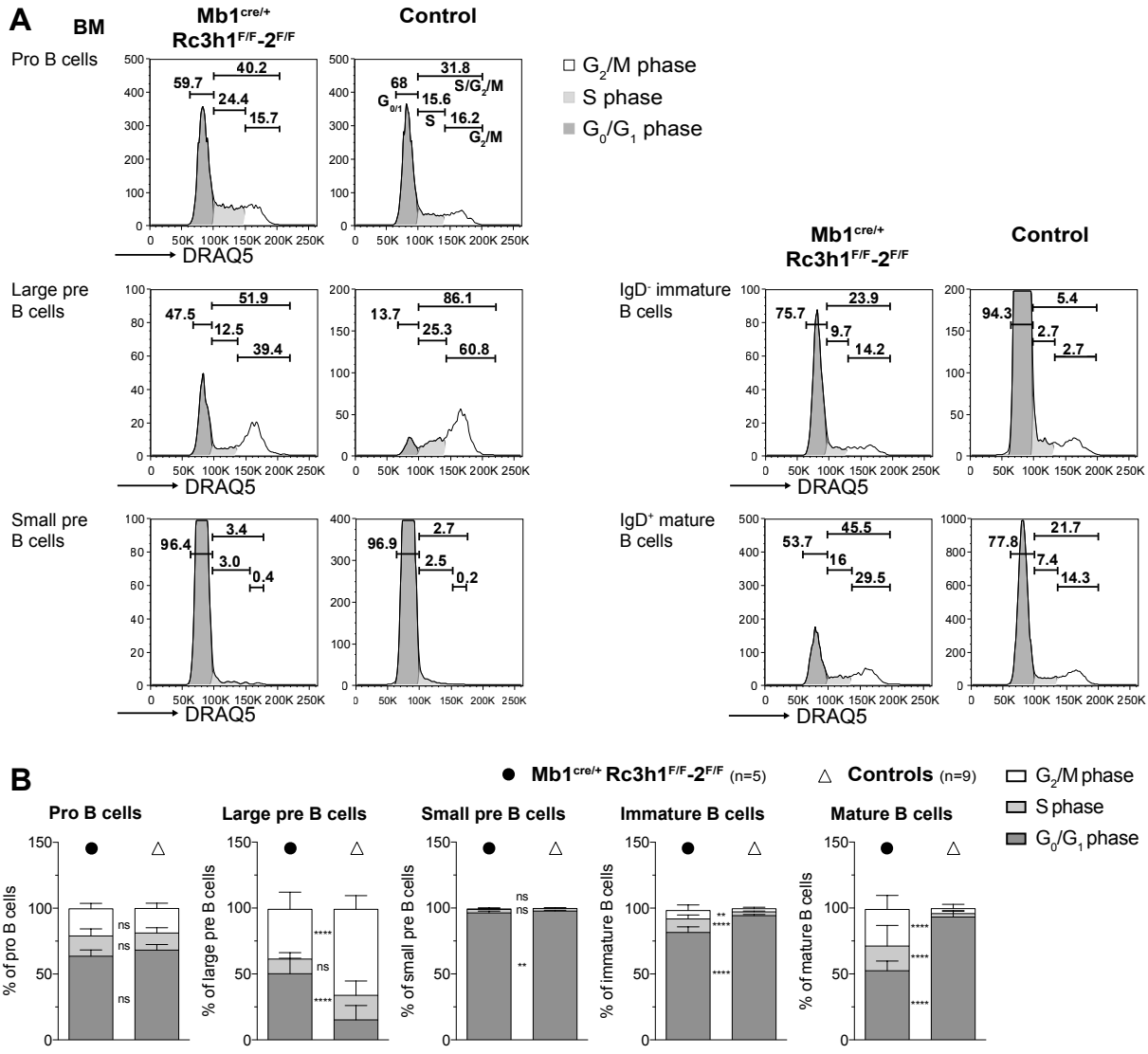

Figure S9: Cell cycle stages of bone marrow B cells in Mb1$^{cre/+}$ Rc3h1$^{F/F}$-2$^{F/F}$ mice.

(A) Representative flow cytometry plots and histograms of indicated bone marrow (BM B cell populations depicting gating and analysis strategy. (B) Percentages of designated B cell populations in cell cycle phases. B cell subsets analysed: pro B B220^{lo} IgM^{-} CD25^{-} c-kit^{+}, large pre B B220^{lo} c-kit^{-} CD25^{+} IgD^{-} IgM^{-} FSC^{hi}; small pre B B220^{lo} c-kit^{-} CD25^{+} IgD^{-} IgM^{-} FSC^{lo}; immature B B220^{+} IgD^{-} IgM^{+}, mature B B220^{hi} IgD^{+}. $G_{0/1}$, S, and G_2/M phase according to DRAQ5 signal intensity as indicated by grey-scale coding ($G_{0/1}$ white, S light grey, G_2/M dark grey). BM: bone marrow. Bars represent mean values and error bars standard deviation. ****p ≤ 0.0001, **p ≤ 0.01, ns non-significant, unpaired t test.

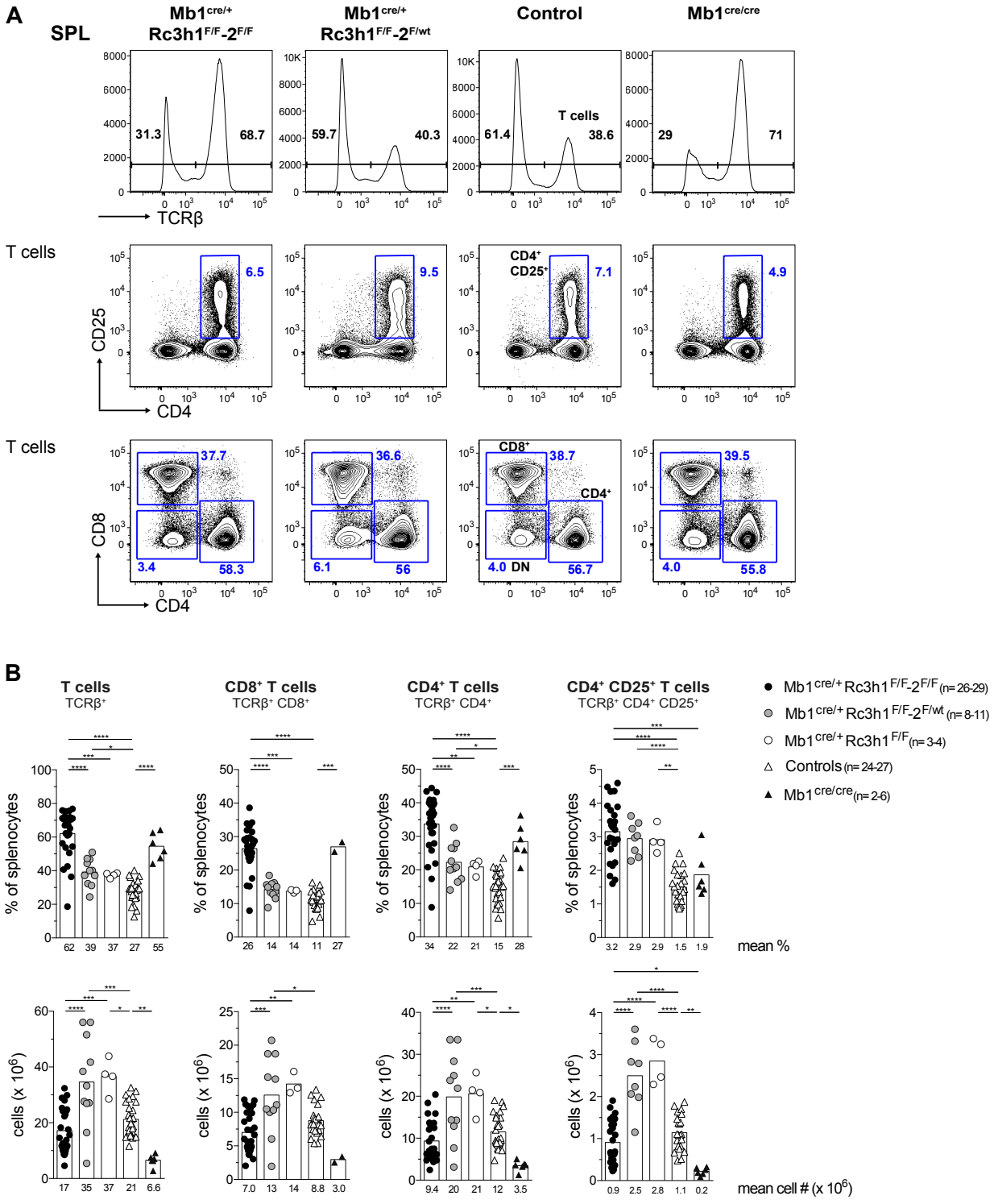

Figure S10: Increase of CD25$^+$ CD4$^+$ T cells in Mb1$^{cre/+}$ Rc3h1$^{F/F}$-2$^{F/F}$ mice, but their T cell compartment otherwise resembles Mb1$^{cre/cre}$ mice.

(A) Representative flow cytometry plots depicting the gating strategy for splenic (SPL) T cells. T cell subsets: T cells TCRβ$^+$; CD4$^+$ T cells TCRβ$^+$ CD4$^+$; CD4$^+$ CD25$^+$ T cells TCRβ$^+$ CD4$^+$ CD25$^+$. (B) Percentages of respective T cell subsets of total SPL cells and total subset cell numbers as determined by flow cytometry. SPL: spleen. Numbers below graphs and bars indicate mean percentages and cell numbers (#). ****p ≤ 0.0001, ***p ≤ 0.001, **p ≤ 0.01, *p ≤ 0.05, ANOVA. Significances for Mb1$^{cre/cre}$ versus Mb1$^{cre/+}$ Rc3h1$^{F/F}$-2$^{F/wt}$ and versus Mb1$^{cre/+}$ Rc3h1$^{F/F}$ are not shown, for CD8$^+$ T cells significances versus Mb1$^{cre/cre}$ (n= 2) were not determined.

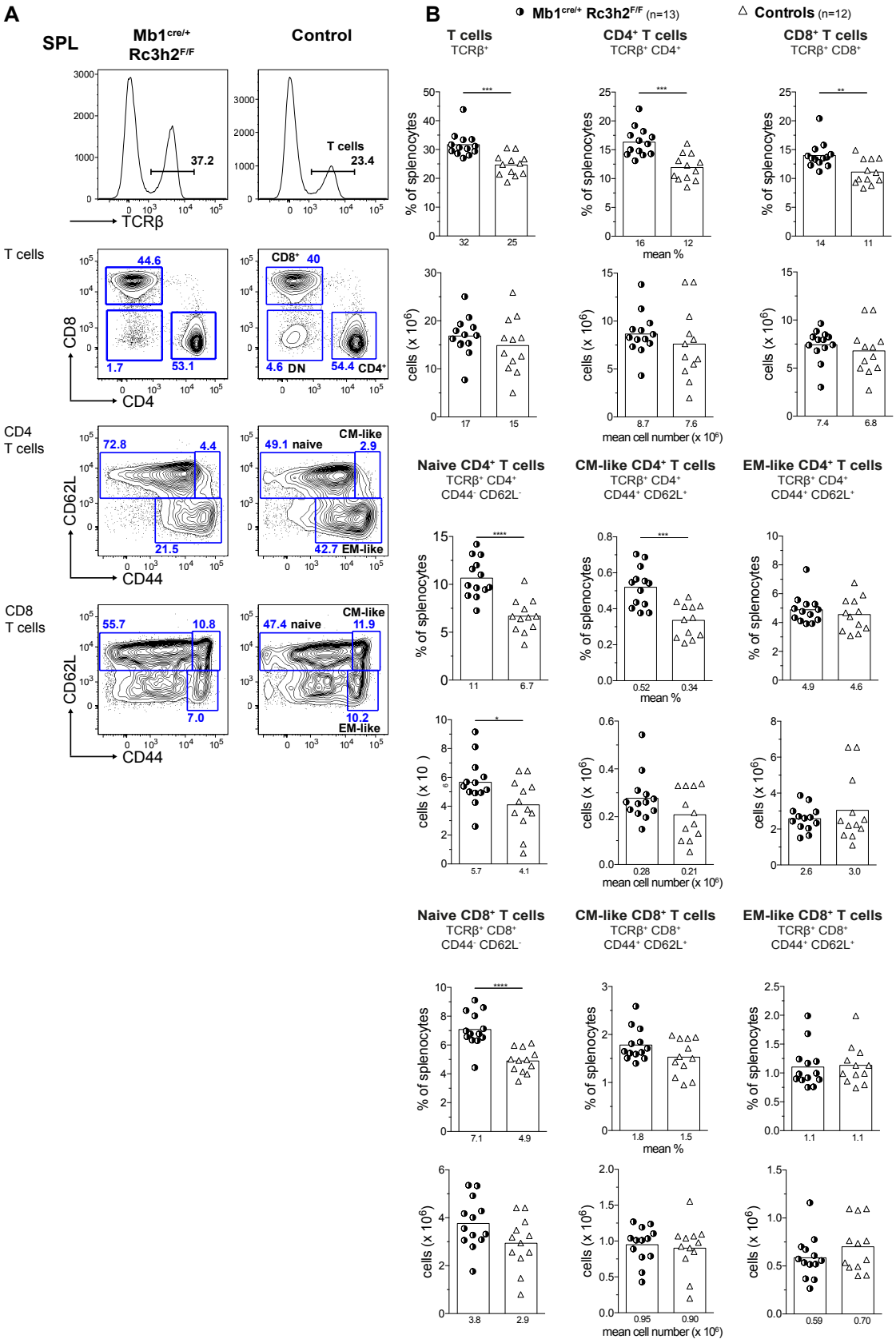

Figure S11: Expansion of naive and CM-like CD4 splenic T cell subsets in Mb1$^{cre/+}$ Rc3h2$^{F/F}$ mice.
(A) Representative flow cytometry histograms of stated splenic (SPL) B cell populations illustrating gating schemes. (B) Percentages of and cell numbers of designated T cell subsets of total splenocytes as determined by flow cytometry. CM: central memory; EM: effector memory. Numbers below graphs and bars represent mean percentages or cell numbers (#). ****p ≤ 0.0001, ***p ≤ 0.001, **p ≤ 0.01, *p ≤ 0.05, unpaired t test.

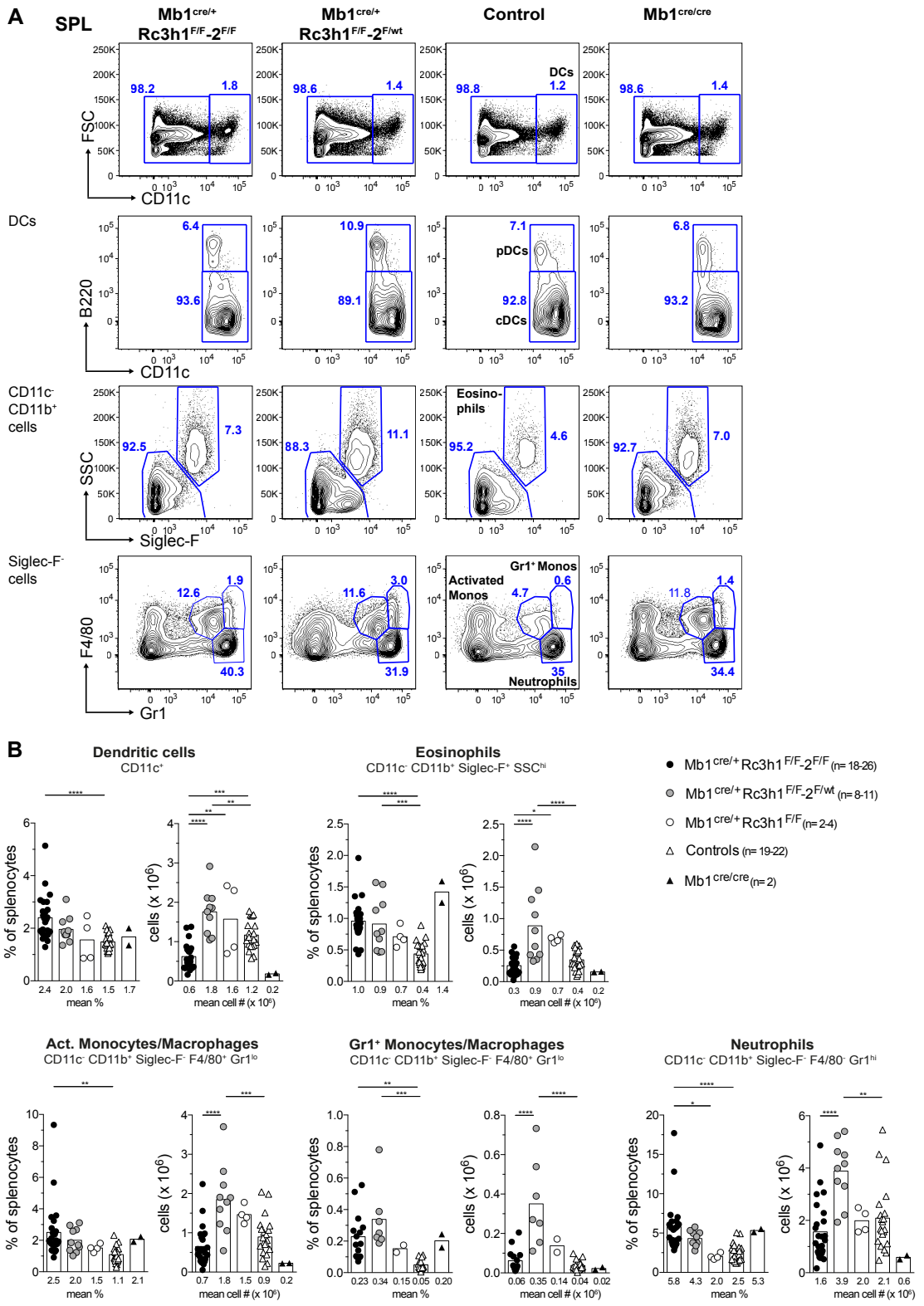

Figure S12: Analysis of splenic myeloid cell populations in Mb1$^{cre/+}$ Rc3h1$^{F/F}$-2$^{F/F}$, Mb1$^{cre/+}$ Rc3h1$^{F/F}$-2$^{F/wt}$ and Mb1$^{cre/+}$ Rc3h1$^{F/F}$ mice.

(A) Representative plots depicting the gating strategy for myeloid cells in spleen (SPL). Myeloid cell populations were analyzed as indicated. (B) Percentages of respective myeloid cell subsets of total splenocytes as determined by flow cytometry. DCs: dendritic cells; Activated Monos: activated monocytes and macrophages; Gr1^{lo}; Gr1^{+} Monos: Gr1 expressing Monocytes. Numbers below graphs and bars show mean values. ****p ≤ 0.0001, ***p ≤ 0.001, **p ≤ 0.01, *p ≤ 0.05, ANOVA. Significances versus Mb1$^{cre/cre}$ (n= 2) were not determined and for Gr1^{+} Monocytes also not compared to Mb1$^{cre/+}$ Rc3h1$^{F/F}$ (n= 2).

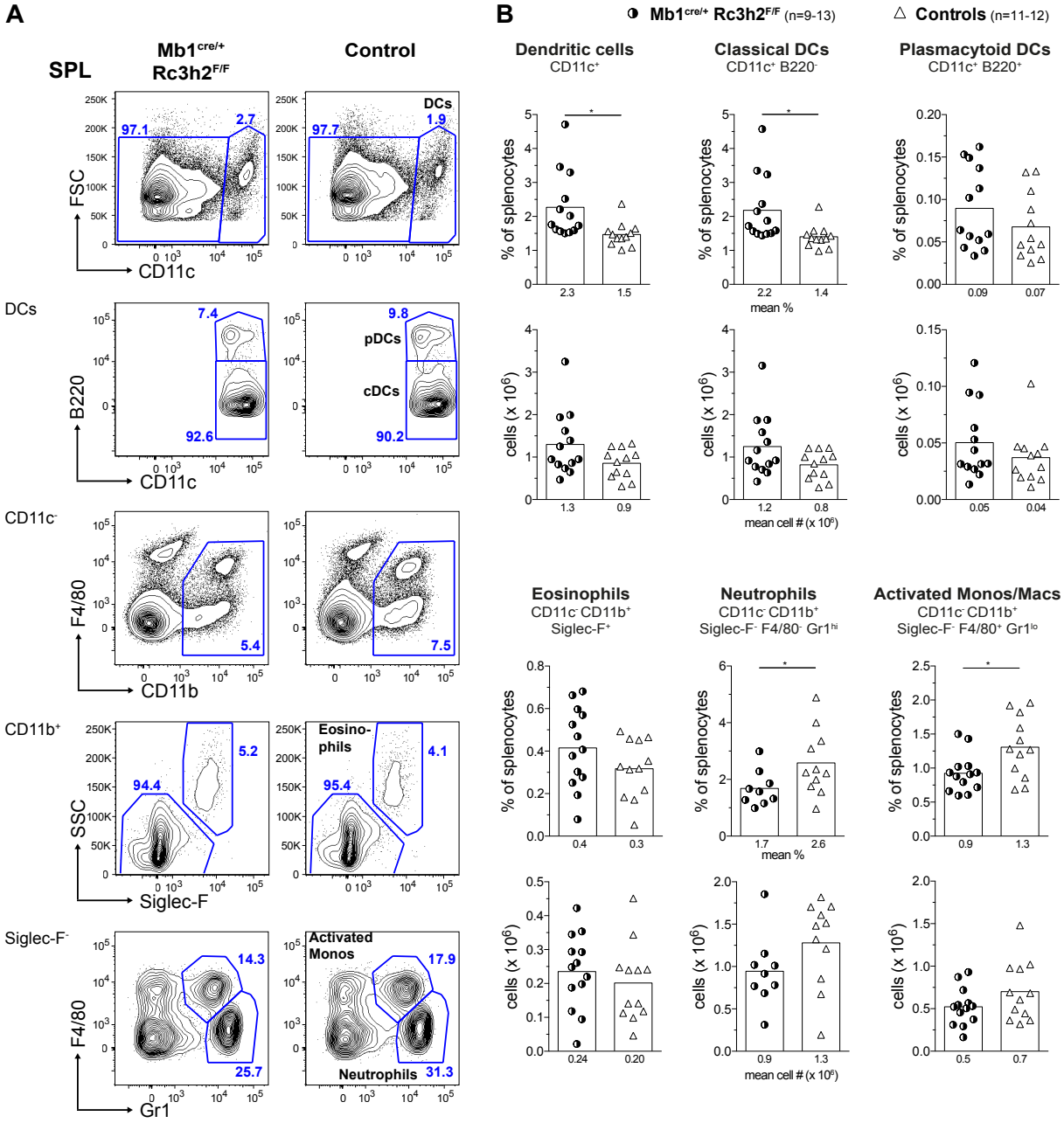

Figure S13: Analysis of myeloid cells in the spleen of Mb1$^{cre/+}$ Rc3h2$^{F/F}$ mice.
(A) Representative flow cytometric analysis illustrating gating strategy for myeloid populations in the spleen (SPL). (B) Percentages of stated myeloid cell subsets of total splenocytes and total cell numbers as determined by flow cytometry. DCs: dendritic cells, cDCs: classical DCs; pDCs: plasmacytoid DCs; Activated Monos: activated monocytes and macrophages. Numbers below graphs and bars indicate mean mean percentages and cell numbers (#). *p ≤ 0.05, unpaired t test.

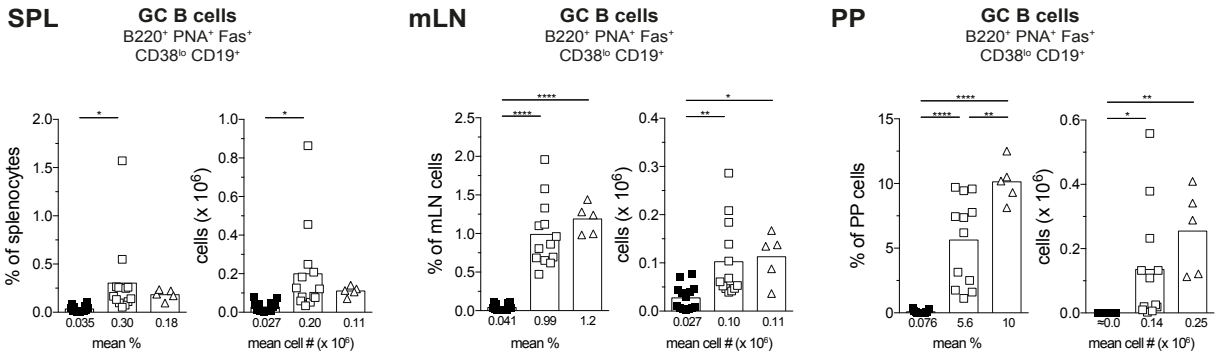

Figure S14: Near absence of splenic and GALT Mb1$^{cre/+}$ Rc3h1$^{F/F}$-2$^{F/F}$ IgH^{MOG} germinal center B cells.
(A) Percentages of stated B cell subsets of total splenic (SPL) cells and total subset cell numbers as determined by flow cytometry. (B) Percentages and total cell numbers (#) of GC B cells of total SPL, mLN or PP cells as analyzed by flow cytometry. Calculated cell numbers of < 100 were rounded to 0 and denoted as ≈0.0. GALT: gut-associated lymphoid tissue; mLN: mesenteric lymph node; PP: Peyer's patches; GC: germinal center. Numbers below graphs and bars indicate mean percentages or cell numbers. ****$p \leq 0.0001$, **$p \leq 0.01$, *$p \leq 0.05$, ANOVA.

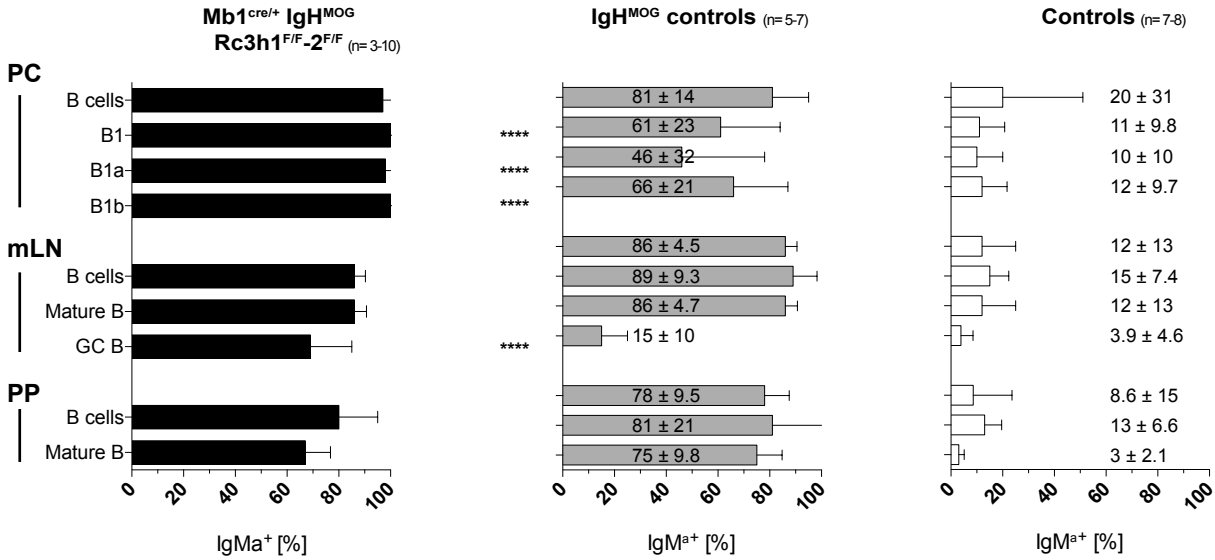

Figure S15: Peritoneal cavity B1 cell populations of Mb1$^{cre/+}$ Rc3h1$^{F/F}$-2$^{F/F}$ IgH^{MOG} mice are largely IgM^{a}-positive.

Percentages of IgM^{a+} B cell subsets among the respective subsets. Black * represent significant differences between cell populations from Mb1$^{cre/+}$ Rc3h1$^{F/F}$-2$^{F/F}$ IgH^{MOG} and IgH^{MOG} controls. The positive signal in control samples represents background. Gated B cell subsets: B cells B220^{+}; B1 CD19^{+} B220^{lo}; B1a CD19^{+} B220^{lo} CD43^{+} CD5^{+}, B1a CD19^{+} B220^{lo} CD5^{-} immature B B220^{+} AA4.1^{+}; mature B B220^{+} AA4.1^{-}; GC B B220^{+} CD19^{+} PNA^{+} Fas^{+} CD38^{lo}. BM: bone marrow; PC: peritoneal cavity; mLN: mesenteric lymph nodes; PP: Peyer's patches; GC: germinal centers. Bars indicate mean values and error bars standard deviation. ****p ≤ 0.0001, ANOVA.

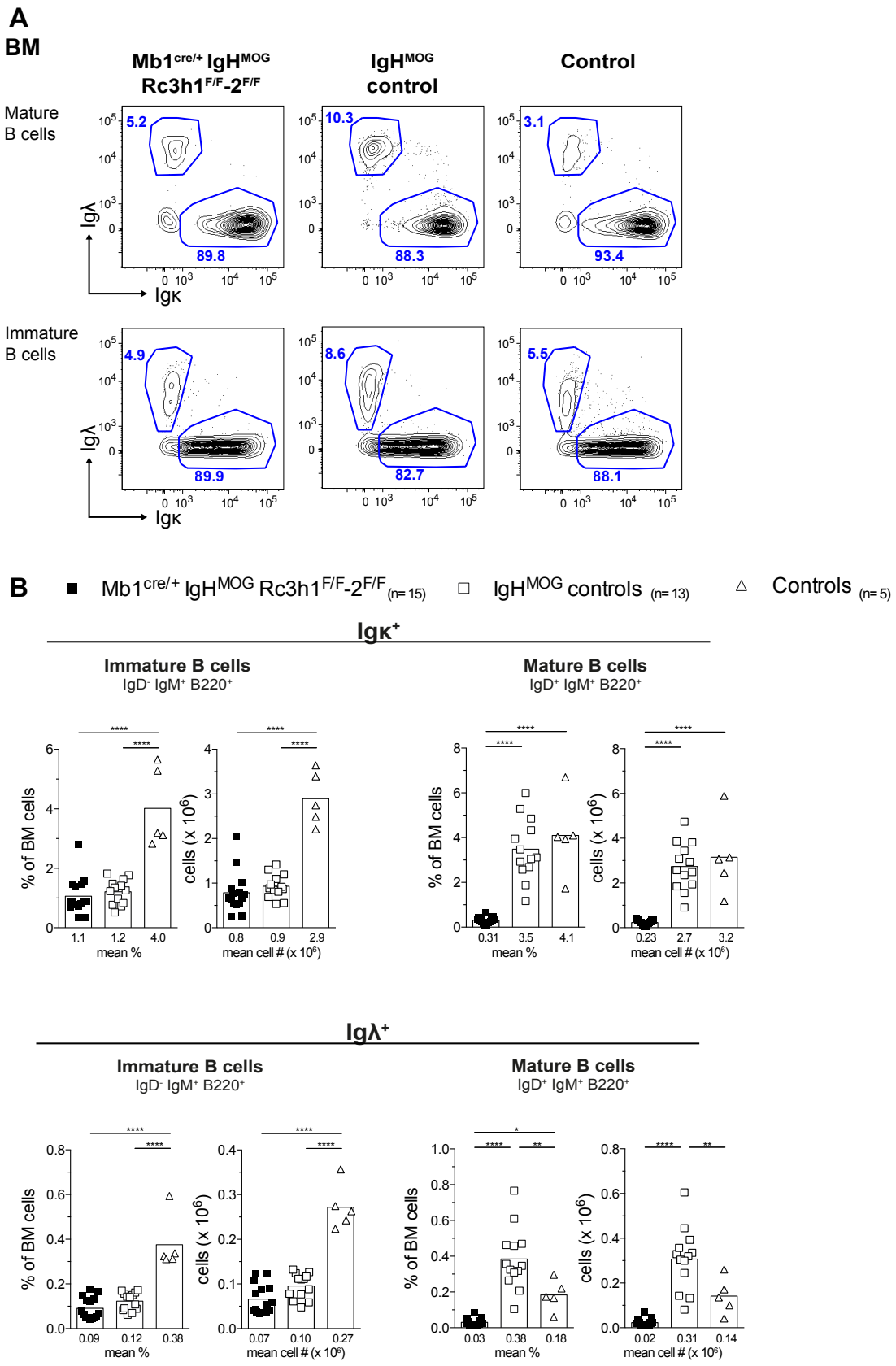

Figure S16: Analysis of surface expression of Igκ and Igλ (λ1, 2 and 3) on BM B cells of Mb1$^{cre/+}$ Rc3h1$^{F/F}$-2$^{F/F}$ IgH^{MOG} mice.

(A) Representative flow cytometric analysis of bone marrow (BM) B cells. (B) Percentages of indicated Igκ$^+$ or Igλ$^+$ B cell subsets among viable cells of BM and total cell numbers. Numbers below graphs and bars show mean percentages or cell numbers (#). ****p ≤ 0.0001, **p ≤ 0.01, *p ≤ 0.05, ANOVA.

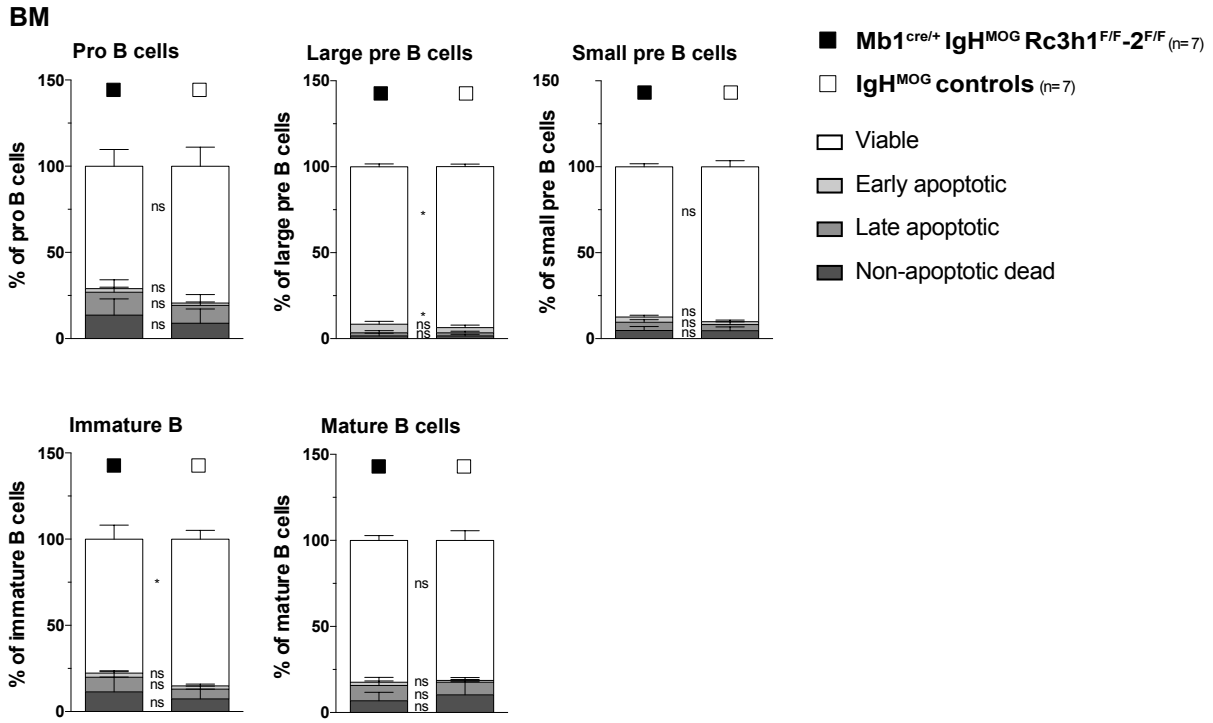

Figure S17: Minor reduction of the fraction of viable pre and immature B cells in Mb1$^{cre/+}$ Rc3h1$^{F/F}$-2$^{F/F}$ IgH^{MOG} mice.

For staining active caspases (caspglow stain as in Fig. 27), *ex vivo* BM cells were cultured for 1h *in vitro*. Quantification of percentages of viable, early apoptotic, late apoptotic and non-apoptotic dead cells of BM cell subsets as determined by flow cytometry in *ex vivo* cells shown as stacked bar charts. Viable caspglow$^-$ 7-AAD$^-$; early apoptotic caspglow$^+$ 7-AAD$^-$, late apoptotic caspglow$^+$ 7-AAD$^+$, non-apoptotic dead caspglow$^-$ 7-AAD$^+$. Gated B cell subsets: pro B B220^{lo} IgM$^-$ CD25$^-$ c-kit$^+$, large pre B B220^{lo} c-kit$^-$ CD25$^+$ IgD$^-$ IgM$^-$ FSC^{hi}; small pre B B220^{lo} c-kit$^-$ CD25$^+$ IgD$^-$ IgM$^-$ FSC^{lo}; immature B B220$^+$ IgD$^-$ IgM$^+$, mature B B220^{hi} IgD$^+$. BM: bone marrow. Bars represent mean values and error bars standard deviation. *$p \leq 0.05$, ns non-significant, unpaired t test.

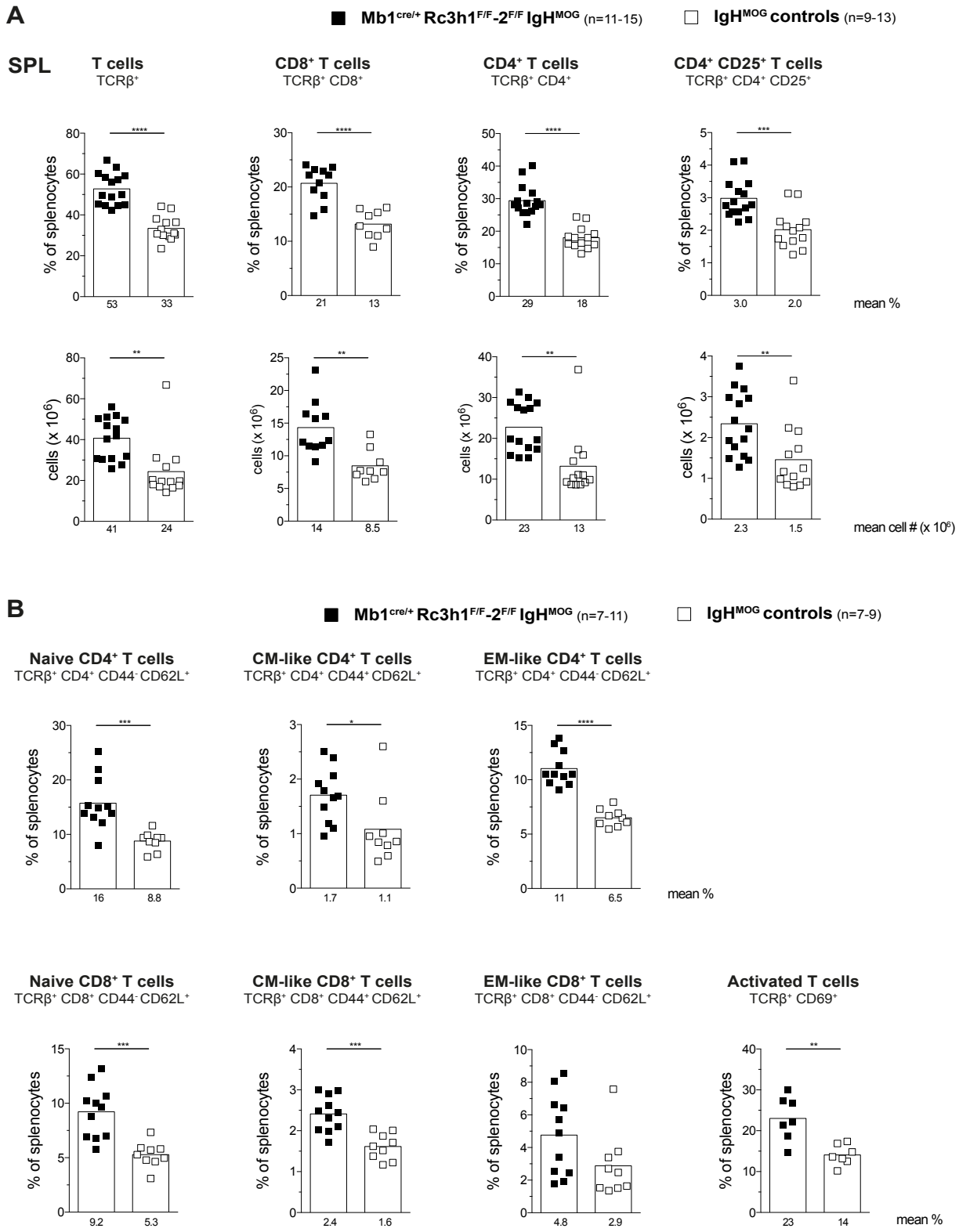

Figure S18: T cell expansion in the spleen of Mb1$^{cre/+}$ Rc3h1$^{F/F}$-2$^{F/F}$ IgH^{MOG} mice.
(A) Percentages of respective T cell subsets of total splenocytes and total subset cell numbers as determined by flow cytometry. (B) Percentages of designated T cell subsets of total splenocytes as determined by flow cytometry. T cell subsets gated as indicated. SPL: spleen, CM: central memory; EM: effector memory. Numbers below graphs and bars show mean percentages and cell numbers (#). ****$p \leq 0.0001$, ***$p \leq 0.001$, **$p \leq 0.01$, *$p \leq 0.05$, unpaired t test.

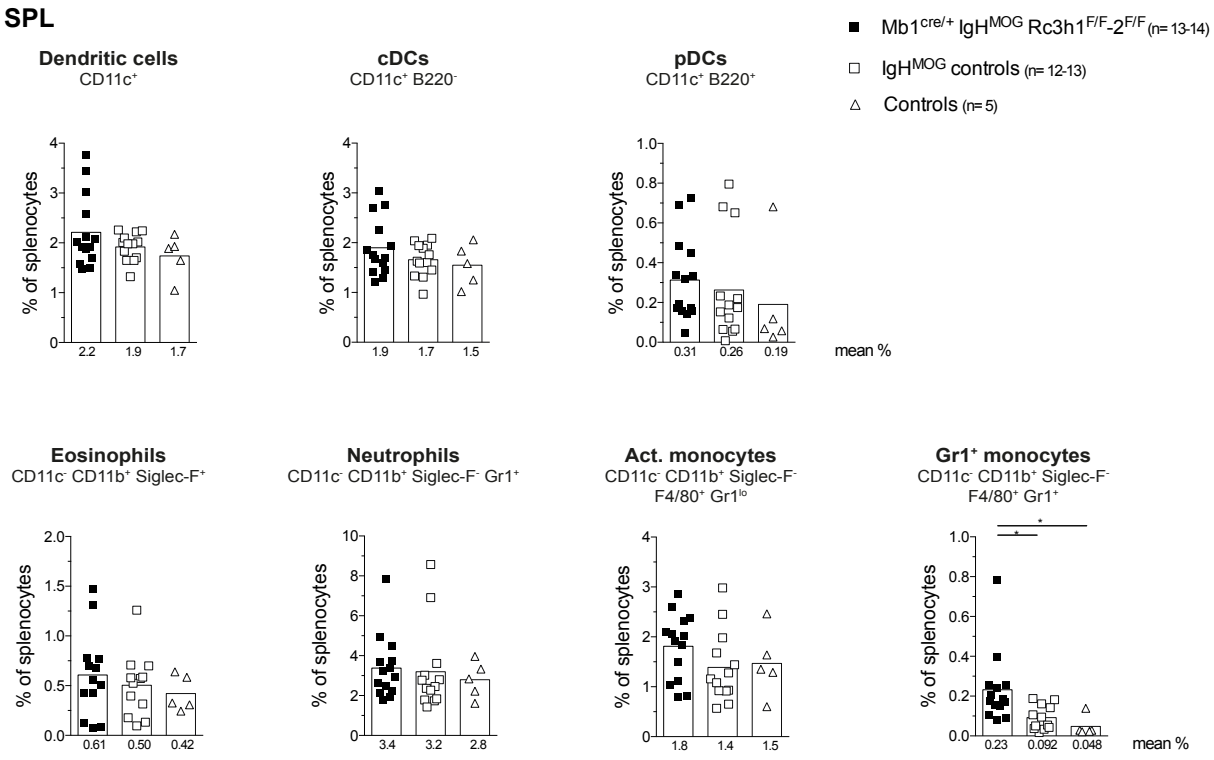

Figure S19: Myeloid cell populations are not altered in Mb1$^{cre/+}$ Rc3h1$^{F/F}$-2$^{F/F}$ IgH^{MOG} mice.
Percentages of respective myeloid cell subsets of total SPL cells as determined by flow cytometry. Myeloid cells were gated as indicated. SPL: spleen, cDCs: classical dendritic cells (DCs); pDCs: plasmacytoid dendritic cells; Act. Monocytes: activated monocytes and macrophages. Numbers below graphs and bars represent mean percentages. *$p \leq 0.05$, ANOVA.

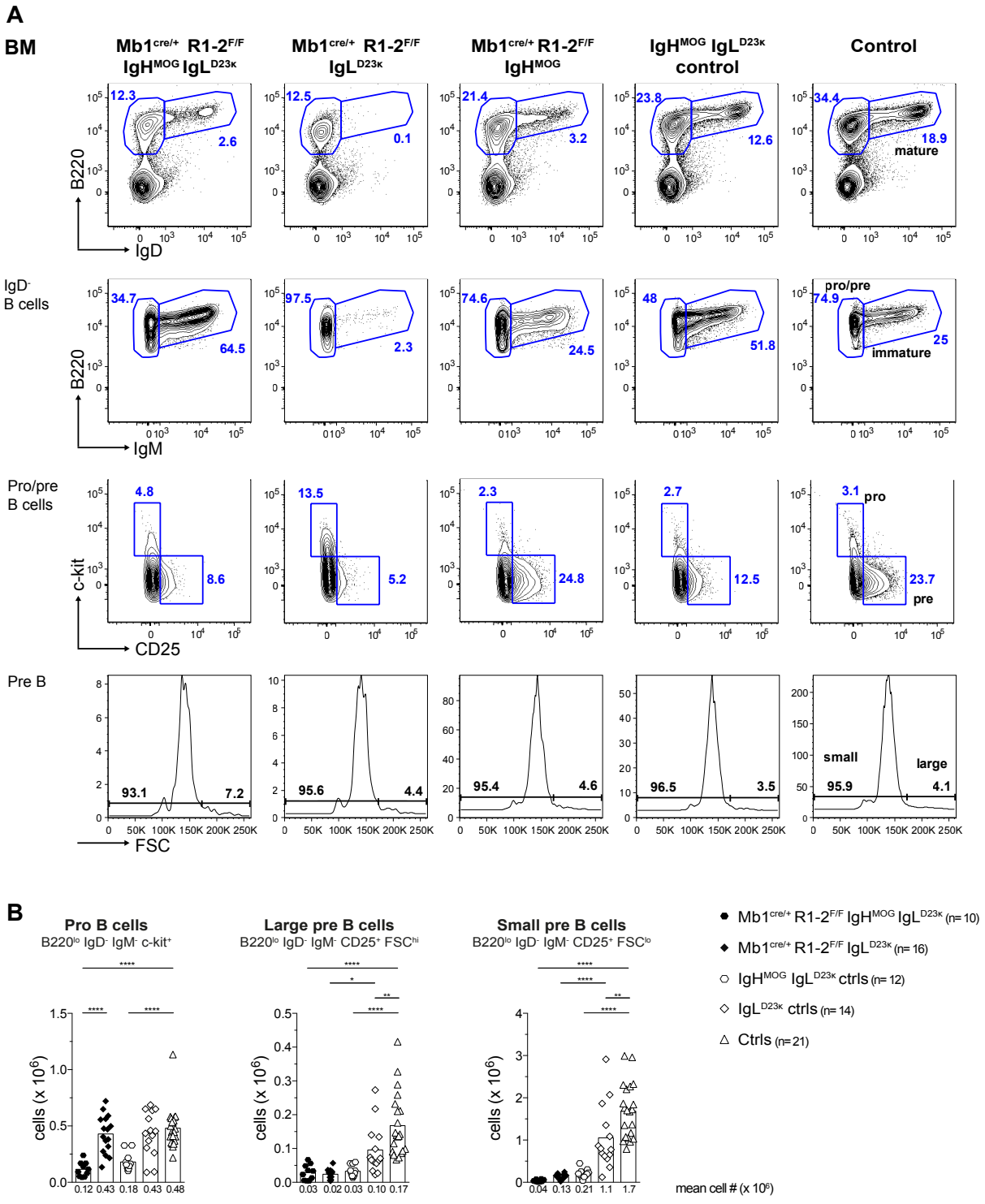

Figure S20: Pro and pre B bone marrow B cell populations in Mb1$^{cre/+}$ Rc3h1-2$^{F/F}$ IgH^{MOG} IgL^{D23κ} and Mb1$^{cre/+}$ Rc3h1-2$^{F/F}$ IgL^{D23κ} mice.

(A) Representative flow cytometry plots depicting the gating strategy for bone marrow (BM) B cells. (B) Total subset cell numbers of stated BM B cells as determined by flow cytometry. The genotypes represented in the bar charts differ from (A). Ctrls: controls; R: Rc3h; BM: bone marrow. Numbers below graphs and bars indicate mean cell numbers (#). ****p ≤ 0.0001, ***p ≤ 0.001, **p ≤ 0.01, *p ≤ 0.05, ANOVA. Significances for Mb1$^{cre/+}$ R1-2$^{F/F}$ IgH^{MOG} IgL^{D23κ} and IgH^{MOG} IgL^{D23κ} ctrls versus IgL^{D23κ} ctrls and Mb1$^{cre/+}$ R1-2$^{F/F}$ IgL^{D23κ} versus IgH^{MOG} IgL^{D23κ} ctrls and ctrls are not shown.

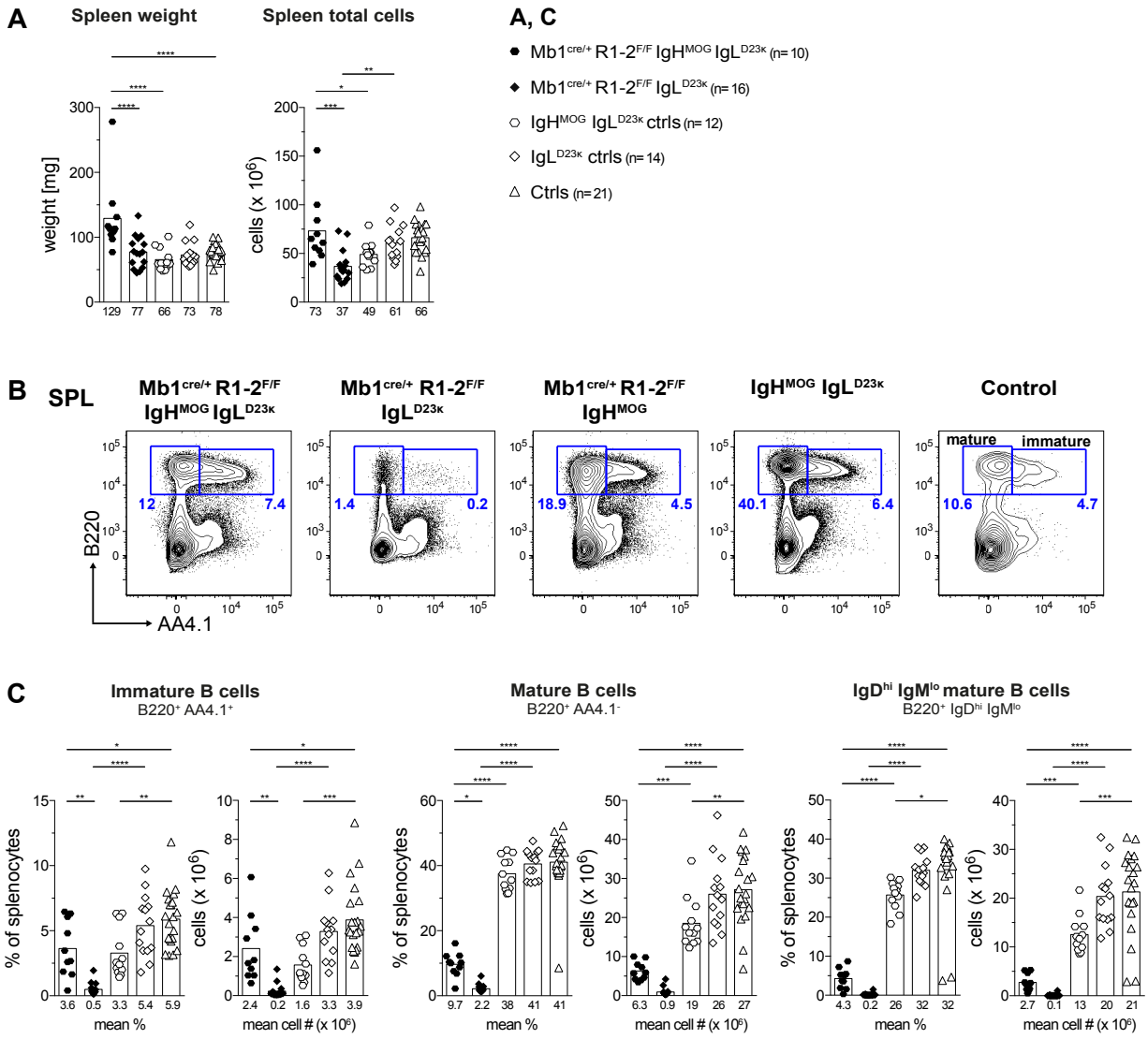

Figure S21: Near absence of splenic B cells in Mb1$^{cre/+}$ Rc3h1-2$^{F/F}$ IgL^{D23κ} mice, while mature splenic B cells are strongly reduced in Mb1$^{cre/+}$ Rc3h1-2$^{F/F}$ IgH^{MOG} IgL^{D23κ} mice.

(A) Spleen weight and total splenocyte number of stated mice. (B) Representative flow cytometric analysis of splenic (SPL) B cells. (C) Percentages of indicated B cell subsets among viable splenocytes and total cell numbers; R: Rc3h. Numbers below graphs and bars represent mean values. ****p ≤ 0.0001, ***p ≤ 0.001, **p ≤ 0.01, *p ≤ 0.05, ANOVA. Significances for Mb1$^{cre/+}$ R1-2$^{F/F}$ IgH^{MOG} IgL^{D23κ} and IgH^{MOG} IgL^{D23κ} ctrls versus IgL^{D23κ} ctrls and Mb1$^{cre/+}$ R1-2$^{F/F}$ IgL^{D23κ} versus IgH^{MOG} IgL^{D23κ} ctrls and ctrls are not shown.

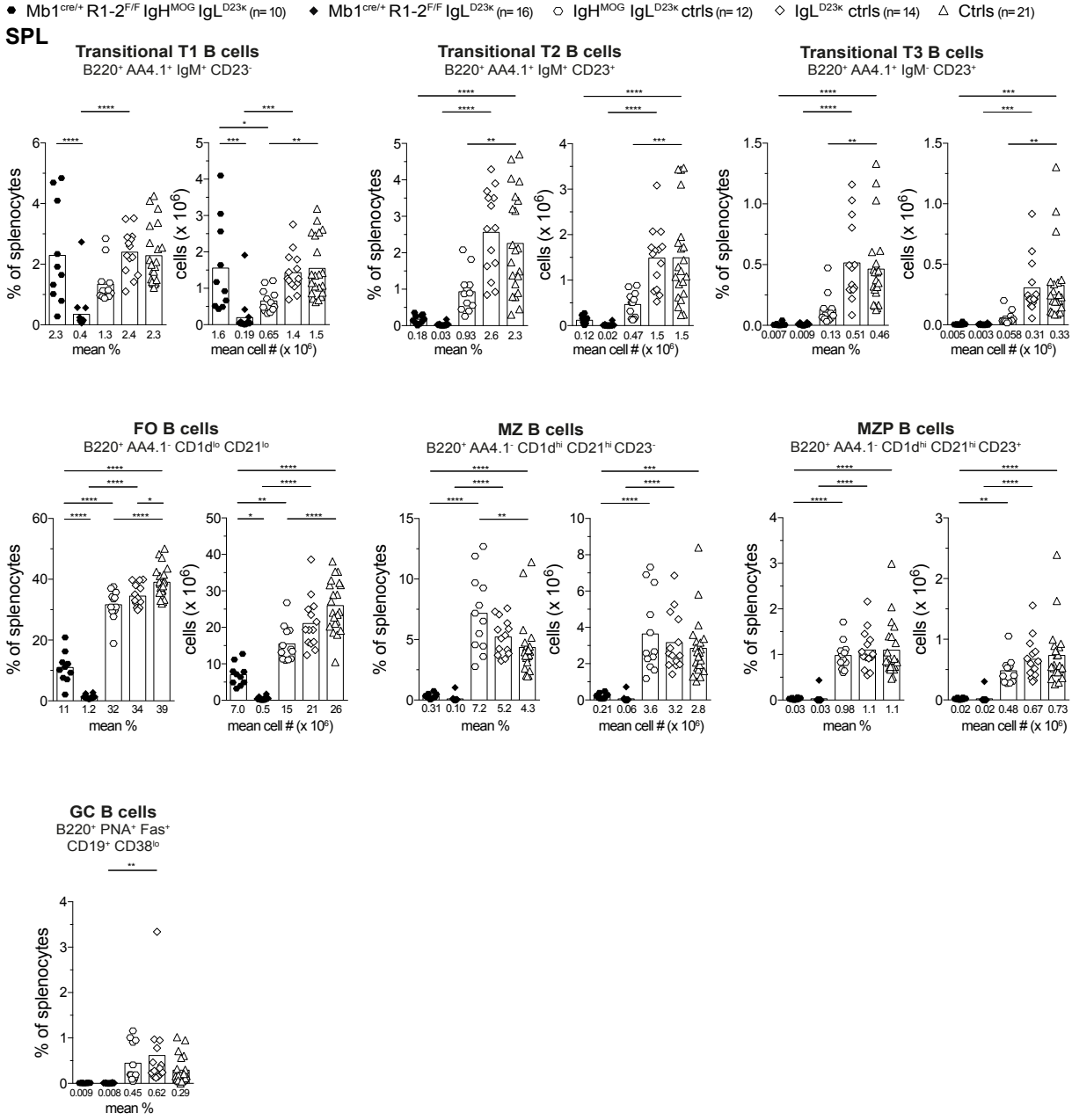

Figure S22: Analysis of splenic B cell populations in Mb1$^{cre/+}$ Rc3h1-2$^{F/F}$ IgH^{MOG} IgL$^{D23\kappa}$ mice and Mb1$^{cre/+}$ Rc3h1-2$^{F/F}$ IgL$^{D23\kappa}$ mice.

Percentages of indicated B cell subsets among viable cells of SPL (spleen) and total cell numbers. FO: follicular; MZ: mature marginal zone; MZP: marginal zone precursor; GC: germinal center; R: Rc3h. Numbers below graphs and bars represent mean percentages and cell numbers (#). ****p ≤ 0.0001, ***p ≤ 0.001, **p ≤ 0.01, *p ≤ 0.05, ANOVA. Significances for Mb1$^{cre/+}$ R1-2$^{F/F}$ IgH^{MOG} IgL$^{D23\kappa}$ and IgH^{MOG} IgL$^{D23\kappa}$ ctrls versus IgL$^{D23\kappa}$ ctrls and Mb1$^{cre/+}$ R1-2$^{F/F}$ IgL$^{D23\kappa}$ versus IgH^{MOG} IgL$^{D23\kappa}$ ctrls and ctrls are not shown.

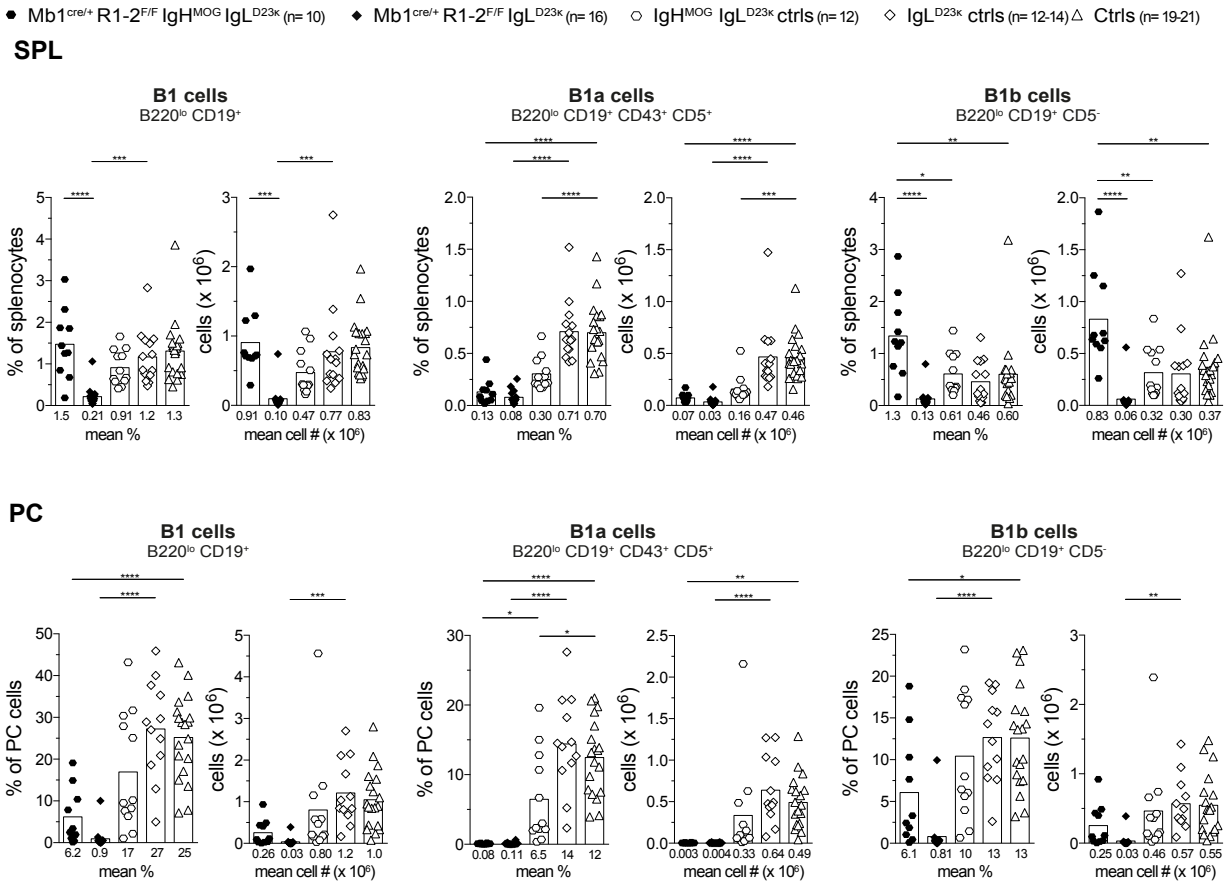

Figure S23: Lack of splenic and peritoneal cavity B1 cells in Mb1$^{cre/+}$ Rc3h1-2$^{F/F}$ IgL^{D23κ} mice while the splenic B1b subset is increased in Mb1$^{cre/+}$ Rc3h1-2$^{F/F}$ IgH^{MOG} IgL^{D23κ} mice.

Percentages of indicated B cell subsets among viable cells of SPL or PC and total cell numbers; R: Rc3h. Numbers below graphs and bars show mean percentages and cell numbers (#). SPL: spleen; PC: peritoneal cavity; R: Rc3h. ****p ≤ 0.0001, ***p ≤ 0.001, **p ≤ 0.01, *p ≤ 0.05, ANOVA. Significances for Mb1$^{cre/+}$ R1-2$^{F/F}$ IgH^{MOG} IgL^{D23κ} and IgH^{MOG} IgL^{D23κ} ctrls versus IgL^{D23κ} ctrls and Mb1$^{cre/+}$ R1-2$^{F/F}$ IgL^{D23κ} versus IgH^{MOG} IgL^{D23κ} ctrls and ctrls are not shown.

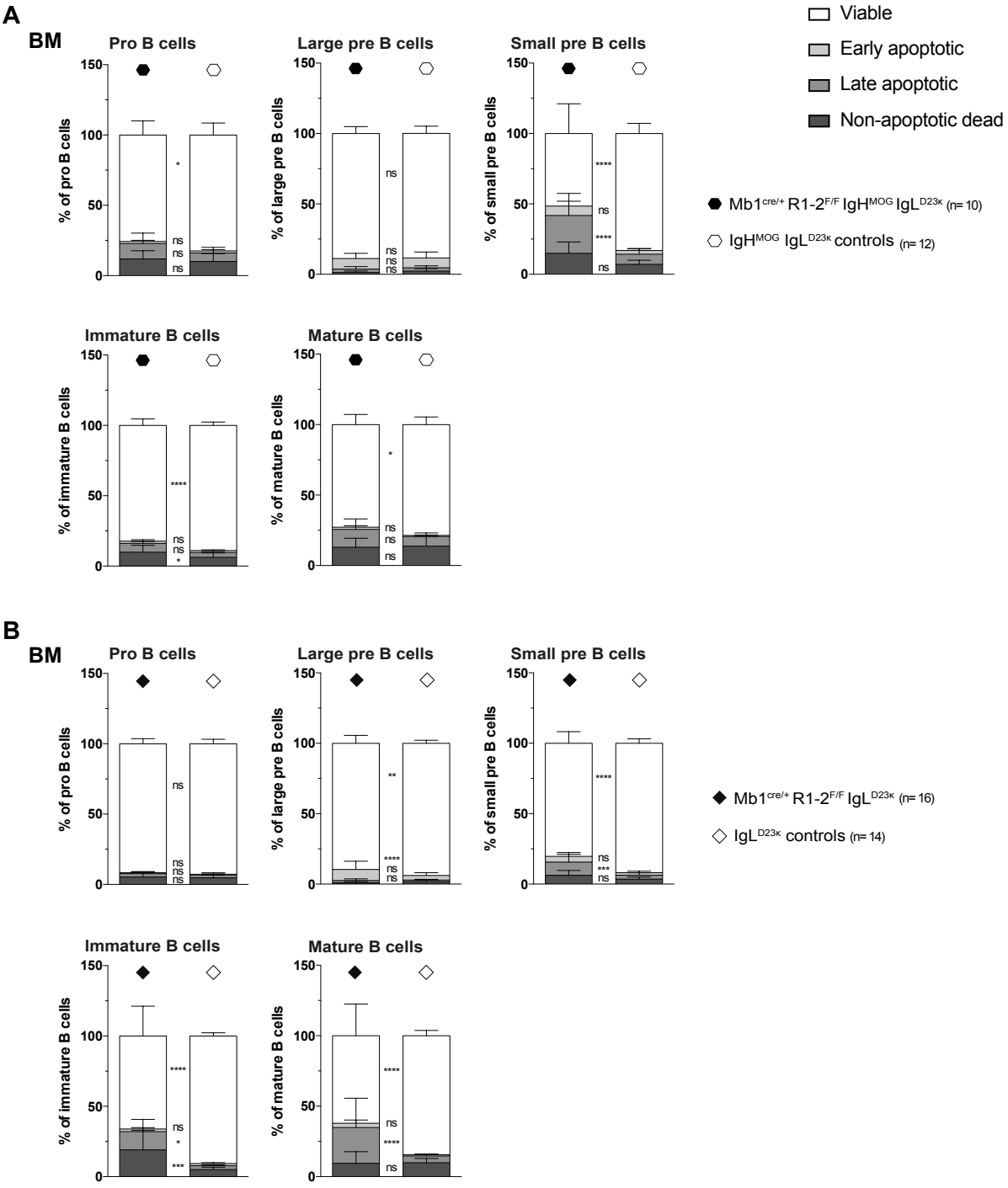

Figure S24: Strongly reduced ratio of viable small pre B cells in Mb1$^{cre/+}$ Rc3h1-2$^{F/F}$ IgH^{MOG} IgL^{D23κ} mice and immature and mature B cells in Mb1$^{cre/+}$ Rc3h1-2$^{F/F}$ IgL^{D23κ} mice.

Caspglow stain was performed as described in Fig. 27 for Mb1$^{cre/+}$ Rc3h1-2$^{F/F}$ IgH^{MOG} IgL^{D23κ} mice (A) and Mb1$^{cre/+}$ Rc3h1-2$^{F/F}$ IgL^{D23κ} mice (B). Quantification of percentages of viable, early apoptotic, late apoptotic and non-apoptotic dead cells of BM cell subsets as determined by flow cytometry in *ex vivo* cells shown as stacked bar charts. Viable caspglow$^-$ 7-AAD$^-$; early apoptotic caspglow$^+$ 7-AAD$^-$, late apoptotic caspglow$^+$ 7-AAD$^+$, non-apoptotic dead caspglow$^-$ 7-AAD$^+$. Gated B cell subsets: pro B B220^{lo} IgM$^-$ CD25$^-$ c-kit$^+$, large pre B B220^{lo} c-kit$^-$ CD25$^+$ IgD$^-$ IgM$^-$ FSC^{hi}; small pre B B220^{lo} c-kit$^-$ CD25$^+$ IgD$^-$ IgM$^-$ FSC^{lo}; immature B B220$^+$ IgD$^-$ IgM$^+$, mature B B220^{hi} IgD$^+$. Bars represent mean values and error bars standard deviation. ****p ≤ 0.0001, ***p ≤ 0.001, **p ≤ 0.01, *p ≤ 0.05, ns non-significant, unpaired t test.

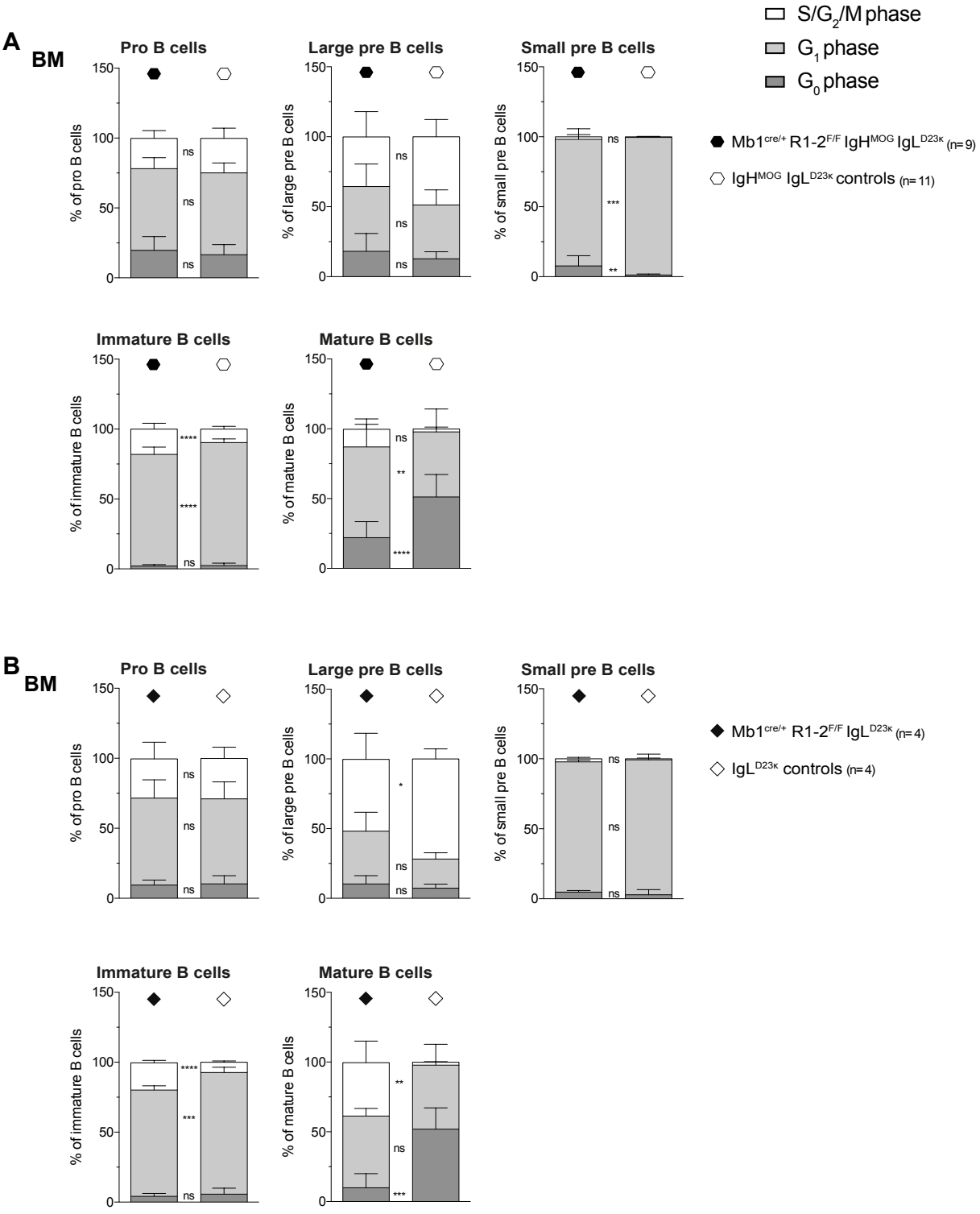

Figure S25: Cell cycle analysis of bone marrow B cell populations in Mb1$^{cre/+}$ Rc3h1-2$^{F/F}$ IgH^{MOG} IgL^{D23κ} and Mb1$^{cre/+}$ Rc3h1-2$^{F/F}$ IgL^{D23κ} mice.

Stacked bar chart representation of cell cycle analysis (Ki67 and DRAQ5-based) of indicated B cell populations. Analysis was performed as in Fig. 28. Bars show mean values and error bars standard deviation. BM: bone marrow. Cell cycle phases were distinguished as follow: G_0 phase (dark grey) Ki67$^-$ DRAQ5^{lo}; G_1 phase (light grey) Ki67$^+$ DRAQ5^{lo}; S/G_2/M phase (white) Ki67$^+$ DRAQ5^{hi}. Gated B cell subsets: pro B B220^{lo} IgM$^-$ CD25$^-$ c-kit$^+$, large pre B B220^{lo} c-kit$^-$ CD25$^+$ IgD$^-$ IgM$^-$ FSC^{hi}; small pre B B220^{lo} c-kit$^-$ CD25$^+$ IgD$^-$ IgM$^-$ FSC^{lo}; immature B B220$^+$ IgD$^-$ IgM$^+$, mature B B220^{hi} IgD$^+$. ****p ≤ 0.0001, **p ≤ 0.01, *p ≤ 0.05, ns non-significant, unpaired t test.

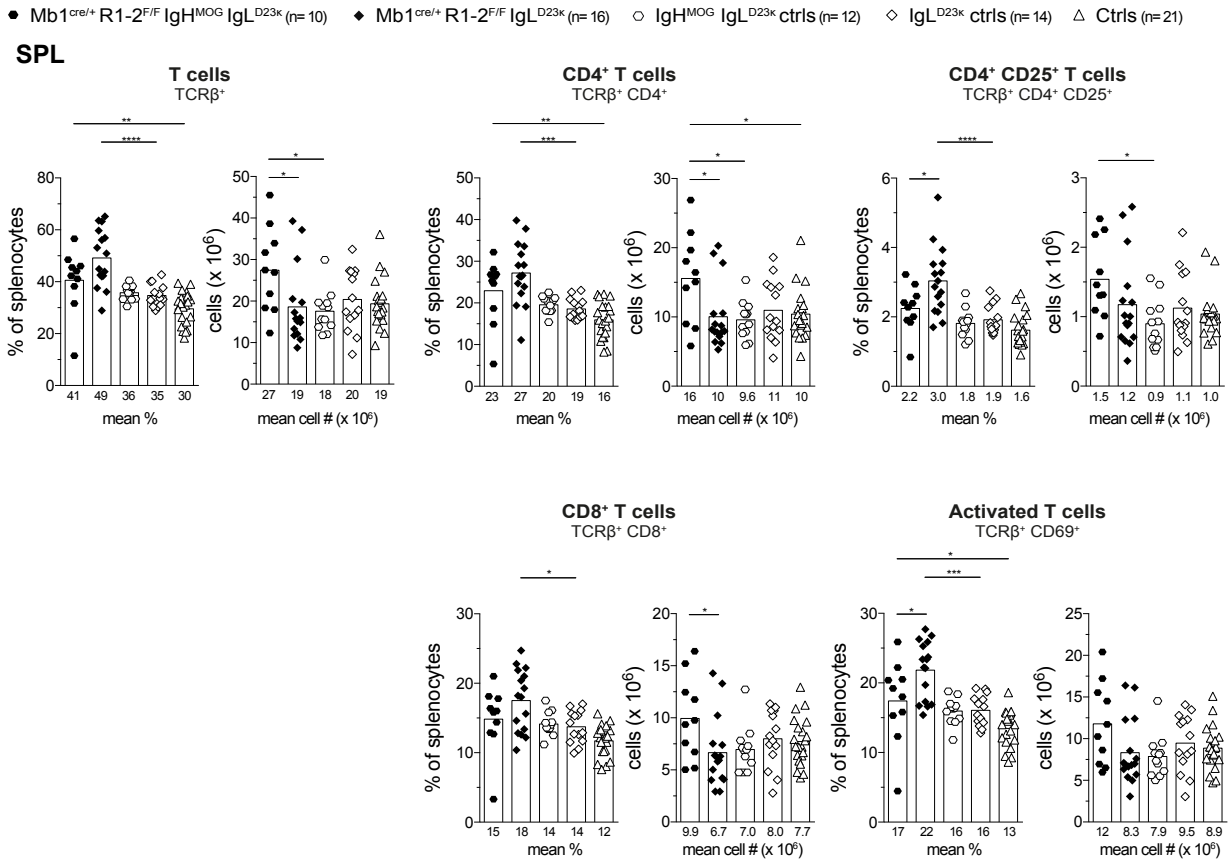

Figure S26: Expanded splenic T cell compartment in Mb1$^{cre/+}$ Rc3h1-2$^{F/F}$ IgH^{MOG} IgL$^{D23\kappa}$ mice.
Percentages of respective T cell subsets of total SPL cells and total subset cell numbers as determined by flow cytometry. Gating of T cell subsets as indicated. Ctrls: controls; R: Rc3h; SPL: spleen. Numbers below graphs and bars indicate mean values. ****p ≤ 0.0001, ***p ≤ 0.001, **p ≤ 0.01, *p ≤ 0.05; ANOVA. Significances for Mb1$^{cre/+}$ R1-2$^{F/F}$ IgH^{MOG} IgL$^{D23\kappa}$ and IgH^{MOG} IgL$^{D23\kappa}$ ctrls versus IgL$^{D23\kappa}$ ctrls and Mb1$^{cre/+}$ R1-2$^{F/F}$ IgL$^{D23\kappa}$ versus IgH^{MOG} IgL$^{D23\kappa}$ ctrls and ctrls are not shown.

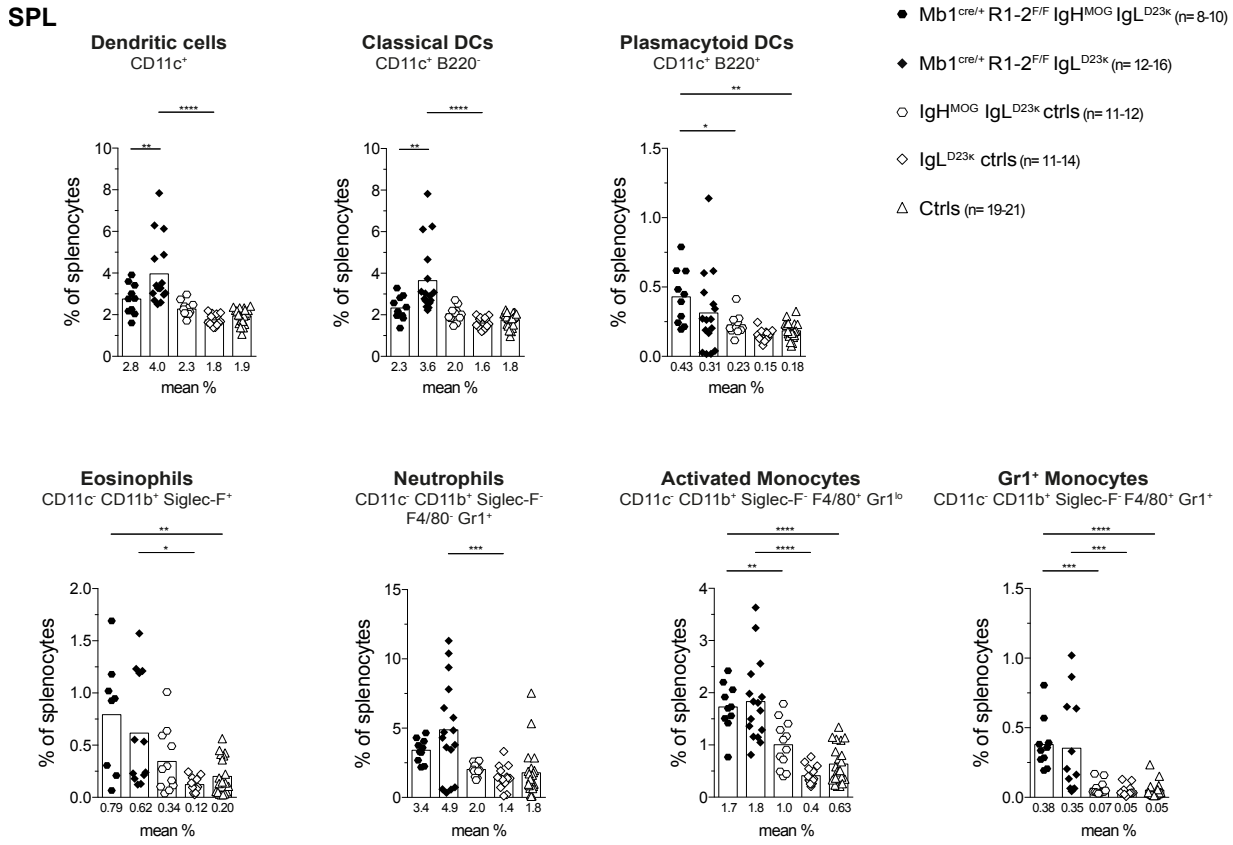

Figure S27: Expansion of myeloid cell populations in Mb1$^{cre/+}$ Rc3h1-2$^{F/F}$ IgH^{MOG} IgL$^{D23\kappa}$ mice.
Percentages of indicated myeloid cell subsets of total splenocytes as determined by flow cytometry. Gating of myeloid cell types as indicated. Ctrls: controls; R: Rc3h; SPL: spleen; DCs: Dendritic cells; Monocytes: Macrophages and Monocytes. Numbers below graphs and bars show mean percentages. ****$p \leq 0.0001$, ***$p \leq 0.001$, **$p \leq 0.01$, *$p \leq 0.05$, ANOVA. Significances for Mb1$^{cre/+}$ R1-2$^{F/F}$ IgH^{MOG} IgL$^{D23\kappa}$ and IgH^{MOG} IgL$^{D23\kappa}$ ctrls versus IgL$^{D23\kappa}$ ctrls and Mb1$^{cre/+}$ R1-2$^{F/F}$ IgL$^{D23\kappa}$ versus IgH^{MOG} IgL$^{D23\kappa}$ ctrls and ctrls are not shown.

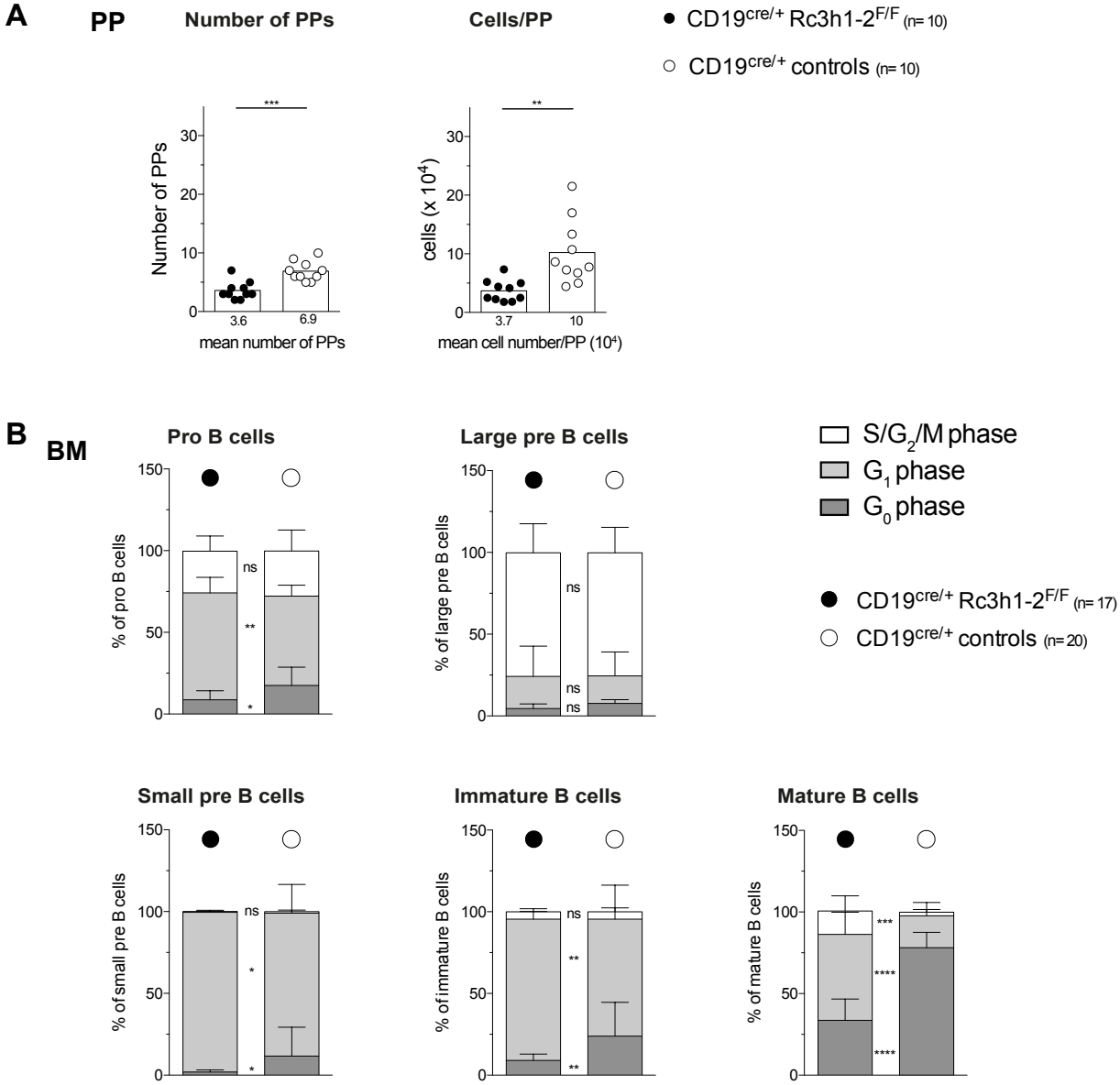

Figure S28: Number of Peyer's patches and their cellularity are decreased (A) and proliferation of mature recirculating B cells is increased in CD19$^{cre/+}$ Rc3h1-2$^{F/F}$ mice (B).

(A) Total number of Peyer's patches (PP) and total cell count per PP. Further analyses of GALT B cells as well as analyses of GC B cells in CD19$^{cre/+}$ Rc3h1-2$^{F/F}$ mice were performed by my colleague Dr. Maike Kober and were therefore excluded from my thesis. (B) Percentages of designated B cell populations in different cell cycle phases. Analysis performed as in Fig. 28. Cell cycle phases distinguished as shown in Fig. 28, briefly: G_0 phase (dark grey) Ki67$^-$ DRAQ5^{lo}; G_1 phase (light grey) Ki67$^+$ DRAQ5^{lo}; S/G_2/M phase (white) Ki67$^+$ DRAQ5^{hi}. Gated B cell subsets: pro B B220^{lo} IgM$^-$ CD25$^-$ c-kit$^+$, large pre B B220^{lo} c-kit$^-$ CD25$^+$ IgD$^-$ IgM$^-$ FSC^{hi}; small pre B B220^{lo} c-kit$^-$ CD25$^+$ IgD$^-$ IgM$^-$ FSC^{lo}; immature B B220$^+$ IgD$^-$ IgM$^+$, mature B B220^{hi} IgD$^+$. GALT: gut-associated lymphoid tissue. Numbers below graphs and bars represent mean values. ****p ≤ 0.0001, ***p ≤ 0.001, **p ≤ 0.01, *p ≤ 0.05, ns non-significant, (A) paired and (B) unpaired t test.

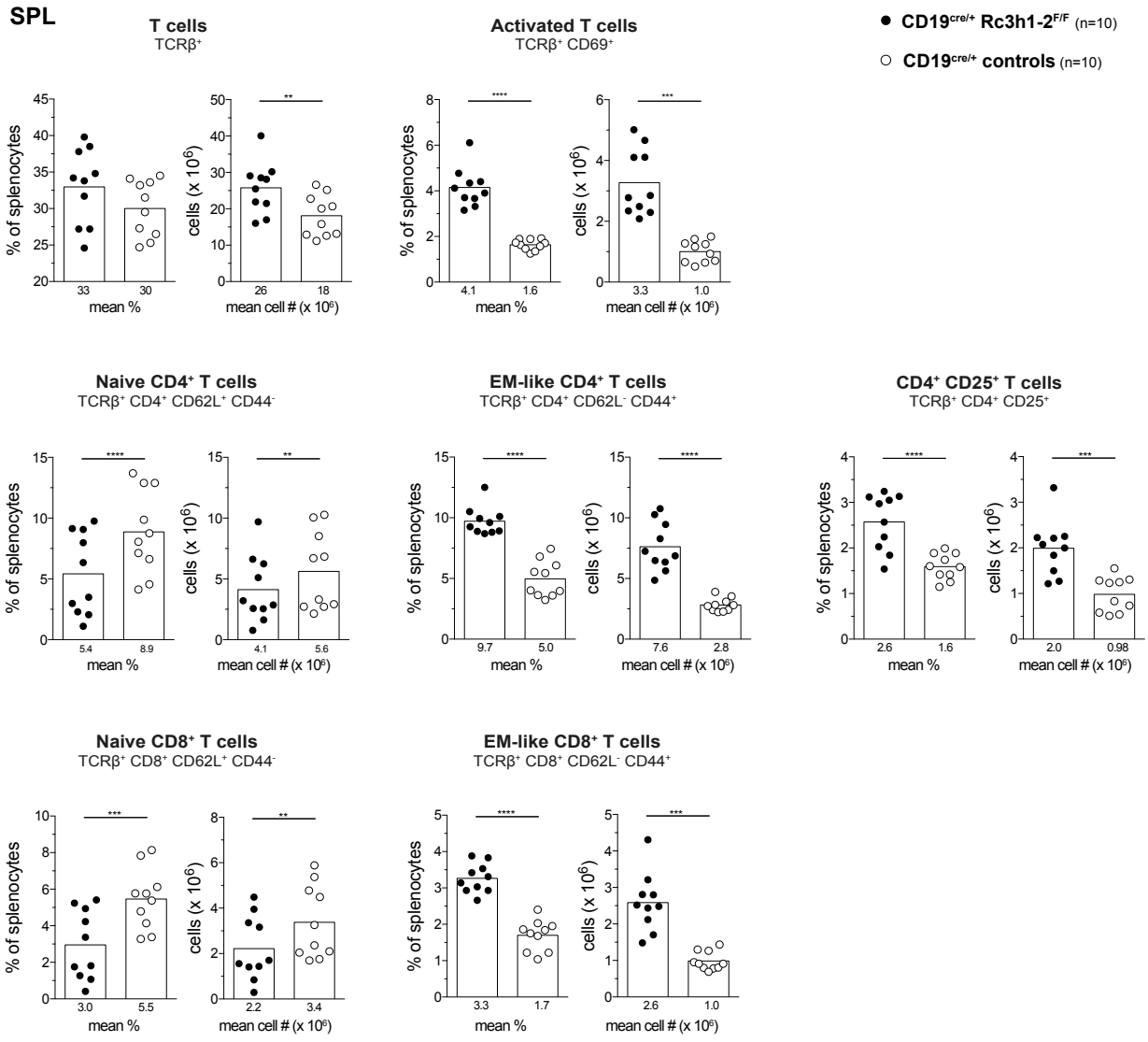

Figure S29: Expansion of the splenic T cell compartment in CD19$^{cre/+}$ Rc3h1-2$^{F/F}$ mice.
Percentages of indicated T cell subsets among viable cells of SPL (spleen) and total cell numbers as determined by flow cytometry. EM: effector memory; CM: central memory. Numbers below graphs and bars show mean values. ****$p \leq 0.0001$, ***$p \leq 0.001$, **$p \leq 0.01$, paired t test.

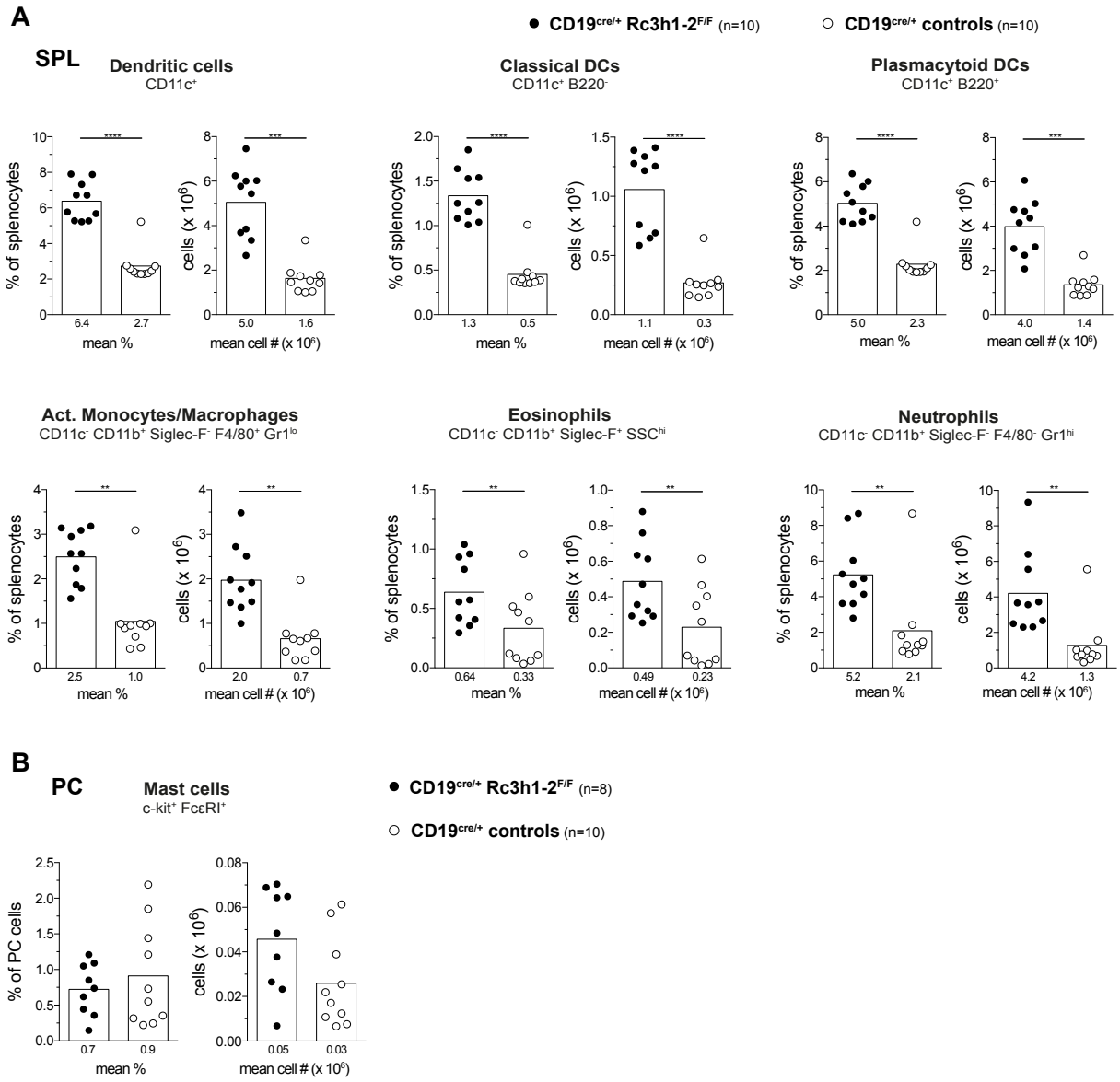

Figure S30: Expansion of splenic myeloid populations and peritoneal cavity mast cells in CD19$^{cre/+}$ Rc3h1-2$^{F/F}$ mice.

(A) Percentages of indicated myeloid cell populations among viable cells of SPL (spleen) and (B) percentages of mast cells of viable cells of peritoneal cavity (PC) and total cell number as determined by flow cytometry. DC: dendritic cells; Act: activated. Numbers below graphs and bars indicate mean values. ****p ≤ 0.0001, ***p ≤ 0.001, **p ≤ 0.01, (A) paired t test, (B) unpaired t test.

References

1. Liston, A. and S.L. Masters, *Homeostasis-altering molecular processes as mechanisms of inflammasome activation.* Nat Rev Immunol, 2017. **17**(3): p. 208-214.
2. Goodnow, C.C., et al., *Control systems and decision making for antibody production.* Nat Immunol, 2010. **11**(8): p. 681-8.
3. Nemazee, D., *Receptor editing in lymphocyte development and central tolerance.* Nat Rev Immunol, 2006. **6**(10): p. 728-40.
4. Zhao, E., et al., *Bone marrow and the control of immunity.* Cell Mol Immunol, 2012. **9**(1): p. 11-9.
5. Yu, V.W. and D.T. Scadden, *Heterogeneity of the bone marrow niche.* Curr Opin Hematol, 2016. **23**(4): p. 331-8.
6. Dorshkind, K. and E. Montecino-Rodriguez, *Fetal B-cell lymphopoiesis and the emergence of B-1-cell potential.* Nat Rev Immunol, 2007. **7**(3): p. 213-9.
7. Tsuneto, M., et al., *Environments of B cell development.* Immunol Lett, 2014. **157**(1-2): p. 60-3.
8. Luc, S., N. Buza-Vidas, and S.E. Jacobsen, *Delineating the cellular pathways of hematopoietic lineage commitment.* Semin Immunol, 2008. **20**(4): p. 213-20.
9. Cabezas-Wallscheid, N. and A. Trumpp, *STEM CELLS. Potency finds its niches.* Science, 2016. **351**(6269): p. 126-7.
10. Bain, G., et al., *E2A proteins are required for proper B cell development and initiation of immunoglobulin gene rearrangements.* Cell, 1994. **79**(5): p. 885-92.
11. Choukrallah, M.A., et al., *Enhancer repertoires are reshaped independently of early priming and heterochromatin dynamics during B cell differentiation.* Nat Commun, 2015. **6**: p. 8324.
12. Zhuang, Y., P. Soriano, and H. Weintraub, *The helix-loop-helix gene E2A is required for B cell formation.* Cell, 1994. **79**(5): p. 875-84.
13. Hagman, J., et al., *EBF contains a novel zinc coordination motif and multiple dimerization and transcriptional activation domains.* EMBO J, 1995. **14**(12): p. 2907-16.
14. Lin, H. and R. Grosschedl, *Failure of B-cell differentiation in mice lacking the transcription factor EBF.* Nature, 1995. **376**(6537): p. 263-7.
15. Cobaleda, C., et al., *Pax5: the guardian of B cell identity and function.* Nat Immunol, 2007. **8**(5): p. 463-70.
16. Nutt, S.L., et al., *Commitment to the B-lymphoid lineage depends on the transcription factor Pax5.* Nature, 1999. **401**(6753): p. 556-62.
17. Urbanek, P., et al., *Complete block of early B cell differentiation and altered patterning of the posterior midbrain in mice lacking Pax5/BSAP.* Cell, 1994. **79**(5): p. 901-12.

18. Hagman, J., J. Ramirez, and K. Lukin, *B lymphocyte lineage specification, commitment and epigenetic control of transcription by early B cell factor 1.* Curr Top Microbiol Immunol, 2012. **356**: p. 17-38.

19. Jung, D., et al., *Mechanism and control of V(D)J recombination at the immunoglobulin heavy chain locus.* Annu Rev Immunol, 2006. **24**: p. 541-70.

20. Hardy, R.R. and K. Hayakawa, *B cell development pathways.* Annu Rev Immunol, 2001. **19**: p. 595-621.

21. Davis, A.J. and D.J. Chen, *DNA double strand break repair via non-homologous end-joining.* Transl Cancer Res, 2013. **2**(3): p. 130-143.

22. Alt, F.W., et al., *Mechanisms of programmed DNA lesions and genomic instability in the immune system.* Cell, 2013. **152**(3): p. 417-29.

23. Schatz, D.G. and P.C. Swanson, *V(D)J recombination: mechanisms of initiation.* Annu Rev Genet, 2011. **45**: p. 167-202.

24. Feeney, A.J., A. Tang, and K.M. Ogwaro, *B-cell repertoire formation: role of the recombination signal sequence in non-random V segment utilization.* Immunol Rev, 2000. **175**: p. 59-69.

25. Schatz, D.G. and Y. Ji, *Recombination centres and the orchestration of V(D)J recombination.* Nat Rev Immunol, 2011. **11**(4): p. 251-63.

26. Daitch, L.E., et al., *Transcription and recombination of the murine RS element.* J Immunol, 1992. **149**(3): p. 832-40.

27. Zhou, X., Y. Xiang, and W.T. Garrard, *The Igkappa gene enhancers, E3′ and Ed, are essential for triggering transcription.* J Immunol, 2010. **185**(12): p. 7544-52.

28. Oberdoerffer, P., T.I. Novobrantseva, and K. Rajewsky, *Expression of a targeted lambda 1 light chain gene is developmentally regulated and independent of Ig kappa rearrangements.* J Exp Med, 2003. **197**(9): p. 1165-72.

29. Panigrahi, A.K., et al., *RS rearrangement frequency as a marker of receptor editing in lupus and type 1 diabetes.* J Exp Med, 2008. **205**(13): p. 2985-94.

30. Corneo, B., et al., *Rag mutations reveal robust alternative end joining.* Nature, 2007. **449**(7161): p. 483-6.

31. Lescale, C. and L. Deriano, *The RAG recombinase: Beyond breaking.* Mech Ageing Dev, 2016.

32. Lieber, M.R., *Mechanisms of human lymphoid chromosomal translocations.* Nat Rev Cancer, 2016. **16**(6): p. 387-98.

33. Mombaerts, P., et al., *RAG-1-deficient mice have no mature B and T lymphocytes.* Cell, 1992. **68**(5): p. 869-77.

34. Shinkai, Y., et al., *RAG-2-deficient mice lack mature lymphocytes owing to inability to initiate V(D)J rearrangement.* Cell, 1992. **68**(5): p. 855-67.

35. Hu, J., et al., *Chromosomal Loop Domains Direct the Recombination of Antigen Receptor Genes.* Cell, 2015. **163**(4): p. 947-59.

36. Rommel, P.C., et al., *RAG1/2 induces genomic insertions by mobilizing DNA into RAG1/2-independent breaks.* J Exp Med, 2017. **214**(3): p. 815-831.

37. Perlot, T. and F.W. Alt, *Cis-regulatory elements and epigenetic changes control genomic rearrangements of the IgH locus.* Adv Immunol, 2008. **99**: p. 1-32.

38. Ebert, A., et al., *Control of antigen receptor diversity through spatial regulation of V(D)J recombination.* Cold Spring Harb Symp Quant Biol, 2013. **78**: p. 11-21.

39. Yancopoulos, G.D. and F.W. Alt, *Developmentally controlled and tissue-specific expression of unrearranged VH gene segments.* Cell, 1985. **40**(2): p. 271-81.

40. Alt, F.W., et al., *Regulation of genome rearrangement events during lymphocyte differentiation.* Immunol Rev, 1986. **89**: p. 5-30.

41. Nagasawa, T., *Microenvironmental niches in the bone marrow required for B-cell development.* Nat Rev Immunol, 2006. **6**(2): p. 107-16.

42. Herzog, S., M. Reth, and H. Jumaa, *Regulation of B-cell proliferation and differentiation by pre-B-cell receptor signalling.* Nat Rev Immunol, 2009. **9**(3): p. 195-205.

43. Hwang, J.K., F.W. Alt, and L.S. Yeap, *Related Mechanisms of Antibody Somatic Hypermutation and Class Switch Recombination.* Microbiol Spectr, 2015. **3**(1): p. MDNA3-0037-2014.

44. Roy, A.L., R. Sen, and R.G. Roeder, *Enhancer-promoter communication and transcriptional regulation of Igh.* Trends Immunol, 2011. **32**(11): p. 532-9.

45. Yabas, M., H. Elliott, and G.E. Hoyne, *The Role of Alternative Splicing in the Control of Immune Homeostasis and Cellular Differentiation.* Int. J. Mol. Sci., 2016. **17**(3): p. 1-21.

46. Enders, A., et al., *Zinc-finger protein ZFP318 is essential for expression of IgD, the alternatively spliced Igh product made by mature B lymphocytes.* Proc Natl Acad Sci U S A, 2014. **111**(12): p. 4513-8.

47. Geier, J.K. and M.S. Schlissel, *Pre-BCR signals and the control of Ig gene rearrangements.* Semin Immunol, 2006. **18**(1): p. 31-9.

48. Guloglu, F.B. and C.A. Roman, *Precursor B cell receptor signaling activity can be uncoupled from surface expression.* J Immunol, 2006. **176**(11): p. 6862-72.

49. Lutz, J., et al., *Pro-B cells sense productive immunoglobulin heavy chain rearrangement irrespective of polypeptide production.* Proc Natl Acad Sci U S A, 2011. **108**(26): p. 10644-9.

50. Melchers, F., et al., *Repertoire selection by pre-B-cell receptors and B-cell receptors, and genetic control of B-cell development from immature to mature B cells.* Immunol Rev, 2000. **175**: p. 33-46.

51. Gopalakrishnan, S., P.L. Collins, and E.M. Oltz, *Control of Ig gene assembly: lessons from premature activation.* EMBO J, 2013. **32**(10): p. 1350-1.

52. Pelanda, R. and R.M. Torres, *Central B-cell tolerance: where selection begins.* Cold Spring Harb Perspect Biol, 2012. **4**(4): p. a007146.

53. Grandien, A., et al., *Negative selection of multireactive B cell clones in normal adult mice.* Eur J Immunol, 1994. **24**(6): p. 1345-52.

54. Wardemann, H., et al., *Predominant autoantibody production by early human B cell precursors.* Science, 2003. **301**(5638): p. 1374-7.

55. Lutz, J., W. Muller, and H.M. Jack, *VH replacement rescues progenitor B cells with two nonproductive VDJ alleles.* J Immunol, 2006. **177**(10): p. 7007-14.

56. Reth, M.G., S. Jackson, and F.W. Alt, *VHDJH formation and DJH replacement during pre-B differentiation: non-random usage of gene segments.* EMBO J, 1986. **5**(9): p. 2131-8.

57. Sun, A., et al., *VH replacement in primary immunoglobulin repertoire diversification.* Proc Natl Acad Sci U S A, 2015. **112**(5): p. E458-66.

58. Zhang, L., et al., *Coupling of V(D)J recombination to the cell cycle suppresses genomic instability and lymphoid tumorigenesis.* Immunity, 2011. **34**(2): p. 163-74.

59. Ochiai, K., et al., *A self-reinforcing regulatory network triggered by limiting IL-7 activates pre-BCR signaling and differentiation.* Nat Immunol, 2012. **13**(3): p. 300-7.

60. Clark, M.R., et al., *Orchestrating B cell lymphopoiesis through interplay of IL-7 receptor and pre-B cell receptor signalling.* Nat Rev Immunol, 2014. **14**(2): p. 69-80.

61. Corfe, S.A. and C.J. Paige, *The many roles of IL-7 in B cell development; mediator of survival, proliferation and differentiation.* Semin Immunol, 2012. **24**(3): p. 198-208.

62. Dengler, H.S., et al., *Distinct functions for the transcription factor Foxo1 at various stages of B cell differentiation.* Nat Immunol, 2008. **9**(12): p. 1388-98.

63. Herzog, S., et al., *SLP-65 regulates immunoglobulin light chain gene recombination through the PI(3)K-PKB-Foxo pathway.* Nat Immunol, 2008. **9**(6): p. 623-31.

64. Itoh-Nakadai, A., et al., *The transcription repressors Bach2 and Bach1 promote B cell development by repressing the myeloid program.* Nat Immunol, 2014. **15**(12): p. 1171-80.

65. Swaminathan, S., C. Duy, and M. Muschen, *BACH2-BCL6 balance regulates selection at the pre-B cell receptor checkpoint.* Trends Immunol, 2014. **35**(3): p. 131-7.

66. Rolink, A.G., et al., *Precursor B cell receptor-dependent B cell proliferation and differentiation does not require the bone marrow or fetal liver environment.* J Exp Med, 2000. **191**(1): p. 23-32.

67. Rickert, R.C., *New insights into pre-BCR and BCR signalling with relevance to B cell malignancies.* Nat Rev Immunol, 2013. **13**(8): p. 578-91.

68. Duy, C., et al., *BCL6 is critical for the development of a diverse primary B cell repertoire.* J Exp Med, 2010. **207**(6): p. 1209-21.

69. Ma, S., et al., *Interferon regulatory factors 4 and 8 induce the expression of Ikaros and Aiolos to down-regulate pre-B-cell receptor and promote cell-cycle withdrawal in pre-B-cell development.* Blood, 2008. **111**(3): p. 1396-403.

70. Merkenschlager, M., *Ikaros in immune receptor signaling, lymphocyte differentiation, and function.* FEBS Lett, 2010. **584**(24): p. 4910-4.

71. Mandal, M., et al., *Epigenetic repression of the Igk locus by STAT5-mediated recruitment of the histone methyltransferase Ezh2.* Nat Immunol, 2011. **12**(12): p. 1212-20.

72. Powers, S.E., et al., *Subnuclear cyclin D3 compartments and the coordinated regulation of proliferation and immunoglobulin variable gene repression.* J Exp Med, 2012. **209**(12): p. 2199-213.

73. Ciriza, J., et al., *The migration of hematopoietic progenitors from the fetal liver to the fetal bone marrow: lessons learned and possible clinical applications.* Exp Hematol, 2013. **41**(5): p. 411-23.

74. Ma, Q., et al., *Impaired B-lymphopoiesis, myelopoiesis, and derailed cerebellar neuron migration in CXCR4- and SDF-1-deficient mice.* Proc Natl Acad Sci U S A, 1998. **95**(16): p. 9448-53.

75. Nagasawa, T., et al., *Defects of B-cell lymphopoiesis and bone-marrow myelopoiesis in mice lacking the CXC chemokine PBSF/SDF-1.* Nature, 1996. **382**(6592): p. 635-8.

76. Park, S.Y., et al., *Focal adhesion kinase regulates the localization and retention of pro-B cells in bone marrow microenvironments.* J Immunol, 2013. **190**(3): p. 1094-102.

77. Tokoyoda, K., et al., *Cellular niches controlling B lymphocyte behavior within bone marrow during development.* Immunity, 2004. **20**(6): p. 707-18.

78. Nadrah, K., T.C. Beck, and J.P. Pereira, *Immature B Cell Egress from Bone Marrow Is SOCS3 Independent.* PLoS One, 2015. **10**(8): p. e0136061.

79. Johnson, K., et al., *Regulation of immunoglobulin light-chain recombination by the transcription factor IRF-4 and the attenuation of interleukin-7 signaling.* Immunity, 2008. **28**(3): p. 335-45.

80. Beck, T.C., et al., *CXCR4 and a cell-extrinsic mechanism control immature B lymphocyte egress from bone marrow.* J Exp Med, 2014. **211**(13): p. 2567-81.

81. Wang, A., et al., *CXCR4/CXCL12 hyperexpression plays a pivotal role in the pathogenesis of lupus.* J Immunol, 2009. **182**(7): p. 4448-58.

82. Srinivasan, L., et al., *PI3 kinase signals BCR-dependent mature B cell survival.* Cell, 2009. **139**(3): p. 573-86.

83. Pioli, P.D., et al., *Zfp318 regulates IgD expression by abrogating transcription termination within the Ighm/Ighd locus.* J Immunol, 2014. **193**(5): p. 2546-53.

84. Allman, D. and S. Pillai, *Peripheral B cell subsets.* Curr Opin Immunol, 2008. **20**(2): p. 149-57.

85. Pillai, S. and A. Cariappa, *The follicular versus marginal zone B lymphocyte cell fate decision.* Nat Rev Immunol, 2009. **9**(11): p. 767-77.

86. Merrell, K.T., et al., *Identification of anergic B cells within a wild-type repertoire.* Immunity, 2006. **25**(6): p. 953-62.

87. Ubelhart, R. and H. Jumaa, *Autoreactivity and the positive selection of B cells.* Eur J Immunol, 2015. **45**(11): p. 2971-7.

88. Stadanlick, J.E. and M.P. Cancro, *BAFF and the plasticity of peripheral B cell tolerance.* Curr Opin Immunol, 2008. **20**(2): p. 158-61.

89. Zikherman, J., R. Parameswaran, and A. Weiss, *Endogenous antigen tunes the responsiveness of naive B cells but not T cells.* Nature, 2012. **489**(7414): p. 160-4.

90. Casola, S., *Control of peripheral B-cell development.* Curr Opin Immunol, 2007. **19**(2): p. 143-9.

91. Sasaki, Y., et al., *Canonical NF-kappaB activity, dispensable for B cell development, replaces BAFF-receptor signals and promotes B cell proliferation upon activation.* Immunity, 2006. **24**(6): p. 729-39.

92. Tan, J.B., et al., *Lunatic and manic fringe cooperatively enhance marginal zone B cell precursor competition for delta-like 1 in splenic endothelial niches.* Immunity, 2009. **30**(2): p. 254-63.

93. Fasnacht, N., et al., *Specific fibroblastic niches in secondary lymphoid organs orchestrate distinct Notch-regulated immune responses.* J Exp Med, 2014. **211**(11): p. 2265-79.

94. Zouali, M. and Y. Richard, *Marginal zone B-cells, a gatekeeper of innate immunity.* Front Immunol, 2011. **2**: p. 63.

95. Montecino-Rodriguez, E. and K. Dorshkind, *B-1 B cell development in the fetus and adult.* Immunity, 2012. **36**(1): p. 13-21.

96. Baumgarth, N., *The double life of a B-1 cell: self-reactivity selects for protective effector functions.* Nat Rev Immunol, 2011. **11**(1): p. 34-46.

97. Boes, M., et al., *Enhanced B-1 cell development, but impaired IgG antibody responses in mice deficient in secreted IgM.* J Immunol, 1998. **160**(10): p. 4776-87.

98. Tangye, S.G., *To B1 or not to B1: that really is still the question!* Blood, 2013. **121**(26): p. 5109-10.

99. Berland, R. and H.H. Wortis, *Origins and functions of B-1 cells with notes on the role of CD5.* Annu Rev Immunol, 2002. **20**: p. 253-300.

100. Casola, S., et al., *B cell receptor signal strength determines B cell fate.* Nat Immunol, 2004. **5**(3): p. 317-27.

101. Lam, K.P. and K. Rajewsky, *B cell antigen receptor specificity and surface density together determine B-1 versus B-2 cell development.* J Exp Med, 1999. **190**(4): p. 471-7.

102. Thome, M., *CARMA1, BCL-10 and MALT1 in lymphocyte development and activation.* Nat Rev Immunol, 2004. **4**(5): p. 348-59.

103. Kurosaki, T. and J. Wienands, *Preface. Regulatory signal networks of the B cell antigen receptor.* Curr Top Microbiol Immunol, 2016. **393**: p. v-vi.

104. Sindhava, V.J. and S. Bondada, *Multiple regulatory mechanisms control B-1 B cell activation.* Front Immunol, 2012. **3**: p. 372.

105. Crotty, S., *A brief history of T cell help to B cells.* Nat Rev Immunol, 2015. **15**(3): p. 185-9.

106. Takemori, T., et al., *Generation of memory B cells inside and outside germinal centers.* Eur J Immunol, 2014. **44**(5): p. 1258-64.

107. Vinuesa, C.G. and P.P. Chang, *Innate B cell helpers reveal novel types of antibody responses.* Nat Immunol, 2013. **14**(2): p. 119-26.

108. Nutt, S.L., et al., *The generation of antibody-secreting plasma cells.* Nat Rev Immunol, 2015. **15**(3): p. 160-71.

109. Allen, C.D., T. Okada, and J.G. Cyster, *Germinal-center organization and cellular dynamics.* Immunity, 2007. **27**(2): p. 190-202.

110. De Silva, N.S. and U. Klein, *Dynamics of B cells in germinal centres.* Nat Rev Immunol, 2015. **15**(3): p. 137-48.

111. Victora, G.D., *SnapShot: the germinal center reaction.* Cell, 2014. **159**(3): p. 700-700 e1.

112. Casola, S. and K. Rajewsky, *B cell recruitment and selection in mouse GALT germinal centers.* Curr Top Microbiol Immunol, 2006. **308**: p. 155-71.

113. Ferretti, E., et al., *IL-17 superfamily cytokines modulate normal germinal center B cell migration.* J Leukoc Biol, 2016. **100**(5): p. 913-918.

114. Victora, G.D. and M.C. Nussenzweig, *Germinal centers.* Annu Rev Immunol, 2012. **30**: p. 429-57.

115. Green, J.A., et al., *The sphingosine 1-phosphate receptor S1P(2) maintains the homeostasis of germinal center B cells and promotes niche confinement.* Nat Immunol, 2011. **12**(7): p. 672-80.

116. Kitano, M., et al., *Bcl6 protein expression shapes pre-germinal center B cell dynamics and follicular helper T cell heterogeneity.* Immunity, 2011. **34**(6): p. 961-72.

117. Bollig, N., et al., *Transcription factor IRF4 determines germinal center formation through follicular T-helper cell differentiation.* Proc Natl Acad Sci U S A, 2012. **109**(22): p. 8664-9.

118. Ochiai, K., et al., *Transcriptional regulation of germinal center B and plasma cell fates by dynamical control of IRF4.* Immunity, 2013. **38**(5): p. 918-29.

119. Willis, S.N., et al., *Transcription factor IRF4 regulates germinal center cell formation through a B cell-intrinsic mechanism.* J Immunol, 2014. **192**(7): p. 3200-6.

120. Dominguez, P.M., et al., *DNA Methylation Dynamics of Germinal Center B Cells Are Mediated by AID.* Cell Rep, 2015. **12**(12): p. 2086-98.

121. Ramezani-Rad, P. and R.C. Rickert, *Murine models of germinal center derived-lymphomas.* Curr Opin Immunol, 2017. **45**: p. 31-36.

122. Sander, S., et al., *PI3 Kinase and FOXO1 Transcription Factor Activity Differentially Control B Cells in the Germinal Center Light and Dark Zones.* Immunity, 2015. **43**(6): p. 1075-86.

123. Calado, D.P., et al., *Constitutive canonical NF-kappaB activation cooperates with disruption of BLIMP1 in the pathogenesis of activated B cell-like diffuse large cell lymphoma.* Cancer Cell, 2010. **18**(6): p. 580-9.

124. Gloury, R., et al., *Dynamic changes in Id3 and E-protein activity orchestrate germinal center and plasma cell development.* J Exp Med, 2016. **213**(6): p. 1095-111.

125. Berek, C., A. Berger, and M. Apel, *Maturation of the immune response in germinal centers.* Cell, 1991. **67**(6): p. 1121-9.

126. Rajewsky, K., I. Forster, and A. Cumano, *Evolutionary and somatic selection of the antibody repertoire in the mouse.* Science, 1987. **238**(4830): p. 1088-94.

127. Di Noia, J.M. and M.S. Neuberger, *Molecular mechanisms of antibody somatic hypermutation.* Annu Rev Biochem, 2007. **76**: p. 1-22.

128. Yeap, L.S., et al., *Sequence-Intrinsic Mechanisms that Target AID Mutational Outcomes on Antibody Genes.* Cell, 2015. **163**(5): p. 1124-37.

129. Nussenzweig, A. and M.C. Nussenzweig, *Origin of chromosomal translocations in lymphoid cancer.* Cell, 2010. **141**(1): p. 27-38.

130. Wang, Q., et al., *The cell cycle restricts activation-induced cytidine deaminase activity to early G1.* J Exp Med, 2017. **214**(1): p. 49-58.

131. Teng, G. and F.N. Papavasiliou, *Immunoglobulin somatic hypermutation.* Annu Rev Genet, 2007. **41**: p. 107-20.

132. Allen, C.D., *Germinal center quality control: death by Fas.* Immunity, 2015. **42**(5): p. 783-5.

133. Brink, R., *The imperfect control of self-reactive germinal center B cells.* Curr Opin Immunol, 2014. **28**: p. 97-101.

134. Vinuesa, C.G., I. Sanz, and M.C. Cook, *Dysregulation of germinal centres in autoimmune disease.* Nat Rev Immunol, 2009. **9**(12): p. 845-57.

135. Zhang, Y., L. Garcia-Ibanez, and K.M. Toellner, *Regulation of germinal center B-cell differentiation.* Immunol Rev, 2016. **270**(1): p. 8-19.

136. Shulman, Z., et al., *Dynamic signaling by T follicular helper cells during germinal center B cell selection.* Science, 2014. **345**(6200): p. 1058-62.

137. Victora, G.D., et al., *Germinal center dynamics revealed by multiphoton microscopy with a photoactivatable fluorescent reporter.* Cell, 2010. **143**(4): p. 592-605.

138. Courtney, A.H., et al., *Synthetic antigens reveal dynamics of BCR endocytosis during inhibitory signaling.* ACS Chem Biol, 2014. **9**(1): p. 202-10.

139. Khalil, A.M., J.C. Cambier, and M.J. Shlomchik, *B cell receptor signal transduction in the GC is short-circuited by high phosphatase activity.* Science, 2012. **336**(6085): p. 1178-81.

140. Yang, Z., et al., *Regulation of B cell fate by chronic activity of the IgE B cell receptor.* Elife, 2016. **5**.

141. MacLennan, I.C., *Germinal centers.* Annu Rev Immunol, 1994. **12**: p. 117-39.

142. Nutt, S.L. and D.M. Tarlinton, *Germinal center B and follicular helper T cells: siblings, cousins or just good friends?* Nat Immunol, 2011. **12**(6): p. 472-7.

143. Sage, P.T. and A.H. Sharpe, *T follicular regulatory cells.* Immunol Rev, 2016. **271**(1): p. 246-59.

144. Vinuesa, C.G., et al., *Follicular Helper T Cells.* Annu Rev Immunol, 2016. **34**: p. 335-68.

145. Vikstrom, I., et al., *Mcl-1 is essential for germinal center formation and B cell memory.* Science, 2010. **330**(6007): p. 1095-9.

146. Cruz, A.C., et al., *Fas/CD95 prevents autoimmunity independently of lipid raft localization and efficient apoptosis induction.* Nat Commun, 2016. **7**: p. 13895.

147. Hao, Z., et al., *Fas receptor expression in germinal-center B cells is essential for T and B lymphocyte homeostasis.* Immunity, 2008. **29**(4): p. 615-27.

148. Zhang, Y., et al., *Germinal center B cells govern their own fate via antibody feedback.* J Exp Med, 2013. **210**(3): p. 457-64.

149. Muramatsu, M., et al., *Specific expression of activation-induced cytidine deaminase (AID), a novel member of the RNA-editing deaminase family in germinal center B cells.* J Biol Chem, 1999. **274**(26): p. 18470-6.

150. Shinkura, R., et al., *Separate domains of AID are required for somatic hypermutation and class-switch recombination.* Nat Immunol, 2004. **5**(7): p. 707-12.

151. Liu, M. and D.G. Schatz, *Balancing AID and DNA repair during somatic hypermutation.* Trends Immunol, 2009. **30**(4): p. 173-81.

152. Weisel, F. and M. Shlomchik, *Memory B Cells of Mice and Humans.* Annu Rev Immunol, 2017. **35**: p. 255-284.

153. Kurosaki, T., K. Kometani, and W. Ise, *Memory B cells.* Nat Rev Immunol, 2015. **15**(3): p. 149-59.

154. McHeyzer-Williams, M., et al., *Molecular programming of B cell memory.* Nat Rev Immunol, 2011. **12**(1): p. 24-34.

155. Saito, M., et al., *A signaling pathway mediating downregulation of BCL6 in germinal center B cells is blocked by BCL6 gene alterations in B cell lymphoma.* Cancer Cell, 2007. **12**(3): p. 280-92.

156. Recaldin, T. and D.J. Fear, *Transcription factors regulating B cell fate in the germinal centre.* Clin Exp Immunol, 2016. **183**(1): p. 65-75.

157. Grootjans, J., et al., *The unfolded protein response in immunity and inflammation.* Nat Rev Immunol, 2016. **16**(8): p. 469-84.

158. Pengo, N., et al., *Plasma cells require autophagy for sustainable immunoglobulin production.* Nat Immunol, 2013. **14**(3): p. 298-305.

159. Kometani, K. and T. Kurosaki, *Differentiation and maintenance of long-lived plasma cells.* Curr Opin Immunol, 2015. **33**: p. 64-9.

160. Peperzak, V., et al., *Mcl-1 is essential for the survival of plasma cells.* Nat Immunol, 2013. **14**(3): p. 290-7.

161. Vinuesa, C.G., et al., *A RING-type ubiquitin ligase family member required to repress follicular helper T cells and autoimmunity.* Nature, 2005. **435**(7041): p. 452-8.

162. Linterman, M.A., et al., *Follicular helper T cells are required for systemic autoimmunity.* J Exp Med, 2009. **206**(3): p. 561-76.

163. Siess, D.C., et al., *A human gene coding for a membrane-associated nucleic acid-binding protein.* J Biol Chem, 2000. **275**(43): p. 33655-62.

164. Heissmeyer, V., K.M. Ansel, and A. Rao, *A plague of autoantibodies.* Nat Immunol, 2005. **6**(7): p. 642-4.

165. Glasmacher, E., et al., *Roquin binds inducible costimulator mRNA and effectors of mRNA decay to induce microRNA-independent post-transcriptional repression.* Nat Immunol, 2010. **11**(8): p. 725-33.

166. Linterman, M.A., et al., *Roquin differentiates the specialized functions of duplicated T cell costimulatory receptor genes CD28 and ICOS.* Immunity, 2009. **30**(2): p. 228-41.

167. Lee, S.K., et al., *Interferon-gamma excess leads to pathogenic accumulation of follicular helper T cells and germinal centers.* Immunity, 2012. **37**(5): p. 880-92.

168. Chang, P.P., et al., *Breakdown in repression of IFN-gamma mRNA leads to accumulation of self-reactive effector CD8+ T cells.* J Immunol, 2012. **189**(2): p. 701-10.

169. Labno, A., R. Tomecki, and A. Dziembowski, *Cytoplasmic RNA decay pathways - Enzymes and mechanisms.* Biochim Biophys Acta, 2016. **1863**(12): p. 3125-3147.

170. Braun, K.A. and E.T. Young, *Coupling mRNA synthesis and decay.* Mol Cell Biol, 2014. **34**(22): p. 4078-87.

171. Goetz, A.E. and M. Wilkinson, *Stress and the nonsense-mediated RNA decay pathway.* Cell Mol Life Sci, 2017.

172. Hogg, J.R., *Viral Evasion and Manipulation of Host RNA Quality Control Pathways.* J Virol, 2016. **90**(16): p. 7010-8.

173. Hug, N., D. Longman, and J.F. Caceres, *Mechanism and regulation of the nonsense-mediated decay pathway.* Nucleic Acids Res, 2016. **44**(4): p. 1483-95.

174. Decker, C.J. and R. Parker, *P-bodies and stress granules: possible roles in the control of translation and mRNA degradation.* Cold Spring Harb Perspect Biol, 2012. **4**(9): p. a012286.

175. Mauer, J., et al., *Reversible methylation of m6Am in the 5' cap controls mRNA stability.* Nature, 2017. **541**(7637): p. 371-375.

176. Merrick, W.C., *Eukaryotic protein synthesis: still a mystery.* J Biol Chem, 2010. **285**(28): p. 21197-201.

177. Eulalio, A., I. Behm-Ansmant, and E. Izaurralde, *P bodies: at the crossroads of post-transcriptional pathways.* Nat Rev Mol Cell Biol, 2007. **8**(1): p. 9-22.

178. Garneau, N.L., J. Wilusz, and C.J. Wilusz, *The highways and byways of mRNA decay.* Nat Rev Mol Cell Biol, 2007. **8**(2): p. 113-26.

179. Grudzien-Nogalska, E. and M. Kiledjian, *New insights into decapping enzymes and selective mRNA decay.* Wiley Interdiscip Rev RNA, 2017. **8**(1).

180. Uehata, T. and S. Akira, *mRNA degradation by the endoribonuclease Regnase-1/ZC3H12a/MCPIP-1.* Biochim Biophys Acta, 2013. **1829**(6-7): p. 708-13.

181. Anderson, P., *Post-transcriptional control of cytokine production.* Nat Immunol, 2008. **9**(4): p. 353-9.

182. Vlasova-St Louis, I. and P.R. Bohjanen, *Post-transcriptional regulation of cytokine and growth factor signaling in cancer.* Cytokine Growth Factor Rev, 2017. **33**: p. 83-93.

183. Braun, J.E., E. Huntzinger, and E. Izaurralde, *The role of GW182 proteins in miRNA-mediated gene silencing.* Adv Exp Med Biol, 2013. **768**: p. 147-63.

184. Niinuma, S. and Y. Tomari, *ATP is dispensable for both miRNA- and Smaug-mediated deadenylation reactions.* RNA, 2017. **23**(6): p. 866-871.

185. Suzuki, A., et al., *Dead end1 is an essential partner of NANOS2 for selective binding of target RNAs in male germ cell development.* EMBO Rep, 2016. **17**(1): p. 37-46.

186. Wahle, E. and G.S. Winkler, *RNA decay machines: deadenylation by the Ccr4-not and Pan2-Pan3 complexes.* Biochim Biophys Acta, 2013. **1829**(6-7): p. 561-70.

187. Schlundt, A., et al., *RNA recognition by Roquin in posttranscriptional gene regulation.* Wiley Interdiscip Rev RNA, 2016. **7**(4): p. 455-69.

188. Sakurai, S., U. Ohto, and T. Shimizu, *Structure of human Roquin-2 and its complex with constitutive-decay element RNA.* Acta Crystallogr F Struct Biol Commun, 2015. **71**(Pt 8): p. 1048-54.

189. Kersey, P.J., et al., *Ensembl Genomes 2016: more genomes, more complexity.* Nucleic Acids Res, 2016. **44**(D1): p. D574-80.

190. Heissmeyer, V. and K.U. Vogel, *Molecular control of Tfh-cell differentiation by Roquin family proteins.* Immunol Rev, 2013. **253**(1): p. 273-89.

191. Vogel, K.U., et al., *Roquin paralogs 1 and 2 redundantly repress the Icos and Ox40 costimulator mRNAs and control follicular helper T cell differentiation.* Immunity, 2013. **38**(4): p. 655-68.

192. Athanasopoulos, V., et al., *The ROQUIN family of proteins localizes to stress granules via the ROQ domain and binds target mRNAs.* FEBS J, 2010. **277**(9): p. 2109-27.

193. Schaefer, J.S., et al., *Selective upregulation of microRNA expression in peripheral blood leukocytes in IL-10-/- mice precedes expression in the colon.* J Immunol, 2011. **187**(11): p. 5834-41.

194. Schaefer, J.S., D. Montufar-Solis, and J.R. Klein, *A role for IL-10 in the transcriptional regulation of Roquin-1.* Gene, 2014. **549**(1): p. 134-40.

195. Carey, A.J., C.K. Tan, and G.C. Ulett, *Infection-induced IL-10 and JAK-STAT: A review of the molecular circuitry controlling immune hyperactivity in response to pathogenic microbes.* JAKSTAT, 2012. **1**(3): p. 159-67.

196. Leppek, K., et al., *Roquin promotes constitutive mRNA decay via a conserved class of stem-loop recognition motifs.* Cell, 2013. **153**(4): p. 869-81.

197. Srivastava, M., et al., *Roquin binds microRNA-146a and Argonaute2 to regulate microRNA homeostasis.* Nat Commun, 2015. **6**: p. 6253.

198. Gewies, A., et al., *Uncoupling Malt1 threshold function from paracaspase activity results in destructive autoimmune inflammation.* Cell Rep, 2014. **9**(4): p. 1292-305.

199. Jeltsch, K.M., et al., *Cleavage of roquin and regnase-1 by the paracaspase MALT1 releases their cooperatively repressed targets to promote T(H)17 differentiation.* Nat Immunol, 2014. **15**(11): p. 1079-89.

200. Meininger, I. and D. Krappmann, *Lymphocyte signaling and activation by the CARMA1-BCL10-MALT1 signalosome.* Biol Chem, 2016. **397**(12): p. 1315-1333.

201. Mino, T., et al., *Regnase-1 and Roquin Regulate a Common Element in Inflammatory mRNAs by Spatiotemporally Distinct Mechanisms.* Cell, 2015. **161**(5): p. 1058-73.

202. Pratama, A., et al., *Roquin-2 shares functions with its paralog Roquin-1 in the repression of mRNAs controlling T follicular helper cells and systemic inflammation.* Immunity, 2013. **38**(4): p. 669-80.

203. Zhang, Q., et al., *New Insights into the RNA-Binding and E3 Ubiquitin Ligase Activities of Roquins.* Sci Rep, 2015. **5**: p. 15660.

204. Ramiscal, R.R., et al., *Attenuation of AMPK signaling by ROQUIN promotes T follicular helper cell formation.* Elife, 2015. **4**.

205. Schlundt, A., et al., *Structural basis for RNA recognition in roquin-mediated post-transcriptional gene regulation.* Nat Struct Mol Biol, 2014. **21**(8): p. 671-8.

206. Schuetz, A., et al., *Roquin binding to target mRNAs involves a winged helix-turn-helix motif.* Nat Commun, 2014. **5**: p. 5701.

207. Tan, D., et al., *The ROQ domain of Roquin recognizes mRNA constitutive-decay element and double-stranded RNA.* Nat Struct Mol Biol, 2014. **21**(8): p. 679-85.

208. Codutti, L., et al., *A Distinct, Sequence-Induced Conformation Is Required for Recognition of the Constitutive Decay Element RNA by Roquin.* Structure, 2015. **23**(8): p. 1437-47.

209. Murakawa, Y., et al., *RC3H1 post-transcriptionally regulates A20 mRNA and modulates the activity of the IKK/NF-kappaB pathway.* Nat Commun, 2015. **6**: p. 7367.

210. Janowski, R., et al., *Roquin recognizes a non-canonical hexaloop structure in the 3′-UTR of Ox40.* Nat Commun, 2016. **7**: p. 11032.

211. Li, W., et al., *RLE-1, an E3 ubiquitin ligase, regulates C. elegans aging by catalyzing DAF-16 polyubiquitination.* Dev Cell, 2007. **12**(2): p. 235-46.

212. Bertossi, A., et al., *Loss of Roquin induces early death and immune deregulation but not autoimmunity.* J Exp Med, 2011. **208**(9): p. 1749-56.

213. Maruyama, T., et al., *Roquin-2 promotes ubiquitin-mediated degradation of ASK1 to regulate stress responses.* Sci Signal, 2014. **7**(309): p. ra8.

214. Yamamoto, M., et al., *Key function for the Ubc13 E2 ubiquitin-conjugating enzyme in immune receptor signaling.* Nat Immunol, 2006. **7**(9): p. 962-70.

215. Dhodapkar, M.V. and V. Kumar, *Type II NKT Cells and Their Emerging Role in Health and Disease.* J Immunol, 2017. **198**(3): p. 1015-1021.

216. Drees, C., et al., *Roquin Paralogs Differentially Regulate Functional NKT Cell Subsets.* J Immunol, 2017. **198**(7): p. 2747-2759.

217. Ji, Y.R., et al., *Over-expression of Roquin aggravates T cell mediated hepatitis in transgenic mice using T cell specific promoter.* Biochem Biophys Res Commun, 2014. **452**(3): p. 822-7.

218. Ji, Y.R., et al., *Enforced expression of roquin protein in T cells exacerbates the incidence and severity of experimental arthritis.* J Biol Chem, 2012. **287**(50): p. 42269-77.

219. Kim, H.J., et al., *The role of Roquin overexpression in the modulation of signaling during in vitro and ex vivo T-cell activation.* Biochem Biophys Res Commun, 2012. **417**(1): p. 280-6.

220. Brunner, C., et al., *B cell-specific transgenic expression of Bcl2 rescues early B lymphopoiesis but not B cell responses in BOB.1/OBF.1-deficient mice.* J Exp Med, 2003. **197**(9): p. 1205-11.

221. Chevrier, S., et al., *Germinal center-independent, IgM-mediated autoimmunity in sanroque mice lacking Obf1.* Immunol Cell Biol, 2014. **92**(1): p. 12-9.

222. Georgiades, P., et al., *VavCre transgenic mice: a tool for mutagenesis in hematopoietic and endothelial lineages.* Genesis, 2002. **34**(4): p. 251-6.

223. Bianco, P., et al., *Bone marrow stromal stem cells: nature, biology, and potential applications.* Stem Cells, 2001. **19**(3): p. 180-92.

224. Hobeika, E., et al., *Testing gene function early in the B cell lineage in mb1-cre mice.* Proc Natl Acad Sci U S A, 2006. **103**(37): p. 13789-94.

225. Rickert, R.C., J. Roes, and K. Rajewsky, *B lymphocyte-specific, Cre-mediated mutagenesis in mice.* Nucleic Acids Res, 1997. **25**(6): p. 1317-8.

226. Litzenburger, T., et al., *B lymphocytes producing demyelinating autoantibodies: development and function in gene-targeted transgenic mice.* J Exp Med, 1998. **188**(1): p. 169-80.

227. Koralov, S.B., et al., *Dicer ablation affects antibody diversity and cell survival in the B lymphocyte lineage.* Cell, 2008. **132**(5): p. 860-74.

228. Heger, K., et al., *CreER(T2) expression from within the c-Kit gene locus allows efficient inducible gene targeting in and ablation of mast cells.* Eur J Immunol, 2014. **44**(1): p. 296-306.

229. Engler, C., R. Kandzia, and S. Marillonnet, *A one pot, one step, precision cloning method with high throughput capability.* PLoS One, 2008. **3**(11): p. e3647.

230. Ivics, Z., et al., *Molecular reconstruction of Sleeping Beauty, a Tc1-like transposon from fish, and its transposition in human cells.* Cell, 1997. **91**(4): p. 501-10.

231. Scholz, J., et al., *A new method to customize protein expression vectors for fast, efficient and background free parallel cloning.* BMC Biotechnol, 2013. **13**: p. 12.

232. Peitz, M., et al., *Ability of the hydrophobic FGF and basic TAT peptides to promote cellular uptake of recombinant Cre recombinase: a tool for efficient genetic engineering of mammalian genomes.* Proc Natl Acad Sci U S A, 2002. **99**(7): p. 4489-94.

233. Kleinridders, A., et al., *PLRG1 is an essential regulator of cell proliferation and apoptosis during vertebrate development and tissue homeostasis.* Mol Cell Biol, 2009. **29**(11): p. 3173-85.

234. Feltham, R., et al., *Tumor necrosis factor (TNF) signaling, but not TWEAK (TNF-like weak inducer of apoptosis)-triggered cIAP1 (cellular inhibitor of apoptosis protein 1) degradation, requires cIAP1 RING dimerization and E2 binding.* J Biol Chem, 2010. **285**(23): p. 17525-36.

235. Vince, J.E., et al., *TWEAK-FN14 signaling induces lysosomal degradation of a cIAP1-TRAF2 complex to sensitize tumor cells to TNFalpha.* J Cell Biol, 2008. **182**(1): p. 171-84.

236. Schneider, C.A., W.S. Rasband, and K.W. Eliceiri, *NIH Image to ImageJ: 25 years of image analysis.* Nat Methods, 2012. **9**(7): p. 671-5.

237. Raschka, S., J. Bemister-Buffington, and L.A. Kuhn, *Detecting the native ligand orientation by interfacial rigidity: SiteInterlock.* Proteins, 2016. **84**(12): p. 1888-1901.

238. Schmidt-Supprian, M. and K. Rajewsky, *Vagaries of conditional gene targeting.* Nat Immunol, 2007. **8**(7): p. 665-8.

239. Derudder, E., et al., *Development of immunoglobulin lambda-chain-positive B cells, but not editing of immunoglobulin kappa-chain, depends on NF-kappaB signals.* Nat Immunol, 2009. **10**(6): p. 647-54.

240. Liu, H., et al., *Yin Yang 1 is a critical regulator of B-cell development.* Genes Dev, 2007. **21**(10): p. 1179-89.

241. Pelanda, R., et al., *B cell progenitors are arrested in maturation but have intact VDJ recombination in the absence of Ig-alpha and Ig-beta.* J Immunol, 2002. **169**(2): p. 865-72.

242. Heger, K., et al., *A novel Cre recombinase reporter mouse strain facilitates selective and efficient infection of primary immune cells with adenoviral vectors.* Eur J Immunol, 2015. **45**(6): p. 1614-20.

243. Novobrantseva, T.I., et al., *Rearrangement and expression of immunoglobulin light chain genes can precede heavy chain expression during normal B cell development in mice.* J Exp Med, 1999. **189**(1): p. 75-88.

244. Papavasiliou, F., M. Jankovic, and M.C. Nussenzweig, *Surrogate or conventional light chains are required for membrane immunoglobulin mu to activate the precursor B cell transition.* J Exp Med, 1996. **184**(5): p. 2025-30.

245. Schuh, W., et al., *Cutting edge: signaling and cell surface expression of a mu H chain in the absence of lambda 5: a paradigm revisited.* J Immunol, 2003. **171**(7): p. 3343-7.

246. Ubelhart, R., M. Werner, and H. Jumaa, *Assembly and Function of the Precursor B-Cell Receptor.* Curr Top Microbiol Immunol, 2016. **393**: p. 3-25.

247. De Silva, N.S., et al., *The diverse roles of IRF4 in late germinal center B-cell differentiation.* Immunol Rev, 2012. **247**(1): p. 73-92.

248. Ma, S., et al., *Ikaros and Aiolos inhibit pre-B-cell proliferation by directly suppressing c-Myc expression.* Mol Cell Biol, 2010. **30**(17): p. 4149-58.

249. Schweighoffer, E., et al., *Unexpected requirement for ZAP-70 in pre-B cell development and allelic exclusion.* Immunity, 2003. **18**(4): p. 523-33.

250. Melchers, F., *Checkpoints that control B cell development.* J Clin Invest, 2015. **125**(6): p. 2203-10.

251. Opstelten, D. and D.G. Osmond, *Pre-B cells in mouse bone marrow: immunofluorescence stathmokinetic studies of the proliferation of cytoplasmic mu-chain-bearing cells in normal mice.* J Immunol, 1983. **131**(6): p. 2635-40.

252. Osmond, D.G., *Proliferation kinetics and the lifespan of B cells in central and peripheral lymphoid organs.* Curr Opin Immunol, 1991. **3**(2): p. 179-85.

253. Scholzen, T. and J. Gerdes, *The Ki-67 protein: from the known and the unknown.* J Cell Physiol, 2000. **182**(3): p. 311-22.

254. Wojcik, K. and J.W. Dobrucki, *Interaction of a DNA intercalator DRAQ5, and a minor groove binder SYTO17, with chromatin in live cells--influence on chromatin organization and histone-DNA interactions.* Cytometry A, 2008. **73**(6): p. 555-62.

255. Cadera, E.J., et al., *NF-kappaB activity marks cells engaged in receptor editing.* J Exp Med, 2009. **206**(8): p. 1803-16.

256. Matiasova, A., et al., *Flow cytometric determination of 5-bromo-2'-deoxyuridine pharmacokinetics in blood serum after intraperitoneal administration to rats and mice.* Histochem Cell Biol, 2014. **142**(6): p. 703-12.

257. Malbec, O., et al., *Negative regulation of mast cell proliferation by FcgammaRIIB.* Mol Immunol, 2002. **38**(16-18): p. 1295-9.

258. Heger, K., et al., *A20-deficient mast cells exacerbate inflammatory responses in vivo.* PLoS Biol, 2014. **12**(1): p. e1001762.

259. Schmitz, J., et al., *IL-33, an interleukin-1-like cytokine that signals via the IL-1 receptor-related protein ST2 and induces T helper type 2-associated cytokines.* Immunity, 2005. **23**(5): p. 479-90.

260. Bettelli, E., et al., *Myelin oligodendrocyte glycoprotein-specific T and B cells cooperate to induce a Devic-like disease in mice.* J Clin Invest, 2006. **116**(9): p. 2393-402.

261. Krishnamoorthy, G., et al., *Spontaneous opticospinal encephalomyelitis in a double-transgenic mouse model of autoimmune T cell/B cell cooperation.* J Clin Invest, 2006. **116**(9): p. 2385-92.

262. Ayre, D.C., et al., *Dynamic regulation of CD24 expression and release of CD24-containing microvesicles in immature B cells in response to CD24 engagement.* Immunology, 2015. **146**(2): p. 217-33.

263. Nielsen, P.J., et al., *Altered erythrocytes and a leaky block in B-cell development in CD24/HSA-deficient mice.* Blood, 1997. **89**(3): p. 1058-67.

264. Ma, S., et al., *IFN regulatory factor 4 and 8 promote Ig light chain kappa locus activation in pre-B cell development.* J Immunol, 2006. **177**(11): p. 7898-904.

265. Novobrantseva, T., et al., *Stochastic pairing of Ig heavy and light chains frequently generates B cell antigen receptors that are subject to editing in vivo.* Int Immunol, 2005. **17**(4): p. 343-50.

266. Novobrantseva, T., *Expressing a Natural Autoreactive Immunoglobulin Receptor in Vivo. (Doctoral thesis).* Mathematisch-Naturwissenschaftliche Fakultät, 2000. **University of Cologne, Cologne, Germany**.

267. Cazac, B.B. and J. Roes, *TGF-beta receptor controls B cell responsiveness and induction of IgA in vivo.* Immunity, 2000. **13**(4): p. 443-51.

268. Wang, J.H., et al., *Mechanisms promoting translocations in editing and switching peripheral B cells.* Nature, 2009. **460**(7252): p. 231-6.

269. Rosa, P., et al., *Brefeldin A inhibits the formation of constitutive secretory vesicles and immature secretory granules from the trans-Golgi network.* Eur J Cell Biol, 1992. **59**(2): p. 265-74.

270. Hunter, C.A. and S.A. Jones, *IL-6 as a keystone cytokine in health and disease.* Nat Immunol, 2015. **16**(5): p. 448-57.

271. Matsushita, K., et al., *Zc3h12a is an RNase essential for controlling immune responses by regulating mRNA decay.* Nature, 2009. **458**(7242): p. 1185-90.

272. Zheng, N., et al., *Structure of the Cul1-Rbx1-Skp1-F boxSkp2 SCF ubiquitin ligase complex.* Nature, 2002. **416**(6882): p. 703-9.

273. Brandl, A., et al., *The microprocessor component, DGCR8, is essential for early B-cell development in mice.* Eur J Immunol, 2016. **46**(12): p. 2710-2718.

274. Coffre, M., et al., *miRNAs Are Essential for the Regulation of the PI3K/AKT/FOXO Pathway and Receptor Editing during B Cell Maturation.* Cell Rep, 2016. **17**(9): p. 2271-2285.

275. Yu, D., et al., *Roquin represses autoimmunity by limiting inducible T-cell co-stimulator messenger RNA.* Nature, 2007. **450**(7167): p. 299-303.

276. Batista, C.R., et al., *PU.1 Regulates Ig Light Chain Transcription and Rearrangement in Pre-B Cells during B Cell Development.* J Immunol, 2017. **198**(4): p. 1565-1574.

277. Sitte, S., et al., *JAB1 is essential for B cell development and germinal center formation and inversely regulates Fas ligand and Bcl6 expression.* J Immunol, 2012. **188**(6): p. 2677-86.

278. Lu, R., et al., *IRF-4,8 orchestrate the pre-B-to-B transition in lymphocyte development.* Genes Dev, 2003. **17**(14): p. 1703-8.

279. Calame, K., et al., *Mouse Cmu heavy chain immunoglobulin gene segment contains three intervening sequences separating domains.* Nature, 1980. **284**(5755): p. 452-5.

280. Kan, J.L. and M.R. Green, *Pre-mRNA splicing of IgM exons M1 and M2 is directed by a juxtaposed splicing enhancer and inhibitor.* Genes Dev, 1999. **13**(4): p. 462-71.

281. Redecke, V., et al., *Hematopoietic progenitor cell lines with myeloid and lymphoid potential.* Nat Methods, 2013. **10**(8): p. 795-803.

282. Rosenbaum, M., et al., *MZB1 is a GRP94 cochaperone that enables proper immunoglobulin heavy chain biosynthesis upon ER stress.* Genes Dev, 2014. **28**(11): p. 1165-78.

283. Yang, C.Y., et al., *Interaction of CCR4-NOT with EBF1 regulates gene-specific transcription and mRNA stability in B lymphopoiesis.* Genes Dev, 2016. **30**(20): p. 2310-2324.

284. Huttl, S., et al., *Processing of CD74 by the Intramembrane Protease SPPL2a Is Critical for B Cell Receptor Signaling in Transitional B Cells.* J Immunol, 2015. **195**(4): p. 1548-63.

285. Ramadani, F., et al., *The PI3K isoforms p110alpha and p110delta are essential for pre-B cell receptor signaling and B cell development.* Sci Signal, 2010. **3**(134): p. ra60.

286. Heng, T.S., M.W. Painter, and C. Immunological Genome Project, *The Immunological Genome Project: networks of gene expression in immune cells.* Nat Immunol, 2008. **9**(10): p. 1091-4.

287. Cheng, A.M., et al., *Syk tyrosine kinase required for mouse viability and B-cell development.* Nature, 1995. **378**(6554): p. 303-6.

288. Turner, M., et al., *Perinatal lethality and blocked B-cell development in mice lacking the tyrosine kinase Syk.* Nature, 1995. **378**(6554): p. 298-302.

289. Alsadeq, A., et al., *The role of the Syk/Shp-1 kinase-phosphatase equilibrium in B cell development and signaling.* J Immunol, 2014. **193**(1): p. 268-76.

290. Flemming, A., et al., *The adaptor protein SLP-65 acts as a tumor suppressor that limits pre-B cell expansion.* Nat Immunol, 2003. **4**(1): p. 38-43.

291. Jumaa, H., et al., *The absence of SLP65 and Btk blocks B cell development at the preB cell receptor-positive stage.* Eur J Immunol, 2001. **31**(7): p. 2164-9.

292. Sabbattini, P., et al., *Binding of Ikaros to the lambda5 promoter silences transcription through a mechanism that does not require heterochromatin formation.* EMBO J, 2001. **20**(11): p. 2812-22.

293. Thompson, E.C., et al., *Ikaros DNA-binding proteins as integral components of B cell developmental-stage-specific regulatory circuits.* Immunity, 2007. **26**(3): p. 335-44.

294. Nakayama, J., et al., *BLNK suppresses pre-B-cell leukemogenesis through inhibition of JAK3.* Blood, 2009. **113**(7): p. 1483-92.

295. Allman, D., et al., *BCL-6 expression during B-cell activation.* Blood, 1996. **87**(12): p. 5257-68.

296. Basso, K. and R. Dalla-Favera, *Roles of BCL6 in normal and transformed germinal center B cells.* Immunol Rev, 2012. **247**(1): p. 172-83.

297. Oestreich, K.J., S.E. Mohn, and A.S. Weinmann, *Molecular mechanisms that control the expression and activity of Bcl-6 in TH1 cells to regulate flexibility with a TFH-like gene profile.* Nat Immunol, 2012. **13**(4): p. 405-11.

298. Walker, S.R., E.A. Nelson, and D.A. Frank, *STAT5 represses BCL6 expression by binding to a regulatory region frequently mutated in lymphomas.* Oncogene, 2007. **26**(2): p. 224-33.

299. Meixlsperger, S., et al., *Conventional light chains inhibit the autonomous signaling capacity of the B cell receptor.* Immunity, 2007. **26**(3): p. 323-33.

300. Shalem, O., N.E. Sanjana, and F. Zhang, *High-throughput functional genomics using CRISPR-Cas9.* Nat Rev Genet, 2015. **16**(5): p. 299-311.

301. Malin, S., et al., *Role of STAT5 in controlling cell survival and immunoglobulin gene recombination during pro-B cell development.* Nat Immunol, 2010. **11**(2): p. 171-9.

302. Patton, D.T., A.W. Plumb, and N. Abraham, *The survival and differentiation of pro-B and pre-B cells in the bone marrow is dependent on IL-7Ralpha Tyr449.* J Immunol, 2014. **193**(7): p. 3446-55.

303. Dang, J., et al., *The RING domain of Mdm2 can inhibit cell proliferation.* Cancer Res, 2002. **62**(4): p. 1222-30.

304. Thompson, B.J., et al., *Control of hematopoietic stem cell quiescence by the E3 ubiquitin ligase Fbw7.* J Exp Med, 2008. **205**(6): p. 1395-408.

305. Inoue, T., et al., *CNOT3 contributes to early B cell development by controlling Igh rearrangement and p53 mRNA stability.* J Exp Med, 2015. **212**(9): p. 1465-79.

306. Boland, A., et al., *Structure and assembly of the NOT module of the human CCR4-NOT complex.* Nat Struct Mol Biol, 2013. **20**(11): p. 1289-97.

307. Collart, M.A., O.O. Panasenko, and S.I. Nikolaev, *The Not3/5 subunit of the Ccr4-Not complex: a central regulator of gene expression that integrates signals between the cytoplasm and the nucleus in eukaryotic cells.* Cell Signal, 2013. **25**(4): p. 743-51.

308. Sasaki, Y. and K. Iwai, *Roles of the NF-kappaB Pathway in B-Lymphocyte Biology.* Curr Top Microbiol Immunol, 2016. **393**: p. 177-209.

309. Bevington, S. and J. Boyes, *Transcription-coupled eviction of histones H2A/H2B governs V(D)J recombination.* EMBO J, 2013. **32**(10): p. 1381-92.

310. King, J.K., et al., *Regulation of Marginal Zone B-Cell Differentiation by MicroRNA-146a.* Front Immunol, 2016. **7**: p. 670.

311. Gupta-Rossi, N., et al., *Monoubiquitination and endocytosis direct gamma-secretase cleavage of activated Notch receptor.* J Cell Biol, 2004. **166**(1): p. 73-83.

312. Nakagawa, T. and K. Nakayama, *Protein monoubiquitylation: targets and diverse functions.* Genes Cells, 2015. **20**(7): p. 543-62.

313. Laky, K. and B.J. Fowlkes, *Notch signaling in CD4 and CD8 T cell development.* Curr Opin Immunol, 2008. **20**(2): p. 197-202.

314. Hippen, K.L., et al., *In vivo assessment of the relative contributions of deletion, anergy, and editing to B cell self-tolerance.* J Immunol, 2005. **175**(2): p. 909-16.

315. Pelanda, R., et al., *Receptor editing in a transgenic mouse model: site, efficiency, and role in B cell tolerance and antibody diversification.* Immunity, 1997. **7**(6): p. 765-75.

316. Gay, D., et al., *Receptor editing: an approach by autoreactive B cells to escape tolerance.* J Exp Med, 1993. **177**(4): p. 999-1008.

317. Huang, H., et al., *Induction of tolerance in arthritogenic B cells with receptors of differing affinity for self-antigen.* Proc Natl Acad Sci U S A, 2006. **103**(10): p. 3734-9.

318. Cerutti, A., M. Cols, and I. Puga, *Marginal zone B cells: virtues of innate-like antibody-producing lymphocytes.* Nat Rev Immunol, 2013. **13**(2): p. 118-32.

319. Schwickert, T.A., et al., *In vivo imaging of germinal centres reveals a dynamic open structure.* Nature, 2007. **446**(7131): p. 83-7.

320. Lee, P., et al., *Differing Requirements for MALT1 Function in Peripheral B Cell Survival and Differentiation.* J Immunol, 2017. **198**(3): p. 1066-1080.

321. Hasegawa, H., et al., *Expanding Diversity in Molecular Structures and Functions of the IL-6/IL-12 Heterodimeric Cytokine Family.* Front Immunol, 2016. **7**: p. 479.

322. Egwuagu, C.E., et al., *Interleukin 35: Critical regulator of immunity and lymphocyte-mediated diseases.* Cytokine Growth Factor Rev, 2015. **26**(5): p. 587-93.

323. Shen, P., et al., *IL-35-producing B cells are critical regulators of immunity during autoimmune and infectious diseases.* Nature, 2014. **507**(7492): p. 366-70.

List of abbreviations

aa	amino acid
ADE	alternative decay element
AID	activation-induced cytidine deaminase
ANA	anti-nuclear antibodies
APC	allophycocyanin
APRIL	a proliferation inducing ligand
ATK	also known as PKB
BACH2	BTB and CNC homolog 2
BAFF	B cell-activating factor belonging to TNF family
BCL2	anti-apoptotic protein B cell lymphoma 2
BCL6	B cell lymphoma 6
BCMA	B cell maturation antigen
BCR	B cell receptor
BER	base excision repair
Bim	pro-apoptotic protein Bcl-2 interacting mediator of cell death
BLIMP1	B lymphocyte-induced maturation protein 1
BM	bone marrow
$Ca2^+$	calcium ion
(Δ)CAR	truncated version of the human coxsackie adenovirus receptor
CARD	caspase activation and recruitment domain
CARMA1	CARD-containing membrane-associated guanylate kinase-1
Cas	CRISPR-associated
CD	cluster of differentiation
CDE	constitutive decay element
CD40L	CD40 ligand
CDK	cyclin-dependent kinase
c-Myc	myelocytomatosis oncogene cellular homolog
cNHEJ	classical non-homologous end joining repair pathway
CpG	cytosine-guanosine deoxynucleotide-containing oligonucleotides
CRISPR	clustered regulary interspaced short palindromic repeats
CSR	class switch recombination
CXCL	CXC-chemokine ligand
CXCR	CXC-chemokine receptor
DL-1	Delta-like-1

DNA	deoxyribonucleic acid
DNA-PK	DNA-dependent protein kinase
DSB	double strand breaks
DTT	dithiothreitol
DZ	dark zone
EBF	early Bcell factor
ELISA	enzyme-linked immunosorbent assay
EZH2	enhancer of zeste homolog 2
F	floxed – loxP-flanked
FAK	focal adhesion kinase
FCS	fetal calf serum
fDC	follicular dendritic cells
FO	follicular
FOXO	forkhead box O
FSC-A/H	forward scatter area/height
GALT	gut-associated lymphoid tissue
GC	germinal center
GC B	germinal center B cell
GFP	green fluorescent protein
HRP	horseradish peroxidase
ICOS	inducible Tcell co-stimulator
ICOSL	ICOS ligand
IFN	interferon
Ig	immunoglobulin
IgH	immunoglobulin heavy (chain)
IgL	immunoglobulin light (chain)
IL	interleukin
IRES	internal ribosomal entry site
IRF4, 8	interferon regulatory factor 4, 8
LN	lymph nodes
LPS	lipopolysaccharide
LZ	light zone
MALT	mucosa-assocaited lymphoid tissue
MALT1	MALT lymphoma translocation protein 1
MEF	mouse embryonic fibroblasts
MFI	median fluorescence intensity
MHC-II	major histocompatibility complex class II

miRNA	microRNA
mLN	mesenteric lymph nodes
MMR	mismatch repair
MZ	marginal zone
MZP	marginal zone precursor
NF-κB	nuclear factor κ-light-chain-enhancer of activated B cells
PAX5	paired box protein 5
PC	peritoneal cavity
PCR	polymerase chain reaction
PI3K	phosphatidylinositol 3-kinase
PKB	protein kinase B
PNA	peanut agglutinin
PP	Peyer's patches
PVDF	polyvinylidene fluoride
R	Rc3h
RAG	recombination activation gene
RNA	ribonucleic acid
SDS-PAGE	sodium dodecyl sulfate polyacrylamide gel electrophoresis
SHM	somatic hypermutation
SLE	systemic lupus erythematosus
SLP65	SH2-domain-containing leukocytes protein of 65kDa
SPL	spleen
SSC-A/H	side scatter area/height
STAT	signal transducer and activator of transcription
SYK	spleen tyrosine kinase
TCR	T cell receptor
TD	T cell-dependent or thymus-dependent
T_{FH}	follicular helper Tcell
TI	T cell-independent or thymus-independent
TLR	toll-like receptor
TNF(R)	tumor necrosis factor (receptor)
Treg	regulatory Tcell
wt	wild type
XBP-1	X-box-binding protein 1
XRCC4	X-ray repair cross complementing protein 4
ZAP70	70kDa zeta-chain associated protein
7-AAD	7-amino-actinomycin D

Acknowledgements

First and foremost I would like to thank Marc Schmidt-Supprian. His exceptional approach of doing science as well as his idea of research as a collaborative effort have been impressing me since the day I had applied to his lab. I am thankful for his brilliant ideas and constant support during all the years. I am very grateful for the unique opportunity to work on this exciting research project with its many different aspects that allowed me to make very valuable scientific experiences, but also enjoy the company of fantastic researchers and friends.

I would like to thank my Doktormutter Elena Conti for her continuous interest in the project, her smart advice and the amazing opportunity to have collaborated with her as well as Christian Benda and Ajla Hrle from her department on resolving the structure of the ROQ domain. It has been indispensable to get her guidance on this facet of my PhD project as well as her perspective on the whole project.

I am very much indebted to Hans-Martin Jäck, who not just volunteered to become a member of my thesis advisory committee despite the efforts this meant, but whose amenability and helpfulness made learning more about B cell immunology very rewarding. Not to forget his kind invitations to Erlangen and the B cell Fora.

I also want to thank PD Dr. Dietmar Marting, Prof. Dr. Olivia Merkel and Prof. Dr. Klaus Förstemann for taking the time to review my thesis and being members of my PhD board of examiners.

I am very thankful to former and current members of the Schmidt-Supprian laboratory. I greatly appreciate the numerous scientific discussions, the fantastic moral support and being part of this smart bunch, which also contributed to forming lasting friendships. Thank you so much for all the comments and suggestions that helped to improve my project.

I am very much obliged to Christoph Vahl, who with his sheer endless patience introduced me to the potential of flow cytometry. Furthermore, he and Nathalie Vahl made my start in Munich much more pleasant. I would like to thank Klaus Heger and Yuanyuan Chu for sharing their scientific expertise and interesting conversations as well as the many common fun activities around Munich and Christoph Drees for bringing additional positive spirit to the lab. I am very much grateful to Maike Kober and Valeria Soberón, with whom I shared my entire PhD life and many wonderful moments ever since I joined Marc's lab. Your support and company at the desk and bench has been invaluable.

I thank Leonie Kohlhammer, Carina Steinecke and Sabrina Bortoluzzi for bringing fresh ideas and their great willingness to expand the technical know-how in the lab, Mayur Bakshi for fun conversations and contributing his knowledge on the investigation of gene expression and Tim Ammon for lightening up the mood in the office when needed sharing his scientific expertise. I would like to acknowledge the technical support of Claudia Mugler, Julia Knogler, Barbara Habermehl, Kasia Jopek and Madlen Oelsner that only allowed planning huge experiments.

I am very much indebted to Christian Benda and Ajla Hrle for an outstanding collaborative scientific experience and sharing their passion for their field of research.

I am grateful to Sergei Koralov, my former mentor at the IDI in Boston, who really excited me for B cell research and helped greatly in joining Marc's lab.

I also want to thank members of the Fässler department at the Max Planck Institute of Biochemistry and Sabine Suppmann. Likewise I would like to thank Hans-Joerg Schaeffer, Ingrid Wolf and Maximiliane Reif from the coordination office of the International Max Planck Research School for Molecular and Cellular Life Sciences for their support.

Last but certainly not least, I would like particularly to thank my family and friends, whose patience and understanding for my commitment to this PhD project has carried me during these years. I am very grateful for the help, friendship and never-ending moral support of Johanna, Sebastian and Anne Cremer. A huge "thank you" to my parents, Michael and Maria Rieß, for their constant encouragement and counseling as well as the opportunity to start this whole academic journey. I would like to express my deepest and most heartfelt gratitude to my wife Marina Rieß, whose enduring patience, love and encouragement allowed me to overcome any obstacle.